Removal of Copper from Simulated Wastewater by Applying Electromagnetic Adsorption for Locally Prepared Activated Carbon of Banana Peels

Hayder Mohammed Abdul-Hameed
Associate Professor
Engineering College - Baghdad University
email: hayderabdul_hameed@yahoo.com

Israa Nazeh Abeed
Engineering College - Baghdad University
email: Israa717@gmail.com

ABSTRACT

The adsorption of copper ions onto produced activated carbon from banana peels (with particle size 250 µm) in a single component system with applying magnetic field has been studied using fixed bed adsorber. The fixed bed breakthrough curves for the copper ions were investigated. The adsorption capacity for Cu (II) was investigated. It was found that 1) the exposure distance (E.D) and strength of magnetic field (B), affected the degree of adsorption; and 2) experiments showed that removal of Cu ions and accumulative adsorption capacity of adsorbent increase as the exposure distance and strength of magnetic field increase.

Key words: banana peels**;** adsorption; magnetic field

إزالة النحاس من المياه بأستخدام تقنية الأمتزاز الكهرومغناطيسي باستخدام مادة ممتزة منتجة محليا من قشور الموز

حيدر محمد عبد الحميد
استاذ مساعد
كلية الهندسة - جامعة بغداد

اسراء نزيه عبد
كلية الهندسة - جامعة بغداد

الخلاصة

تمت دراسة أمتزاز ايونات النحاس على الكاربون المنشط المنتج من قشور الموز (قطر الجزيئات 250مايكرو) في عملية دفعية وفي عمود الحشوة الثابتة بتسليط المجال الكهرومغناطيسي. تم ايجاد قابلية الأمتزاز التراكمية للمادة المازة .وتم أيجاد أن 1) مسافة التعرض للمجال المغناطيسي وشدة المجال المغناطيسي تؤثر على عملية الأمتزاز ،2) التجارب لهذه الدراسة أظهرت أن إزالة أيونات النحاس وقابلية الأمتزاز التراكمية للمادة المازة تزداد بزيادة مسافة التعرض للمجال المغناطيسي وشدة المجال المغناطيسي.

الكلمات الرئيسية : قشور الموز، أمتزاز، مجال مغناطيسي.

1. INTRODUCTION

The contamination of the environment has become a prime concern since the last few decades. Massive industrialization is continuously releasing wastewater to the ecosystem and the environment, causing contamination and toxicity to all living and non-living species **Hossain, et al., 2012**. The presence of heavy metals in the environment is a major concern due to their hazardous impact **Dragan, et al., 2009**.

Heavy metals will not degrade into harmless end products and are considered toxic for many life forms. Unlike organic pollutants, the majority of which are susceptible to accumulate in living organisms, causing various diseases and disorders. Therefore, the removal of heavy metals from water and wastewater is important to protect public health and ecosystem **Cheung et al., 2001**.

Among the heavy metals, copper is the major available type of heavy metal in the aquatic environment **Hossain et al., 2012**. In 1991, the U.S. Environmental Protection Agency (EPA) established rules for controlling copper level in public water supplies, Maximum Contaminant Level Goal MCLG = 1.3 mg/l according to EPA **EPA, 2013.**

The adsorption process is being widely used by various researchers for the removal of heavy metals from waste streams **Van Lier, 1998.** The purpose of this study was to investigate the effect of exposure distance and strength of magnetic field on the adsorption of Cu (II) on the produced activated carbon from banana peels. The influence of experimental conditions, such as exposure time, strength of magnetic field on the adsorption was studied. This information might be useful for further application in the treatment of waste effluents.

2. EXPERIMENTAL PROCEDURE

2.1 Preparation of Adsorbent

The banana peels were collected from kitchen, washed with tap water to remove external dirt. The wetted banana peels were dried naturally by exposure to the sun light for 14 day in June **Jaishankar, et al., 2014.**

The dried banana peels were grounded in (Agate mortar, Retsch, Type BB1A, Masch.Nr.4323, Germany) and sieved to a size of (250 µm) by using (Sieves, S/N:03007314, Body200 mm×500mm, Germany). Samples with (250 µm) particles size were weighted (20 gm) using (Electrical balance, BL210S, Sartorius, Germany) and placed in the furnace (BARNSTEAD/ THERMOLYNE FURNACE 62700, 1.5KW) as in **Fig.1**. The samples were heated at a rate of (5 ^{o}C/min) where heating rate range was (5-25 ^{o}C/min).

Physical activation method was used, using CO_2 as the activation agent with flow rate of (0.1L/min). Samples were heated to the desired temperature of about (800 ^{o}C) within the range of (500- 900 ^{o}C) and kept for (30min.) **Rashidi, et al., 2012**. Then activated carbons were cooled to room temperature under the nitrogen gas flow rate of (0.1L/min).

2.2 Methods

A glass cylinder of length (80cm) and inner diameter of (3.5cm) was used. A mesh, before and after produced activated carbon was placed to prevent loss of produced activated carbon from the bed and to ensure a good distribution of it then the solution of (copper sulfate) was introduced through it as shown in **Fig 2.**.

A plastic cylindrical container with the volume of (120L) was used to contain the wastewater. One rotameter was used to measure the flow rate of a range of (5- 100 L/h). The copper ions solution was prepared with required concentration (1mg/L) by dissolving (0.0787gm) in each (20L) of distilled water by using Eq. (1):

$$W = C * V * \frac{\mathcal{M}_{wt}}{At_{wt}} \qquad (1)$$

Copper ions solution was introduced in the cylindrical plastic container and pumped through the bed by two pumps (Reshan, UN 130017, 2.5m, 1400L/hr). In flow was controlled by rotameter.

Continuous system was achieved to measure the breakthrough curve for Cu (II) with applying magnetic field and carried out at various conditions. Experiments were carried out at various E.D and B, keeping the other variables constant for a given run. The experimental procedures for continuous system are listed below:

1. The optimum exposure distance was obtained by conducting three values of exposure distances of (10, 25, 40 cm) (different exposure distances were achieved by inserting or removing number of electrical relays). The wastewater was passed through magnetic field with different exposure distance. Samples were taken from the exit every (10min) and analyzed.
2. The magnetic field strength B was obtained by conducting different values of magnetic field strength B by changing voltage. DC type of electrical current was used. The values of it were (0.05, 0.12, 0.21, 0.27Am) and the values of B for the Dc current used were (50,170, 260, 325 Gauss) respectively.

The breakthrough curves were determined by plotting relating effluent concentration (C_e/C_o) against time**.**

3. ANALYSIS

Dissolved metal concentrations in solution were determined by a flame atomic absorption spectrophotometer AAS (GBC 933, Australia) in the environmental engineering lab. The characteristic wavelength used in analysis for Cu^{+2} is equal to (324.7 nm) used by AAS for studied metal.

4. RESULTS AND DISSCUSIONS

1. Effect of Magnetic Field Strength (B Gauss)

The breakthrough curves of the Cu^{+2} adsorbed onto produced activated carbon were shown in **Fig.3** at different magnetic field strength (50, 170, 260 and 325Gauss) by keeping all the other parameters constant. E.D=40cm, pH=7, C_o=1 mg/l, particle size=250μm, weight of adsorbent$_c$ = 6gm, flow rate=0.25L/min.

Investigation of these curves clears that the breakpoint is increased with increasing magnetic field strength (B), this is because increasing in B gives more reduction in Zeta Potential for Cu^{+2} by exposure for magnatic field effect which enhanced adsoption process by increasing the capacity, **Ni'am, et al., 2006** as in table 1.

2. Effect of Exposure Distance for Magnetic Field

The breakthrough curves of Cu^{+2} present in solution adsorb on produced activated carbon were shown in **Fig.4** at different exposure distances (10, 25, 40 cm) and fixing other parameters, C_o and weight of adsorbent$_c$ of (1mg/l) and (6gm) respectively. B=325 Gauss, pH=7 , particle size=250 µm and flow rate=0.25L/min.

Investigation of these curves clears that the breakpoint is increased with increasing exposure distance for magnetic field, this occurs because the increased exposure distance gives sufficient contact time for Cu^{+2} to be exposured for magnatic field. Consequently this behavior would result in more reduction in Zeta Potential **Ni'am, et al., 2006.**

Fig.4 reveals clearly that the optimum exposure distance found (40cm). Because more magnetic field act on Cu^{+2} then less repulsed from each other by the magnetic force exerted on them resulting for lowering the Zeta Potential for the ions and adsorption process enhanced by this behavior and the total accumulative capacity value increase as the exposure distance increases **Fadhil, 2015.**

REFREANCE

- Cheung, C. W., Porter J. F., Mckay, G., 2001, *Sorption kinetic analysis for the removal of cadmium ions from effluents using bone char*, Water Research, Vol. 35, PP. 605-621.

- Dragan, E. S., and Dinu, M. V., 2009, *Removal of copper ions from aqueous solution by adsorption on ionic hybrids based on chitosan and clinoptilolite*, Ion Exchange Letters 2. vscht.cz, Vol. 2, PP. 15-18.

- EPA,2013,http://water.epa.gov/drink/contaminants/basicinformation/copper.cfm, Environmental Protection Agency.

- Fadhil, S. H., 2015, *The Usage of Electromagnetic Field for the Removal of Suspended Solids from Municipal Wastewater*, University of Baghdad, College of Engineering, M.Sc. Thesis.

- Hossain, M. A., Ngo, H. H., Guo, W. S., Nguyen, T. V., 2012, *Removal of Copper from Water by Adsorption onto Banana Peel as Bioadsorbent*, International Journal of GEOMATE, Vol. 2, No. 2, PP. 227-234.

- Jaishankar, M. , Mathew B. B., Shah, M. S., Murthy, K. T. P., Gowda, S. K. R., 2014, *Biosoption of Few Heavy Metal Ions Using Agricultural Wastes*, Journal of Environment Pollution and Human Health, Vol. 2, No. 1, PP. 1-6.

- Ni'am, M. F., Othman, F., Sohaili, J., Fauzia, Z., 2006, *Combined Magnetic Field and Electrocoagulation Process for Suspended Solid Removal from Wastewater*, Putrajaya, Malaysia, PP. 384-393.

- Rashidi, N. A., Yusup, S., Ahmad, M. M., Mohamed, N. M., Hameed, B. H., 2012, *Activated Carbon from the Renewable Agricultural Residues Using Single Step Physical Activation: A Preliminary Analysis*, APCBEE Procedia, Vol. 3, PP. 84 – 92.

- Van-lier, B. M., 1998, *Modeling and Prediction of Specific Compounds Adsoption by Activated Carbon and Synthetic Adsorbents*, Water Research, 14, PP.1719-1728.

NOMENCLATURE

AAS = flame atomic absorption spectrophotometer.
B= strength of magnetic field, Gauss.
C_o= initial concentration.
E.D= exposure distance, cm.
$q_{accu.}$= accumulated capacity, mg/gm.

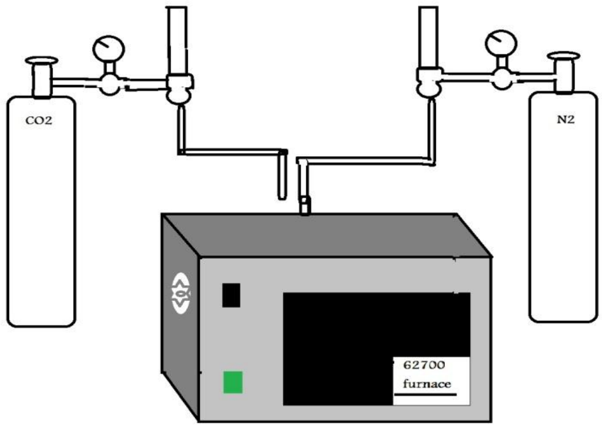

Figure 1. Diagram of the carbonization and activation process furnace.

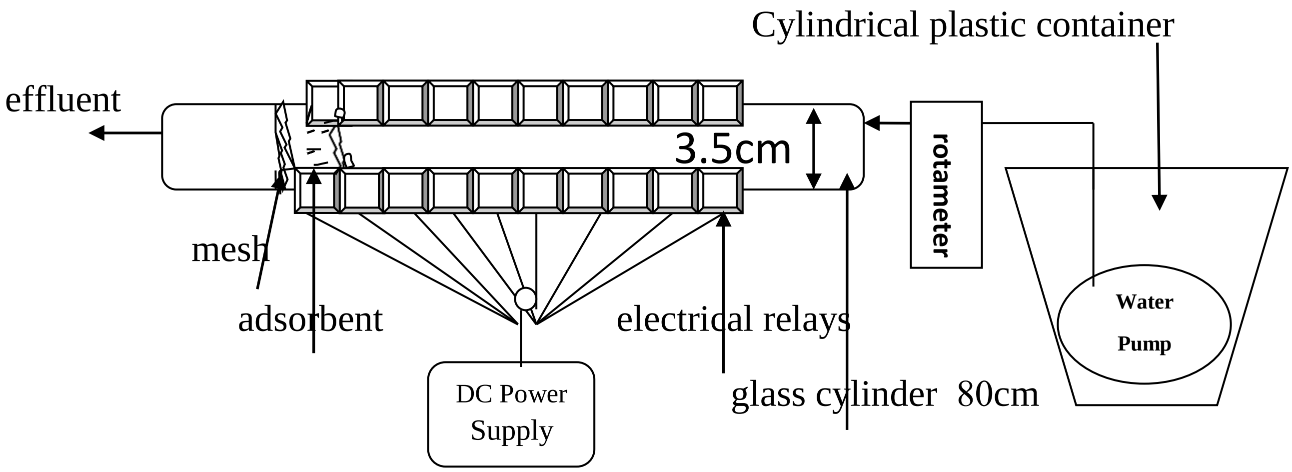

Figure 2. Schematic diagram of the system.

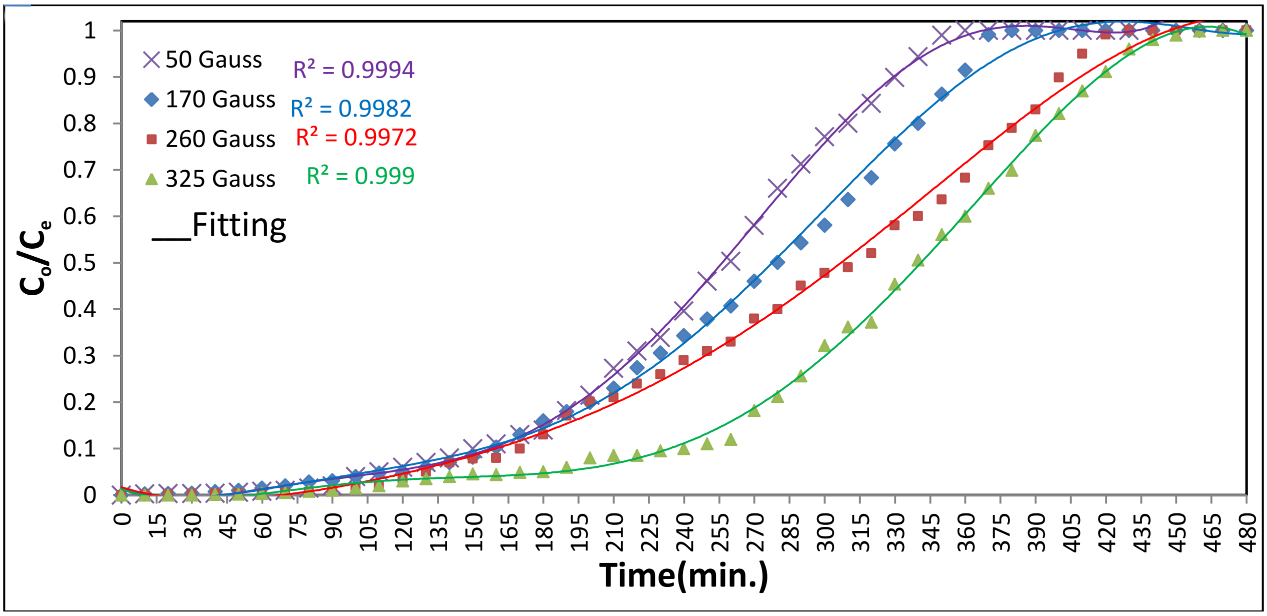

Figure 3. Breakthrough curves for adsorption of Cu^{+2} onto produced activated carbon at different magnetic field (B Gauss)

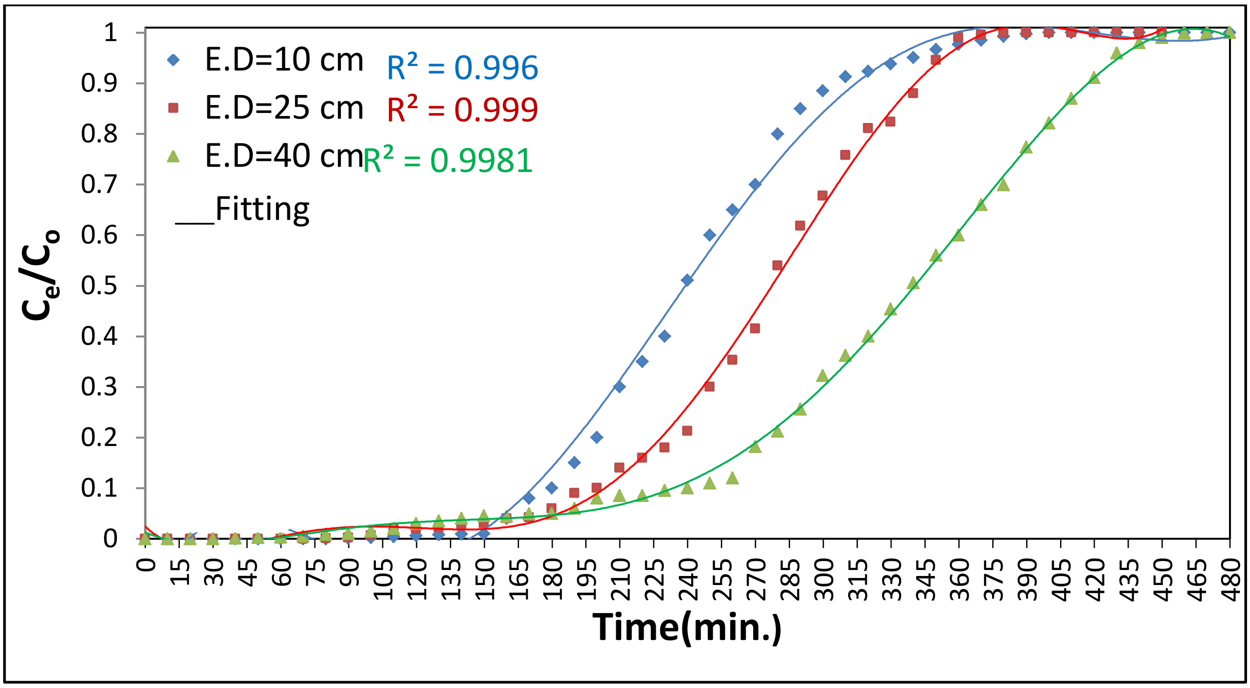

Figure 4. Breakthrough curves for adsorption of Cu^{+2} onto produced activated carbon for different exposure distances.

Table 1. Total accumulated capacity applying magnetic field.

Variable parameter in experiments		**Total $q_{accu.}$ (mg/gm)**
Exposuer distance	E.D=10cm	9.04
	E.D=25cm	11.14
	E.D=40cm	13.49
Magnetic field strength	B=50 Gauss	10.1
	B=170 Gauss	10.8
	B=260 Gauss	12.05
	B=325 Gauss	13.5

Effect of Air Bubbles on Heat Transfer Coefficient in Turbulent Convection Flow

Assit.Prof. Akram W. Ezzat
Mechanical Eng. Dept.
University of Baghdad
email: akramwahbi@yahoo.ie

Prof.Dr. Najdat N. Abdullah
Mechanical Eng. Dept.
University of Baghdad
email: najdat_abdulla @yahoo.co.uk

Sajida Lafta Ghashim
Mechanical Eng. Dept.
University of Baghdad
email: sajda_lafta@yahoo.com

ABSTRACT

Experimental and numerical studies have been conducted for the effect of injected air bubbles on the heat transfer coefficient through the water flow in a vertical pipe under the influence of uniform heat flux. The investigated parameters were water flow rate of (10, 14 and 18) lit/min, air flow rate of (1.5, 3 and 4) lit/min for subjected heat fluxes of (27264, 36316 and 45398) W/m^2. The energy, momentum and continuity equations were solved numerically to describe the motion of flow. Turbulence models k-ε was implemented. The mathematical model is using a CFD code Fluent (Ansys15). The water was used as continuous phase while the air was represented as dispersed phase. The experimental work includes design, build and instrument a test rig for that purpose. A circular vertical copper pipe test section of (length=0.7m, diameter= 0.05m, thickness= 1.5mm) is designed and constructed, heated by an electrical heater fixed on its outer surface. Water temperature at inlet is kept constant at (32°C). Water inlet and outlet temperatures, as well as radial temperature distribution within the pipe at seven sections along it between pipe surface and its center are measured. The results revealed that the secondary flow created by air bubbles have significant effects on heat transfer enhancement and temperature profile. It is observed, that averaged Nusselt number enhancement for low heat flux of 27264 W/m^2 and 4 lit/min air bubbles was 33.3 % and 23% in numerical and experimental, respectively.

Keywords: turbulent flow, two phase flow, enhancement of heat transfer, air bubbles.

تاثير فقاعات الهواء على معامل انتقال الحرارة في جريان الحمل المضطرب

أ.م.د. اكرم وهبي عزت
قسم الهندسة الميكانيكية
جامعة بغداد

أ.د. نجدت نشات عبد الله
قسم الهندسة الميكانيكية
جامعة بغداد

م. ساجدة لفته غشيم
قسم الهندسة الميكانيكية
جامعة بغداد/ طالبة دكتوراه

الخلاصة :اجريت دراسة عملية ونظرية حول تاثير حقن فقاعات الهواء على معامل انتقال الحرارة خلال جريان الماء في انبوب عمودي تحت تاثير الفيض الحراري المنتظم . والمتغيرات المدروسة كانت قيم معدل تدفق الماء (10 ,18,14) لتر/ دقيقة ، وقيم معدل تدفق الهواء (1.5 ,4,3) لتر/ دقيقة لفيض حراري مقداره (27264, 36316 ,45398) واط/ مترمربع .حلت معادلات الزخم والاستمرارية والطاقة عدديا باستخدام البرنامج الجاهز فلونت (انسس 15) لوصف حركة الجريان بالاضافة الى معادلات نموذج الاضطراب. تم بناء منظومة في الجانب العملي تتكون من مجموعة من الاجزاء من ضمنها مقطع الاختبار وهو عبارة عن انبوب عمودي دائري مصنوع من النحاس ومسخنة بواسطة مسخن كهربائي على السطح الخارجي . ابعاد الاسطوانة النحاسية كانت طول 70 سم وقطر 5 سم وسمك 1.5 ملم . تم استخدام الماء بدرجة حرارة دخول ثابتة 32 درجة مئوية . تم قياس درجة حرارة الماء في الدخول والخروج بالاضافة الى قياس درجات الحرارة على طول الانبوب في سبع مقاطع موزعة بين مركز

الاسطوانة والى الجدار. اظهرت النتائج ان وجود فقاعات الهواء تسبب جريان ثانوي داخل مقطع الاختبار له تاثيرعلى تحسين معامل انتقال الحرارة وتوزيع درجات الحرارة. اظهرت النتائج النظرية والعملية انه عند استخدام فيض حراري منخفض 27264 W/m^2 ومعدل تدفق الهواء 4 لتر/ دقيقة تحسن معدل Nusselt number بمقدار 33.3% و23% على التوالي.

الكلمات الرئيسية:الجريان المضطرب ، الجريان الثنائي الطور ، تحسين معامل انتقال الحرارة ، فقاعات الهواء .

1. INTRODUCTION

Multiphase or two phase flow plays an important role in application of enhancement heat transfer such as heat exchangers, chemical reactors, cooling devices, solar collectors and nuclear reactors. Bubble motion close to a wall plays an effective technique for enhanced heat transfer rate. **Kenning,** and **Kao, 1972,** investigated experimentally the effect of small gas bubbles of (N_2) flowing upward in channel with rectangular cross-section on the convective heat transfer parameters. Superficial air velocity of (0.11, 0.022 and 0.044) m/s and superficial water velocity of (0.6, 1.2 and 1.8) m/s were used in the experiments. The boundary conditions related to applied heat fluxes ranged (20- 300) kW/m^2. Bubbles diameter of (1.5 mm) was injected in the channel. The results showed heat transfer coefficients enhancement was mainly due to the secondary flow production. The rate of heat transfer was approximately 50 % higher than that for a single phase flow. **Tokuhiro,** and **Lykoudis, 1994,** investigated experimentally Nitrogen gas bubbles injection in mercury in a vertical enclosure. The vertical enclosure contained in one side a heated plate**.** The experiments were conducted using heat flux ranged $370 < q'' < 16000$ W/ mm^2 and rate of bubble injection (0.9 to 9.2) cm^3/s .The results showed coefficient of heat transfer enhancement due to bubbles injection at low heat flux was more than that at higher heat fluxes**.** Also, heat transfer coefficient was approximately 2-3 times higher than that for a single phase flow, while at high heat fluxes, the influence of enhancement was not recognized. **Celata et al., 1999,** studied experimentally a turbulent upward mixed convection flow of water in a vertical pipe. Air injection was used to enhance heat transfer coefficient. Experiments had been carried out in a stainless steel tube with heat flux of (4.8 -178.5) kW/m^2, Reynolds number (1160- 24000), liquid mass flow rate (80-850) Kg/h and gas mass flow rate (40-1800) g/h. Also, the flow pattern was illustrated by using plexiglas tube and prediction of the heat transfer coefficient by using correlation equations. The results showed that, gas phase caused secondary flow and disturbance in the velocity profile, therefore, turbulence increased locally by air bubbles effect which greatly enhanced the heat transfer coefficient. Also, results illustrated that the coefficient of heat transfer with injection of air bubbles was approximately 10 times higher than that for a single phase flow. **Wolters, 2003,** studied experimentally and numerically gas injection in mercury in vertical enclosure heated with constant heat flux in one side and cooled in other side. Thermocouples and double-conductivity probes were used to measure and calculate the local heat transfer and void fraction. The experiments were conducted using range of heat flux (370 to 16000) W/m^2.The results showed a significant heat transfer enhancement was obtained during bubble injection utilization. For high heat fluxes the local Nusselt number was slightly decreased, probably because the effect of the stratified bulk fluid was decreased. The comparison between experimental and numerical results showed a reasonable agreement. **Kim,** and **Ghajar, 2006**, investigated experimentally the non-change phase of gas–liquid flow in horizontal pipes. Series of experiments had been carried out in order to clarify the flow pattern of heat transfer. The test section used in the experiments was made of stainless steel of (27.9 mm) inner diameter with ratio of length to diameter equals to (100). The experiments were conducted using range of heat flux (3000 to 10600) W/m^2.The Reynolds numbers at (820-26000) for water and (560-48000) for air. The results cleared that the rate of heat transfer increased with increasing Reynolds number. **Zimmerman et al., 2006,** investigated experimentally air bubble –water flows in a horizontal pipe**.** Superficial velocity (24.2-41.5) m/s for water and (0.02-0.09) m/s for air were utilized in the experiments. Speed video camera and conductive tomography technique were used to visualize flow patterns and measured film thickness. Infrared thermo-graphic method was used to measure temperature of the wall. The results showed that heat transfer coefficient at the bottom were higher than that at the top of the pipe. Also, local and average Nusselt number correlations were obtained. **Sakr et al., 2012,** studied numerically various turbulence models effect on turbulent bubbly flow through a vertical pipe and a pipe sudden expansion by using Eulerian's model. The momentum and continuity equations were used to describe the motion of flow. Different types of turbulence models: k-ε, extended k-ε and shear-stress transport k-ω turbulence models were implemented. Finite volume method was used to solve the equation of the system. Water was used as working fluid and air bubbles were used in this study. The water was used as a continuous phase while the air was represented as dispersed phase. The liquid Reynolds number of 78500 and bubble diameter of 2 mm were used in the experiments. It was concluded that, SST k-ω model plays an important role in comparison with other turbulence models. **Hameed, 2013,** investigated experimentally the effects of inclination angle of multiphase flow in pipe of square cross section. Inclination angles of 5°, 10°, and 15° were implemented. The following water and air superficial velocities of (1.1506 and 1.4815) m/s and (0.164 and 0.411) m/s were used in the experiments. The liquid Reynolds number was varied from (740 to 26000), and the gas Reynolds number was varied from (560 to 48000). Eight thermocouples type K distributed along the test section were used to measure the temperatures and to find local heat transfer coefficient. High speed camera was used to describe the flow regimes, along test section. The results showed that coefficient of heat transfer for multiphase flow increased with increasing flow rate of water, air, and inclination angle of test section. Correlation equations on average Nusselt number were obtained for three inclination angles of (5^o, 10^o and 15^o). **Dizaji,** and **Jafarmadar, 2014**, investigated experimentally air injected flow into a liquid fluid of a horizontal double pipe heat exchanger to enhance heat transfer rate. Following conditions were based on, for cold water side of the heat exchangers: flow rate (0.083 kg/s), inlet temperature (25°C) and Reynolds number (4000), while for hot water side: inlet temperature (40°C), flow rate from (0.0831 to 0.2495) Kg/s, Reynolds number from (5000 to 16000) and air mass flow rate of (0.098×10^{-3}) Kg/s. The effects of air bubbles injected into the inner and outer tubes on heat exchanger were examined. The results showed that the presence of bubbles in outer tube of heat exchanger was more effective than that injected into the inner tube because of accumulation of air bubbles near the inner side of the outer tube. The maximum Nusselt number was about (6% - 35%) and effectiveness of heat exchanger was reached about (10%- 40%). **Hanafizadeh et al., 2014,** used two models, volume of fluid (VOF) and Eulerian for modeling air- water two- phase flow in up riser pipe for lift pump applications. CFD package was used to solve the conservation equations for two models. Different regimes through flowing gas-liquid flow in vertical pipes were observed: bubbly, slug, churn and annular. Conservation equations of mass and momentum were used in two directions (radial and axial). Effect of turbulence of the flow was computed by k-ε model. Test section was of (5cm) diameter and (1m) long. The results showed that for bubbly, slug and churn regimes were more appropriate for simulating by volume of fluid, while Eulerian's model was good for prediction of annular flow regime. **Sanati, 2015,** studied air bubble – water two phase flow in vertical pipe using k-ε model (mixture approach) and empirical correlations. The following conditions were used during the experimental work: superficial velocity (0.18 to 1.06) m/s and (0.03 to 3.1) m/s for water and air respectively. The test section used in the experiments had different lengths (12.3 and 24) m under the same diameter. The two phase flow was governed by the Navier–Stokes equations, continuity equation and finite-volume method was used. Flow pattern and pressure distributions had been carried out in order to clarify the numerical results. It was concluded that the increasing in gas velocity was accompanied with increasing of void fraction which subsequently reduced total pressure loss in pipe but increased liquid velocity followed by reducing the void fraction and this led to increase of total pressure loss in pipe. Theoretical results showed agreement with the experimental results. **Rzehak,** and **Kriebitzsch, 2015,** investigated numerically turbulent bubbly flow through a vertical pipe. Both codes CFX and with OpenFOAM were used to simulate the results. Euler–Euler method was used in this model with turbulence model. Effect of bubbles on volume fraction of gas, velocity of liquid turbulent kinetic energy and turbulent viscosity were studied. It was concluded that, two codes peak value of gas volume fraction were predicted near the wall. Low value of profile for velocity was in the center and decreased to zero at the wall. Large value of turbulent kinetic energy was found by CFX code. Also, turbulent viscosity near the wall region had large value by CFX results. **Dabiri,** and **Tryggvason, 2015,** investigated numerically the effect of air bubbles on the turbulent upward flow between two parallel walls with a uniform heat flux. The following conditions were used during the experimental work: Reynolds number up to (5600) and bubble diameter (1.35mm). Series of experiments had been carried out in order to clarify the flow pattern on heat transfer coefficient and temperature distribution along vertical channel. The two-phase flow was governed by the Navier–Stokes equations, energy equation and finite-volume method was used for solution. They concluded that, an increase of (3%) in volume fraction of bubbles caused an increase of (60%) in Nusselt number.

The objective of the present work is to investigate numerically and experimentally the thermal effect of injecting air bubble in water flowing in vertical mounted pipe subjected to a uniform heat flux. Ranges of studied parameters are: water flow rate of (10, 14 and 18) lit/min, air flow rate of (1.5, 3, and 4) lit/min and heat fluxes (27264, 36316 and 45398) W/m^2. Numerical solution is carried out using a CFD code Fluent (Ansys15) and Gambit 2.2.30. Novelty of the this work is to measure the temperature of the liquid near the heated wall and the effect of air bubbles on Nusselt number in vertical circular pipe at constant heat flux numerically and experimentally.

2. EXPERIMENTAL WORKE

The experimental apparatus is shown photographically in **Fig.1** and diagrammatically in **Fig.2**. The test rig consists of the following items:

2.1 Test Section

The test section is a circular cross section channel manufactured from copper**.** The inside and outside diameters of the test section are (50mm) and (53mm) respectively. Test section length is (0.7m). Circular holes of (d=8 mm) are drilled in the surface of the cylinder. These holes are sealed by plugs of (d=8 mm) for penetration of thermocouple wires, pressure sensor and electric electrodes. The remained penetration areas are covered by silicon that withstands temperature up to 200℃. The outer tube surface was heated electrically using an electrical heater. The heater consists of two nickel-chrome wires of (1mm) in diameter, (3m) length. The wire is wrapped along its length around test section. The maximum power in each wire is (3000 W) ensuring total power of (6000 W). The bare wires of the heater are electrically insulated by Ceramic beads. The heater is supplied with AC-current from voltage regulator. The circuit is connected to digital voltage regulator to control the current according to the desired heat flux. Clamp meter is used to measure the current passing through the heater. The heater is covered by a (2 in) layer of fiberglass that withstands temperature up to (700 - 850°C) to ensure a reliable insulation for the heater and to concentrate the generated heat in the water flowing inside test section. Aluminum plate covers the material. The temperature inside the test section is measured by thirty five thermocouples type K (chromium - aluminum) distributed within seven sections along the length of copper pipe. The thermocouples are installed in equal space (10 cm) apart at seven positions. Additional thermocouples are installed inside the tube to measure water temperature in the inlet and the outlet of the pipe as shown in **Fig. 3**.The end of thermocouple wires is connected with standard male plug in order to connect them with the digital thermometer. The system used to inject air bubbles in the test consists of (2 mm) diameter of capillary tube made of copper and compressor is used to provide the compressed air. The system is equipped with air flow meter and valve to control and measure the air bubbles generation rate.

2.2 Heat Exchanger (Double pipe helical coil)

Double pipe heat exchanger manufactured from copper is used in the present experiments. It consists of one pipe placed concentrically inside another pipe with larger diameter. The dimensions of the inner diameter and outer diameter are 1.6 cm and 2.3 cm respectively. The length of tube is 6m long. The purpose of the heat exchanger is to remove heat from outlet flow water of the test section and control water inlet temperature.

2.3 Pump

The water flowing in the circuit is divided between the test section and the bypass pipe. The purpose of the bypass pipe is to control water flow rate and pressure in the test section through a control valve. Another line is used in the circuit of heat exchanger to control the temperature of water enter test section.

2.4 Supply Liquid Water Tank

A water tank of (37 liter) with dimensions of (33x53x43) cm and (0.5 cm) plate thickness is placed at the same level of centrifugal pump and connected to the cold water inlet which is supplied from the water line in Laboratory.

2.5 Pipes and Valves

Polyvinyl chloride (PVC) pipe of (1/2 in) diameter is used to connect the parts of the system. The system consists of four valves.

3. MEASUREMENT AND CONTROL SYSTEMS

3.1 Electrical Power Measurement

- Voltage regulator (variance) is connected to the power supply for the purpose of adjusting the power input rate of the heater as required. A digital voltmeter is linked to the circuit in parallel with heater element to measure heater voltage.
- Hydrogen bubbles generation circuit consists of voltage regulator device (variance) and two multi-meter. Digital one is used to measure the current and the other is used to measure the output voltage from Variance.
- Digital watt meter is used to measure the heater power directly.
- Clamp multi-meter is used to measure the current passes through the heaters for cross checking.

3.2 Temperature Measurement

Digital thermometer type (12 channels temperature recorder with SD card data logger - model: BTM - 4208SD - Lutron Company - Taiwan) is used to measure the temperature.

4. HEAT TRANSFER CALCULATIONS

4. 1 Heat Flux

The net heat flux is determined from recording the electrical power supplied to the heater and applying the following equation**, Salman,** and **Mohammed, 2007**:

$$\mathrm{Po} = \mathrm{I.Vo} \tag{1}$$

The heat transfer from the heated wall:

$$\emptyset_{conv} = Po - \emptyset_{loss} \tag{2}$$

Where:

$\emptyset_{loss}$ is the total conduction heat losses and radiation lasses.

$$\emptyset_{losses} = \emptyset_{cond} + \emptyset_{rad} \tag{3}$$

$\emptyset_{radiation}$ is very small, so it can be neglected.

$$\emptyset_{loss} = \frac{T_{wall} - T_{aluminum}}{\frac{ln\frac{r_2}{r_1}}{2\pi\lambda_{pipe}L} + \frac{ln\frac{r_3}{r_2}}{2\pi\lambda_{in.1}L} + \frac{ln\frac{r_4}{r_3}}{2\pi\lambda_{in.2}L} + \frac{ln\frac{r_5}{r_4}}{2\pi\lambda_{aluminum}L}} \tag{4}$$

The convection heat flux can be represented by:

$$q" = \frac{\emptyset_{conv}}{A_s} \tag{5}$$

Where: $A_s = \pi \times D_i \times L$

The bulk temperature profile along the length of tube can be represented by the following equation:

$$T_{b2}(x) = T_{b1} + \frac{q"\,px}{\dot{m}cp} \tag{6}$$

The local heat transfer coefficient is expressed as:

$$h(x) = \frac{q"}{(T_{wall(x)} - T_{b2(x)})} \tag{7}$$

Average heat transfer coefficient

$$h = \frac{1}{x}\int_0^x h(x)dx \tag{8}$$

Local Nusselt number is calculated using following equation:

$$Nu(x) = \frac{h(x)Di}{\lambda} \tag{9}$$

Average Nusselt number

$$Nu = \frac{1}{x}\int_0^x Nu(x)dx \tag{10}$$

The Reynolds number can be defined according to the particle diameter and the fluid velocity at the inlet as:

$$Re = \frac{\rho u D_i}{\mu} \tag{11}$$

4.2 Volume Fraction

Volume fraction in a gas-liquid flow may be defined as**, Kitagawa et al., 2008**:

$$\alpha = \frac{Q_{air}}{Q_{water} + Q_{air}} \tag{12}$$

4.3 Measurement of Air Bubble Diameter

The average initial bubbles size is elaborated by, **Azad,** and **Syeda, 2006:**

$$d_{airbubble} = dc\left[1.88\left(\frac{u_c}{\sqrt{g.d_c}}\right)^{1/3}\right] \tag{13}$$

5. CFD SIMULATION

For multiphase, the Eulerian model approach was used to describe multiphase flow in three dimensions. Its approach treats the continuity, momentum, energy and equation of turbulence model for each phase, **Sakr et al., 2012.**The mathematical model was solved by using a CFD Code Fluent (Ansys15) and Gambit 2.2.30.The water was used as working fluid. Air bubbles injection was from two sides of pipe as shown in **Fig.4.**

Assumptions:

1. Steady and turbulent incompressible flow.
2. Three dimensional flows.
3. The properties of both gas and fluid were assumed to be constant.
4. Effect of surface tension were neglected.

With all the equations below for phase k (c: continuous and d: dispersed).

-The continuity equation (solved for each phase)

$$\frac{\partial}{\partial x_i}(\alpha\rho u_i)_k = 0.0 \tag{14}$$

The volume fractions were assumed to be equal to one.

$$\alpha_c + \alpha_d = 1.0 \tag{15}$$

- Momentum equation (solved for each phase)

$$\boldsymbol{\frac{\partial}{\partial x_i}\left(\alpha\rho u_i u_j\right)_k = -\alpha\frac{\partial P}{\partial x_i} \pm \alpha\rho g + \frac{\partial}{\partial x_j}\left[\alpha\mu\left(\frac{\partial u_i}{\partial x_j} + \frac{\partial u_j}{\partial x_i} - \frac{2}{3}\delta_{ij}\frac{\partial u_l}{\partial x_l}\right)\right]_k + \frac{\partial}{\partial x_j}\left(-\rho \acute{u}_i \acute{u}_j\right)_k \mp M_k}$$

(16)

Where:

$$-\rho\acute{u}_i\acute{u}_j = \mu_t\left(\frac{\partial u_i}{\partial x_j} + \frac{\partial u_j}{\partial x_i}\right) - \frac{2}{3}\left(\rho k + \mu_t\frac{\partial u_k}{\partial x_k}\right)\delta_{ij} \tag{17}$$

Where:

$\delta_{ij} = 1 \quad if\, i = j$

$\delta_{ij} = 0 \quad if\, i \neq j$

The interface momentum transfer term M_k was given as follows, **Troshko,** and **Hassan, 2001, & Sakr et al., 2012**:

$$M_k = {M_k}^d + {M_k}^L + {M_k}^W + {M_k}^{td} \tag{18}$$

❖ The drag force was expressed as describes:

$${M_c}^d = -{M_d}^d = \frac{3}{4}\frac{C_D}{d_b}\alpha_d\alpha_c|u_d - u_c|(u_d - u_c) \tag{19}$$

Where:

$C_D =$ Drag coefficient depends on the particle Reynolds number as given below:

$$C_D = \begin{cases} \frac{24}{R_e}\left(1 + 0.15{R_e}^{0.687}\right) & Re \leq 1000 \\ 0.44 & Re > 1000 \end{cases} \quad (20)$$

Relative Reynolds number was given by:

$$Re = \frac{\rho_c|u_d - u_c|d_b}{\mu_c} \quad (21)$$

❖ The lift force was expressed as:

$$M_c{}^L = -M_d{}^L = C_L\alpha_c\alpha_d\rho_c(u_d - u_c) \times (\nabla \times u_c) \quad (22)$$

Where:
C_L = Lift force coefficient
$C_L = 0.06$ (Turbulent bubbly flows in vertical pipes)

❖ Wall lubrication force was defined as:

$$M_c{}^W = -M_d{}^W = \frac{\alpha_c\alpha_d\rho_c|u_d - u_c|}{d_b} max\left(0, C_{w1} + C_{w2}\frac{d}{y_w}\right)n_w \quad (23)$$

Where:
n_w = Outward vector normal to the wall.
y_w = Distance from the wall.
C_{W1}= -0.01
C_{W2}= 0.05

❖ The turbulent dispersion force was formulated as :

$$M_c{}^{td} = -M_d{}^{td} = -C_{td}\rho_c k_c \nabla\alpha_c \quad (24)$$

Where:
k_c= Turbulence kinetic energy of liquid per unit mass.
C_{td} = Coefficient of turbulent dispersion force ($C_{td} = 0.09\ to\ 0.1$) .
$\nabla\alpha_c$ = The gradient of dispersed volume fraction

- Energy equation **(**solved for each phase)

$$\frac{\partial}{\partial x_i}(\alpha\rho T u_i)_k = \alpha\left\{\frac{\partial}{\partial x_i}\left[\mathrm{c_p}\left(\frac{\mu}{\mathrm{pr}} + \frac{\mu_t}{\sigma_t}\right)\frac{\partial \mathrm{T_i}}{\partial x_j}\right]\right\}_k \quad (25)$$

-Turbulence modeling

The general transport equations for turbulence models adopted are given below**, Rzehak,** and **Kriebitzsch, 2015** & **Dhotre, et al. 2007**:

-Turbulent kinetic energy

$$\frac{\partial}{\partial x_j}(\alpha\rho u_i K)_k = \frac{\partial}{\partial x_j}\left[\left(\mu + \frac{\mu_t}{\sigma_k}\right)\frac{\partial K}{\partial x_j}\right]_Z + \alpha(\mathrm{G_K} - \rho\varepsilon) + \mathrm{ST_K} \quad (26)$$

-Turbulent dissipation rate

$$\frac{\partial}{\partial x_j}(\alpha\rho u\varepsilon)_k = \frac{\partial}{\partial x_j}\left[\left(\mu + \frac{\mu_t}{\sigma_\varepsilon}\right)\frac{\partial\varepsilon}{\partial x_j}\right]_k + \alpha\left(\frac{c_{\varepsilon1}G_K\varepsilon}{K} - \frac{c_{\varepsilon2}\varepsilon^2\rho}{K}\right) + ST_\varepsilon \qquad (27)$$

Where:

$$ST_K = C_{K3}C_f\rho_c\alpha_c\alpha_d K \qquad (28)$$

$$ST_\varepsilon = C_{\varepsilon3}C_f\rho_c\alpha_c\alpha_d\varepsilon \qquad (29)$$

$$C_f = \frac{3}{4}\frac{C_D}{d_b}|u_d - u_c| \qquad (30)$$

$C_{K3} = 0.75$

$C_{\varepsilon3} = 0.6$

5.2 Mesh for Multiphase Flow

Three dimensional mesh generations as shown in **Figs.5** and **6,** was used for the air-water two-phase flow along a large vertical pipe. Air bubbles were used to inject in the water by small capillary tube with diameter (2mm) by two sides of the pipe. The mesh consisted of large vertical pipe and connected with another very small pipe mesh with dimension of (0.003 m) long and (0.002 m) in diameter for small capillary tube injected air bubbles. 347210 cells and 65220 nodes were used in the analysis.

6. RESULTS AND DISCUSSIONS

6.1 Results of the Two-Phase Flow (Numerical & experimental)

Fig.7 shows numerical results of temperature variation along the cylinder length and its radial distances at water flow rate (10 lit/min), heat flux (27264 W/m^2) and bubbles flow rates (1.5, 3 and 4 lit/min).The figures reveal that, water temperature increases along the length of cylinder with increasing distance from cylinder inlet and in the cylinder wall direction. The presence of air bubbles increases the velocity near the walls and reduces it in the center. The presence of bubbles increases the mixing (cold water and warm water) and thus reduces the temperature differences between the wall and the bulk water. Experimental results illustrated in **Fig.8** shows the difference with numerical results due to the influence of losses through experimental test and accuracy of measuring device.

Fig.9 shows numerical and experimental results of bulk temperature variation with dimensionless length of cylinder at different water flow rates (10 ,14 and 18) lit/min, heat fluxes (27264 and 36316 W/m^2) and bubbles flow rates (0,1.5 , 3 and 4) lit/min. It is obvious from the figure that at constant heat flux, the bulk temperature is inversely proportional to water flow rate as this temperature decreases by increasing Reynolds number. Also, the observed cases show that, mixing increases by bubbles increases the bulk temperature. The behavior of experimental results of bulk temperature is similar to those related to numerical results but with increased values. Similar trends were shown for heat flux 36316 W/m^2.

Fig.10 shows the results of wall temperature variation with dimensionless length of cylinder with different values of water flow rates (10, 14 and 18) lit/min, heat fluxes (27264 and 36316) W/m^2 and bubbles flow rates (0,1.5,3 and 4) lit/min. It illustrates that the wall temperature in the case of injection air bubbles is much lower than that in the case of without bubbles because bubbles increase mixing between hot and cold streams. From numerical results, at heat flux (27264 W/m^2), maximum reduction of wall temperature was 29% at water flow rates (10) lit/min and bubbles flow rate (4 lit/min), while maximum reduction 20% for the same conditions was found in experimental test.

Fig.11 shows the results of local Nusselt number variation with length of cylinder for different values of water flow rates, heat fluxes and bubbles flow rates. The results show that bubbles injection causes secondary flow and disturbance in the velocity profile which increases turbulence locally by air bubbles effect and enhance the local Nusselt number. For the same heat flux the local Nusselt number value increases as the rate of bubbles injection increases. From numerical results, it was noticed that, at heat flux (27264 W/m^2) local Nusselt number increased 31% when bubbles flow rate (4 lit/min), while it increased 17% at minimum value of bubbles flow rate (1.5 lit/min) for the same value of water flow rates (10) lit/min. Level of increased local Nusselt number from experimental results is more than numerical results.

Fig.12 shows the results of average Nu variation versus Re at different values of heat fluxes and air bubbles flow rates. The effect of secondary flow by bubbles injection is significant at lower heat fluxes and lower flow rates. As seen from this figures, the secondary flow by air bubbles injection causes increase in average Nusselt number as Reynolds number decreases. Also the average Nu number increases as bubbles flow rates increases. The enhancement related to the average Nusselt number is shown in **Table 1.**

The variation of ratio of average Nuo/Nu with Re number at heat flux 27264 W/m^2 is shown in **Fig.13a**.The ratio decreases with Re number increase, because bubble motion moves away from the wall. It illustrates that an increase in air bubbles injection rate causes an increase in the average Nuo/Nu ratio. Also, the results show a similar trend obtained for q"=36316 W/m^2 and q"=45398 W/m^2, however, the ratio of average Nuo/Nu decreases as heat flux increases.

Comparison of present work was made for two phase flow with the work of **Celata et al., 1999,** which was considered to be the best one to compare as shown in **Fig.14** and a good agreement was observed.

6.2 Correlations of Average Nusselt Number

The correlation of average Nusselt number (Nu) with (Ra/Re) that covers the experimental results:

$$Nu = c(Ra/Re)^n \tag{31}$$

Where c and n are empirical constants. Each of these constant is presented in **Table 2** for range of: (Re = 5269 to 10528 and Gr=1.42 x10^8 to 2.39 x 10^{10})

7. CONCLUSIOS

1. The difference between experimental and numerical results was due to the influence of losses through experimental test and accuracy of measuring devices.
2. The enhancement of average Nusselt number ratio with effect of air bubbles to that without bubbles increased from (1.02 to 1.32).
3. Air bubbles injection causes an increase in average Nusselt number with increases in Reynolds number.
4. The high rate of bubbles injection had more effect on heat transfer enhancement.
5. A reduction in wall temperature along test section by injection bubbles increases with increasing the rate of bubble injection.
6. New correlation equations of Nusselt number were obtained from experimental results
7. Reasonable agreement was obtained between measured temperature and theoretical temperature predictions by CFD code.

8. REFERNCES

- Azad, M. A. K., and Syeda, S, R., 2006, *A Numerical Model for Bubble Size Distribution in Turbulent Gas- Liquid Dispersion*, Journal of Chemical Engineering, IEB. Vol.24, No.1, PP.25-34.
- Celata, G. P., Chiaradia, A., Cumo, M., and DAnnibale, F. , 1999, *Heat Transfer Enhancement by Air Injection in Upward Heated Mixed-Convection Flow of Water*, Journal of Multiphase Flow, Vol.25, PP.1033-1052.
- Dizaji, H.S., and Jafarmadar, S., 2014, *Heat Transfer Enhancement Due to Air Bubble Injection into a Horizontal Double Pipe Heat Exchanger* , International Journal of Automotive Engineering ,Vol. 4, No. 4,PP.902-910.
- Dabiri , S., and Tryggvason, G., 2015, *Heat Transfer in Turbulent Bubbly Flow in Vertical Channels*, Journal of Chemical Engineering Science, Vol. 122,No. 27, PP. 101- 113 .
- Dhotre, M.T, Smith,B.L., and Niceno.,B.,2007,CFD *Simulation of Bubbly Flows: Random Dispersion Model*,Journal of Chemical Engineering Science Vol.62, PP.7140-7150.
- Hanafizadeh, P., Moezzi, M., and Saidi, M. H., 2014,*Simulation of Gas-Liquid Two Phase Flow in Upriser Pipe of Gas-Lift Systems*, Energy Equipment and Systems, Vol 2,PP. 25-41 .
- Hameed ,R. H., 2013, *Experimental Investigation of Heat Transfer to Air–Water Flow in Downward Inclined Square Pipe*,Thi-Qar University, Journal for Engineering Sciences, Vol. 4, No. 1,PP. 1-15.
- Kim, J. Y., and Ghajar , A. J., 2006, A *General Heat Transfer Correlation for Non-Boiling Gas–Liquid Flow with Different Flow Patterns in Horizontal Pipes*, International Journal of Multiphase Flow,Vol. 32,PP. 447–465.
- Kitagawa , A., Kosuge , K., Uchida, K., and Hagiwara,Y.,2008,*Heat Transfer Enhancement for Laminar Natural Convection Along a Vertical Plate Due to Sub-Millimeter-Bubble Injection*, Journal of Experiments in Fluids, Vol. 45, PP. 473–484.
- Kenning ,D. B. R. and Kao, Y. S., 1972,*Convection Heat Transfer to Water Containing Bubbles Enhancement Not Dependent on Thermocapillarity*, International Journal of Heat and Mass Transfer, Vol.15, pp.1709-1717.
- Rzehak,R., and Kriebitzsch. S., 2015, *Multiphase CFD-Simulation of Bubbly Pipe Flow: A Code Comparison*,International Journal of Multiphase Flow,Vol.68 , PP.135-152.
- Sakr, I.M., El-Askary, W.A., Balabel, A. and Ibrahim, K., 2012, *Computations of Upward Water/Air Fluid Flow in Vertical Pipes*, CFD Letters, Vol. 4, No.4, PP. 193-213.

- Sanati, A., 2015,*Numerical Simulation of Air–Water Two–Phase Flow in Vertical Pipe Using K-E Model*, International Journal of Engineering& Technology, Vol.4 ,No.1,PP. 61-70.

- Salman,Y. K., and Mohammed , H.A.,2007, *Free Convective Heat Transfer with Different Sections Lengths Placed at the Exit of a Vertical Circular Tube Subjected to a Constant Heat Flux*, Journal of Al- Khwarizmi Engineering ,Vol.3 , No.3 , pp. 31-52.

- Tokuhiro, A.T., Lykoudis, P.S., 1994, *Natural Convection Heat Transfer From a Vertical Plate-I. Enhancement with Gas Injection*, International Journal of Heat Mass Transfer, Vol.37, No.6, PP.997–1003.

- Troshko, A. A., and Hassan,Y. A., 2001. *Two Equatios Turbulence Model of Turbulent Bubbly Flow*, International of Multiphase Flow,Vol. 27,PP.1965-2000.

- Wolters, J., 2003, *Benchmark Activity on Natural Convection Heat Transfer Enhancement in Mercury with Gas Injection*, ZAT-Report No. 379, PP. 1-54.

- Zimmerman, R., Gurevich, M., Mosyak,A., Rozenblit, R., and Hetsroni , G., 2006, *Heat Transfer to Air–Water Annular Flow in a Horizontal Pipe*, International Journal of Multiphase Flow , Vol. 32 , PP. 1-19.

9. NOMENCLATURE

Symbols

A = area of cross section, m^2
A_s = surface area, m^2
$C\mu, C_{\varepsilon 1}, C_{\varepsilon 2}$ = constants in turbulence model, dimensionless
C_D = drag coefficient, dimensionless
C_L = lift force coefficient, dimensionless
C_{td} = turbulent dispersion force constant, dimensionless
C_{w1} , C_{w2} = constants in wall lubrication force, dimensionless
D_i = tube inner diameter, m
D_o = tube outer diameter, m
$d_{airbubble}$= diameter of capillary tube of air bubble, m
dc = diameter of capillary tube, m
g = gravitational acceleration, N/m^2
K = turbulent kinetic energy, dimensionless
k = number of phases, dimensionless
L= length of pipe, m
M_k = interface momentum transfer, N
${M_k}^d$ = drag force, N
${M_k}^L$ =lift force, N

$M_k{}^W$= turbulent dispersion force, N
n_w = outward unit vector is perpendicular to the wall, dimensionless
P = pressure, Pa
Po = electrical power, W
Nu= average Nuesslt number, dimensionless
Nux= local Nusselt number, dimensionless
T_{in} = inlet temperature, ºC
T_{wall} =wall temperature, ºC
$T_{aluminum}$ =alunummim temperature, ºC
T_{b1}= bulk temperature at inlet, ºC
T_{b2} = bulk temperature at outlet, ºC
T_{bulk} = bulk temperature, ºC
uc = air velocity through the capillary tube, m/s
R,X,θ =cylindrical coordinates
Vo = voltage,Volt

Greek Symbols

α = volume fraction, dimensionless
ε = dissipation rate of turbulent kinetic energy, dimensionless
λ = thermal conductivity, (W/m.ºC)
$\emptyset_{conv}$ = convection of heat transfer, W
$\emptyset_{loss}$ = loss of heat transfer, W
$\emptyset_{cond}$ = conduction heat transfer, W

Table 1. Value of enhancement average Nueeslt number.

q" W/m^2	Re	Numerical results			Experimental results		
		Q_{air} (lit/min)			Q_{air}(lit/min)		
		1.5	**3**	**4**	**1.5**	**3**	**4**
27264	5269	12%	25.2%	33.4%	11.1%	19%	26%
	7377	11%	23.6%	31%	10.4%	18%	24.2%
	10528	9%	21.2%	30%	10%	17%	23.5%
36316	5269	8.3%	17%	28%	11.2%	18.4%	25.5%
	7377	7.1%	16.3%	26.2%	10.2%	15.3%	24%
	10528	6.4%	14.7%	24.3%	7.6%	13.45	23%
45398	5269	6.7%	15%	26.4%	9%	16.5%	24.4%
	7377	5.4%	13%	23.4%	8.3%	14.3%	22.2%
	10528	4.6%	11%	22.1%	7.3%	12.3%	20.7%

Table 2. Correlations of the average Nusselt number as a function of Ra/Re.

q"(W/m^2)	Q_{air}(lit/min)	Correlation equation
27264	0.0	Nu=3.366 $(Ra/Re)^{-0.35}$
	1.5	Nu=4.020 $(Ra/Re)^{-0.45}$
	3	Nu=3.404$(Ra/Re)^{-0.33}$
	4	Nu=6.177 $(Ra/Re)^{-0.70}$
36318	0.0	Nu=5.761 $(Ra/Re)^{-0.67}$
	1.5	Nu=3.872 $(Ra/Re)^{-0.41}$
	3	Nu=3.711$(Ra/Re)^{-0.38}$
	4	Nu=4.229 $(Ra/Re)^{-0.45}$
45398	0.0	Nu=5.68 $(Ra/Re)^{-0.57}$
	1.5	Nu=4.553 $(Ra/Re)^{-0.45}$
	3	Nu=5.277$(Ra/Re)^{-0.52}$
	4	Nu=6.394 $(Ra/Re)^{-0.62}$

Figure 1. Photograph of experimental apparatus.

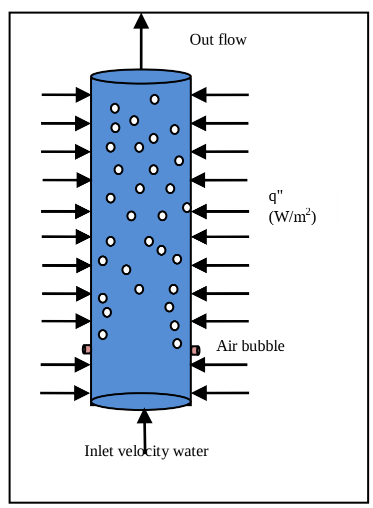

Figure 3. Test section layout with air bubbles injection.

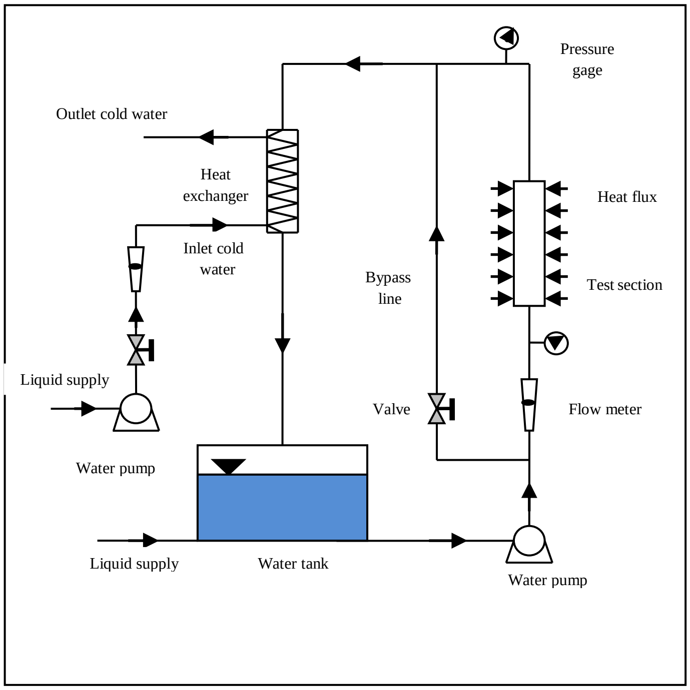

Figure 2. Schematic diagram of the experimental apparatus.

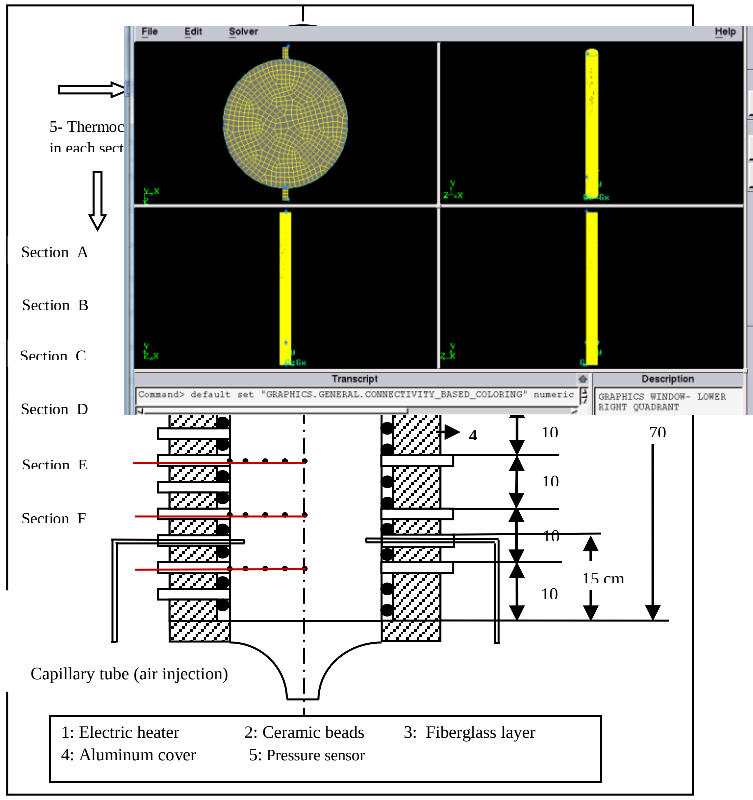

Figure 5. Mesh for multiphase turbulent flow in pipe.

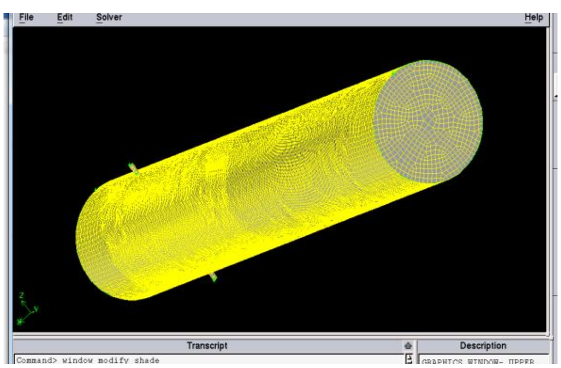

Figure 6. Continued.

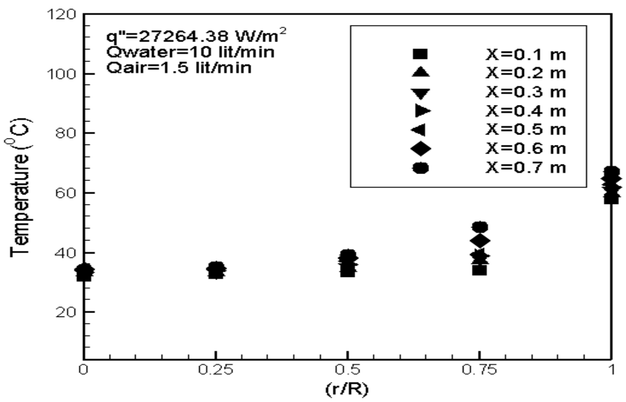

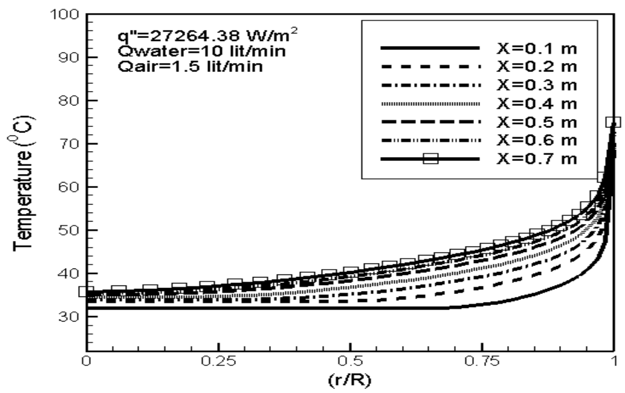

(a) q" =27264 W/m^2

(a) q" =27264 W/m^2

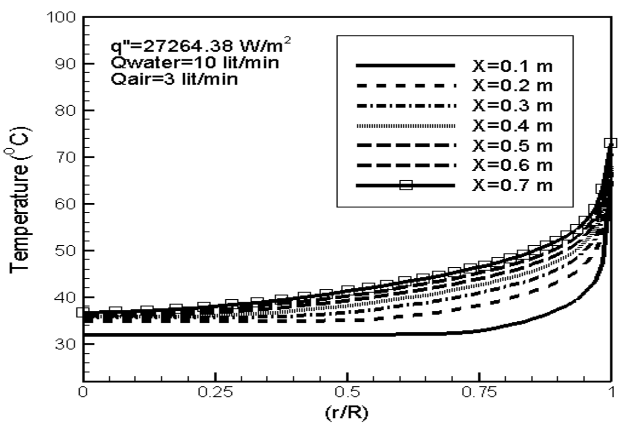

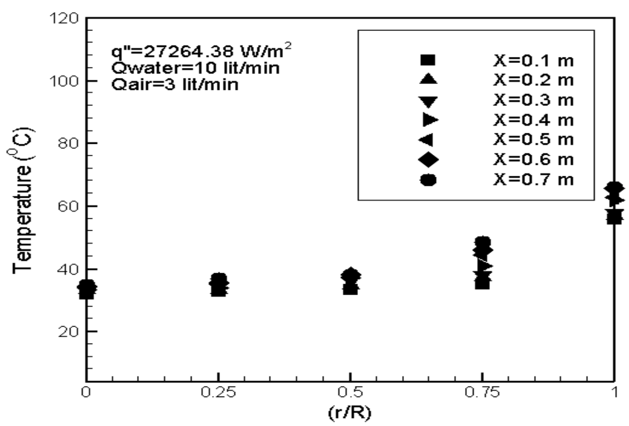

(b) q" =27264 W/m^2

(b) q" =27264 W/m^2

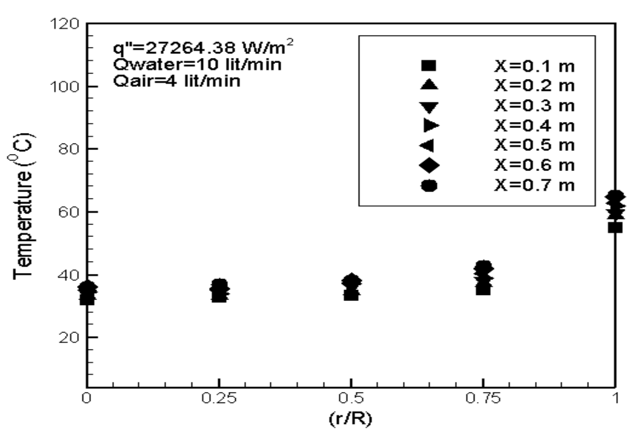

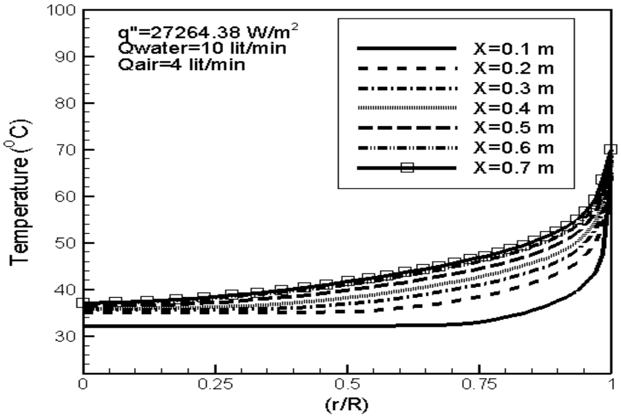

(c) q" =27164 W/m^2

(c) q" =27264 W/m^2

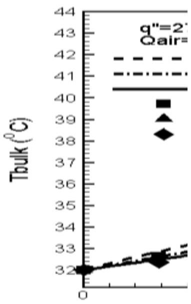

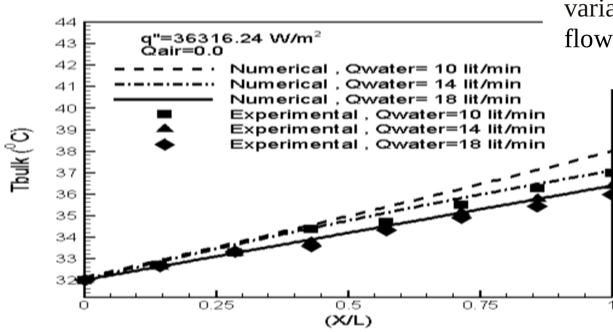

Figure 8
variation
flow rates

Figure 7. Numerical results of temperature variation with cylinder radial distance for different flow rates
and rate of heat fluxes at q"=27264 W/m^2

(a) q" =27264 W/m^2

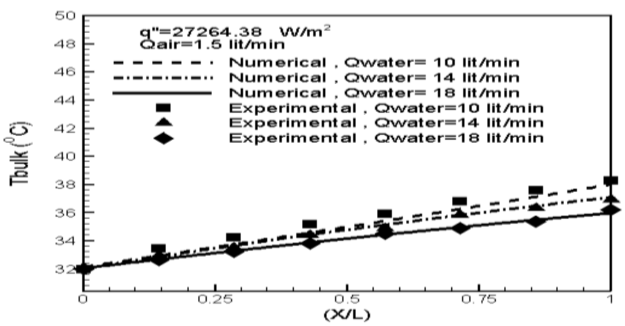

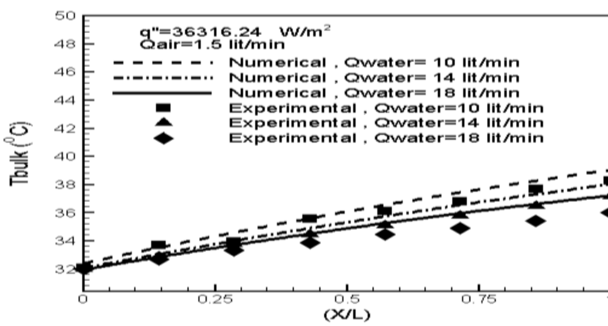

(b) q" =27264 W/m^2

(b) q" =36316 W/m^2

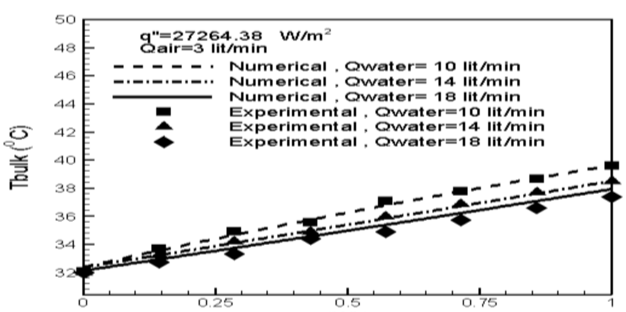

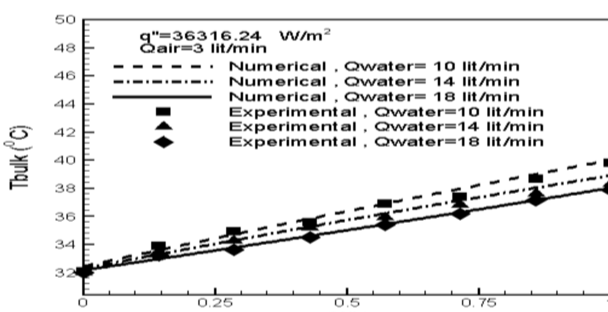

(c) q" =27264 W/m^2

(c) q" =36316 W/m^2

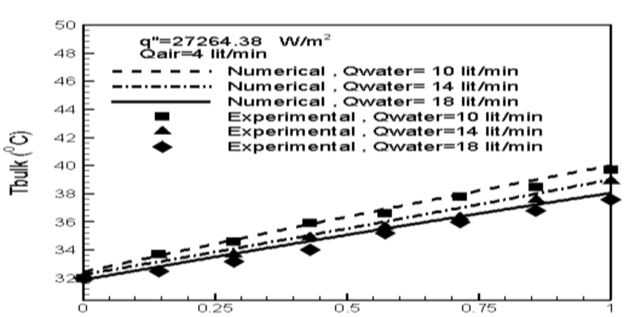

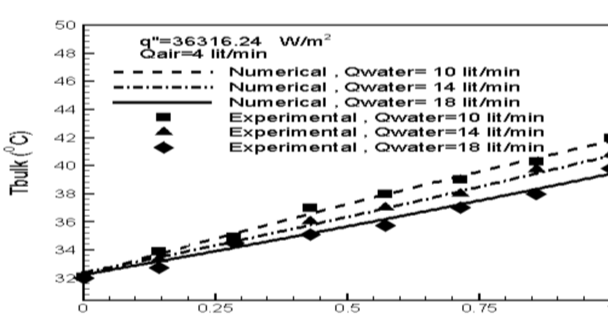

(d) q" =27264 W/m^2

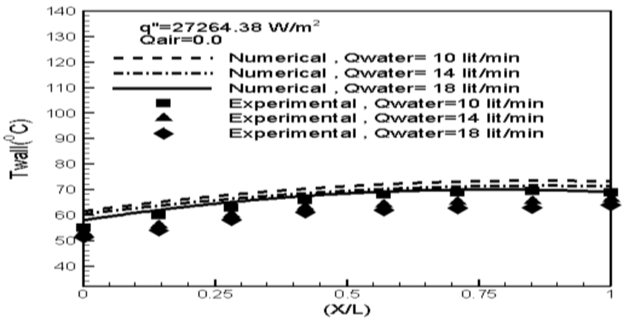

(d) q" =36316 W/m^2

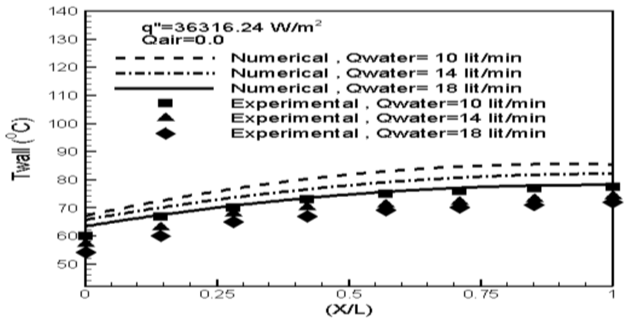

Figure 9. Comparison of numerical and experimental results of bulk temperature variation with length of cylinder for different values of heat fluxes.

(a) q" =27264 W/m^2

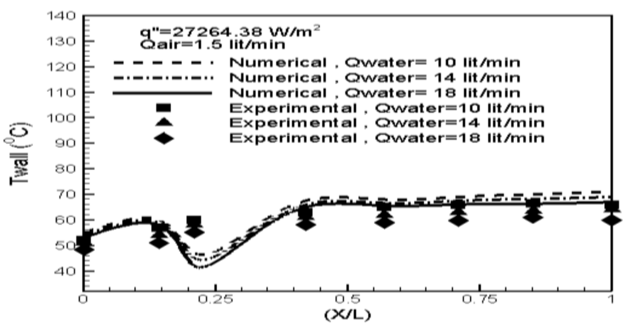

(a) q" =36316 W/m^2

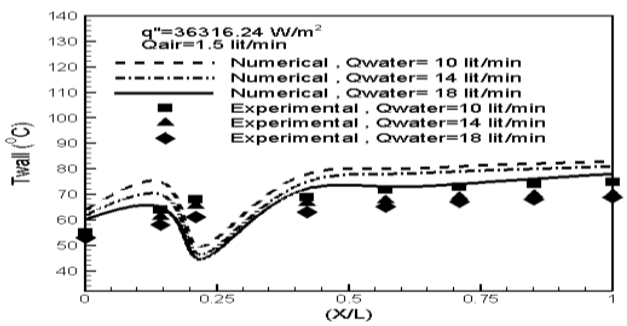

(b) q" =27264 W/m^2

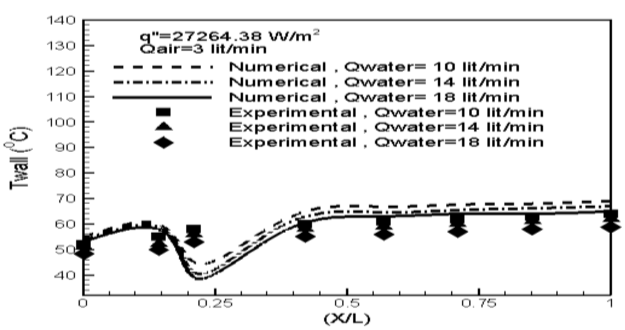

(b) q" =36316 W/m^2

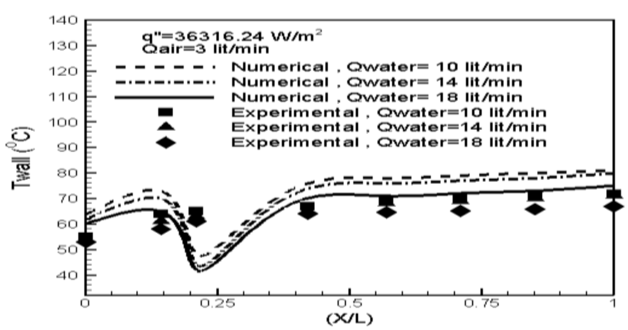

(c)q"=27264 W/m^2

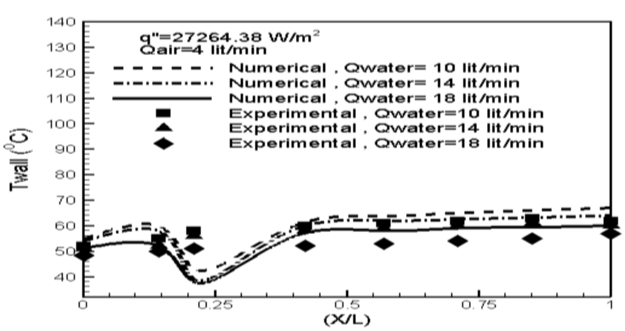

(c)q" =36316W/m^2

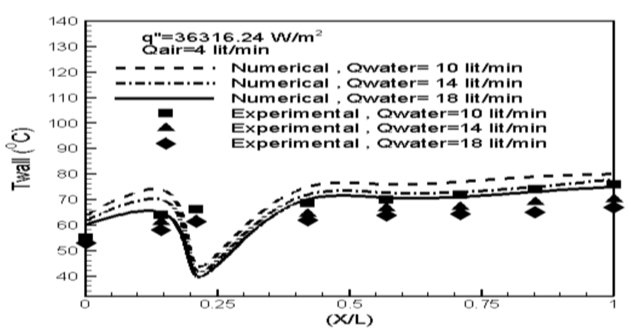

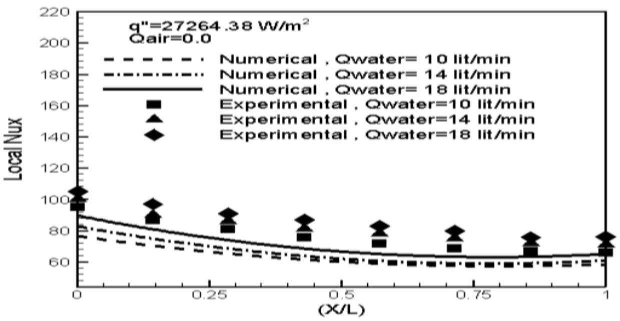

(d)q" =27264 W/m^2

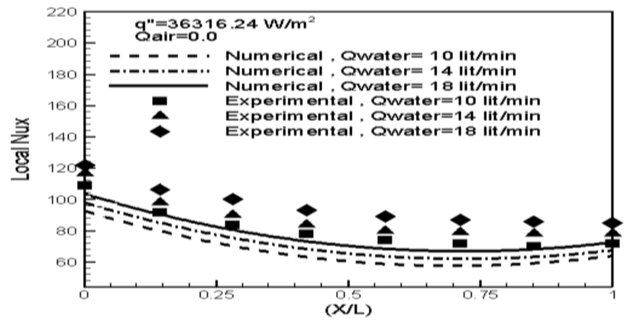

(d) q" =36316 W/m^2

Figure 10. Comparison of numerical and experimental results of wall temperature variation with length of cylinder for different values of heat fluxes.

(a) q" =27264 W/m^2

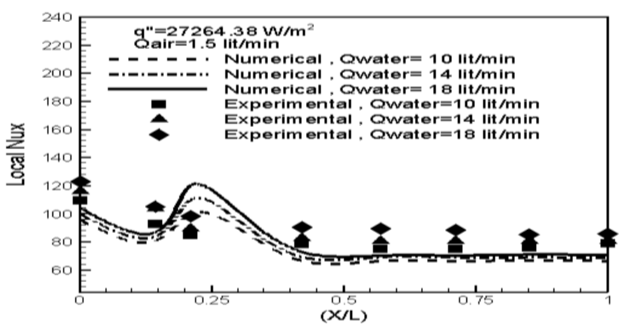

(a) q" =36316 W/m^2

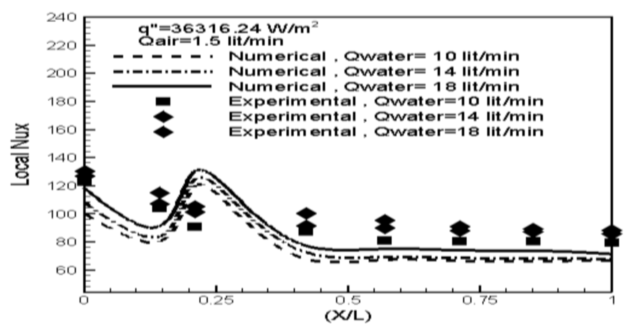

(b) q" =27264 W/m^2

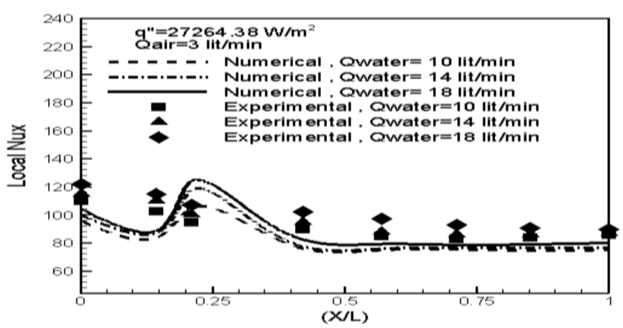

(b) q" =36316 W/m^2

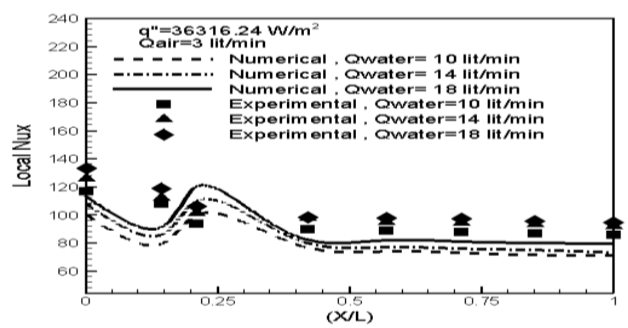

(c) q" =27264 W/m^2

(c) q" =36316 W/m^2

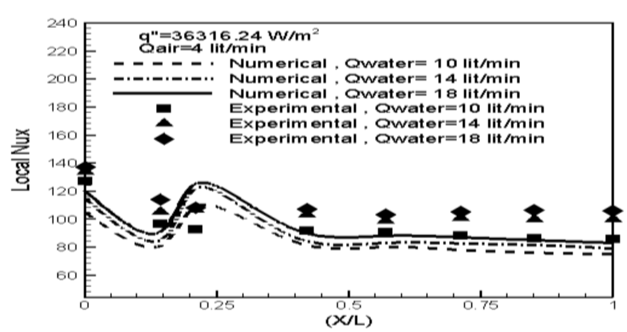

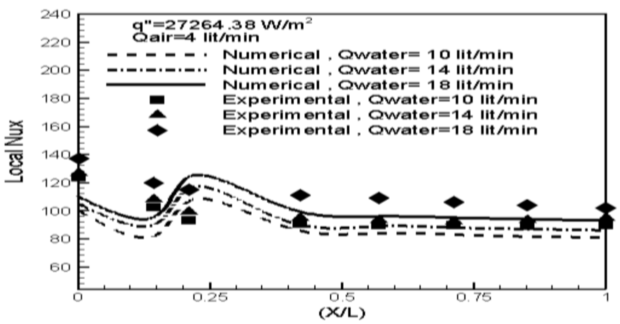

(d) q" =27264 W/m^2

(d) q" =36316 W/m^2

Figure11. Comparison of numerical and experimental results of local Nusselt number variation with length of cylinder for different values of heat fluxes.

(a) q" =27264 W/m^2

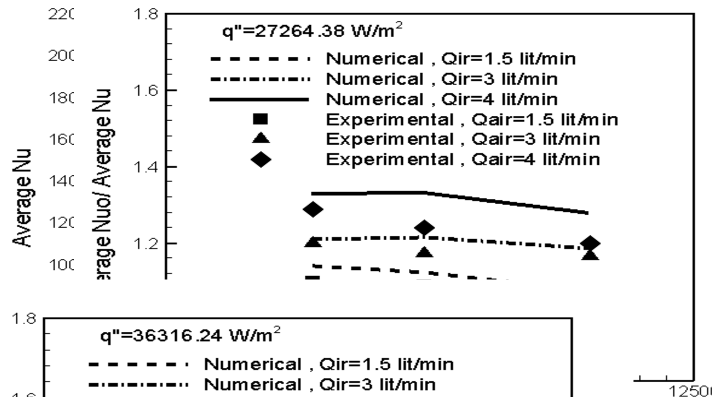

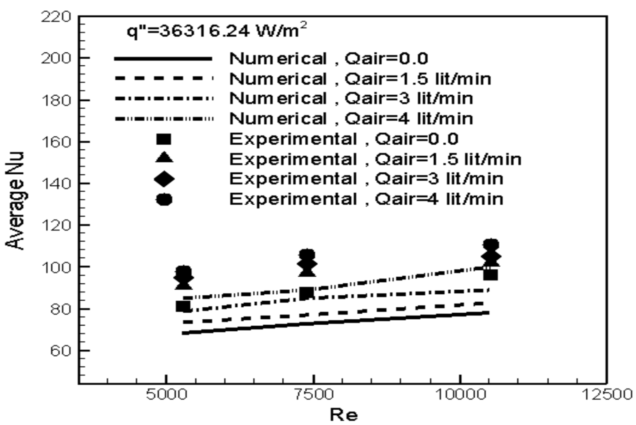

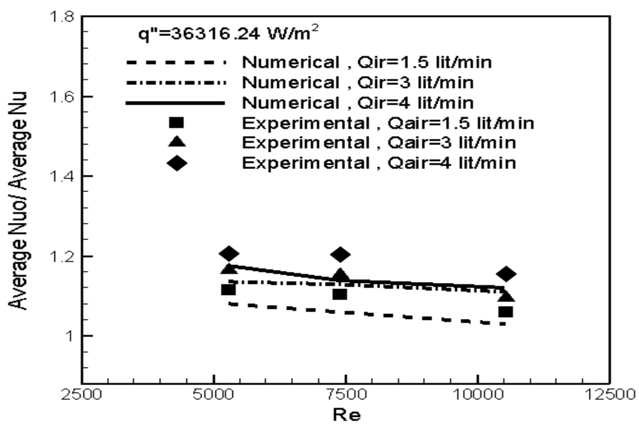

(a) q"=27264 W/m^2

(b) q" =36316 W/m^2

(b) q"=36316 W/m^2

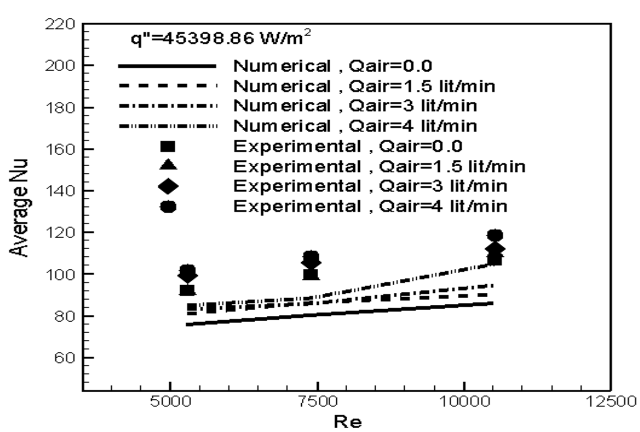

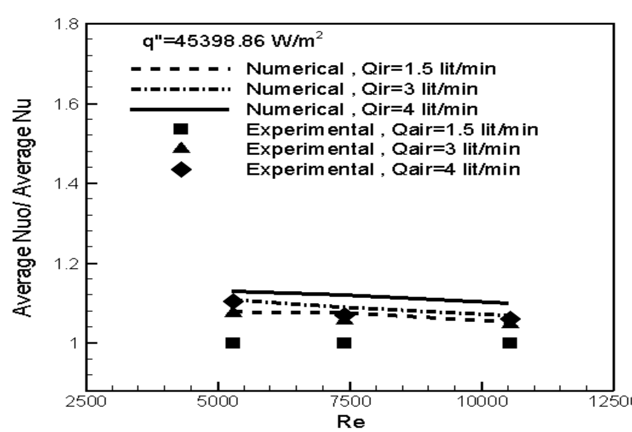

(c) q" =45398 W/m^2

(c) q"=45398 W/m^2

Figure12. Experimental results of average Nu number variation with Re number at different values of heat flux and Q_{air} .

Figure13. Experimental results of ratio of average Nuo/Nu variation with Re number at different values of heat flux and Q_{air} .

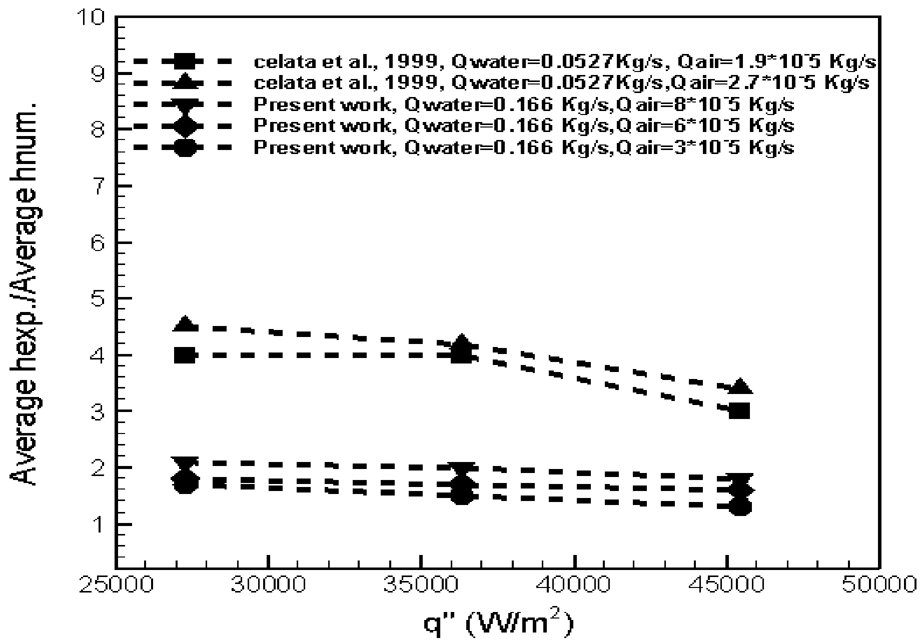

Figure 14. Comparison of the experimental and numerical results of ratio average h experimental / average h numerical for two phase flow with, **Celata et al., 1999**.

Detection and Diagnosis of Induction Motor Faults by Intelligent Techniques

Riyah Najim Kiter
Assistant Professor
Engineering College - Anbar University
riyahnajim@hotmail.com

Mohammed Moanes Ezzaldean
Lecturer
Department of Electrical Engineering – University of Technology
30097@uotechnology.edu.iq

Yousif Ismail Almashhdany
Assistant Professor
Engineering College-Anbar University
yousif_phd@hotmail.com

Fuad Lateef Salim
Instructor
Engineering College-Anbar University
Fuad_L_81@yahoo.com

ABSTRACT

This paper presents a complete design and implementation of a monitoring system for the operation of the three-phase induction motors. This system is built using a personal computer and two types of sensors (current, vibration) to detect some of the mechanical faults that may occur in the motor. The study and examination of several types of faults including (ball bearing and shaft misalignment faults) have been done through the extraction of fault data by using fast Fourier transform (FFT) technique. Results showed that the motor current signature analysis (MCSA) technique, and measurement of vibration technique have high possibility in the detection and diagnosis of most mechanical faults with high accuracy. Subsequently, diagnosis system is developed to determine the status of the motor without the need for an expert. This system is based on artificial neural network (ANN) and it is characterized by speed and accuracy and the ability to detect more than one fault at the same time.

Key words: induction motor, faults detection, diagnosis, intelligent system.

كشف وتشخيص اعطال المحركات الحثية بواسطة التقنيات الذكية

رياح نجم كطر
استاذ مساعد
كلية الهندسة – جامعة الانبار

محمد مؤنس عزالدين
مدرس
قسم الهندسة الكهربائية – الجامعة التكنولوجية

يوسف اسماعيل المشهداني
استاذ مساعد
كلية الهندسة – جامعة الانبار

فؤاد لطيف سالم
طالب
كلية الهندسة – جامعة الانبار

الخلاصة

يقدم هذا البحث تصميما كاملا لمنظومة مراقبة حالة المحرك الحثي ثلاثي الطور، تم بناء هذه المنظومة باستخدام الحاسوب الشخصي و نوعين من المتحسسات (التيارو الاهتزاز) لكشف بعض الاعطال الميكانيكية التي قد تحدث للمحرك. تمت دراسة وفحص عدة انواع من الاعطال تتضمن (اعطال المحامل، عدم محاذات محور الدوران) وذلك عن طريق استخلاص بيانات العطل باستخدام تقنية تحويل فورير السريع وقياس الاهتزاز. بينت النتائج ان تقنيتي تحليل بصمة التيار وقياس الاهتزاز لها امكانية كبيرة في كشف معظم الاعطال الميكانيكية وتشخيصها بدقة عالية. بعد ذلك تم تطوير وربط منظومة ذكية للتشخيص قادرة على تحديد

حالة الماكنة بدون الحاجة الى الشخص الخبير. هذه المنظومة تعتمد على الشبكة العصبية الاصطناعية و تتميز بالسرعة والدقة وقدرتها على كشف وتشخيص اكثر من عطل واحد في نفس الوقت.

الكلمات الرئيسية: المحرك الحثي، اكتشاف الاعطال، تشخيص، نظام ذكي.

1. INTRODUCTION

The alternating current machine is an essential tool in our daily lives contemporary, where they are used in many applications. The induction motors are the most popular kind of electric motor used, where up to about (90%) of motor types are used, **Silva, Cardoso, 2005**. It has the largest share in the industrial field because of its advantages, such as ease of installation, cheap price, and the high rate of (power / weight), so it does not need much maintenance. Despite the presence of the high reliability of the induction motors, the operating conditions will be exposed to different faults. The occurrence of any fault will cause operational problems that lead to stoppage of work, and thus lead to losses in production, as well as the risk of the lives of workers. In order to get a good run, and do not reach to these dangerous stages, the monitoring status of machinist (On-Line Condition Monitoring) helps to avoid the problems by monitoring the state and condition of the motor during operation in order to detect and diagnose the fault at early stages of treatment as soon as possible. There are many techniques that are used to detect and diagnose faults; this depends on the type of extract signal. **Dhuness, 2006**. The treatment methods differ depending on the way of digital processing in dealing with these signals, whether dealing with time domain, frequency domain, or time – frequency domain together, or to calculate the root mean square (RMS), and use fast Fourier transfer (FFT). The greatest development in computer programming techniques and smart systems, led to attract the attention of engineers to use it in diagnosis of machine state. The smart systems are characterized by their efficiency and small size as well as high speed in the process of data processing. Many researches deal with motor faults depending upon various mechanisms and techniques. **Yang, 2004**, and **Pole, 2009**.

The main objectives of this paper can be summarized as:

- Designing and implementing of a fault detection system to detect and diagnose the faults of three-phase induction motor based on monitoring current signal technique, and monitoring vibration technique.
- Developing an intelligent system which is able to detect and diagnose the faults, and determine the type and location of the fault, depending on the artificial neural network (ANN), so this system can work accurately instead of an expert person in the diagnosis process.
- Studying the effect of faults on the three-phase induction motors, by working a deliberate real model of faults that is exposed to the motor in order to get a true practical signal for component that results when the fault occurs.
- Study the behavior of the motor during the period of operation, as well as the study of some factors that lead to an increased level of faults.

2. FAULTS OF INDUCTION MOTORS

Induction motors may be exposed to many faults; these faults are classified to external or internal. The external faults occur because of the power supply and the surrounding environmental conditions while the internal faults occur due to damage in one or more parts of induction motor. In addition, these faults can be classified according to their kinds; i.e. mechanical or electrical fault, **Bhowmik, et al., 2013**.

2.1 Ball Bearing Faults

The ball bearing is important parts in all types of motors, the ball bearing consists of four parts (outer race, inner race, balls and cage), and some bearings contain cover for both sides to prevent oil leakage. The ball bearing that is exposed to harsh conditions during the run of motor lead to inadequate performance, these conditions may be mechanical stresses, unbalanced load, lack of alignment of the rotation axis, environmental conditions, rotor unbalance, lack of lubrication, or overload. All these reasons lead to fatigue ball bearing and lead to rise in temperature and increase in vibration and noise, cracking and collapse of the ball bearing. Faults of ball bearing can be divided into two categories, **Zhang, et al., 2008**:-

- Manufacturing defects, they are the result of a bad installation process, such as misaligned races, eccentric races, off-size rolling, and it contains bad parts.
- Local defect, this defect occurs in the case of use the ball bearing for a long time, it includes a number of damages such as cracks, gaps, pits and scratch. It can detect this type of faults by monitoring frequency as a result of vibration, which is calculated from the following relations, **Singhal,** and **Khandekar, 2013**:-

To calculate the frequency due to outer race defect the following equation can be used:

$$F_{ord} = \left(\frac{N}{2}\right) F_{sh} \ (1 - \frac{D_{ball}}{D_{cage}} cos(\beta)) \tag{1}$$

To calculate the frequency due to inner race defect the following equation can be used:

$$F_{ird} = \left(\frac{N}{2}\right) F_{sh} \ (1 + \frac{D_{ball}}{D_{cage}} cos(\beta)) \tag{2}$$

To calculate the frequency due to ball defect the following equation can be used:

$$F_{bd} = \left(\frac{D_{cage}}{2\, D_{ball}}\right) F_{sh} \left(1 - (\frac{D_{ball}}{D_{cage}} cos(\beta))^2\right) \tag{3}$$

To calculate the frequency due to cage defect the following equation can be used:

$$F_{td} = \left(\frac{F_{sh}}{2}\right) \ (1 - \frac{D_{ball}}{D_{cage}} cos(\beta)) \tag{4}$$

To calculate the frequency due to outer & inner race defect the following equation can be used:

$$F_{re} = 2\, F_{bd} \tag{5}$$

The frequencies result directly proportional to the dimensions of the ball bearing and motor speed. **Fig. 1** shows the variables used in the equations for ball bearing defects which under study. Ball bearing passed through several stages until they reach the stage collapse therefore, these stages must be studied to know the age of ball bearing and to find out when the ball bearing need for maintenance or replacement. These stages are:

1. Resonance wave will be generated in the ball bearing frequency.
2. Damage occurs in the outer race or inner race or ball or cage.
3. During this stage, the value of frequency increases in the bearing, and shows harmonics ($2F_{ird}$, $2F_{ord}$).
4. The value of the frequency increases and the show sideband component at this stage must be replaced the ball bearing.
5. The frequencies will appear equal to multiples of the main rotation frequency (F_{sh}, $2F_{sh}$,$3F_{sh}$,…..).
6. The frequencies will appear equal to multiples of the main rotation frequency up to about ($10F_{sh}$). If the noise of the ball bearing has been very high, it must be replaced at the fastest time.
7. During this stage, there are no frequencies because the motor stop working. The ball bearing does not always pass in all stages because sometimes ball bearing is exposed to the harsh conditions of the operator leading to speed up the failure of the ball bearing, such as fluctuation of load, **Mobius Company, 2008.**

2.2 Shaft Faults

The shaft is exposed to a range of faults that cause damage to ball bearing and increase vibration in the motor, **Clarence,** and **Silva, 2005**. These faults are:-

a. Shaft misalignment

This damage is caused by the lack aligns the axis of rotation between the motor shaft and shaft mechanical load, this fault occur because of putting the motor or mechanical load on an unleveled base. It can detect this damage by monitoring the frequency of current and frequency of vibration ($1F_{sh}$, $2 F_{sh}$, $3 F_{sh}$, …..). This fault can be divided into the following two types:

- Parallel shaft misalignment: This damage occurs because of the parallel motor shaft with mechanical load shaft, and not on one straight line. Displacement, therefore, occurs between the center axis of the motor shaft and the center axis of the mechanical load shaft toward vertical or horizontal direction as shown in **Fig. 2. a**.
- Angular shaft misalignment: It occurs because there is an angle between motor shaft and mechanical load shaft as shown in **Fig. 2. b**.

b. Bent shaft fault

This fault occurs because of unbalanced load, or thermal stresses that lead to curve the shaft and occur of air gap eccentricity fault.

3. METHODS OF FAULTS DETECTION

It is a way to test the motor case by monitoring changes in (temperature, current, vibration, sound, magnetic flux… etc..), during motor operation.

3.1 Current Monitoring

This technique is widely used to diagnose the faults in the induction motors because of the ease of application, high reliability, price licenses, and the need of a few sensors. It obtains a signal of current by choosing suitable sensors for application. The choosing of sensors depends on the sensor type, if the sensor is used to measure, or control, or it is used for the analysis of signal current, and it depends on the type of signal to be measured (AC signal, DC signal). The cost of the sensor varies according to the above factors. There are several types of current sensors, including Shunt Resistance Transducer (SRT), which is the simplest types of sensors, and Current Transformer (CT), which is suitable for measuring the low-lying frequencies. After obtaining the signal current, it detects the fault by using several techniques, some of these technologies are the following, **Gaeid, et al., 2011**.

3.1.1 Motor current signature analysis (MCSA)

It is one of the techniques widely used now, it can easily detect faults, and it needs one sensor. Its working principle is to analyze of an acquired signal current by using one of the signal processing techniques, including analysis of the signal in the domain frequency to monitor the frequency spectrum, or analysis in the domain time or in the domain time-frequency.

3.1.2 Park vector conversion theory

This technique is used to detect faults of unbalance voltage supply and short circuit fault in the stator. The principle of this technique work is to convert the three-phase system into two phase system, then draw two vectors in the plane, where the resulting shape will be circulated if the motor is good and balanced source, but if there is any fault in the source or wires of stator, the output format will be oval, **Ouari 2012.**

3.2 Vibration Monitoring

This technique was a famous technique used a long time ago; it is used to detect faults in electric motors. It now takes an important role in the industrial field because of their ease of use, and it has ability to detect most of the mechanical faults, and some electrical faults. However, this technique has disadvantage because it needs a number of sensors that are in sometimes expensive **Clarence,** and **Silva, 2005**. The working principle of this technique is to measure the vibration signal, or analysis to get the vibration signature. And it is used in this way to measure root mean square (RMS) for the vibration of the signal to compare it with global standards in the table of motor vibration standards according to (ISO 12372), **Mohamadi, et al., 2008**. There are several vibrating sensors that are used for monitoring vibration signal emerging from the motor. These sensors can be divided according to the input signal **Rion Company, 2010**:-

1. Displacement-Vibration Transducer.
2. Velocity-Vibration Transducer.

3. Acceleration-Vibration Transducer.

The acceleration-vibration transducer is a type of sensors that most commonly used at this time, and it was named as the acceleration because of output signal proportional with accelerating. Moreover, the principles of its work are concerned with the conversion of the force supply into an electrical signal proportional to force supply, accordance with Newton's second law (F_M = M×a) **Clarence,** and **Silva, 2005**. Sensor place has great significance in the detection of faults. For example, if the sensor is in vertical position, it will be more sensitive to detect faults of weakness of the motor structure, while in a horizontal position sensor will be more sensible for rotor balance. When putting sensor in axial position, it will be more sensitive to detect the shaft misalignment fault, and bent shaft fault. To overcome these problems, sensors on three axes must be used or use triaxle sensors. **Mobius Company, 2008.** The use of root mean square (RMS), is a simple way, where the value of root mean square (RMS), exceeds the value of the accelerating allowed, this indicates the presence of faults.

3.2.1 Time domain analysis

When the signal analysis is in time domain, the information is taken from the form of the function in the time domain, or by calculating some values by the equations such as, root mean square (RMS). The following equation is used in the calculations in the time domain:-

$$RMS = \sqrt{\frac{1}{N_s} \sum_{n=1}^{N_s} f(n)^2} \tag{6}$$

3.2.2 Frequency domain analysis

When the signal analysis is in frequency domain, the information is taken by noting the frequency spectrum of the signal. There are several techniques for the analysis of signal in frequency space, some of these are, **Al-Hassoon, 2007**:-

1. Fourier series (FS).
2. Fourier transforms (FT).

The focus in the signal analysis in the frequency domain is on the way of fast Fourier transform (FFT).The fast Fourier transform (FFT) is used to reduce the number of calculations compared with the Discrete Fourier Transform (DFT). The number of calculations is equal to (N_s Log_2 N_s). This technique is widely used in all scientific fields, and this type of analysis is used in most analysis devices in industry.

4. INTELLIGENCE SYSTEMS (SMART TECHNOLOGY).

The Artificial Neural Networks (ANN) were well-studied during the past time, it has been successfully applied in the industrial field to monitor and diagnose faults in the motor where it is working rather than an expert in the monitoring process. Also it is faster in data processing and accurate in the diagnosis of fault compared with conventional methods used because it is able to deal with complex relations and it is able to clarify the condition which affects the system that cannot be expressed in mathematical relations. The Artificial Neural Networks (ANN) represents a mathematical tool to deal with the nonlinear changes to bring it closer to the suitable relations by structuring the network and adjusting the weight values within anodes which represents the internal structure of the smart system, **Nelson**, **2004**. There are many types of neural networks, and the system more commonly used is (Feed-Forward Neural Networks) as shown in **Fig. 3**, which can be represented by the following equation, **Patan**, **2008**:

$$Y = F(\sum_{i=1}^{n} w_i \ I_i + b) \tag{7}$$

The detection and diagnosis process consists of four stages:

1- System of data acquisition and signal processing.
2- The process of extracting the information from the signal.
3- The process of detection and diagnosis, fault.
4- The process of classifying the fault type.

Intelligent system is used in the last two steps. Neural network consists of a group of neurons formulated in the form of a layer, and these layers can be divided into three main layers: the input layer through which the data entry, hidden layer which provides the education's ability for the system (it may be more than one layer), and the output layer as shown in **Fig. 4**.The performance of neural network system depends on the relations that contain elements. Each of these elements is trained to perform a specific function, by adjusting the weights and biose of the neurons is achieved.

The first step in training the artificial neural network (ANN), by using (Labview) is developing the network by using various software phrases. Each phrase is customized to deal with one of types neural networks. There are several phrases which are:

- Learning rate (tr).
- Showing the status of training.
- Stopping the training process (Epoch), where the network stops training if the number of iterations equal the number of (Epoch) Limited.
- (Goal) To determine the value of less error.

After the completion process of information, extraction from gaining signal is used by signal processing techniques that are represented by (FFT) technique. It used the artificial neural network system (ANN) to define the relations between the result component and the state of the motor to have identified values of appropriate components (frequency) to detect and identify the faults (amount of the component). The input layer of artificial neural network (ANN) consists of (1920) neurons, and the hidden layer consists of one layer, containing (15) neurons. And the output layer consists of (15) output neurons, with epoch of (1000), and max time (10s), max error (1), and bias (0.9), and the error evaluation is over validation.

5. EXPERIMENTAL WORK

The experimental work contains the faults that are done deliberately in order to simulate the conditions that occur in the motor when the faults are done and shows the techniques used to extract information and analysis of signals in the frequency domain by using fast Fourier transform (FFT), and in the domain time by using the root mean square (RMS). The general layout of the experimental work is shown in **Fig. 5**. The detection and diagnosis system consist of the following items:

5.1 Hardware (Equipment, Tools, and Components).

This includes the following parts:

1. Induction motor, it is an electric three phase induction motor of specifications (1.1KW, 1430r.p.m, 220V, 4Pole).
2. Iron rings, in order to create the detection and diagnosis system, three iron rings wrapped with copper wire were used as current transformers, together with a similar number of iron rings to act as voltage transformers as shown in **Fig. 6**. All the sensors are connected to the data acquisition interface as shown in **Fig. 5**.
3. Vibration sensor of type (Piezoelectric vibration) was attached to the body of the induction motor, as shown in **Fig. 7**.
4. Speedometer used to calculate motor speed as shown in **Fig. 8**. The sensors were linked with the electric motor.
5. Data acquisition interface.
6. Multimeter, in order to measure the current and voltage.
7. DC generator, the generator (2.7A, 110V, 0.297KW, ECC 0.325, 1500 r.p.m) is used to convert mechanical energy into electrical energy as shown in **Fig. 9**.
8. Electrical resistors type of (RHEOSTAT, 50Ω, 10A), is used to increase and decrease the load on the motor by using the power of the electric generator as shown in **Fig.10**.
9. Autotransformer, to change the voltage supply, a 3-phase autotransformer is used.

A general view of the experimental testing system is shown in **Fig. 11**.

5.2 Software

In this work, LabView software is used to implement the program and it includes several steps. The program contains an interface to display faults by lamps arranged in three columns, each lamp is responsible of one kind of faults. They are arranged according to the letters from (A to O). When one of the lamps is active, it means there is a fault. These lamps indicate the following status:-

A- Indicate there is no load, motor health.
B- Indicate there is half load, motor health.
C- Indicate there is a full load, motor health.
D- Indicate there is no load, unbalance of the voltage supply.
E- Indicate there is half load, unbalance of the voltage supply.
F- Indicate there is a full load, unbalance of the voltage supply.
G- Indicate there is no load, fault of shaft misalignment.
H- Indicate there is half load, fault of shaft misalignment.

I- Indicate there is a full load, fault of shaft misalignment.
J- Indicate there is no load, fault of broken rotor bars.
K- Indicate there is half load, fault of broken rotor bars.
L- Indicate there is a full load, fault of broken rotor bars.
M- Indicate there is no load, fault of ball bearings.
N- Indicate there is half load, fault of ball bearings.
O- Indicate there is a full load, fault of ball bearings.

6. SIMULATION OF THE MOTOR FAULTS

6.1 Ball bearing faults

This fault is created by using a set of used ball bearings of the type (6205RS), containing different faults (outer race, inner race, ball, and cage). **Fig. 12** shows the faults of ball bearings. The motor was run in three cases (N.L, H.L, F.L), the bearings have been changed more than once (in order to check the motor at several cases), and the measurements are taken in each case. The frequencies can be calculated using equations (1) through (5), depending on the speed of the motor and the dimensions of the ball bearing. **Table 1** shows the type and dimensions of the ball bearing used, the frequencies are calculated at different speed and load level that are tabulated in **Table 2**.

6.2 Shaft misalignment faults

To create such a sort of faults, a number of thin slides were inserted slide under the motor base at certain angles. And for both cases parallel shaft misalignment, and angular shaft misalignment, many angles is studied and for each case three levels of motor load (N.L, H.L, FL) are considered.

7. RESULTS

7.1 Measuring the Current

7.1.1 Motor with shaft misalignment fault

In the event of shaft misalignment faults for both types (parallel and angular misalignment), the component of vibration (F_{sh}) is transmitting into a current signal, analyzing the current signal is shown in **Fig. 13**. Where a component of rotation frequency and its complications are (F_{sh}, $2F_{sh}$, $3F_{sh}$,….), and the frequency of current signal is (23.5, 47, 70.5,…).

7.1.2 Motor with ball bearing faults

The occurrence of any fault in the bearing caused a generation of a frequency component as illustrated in the equations (1-5). The examination of defective samples of ball bearing is detected and the frequencies are shown in **Fig. 14**. The frequency spectrum in **Fig. 14** shows the presence of the component (78Hz), which represents the component resulting from the defect in the outer race of the bearing (F_{ord}). This indicates that the sample used contains the defect in the outer race. In addition, it is noted that the presence of the component (126Hz) is equal to the value of the component of the fault, plus the value of component wave of source supply.

Some references state that the components of mechanical faults are shown in current signal plus the value of the basic component of source supply, depending on the relation:

$$F_{fault} = F_{defect} \pm f_{supply} \qquad (8)$$

This is clear in **Fig. 14** in which the sample used contains fault in the inner and outer races (F_{re}) at (143Hz), which are equal to the value of the fault component plus the value of the basic component of source supply. The fault component of the cage (F_{td}) was approximately equal to (8.7Hz) and this is not clear in the calculation of frequency, but when adding the value of basic wave frequency (50Hz), it could be found that the value (58.7Hz) was clear.

7.2 Measuring the Vibration

When calculating the value of (RMS) for vibrating signal in the case of health motor, and in the case of faulty motor, so the possibility of knowing the state of the motor, whether it was healthy, or contain the damage, by comparing the (RMS), with (ISO - International Organization for Standardization). **Table 3**, and **Table 4**, shows the value of (RMS), for the motor vibration signal at various loads and different modes of measurement (radial, axial). It is shown that the value of the vibration signal in the case of sensor placed radially-vertical was more sensitive compared with sensor positioned axially, so that sensor in radial form is better than placing it axially at calculating the vibration, except in the case of shaft misalignment. Moreover, motor fault can be detected by note the shape of signal vibration.

7.2.1 Vibration under bearing faults

The vibration signal in the event of a fault in bearings shows that the wave shape will be large deformation. This indicates that the faults of bearing have large effects on the vibrations as shown in **Fig. 15**.

7.2.2 Vibration under shaft misalignment faults

In the event of shaft misalignment faults, both types (parallel shaft misalignment and angular shaft misalignment), reveal a significant change in the shape of the vibration signal compared with the previous faults, as shown in **Fig. 16**.

7.3 Detection and Diagnoses Faults by Intelligent Systems

7.3.1 Normal operation of the health motor

In the case of health motor with full load (F.L), the results were as in **Fig. 17. A**. When trying again with different loads (N.L), (H.L), the result was as in **Fig. 17. B** and **Fig. 17. C**, respectively.

7.3.2 Ball bearing faults

In the case of bearing faults, with full load (F.L), the results were as in **Fig. 18. A** and when it was tried again with different loads (N.L), (H.L), the result was as in **Fig. 18. B**, and **Fig. 18. C** respectively.

7.3.3 Shaft misalignment faults

In the case of shaft misalignment faults, with full load (F.L), the results were as in **Fig. 19. A**. Moreover, when it was tried again with different loads (N.L), (H.L), the result was as in **Fig. 19. B**, **Fig. 19. C**, respectively.

7.3.4 Multi faults (ball bearing and shaft misalignment)

By inserting a number of thin slides under the motor base at certain angles, the motor has a bearing fault. The motor was running for three cases (N.L, H.L, F.L), and the results were taken in each case. With a full load (F.L) the results were as in **Fig. 20. A**. And with different loads (N.L), (H.L), the result was as in **Fig. 20. B**, **Fig. 20. C**, respectively.

8. CONCLUSIONS

According to the current vibration and artificial neural network (ANN) monitoring techniques, it can be concluded that:-

1. The monitoring of motor current technology helps to detect faults by measuring the frequency of the current signal (shaft misalignment, and ball bearing faults) and it seems appropriate to display the components.
2. The motor current signature analysis (MCSA) technique is a technique used in a wide range; also it is good and effective technology in the detection, of the large number of mechanical and electrical faults.
3. The results of vibration monitoring technique also showed the possibility of the diagnosis of the motor case by measuring and monitoring the root mean square (RMS), and comparing it with the standards in the table of (International Organization for Standardization) ISO. In addition, the results showed that choosing the location and direction sensor has an important role in determining the type of fault since some faults appear in a certain direction of the sensor, but they do not appear in the other direction.
4. The use of artificial neural network (ANN) helps in the detection and diagnosis of motor faults at high speed and high accuracy reached to 94% of accuracy.
5. The use of artificial neural network (ANN) is able to detect the compound faults at the same time.

REFERENCES

- Al-Hassoon, W. H., 2007, *Power Quality Measurement Based on Wavelat Transform Techniques*, M. Sc. Thesis, Mosul University, Mosul, Iraq.
- Bhowmik, P. S., Pradhan, S., and Prakash, M., 2013, *Fault Diagnostic and Monitoring Methods of Induction Motor: A Review*. International Journal of Applied Control, Electrical and Electronics Engineering 1.1, PP. 1-18.

- Dhuness, K., 2006, *An Investigation into Aspects of the on-Line Detection of Broken Rotor Bars in Induction Motors*, Magister Ingeneriae Johannesburg University.
- Gaeid, K. S., Ping, H. W., Khalid, M., Salih, A. L., 2011, *Fault Diagnosis of Induction Motor Using Mcsa And Fft***.** Electrical and Electronic Engineering 1.2, PP. 85-92.
- Mohamadi, H., Ahmadi, H., Mohtasebi, S. S., Hasani,S., 2008, *Vibration Condition Techniques for Fault Diagnosis of Electromotor With 1.5 KW Power*, Journal of Applied Sciences 8 (7).
- Mobius Company, 2008, *Condition Monitoring and Vibration Analysis Training, Reference and Diagnostic Tools*, Mobius I Learning Vibration series. (www.mobiusinstitute.com).
- Nelson, A. L., 2004, *Introduction to Artificial Neural Network*, University of South Florida.
- Ourici, A., and Ouari, A., 2012, *Park's Vector Approach to Detect an Inter Turn Stator Fault in a Doubly Fed Induction Machine by a Neural Network.* pp. 25–32.
- Patan, K., 2008, *Artificial Neural Networks for the Modelling and Fault Diagnosis of Technical Processes*, Chapter 8, Springer-Verlag Berlin Heidelberg.
- RION Company**,** 2010, *Catalog Of Vibration Analyzer*, Rion co. LTD.
- Silva, J. L., and Cardoso, A. J., 2005, *Bearing Failures Diagnosis in Three-Phase Induction Motors by Extended Park's Vector Approach*, IEEE.
- Singhal, A., Khandekar, M. A., 2013, *Bearing Fault Detection in Induction Motor Using Motor Current Signature Analysis***,** International Journal of Advanced Research in Electrical, Electronics and Instrumentation Engineering Vol. 2, Issue 7.

- Yang, H., 2004, *Automatic Fault Diagnosis of Rolling Element Bearings Using Wavelet Based Pursuit Features*, Ph. D. Thesis, Queensland University of Technology.
- Zhang, B., Georgoulas, G.,and Orchard, M., 2008 *Rolling Element Bearing Feature Extraction And Anomaly Detection Based On Vibration Monitoring*, 16th Mediterranean Conference on Control and Automation, Congress Centre, Ajaccio, France, IEEE, PP.1792-1797.

NOMENCLATURE

b = amount of deviation from the target, dimensionless.

β = contact angle, degree.

D_{ball} = diameter ball, mm.

D_{cage} = diameter cage, mm.

F = frequency power supply, Hz.

F_{bd} = output frequency due to ball defect, Hz.

F_{ird} = output frequency due to inner race defect, Hz.

F.L = full load, dimensionless.

f(n) = signal discrete.

F_{ord} = output frequency due to outer race defect, Hz.

F_{re} = output frequency due to outer & inner race defect, Hz.

F_s = sampling frequency, Hz.

F_{sh} = shaft rotation frequency, Hz.

F_{td} = output frequency due to cage defect, Hz.

F(x) = non-linear transfer function, dimensionless.

H.L = half load, dimensionless.

Ii = the input data, dimensionless.

N = number of balls in the bearing, dimensionless.

N.L = no load, dimensionless.

Ns = number of simple, dimensionless.

Wi = weights coefficients intracellular, dimensionless.

Y = output neural network, dimensionless.

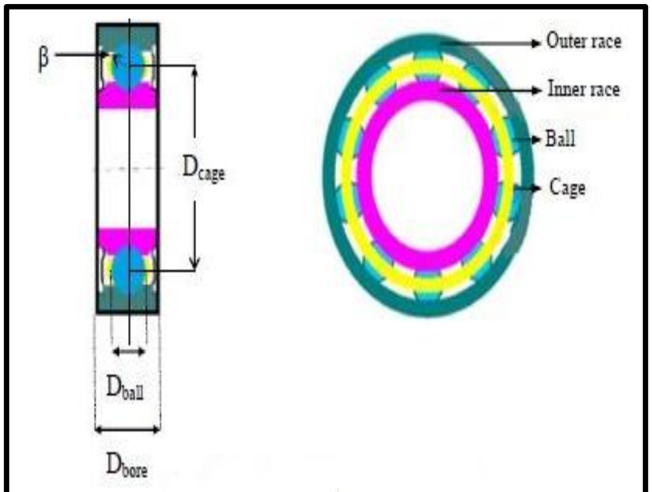

Figure 1. The variables used in the equations for ball bearing

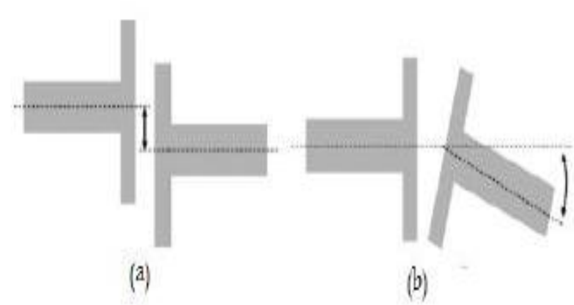

An illustration of (a) Parallel misalignment, (b) Angular misalignment

Figure 2. Type of shaft misalignment

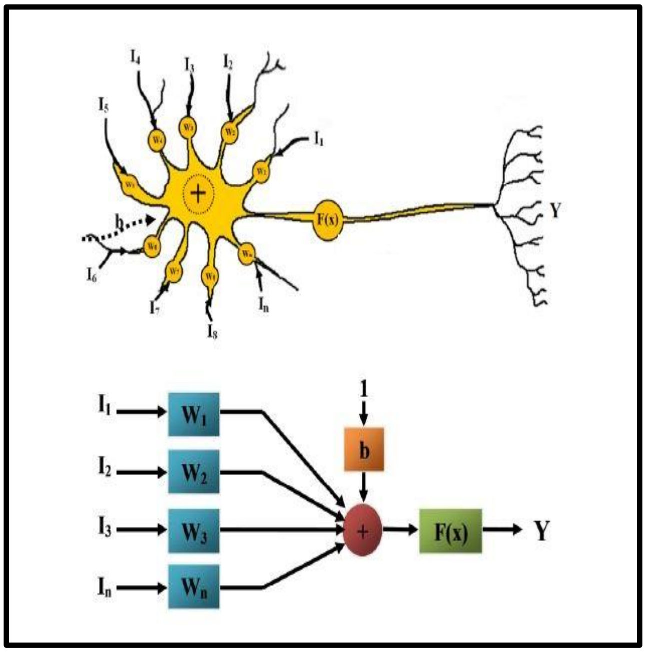

Figure 3. The Mathematical Description for (Feed-Forward Neural Networks).

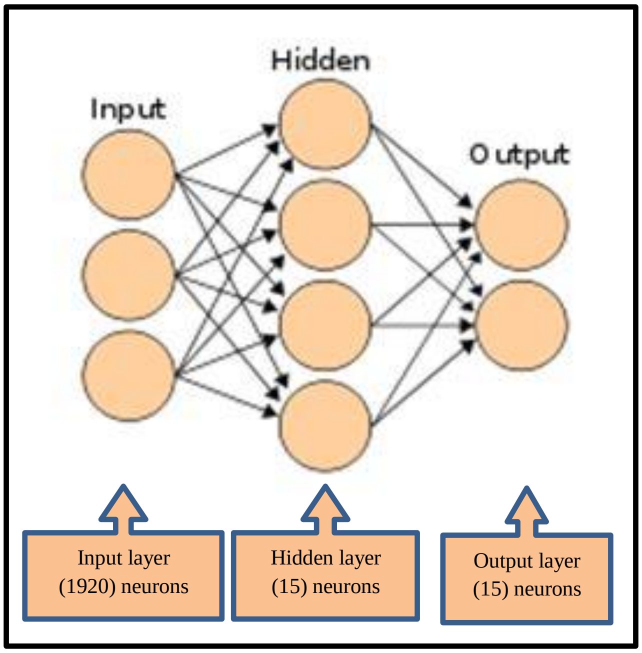

Figure 4. The layers of artificial neural network (ANN), and the way associated together with each

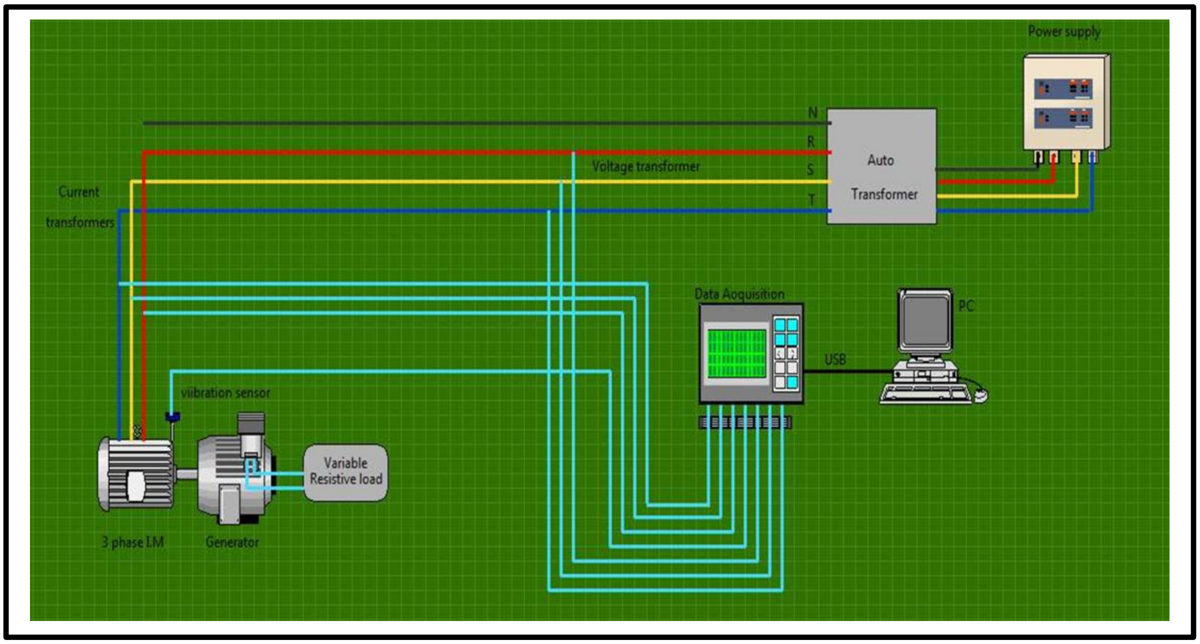

Figure 5. The general layout of the experimental work

(A) Before wrapped

(B) After wrapped

Figure 6. Iron rings

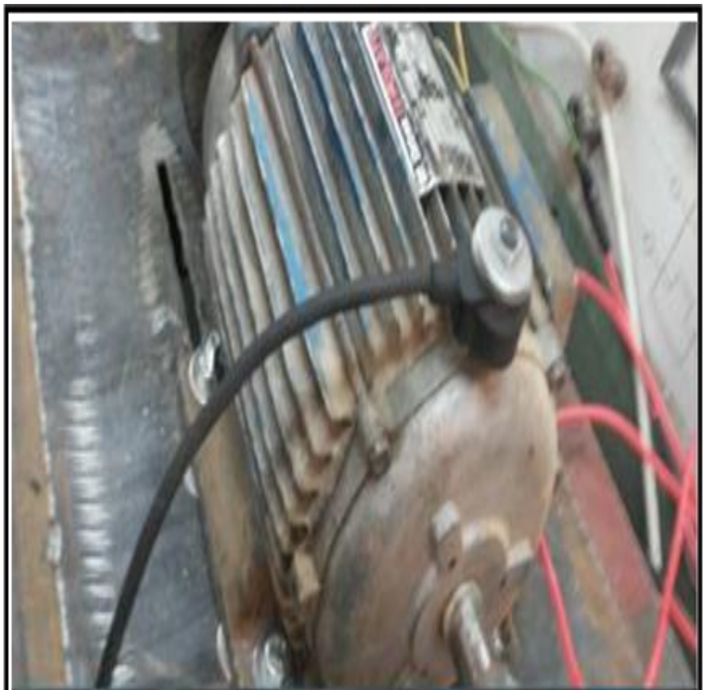

Figure 7. Vibration sensor

Figure 8. Speedometer

Figure 9. Generator

Figure 10. Electric resistance

Figure 11. Detection and diagnosis system

Figure 12. Sample of bearing faults

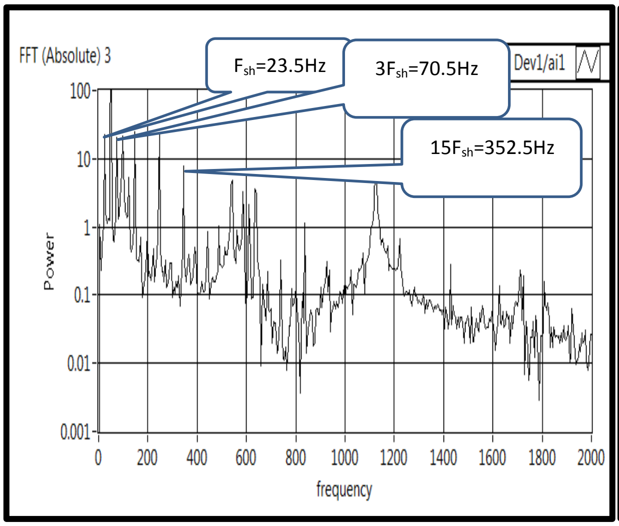

Figure 13. Analysis for shaft misalignment

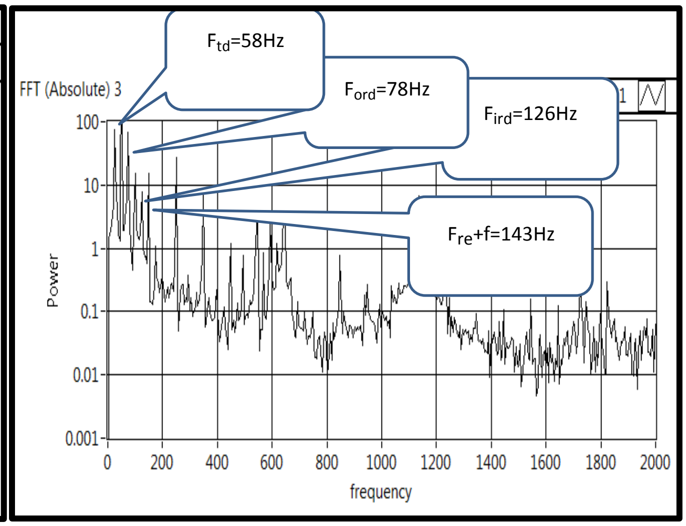

Figure 14. (FFT) Analysis for bearing faults

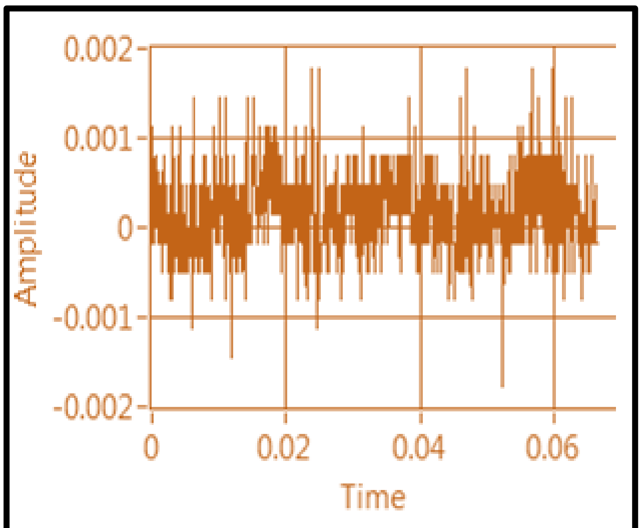

Figure 15. Vibrationsignal in a case of bearing faults

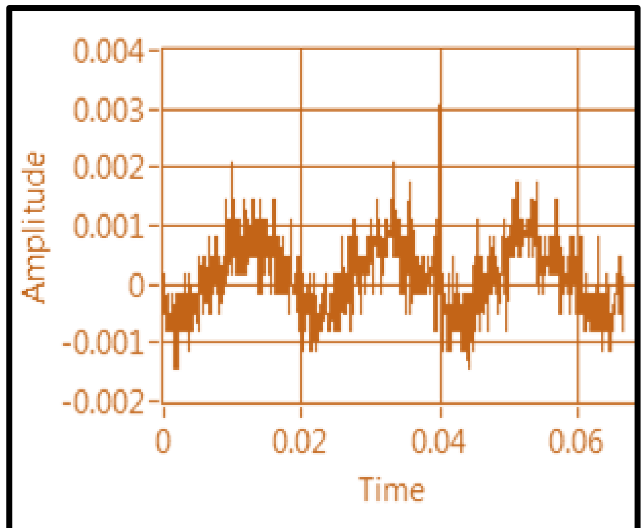

Figure 16. Vibration signal in a case of shaft misalignment faults

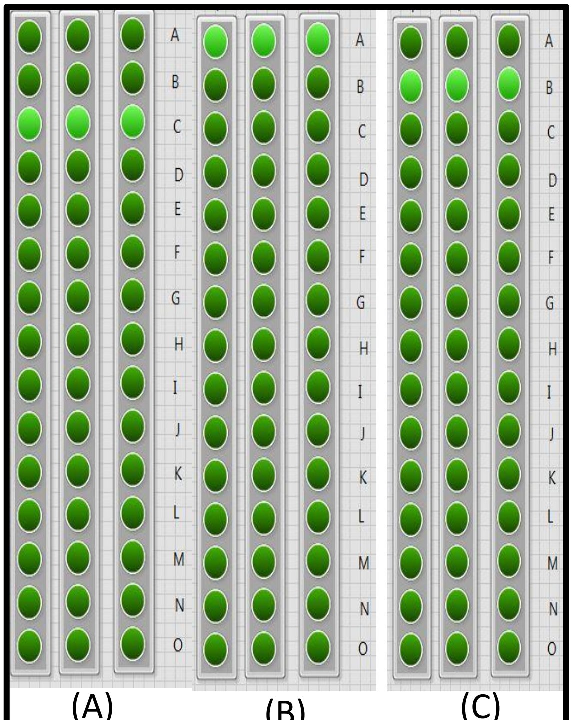

Figure 17. Health motor (A) F.L, (B)N.L, (C) H.L

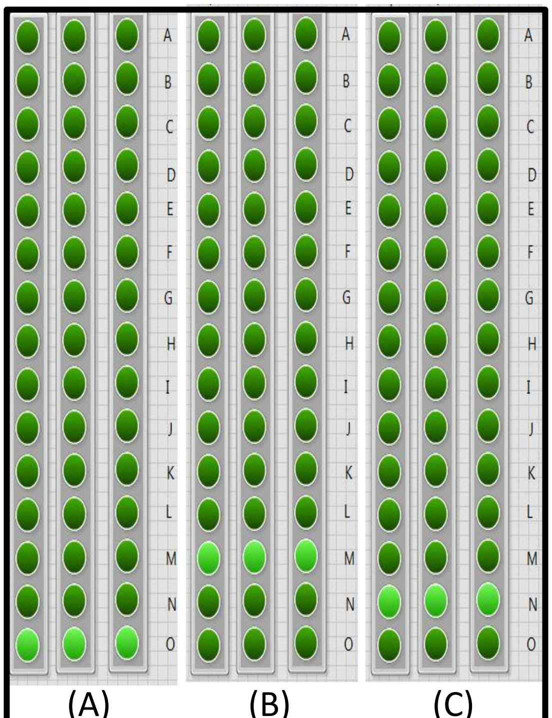

Figure 18. Case of bearing faults(A) F.L, (B) N.L, (C) H.L

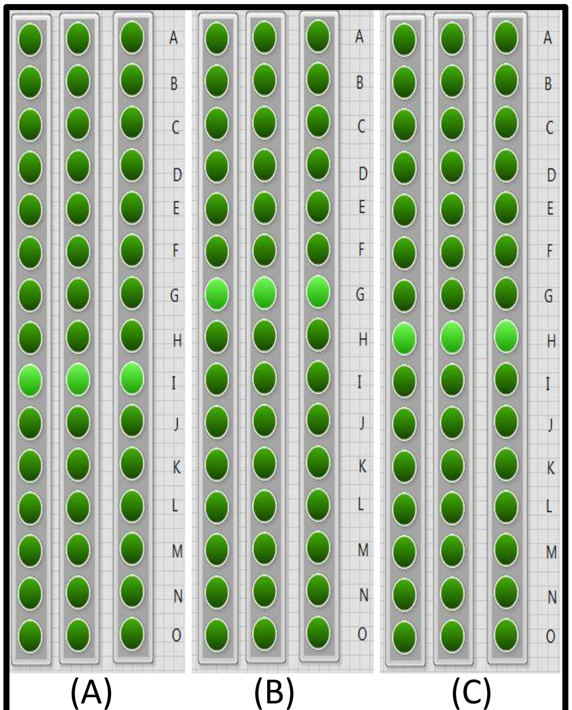

Figure 19. Shaft misalignment faults (A) F.L, (B) N.L, (C) H.L

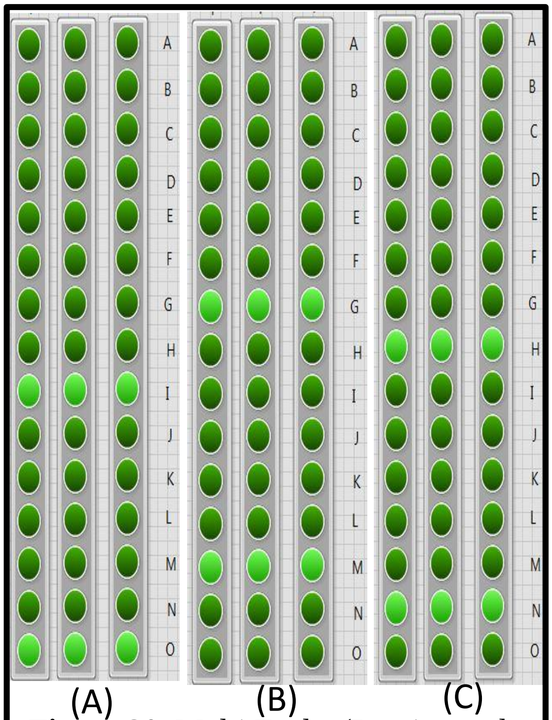

Figure 20. Multi Faults (Bearing and ShaftMisalignment) (A) F.L, (B) N.L,

Table 1. Type, dimensions, defect frequencies for bearing used

Bearing model	6205RS
Number of balls	9
Contact angle (β)	0^o
Outside diameter	52 mm
Inner diameter	25 mm
Cage diameter	38.5 mm
Ball diameter	9 mm
Outer bearing race defect (F_{ord})	3.44Hz
Inner bearing race defect (F_{ird})	5.5Hz
Ball defect (F_{bd})	2.02Hz
Cage defect (F_{td})	0.383Hz
Outer & inner defect (F_{re})	4.04Hz

Table 2. Frequencies for bearing fault

r.p.m	F_{ord}	F_{ird}	F_{bd}	F_{td}	F_{re}
1395	80.12	129	47.2	8.9	94.4
1385	79.3	127.69	46.5	8.8	93
1375	78.96	127.14	46.23	8.75	92.46
1370	78.6	126.58	46.1	8.73	92.2

Table 3. RMS value of vibration velocity (mm/s) when the sensor radial place

Motor case	Value of (RMS)		
	N.L	H.L	F.L
Healthy	0.88	1.3	1.66
Parallel Shaft Misalignment	2.6	2.78	3
Angular Shaft Misalignment	3.3	3.2	3
Bearing	7.5	9.22	10

Table 4. RMS value of vibration velocity (mm/s) when the sensor axial place

Motor Case	Value of (RMS)		
	N.L	H.L	F.L
Parallel Shaft Misalignment	1.9	2.85	3.6
Angular Shaft Misalignment	1.31	2.25	2.73
Bearing	5.5	4.8	3.5

Performance Enhancement of an Air Cooled Air Conditioner with Evaporative Water Mist Pre-cooling

Assistant Professor Dr. Najim Abid Jassim
Mechanical Department - Engineering College - Baghdad University
Email: najmosawe @yahoo.com

ABSTRACT

The present paper deals with experimental investigation of the performance of air cooled split air conditioner, with evaporative water mist pre cooling to increase the cooling capacity and reduce the consumption power under hot and dry climate. This investigation considers how the performance can be enhanced by using water mist to pre-cool ambient air entering the condensers by adiabatic cooling process which depends on the ambient air wet bulb temperature; as well the condensing temperature and condensing pressure will be decreased accordingly. So the cooling capacity would be increased and consumption power would be decreased, consequently the energy ratio, EER would be improved. The performance of air cooled air conditioner with water mist pre cooling; ECAC was compared to the performance of air cooled air conditioner, ACAC which tested under the same ambient condition that is ranged from 25^oC to 52^oC. Test results show that ECAC operating at EER of 10.5 BTV/W. The ECAC had an EER of 47 % higher than that of ACAC under the same and most serve hot and dry condition of 52^oC and 10% relative humidity.

Keywords: air cooled air conditioner, thermal performance, evaporative water mist pre-cooling.

تحسين الاداء الحراري لمكيف هواء مكثفه مبرد بالهواء مع تبريد مسبق بمرذاذ مائي تبخيري

ا.م.د. نجم عبد جاسم
قسم الميكانيك - كلية الهندسة - جامعة بغداد

الخلاصة

يتعامل البحث الحالي مع التحري التجريبي للاداء الحراري لمكيف هواء نوع منفصل مكثفه مبرد بالهواء مع مرذاذ مائي في عملية تبريد اولي للهواء الخارجي الداخل للمكثف لغرض زيادة السعة التبريدية وخفض الطاقة المستهلكة في جو حار وجاف. يوضح هذا التحقق التجريبي كيف يمكن تحسين الاداء الحراري عند استعمال مرذاذ مائي كمبرد اولي لخفض درجة حرارة الهواء الخارجي قبل الدخول الى المكثف بعملية تبريد اديباتي تعتمد على درجة حرارة البصلة الرطبة للهواء كذلك بموجبها يتم خفض درجة حرارة وضغط التكثيف وفقا لذلك. لذا ستزداد السعة التبريدية وستنخفض الطاقة المستهلاكة وبالتالي ستتحسن نسبة كفاءة الطاقة. تم مقارنة الاداء الحراري لمكيف هواء مكثفه مبرد بالهواء مع مرذاذ مائي مع الاداء الحراري لمكيف الهواء مكثفه مبرد بالهواء ACAC والتي اختبرت في نفس ظروف الجو الخارجي عند درجات حرارة هواء خارجي مداها بين 25 ^{o}م و 52 ^{o}م. بينت نتائج الاختبار عند الظروف الاساسية بان ECAC تعمل بنسبة كفاءة طاقة EER مقدارها 10.5. ان نسبة كفاءة الطاقة EER لمكيف الهواء ECAC في ظروف جو سائدة حارة وجافة عند درجة حرار 52 ^{o}م ورطوبة نسبية 10% اعلى بمقدار 47 % من مكيف الهواء ذو مكثف مبرد بالهواء في نفس الظروف.

كلمات رئيسية: مكيف هواء بمكثف مبرد بالهواء، اداء حراري، تبريد اولي بمرذاذ مائي تبخيري.

1. INTRODUCTION

Air-cooled air conditioners are widely used to provide space cooling in air-conditioned buildings due to their flexibility and yet pragmatic and simple energy efficient measures for them are still lacking. The vapor compression refrigeration, VCR is widely used in various cooling applications.
The coefficient of performance, COP of the VCR cycle depends upon various parameters like sub cooling, superheating, suction & discharge pressure of the compressor. COP is also greatly affected due to power consumption of the compressor as it is a major power-consuming element. Increase in the condenser temperature leads to increase the condenser pressure and hence compressor work. Also the increase in condenser pressure causes a reduction in liquid content in the evaporator; consequently the cooling capacity of the cycle will be decreased. So the COP and EER of the system considerably decrease with increasing condenser pressure. The temperature of entering air cooled condenser in a VCR system depends on the ambient air temperature.
Evaporative water mist can reduce the ambient air temperature before entering the air cooled condenser from its dry bulb temperature to approximately its wet bulb temperature. Therefore it is definitely the heat exchange in the condenser will be enhanced, consequently the energy efficiency of the condenser and the coefficient of performance of air conditioner will be improved **ASHRAE, 2009, Birangane and Patil, 2014**.
Hwang et al., 2001 conducted an experiment on the air cooled condenser and water cooled condenser of a household refrigerators. The water cooled condensers were utilized as a tube in the heat exchanger which was known as tube heat exchanger and had inlet for the purpose of cooling water and hot water was collecting at the exit. The air cooled condenser increased the compressor work that's why COP was higher in water cooled condenser case than air cooled condenser.
Radermacher et al., 2001 investigated evaporative cooling and conventional cooling for a split heat pump system. The spilt heat pump consists of two separate sections, one as indoor loop and the other as outdoor chamber for maintaining air temperature in each section. He built wetted rotating disks into the front of air cooled condenser onto an existing split heat pump system as evaporative pre-cooling. The final results showed improved steady state performance; a higher capacity of COP by 11.1 to 21.6%.
Hosoz and Kilicarslan, 2004 performed an experiment on the performance comparison of the air cooled, water cooled, and evaporative cooled condenser used in the refrigeration system. For this, a model was developed in which first air cooled condenser was used and result showed less COP. So, test was performed on water cooled condenser which was implemented to take the heat through water at the condenser which was thrown into the surrounding air. After that, the investigation was done on evaporative condenser. It was found that the water cooled condenser improved the refrigeration effect and COP by 2.9-14.4% and 1.5-10.2% respectively, when compared with evaporative pre-cooling condenser. Furthermore, the refrigerating effect and COP of a condenser with evaporative cooling were 31% and 14.3% higher than that of air cooled respectively.
Hajidavalloo, 2007 investigated incorporation of evaporative cooling in the condenser of window-air-conditioner. An air cooled conditioner was equipped with evaporative pads pre-cooling system and spraying water mist on the pads to cool down the ambient air before entering the condenser. The test results present an enhancement in the thermodynamic characteristics of new system. The consumption power was saved by 16% and the coefficient of performance was improved by 55%.

Nasr and Hassan, 2009 studied a renewal condenser for residential refrigerator. He wrapped the air cooled condenser with wetted cloth sheets to suck the water from a water basin by capillary effect as evaporative pre-cooling. Test results showed that the condenser entering air dry bulb temperature was dropped from the ambient air temperature by up to 9.4℃. So the COP was increased by 18.6%.
The studies of **Yang et al.** and **Yu and Chan, 2009** are based on the application of water mist as evaporative pre-coolers associated with air-cooled chillers of 1105 kW rated cooling capacity to pre-cool ambient air before entering the condenser under climate of Hong Kong. They concluded that this application lower the chiller power by about 15%.
Hajidavalloo and Eghtedari, 2010 investigated about the application of evaporative cooled air condenser instead of air cooled condenser to solve the problem of maintaining higher COP in hot and dry regions. He integrated an evaporative pre-cooling and with air-cooled split air conditioner to indicate its effect on thermodynamic characteristics of a new cycle. Test results showed that application of new system has significant effect on the performance enhancement of the cycle with a rate increase with increasing ambient air temperature.
Faramarzi et al., 2010 examined the performance of an evaporative pre-cool condenser-type roof top packaged air conditioner of 10 tons rated cooling capacity under different USA climates. The variations in cooling capacity, consumption power, energy efficiency ratio, and water consumption under hot and dry conditions were tested and presented. Experimental results show that the ECAC operate at an EER of 13.5 Btu/W. The EER of ECAC was then compared to the EER of air-cooled condenser type air conditioner, ACAC under similar test conditions. The EER of ECAC was found higher than that of ACAC by about to 51% under the approximately same conditions of 46°C dry bulb temperature and 35°C wet-bulb temperature.
Singh et al., 2016 reviewed a study on performance comparison between air cooled and water cooled condenser in compression refrigeration. They built an evaporative pad in front of condenser of forced air cooling to improve the energy efficiency of condenser. Experimental results indicated that the cooling capacity was increased by 2.9 to 14.4 % and the coefficient of performance is enhanced by 1.5 and condenser pre cooling means higher drop in condenser inlet air temperature when compared with air cooled and 10.2 % with respect to evaporative condenser. Due to higher heat exchange and efficiency of evaporative and condenser pre cooling means higher drop in condenser inlet air temperature when compared with air cooled and evaporative condenser. In the study of **Torgal et al., 2016,** the performance of air cooled conditioner with water mist system was tested. The vibrations of cooling capacity and consumption power due to effects of condenser inlet air temperatures was investigated and presented. They coupled the water mist system with the air cooled conditioner as a pre-cool air to increase the cooling capacity, and decrease the compressor power. Experimental results showed that due to the coupling of water mist with air cooled condenser, the cooling capacity of the air-cooled, air conditioner can be increased by 17.5%, and the consumption power can be decreased by 15.5%. So that the COP of the air cooled conditioner could improve by 37%, when the water mist system used as pre-cooling.

The objective of this study was to investigate experimentally the thermal performance of water mist pre-cool air cooled air conditioner, ECAC under Iraqi climate. A water mist assisted air cooled air conditioner was designed, built, instrumented and tested. Experimental tests were conducted by varying the condenser inlet air temperature and water mist spraying rate to investigate their effects on cooling capacity, consumption power and the energy efficiency ratio of air conditioner.

2. SYSTEM DESCRIPTION

A single-stage vapor compression cooled split air conditioner operates with R134 as refrigerant coupled with water mist pre-cooling system is designed, built, instrumented and tested in order to be used for conducting experiments.

Air cooled condenser is refrigerant to air heat exchanger, where heat is transferred sensibly from the refrigerant of condenser high pressure / temperature to forced flowing ambient air depending on the ambient dry bulb temperature.

Evaporative water mist pre-cool condenser is primarily driven by the latent heat of water vaporization depending on the ambient wet bulb temperature. The water mist can be easily vaporized by the ambient air before entering the condenser. The reduction in the temperature of ambient air follows the adiabatic cooling process with constant specific enthalpy. This reduction in the condenser inlet air temperature compared to the ambient temperature causes a decrease in refrigerant condensing temperature and pressure.

Fig. 1 shows two cases of the refrigerant cycle of air conditioner. Case 1-2-3-4-1 refers to air cooled condenser and case 1'-2'-3'-4'-1' refers to water mist pre-cool condenser. It is clear that the consumption power is decreased with decreasing the condensing pressure, while the refrigeration effect is increased. So the coefficient of performance of air conditioner will definitely be increased.
A schematic diagram of the vapor compression refrigeration cycle with all high precision calibrated sensors/transducers was used for measuring all operating is presented in **Fig. 2.**
The experimental test rig shown in **Figs 3, 4** has rated cooling capacity of 3.51 kW for condenser and evaporator inlet air temperatures of 35 and 24^{o}C respectively. It consists of major components, namely a compressor, DX condenser, thermostatic expansion valve and DX evaporator. It is manufactured in China by Discovery Trade Mark with the specifications tabulated in **table.1**.
The condensing unit was equipped with evaporative water mist system. The water mist system consisted of high pressure pump, water filter, copper piping, atomization nozzle and water storage tank. For water consumption measurements a small connection tube at the bottom of the water tank to pellucid flexible tube which is fixed at the tank wall from the outside and practically calibrated and pointed by using a laboratory calibrated carafe to show the change in tank containing volume in liters. The water mist system was used to deliver water at rate of 0.17-0.5 L/min and pressure of 70-100 bars. It is manufactured in Italy by Inter Pump Group with the specifications tabulated in **table.2**.

The experimental test rig is equipped with a calibrated thermocouples type T and relative humidity sensors, H with uncertainties of ± 0.2, and ± 0.1 respectively. The thermocouples are fixed at the condenser and evaporator to measure the refrigerant condensing and evaporation temperatures, Also thermocouples and relative humidity devices are fixed at the inlets and outlets of condenser and evaporator to determine the enthalpy values of air.
A calibrated refrigerant rotameter is fixed at the liquid line to measure the mass flow rate with uncertainty of ± 0.5 Kg/h. The rig is equipped with a calibrated watt meter to measure the consumption power. All tests were performed in an identical manner and at steady state. All experiment tests were conducted at approximately constant room temperature of 25 ^{o}C and repeated with varying the condenser inlet air temperature from 25 to 52 ^{o}C.

3. SYSTEM ANALYSIS

Air cooled air conditioner, ACAC

To investigate the performance of air condition on operated parameters must be measured such as consumption power, W_C. The supply and return evaporator air temperatures are $T_{e,s}$ and $T_{e,r}$, entering and leaving condenser air temperatures are $T_{c,e}$ and $T_{c,l}$. The refrigerant condensing and evaporative temperatures are T_{cd} and T_{ev}.

The cooling capacity of air conditioner, Q_L is obtained by using the following equation:

$$Q_L = \rho_a V_{ev} (h_{e,r} - h_{e,s}) \quad (1)$$

Where: ρ_a is the density of air, kg/m^3 and V_{ev} is the evaporator fan flow rate of air, m^3/s.

and $h_{e,r}$ and $h_{e,s}$ are enthalpies of the air at evaporator inlet and outlet, respectively, kJ/kg.

The heat rejection by the condenser, Q_H is obtained by using the following equation:

$$Q_H = Q_L + W_C \quad (2)$$

The COP of air conditioner is the cooling capacity, Q_L over consumption power, W_C, as follow:

$$COP = Q_L / W_C \quad (3)$$

The EER of air conditioner is the ratio of cooling capacity in Btu to consumption power in watt as:

$$EER = 3.418\ Q_L / W_C \quad (4)$$

The cooling capacity $Q_{L,}$ consumption power, W_C and heat rejected, Q_H are varied with varying the condensing temperature, T_{cd}.

Air conditioner with water mist, ECAC

When a water pump operates to spray water mist, the ambient air temperature T_{db}, follows the adiabatic cooling process and reduced to $T_{db}^{/}$. And the humidity ratio is increased from W_{db} to $W_{db}^{/}$. This is dependent on air its mass rate and mist spraying rate as given by:

$$m_{mist} = \rho_a V_{cd}\ \Delta W \quad (5)$$

Where: ρ_a is the density of air, kg/m^3 and V_{cd} is the condenser fan flow rate of air, m^3/s.

and ΔW is the humidity ratio rise ($\Delta W = W_{db}^{/} - W_{db}$) water vapor to air mass ratio, kg_v/kg_a

All the measured data taken from experimental tests were used as primary given data in computing secondary output parameters such as: cooling capacity, coefficient of performance, and the energy efficiency ratio.

4. RESULTS AND DISCUSSIONS

In order to enhance the thermal performance of air cooled air conditioner a water mist system is coupled with air cooled air condenser. By the adiabatic cooling process taking place in the evaporative water mist pre-cooling, the temperature of condenser inlet air will be decreased compared with the ambient temperature, as well the condensing temperature and condensing pressure will be decreased accordingly.
The baseline reveals a cooling capacity, consumption power and energy efficiency ratio at ambient temperature of 35°C. The normalization is the ratio of test data at any ambient temperature to its value at baseline test temperature.
Fig. 5 illustrates the variation in cooling capacity of air conditioner with varying the condenser inlet air temperature. As can be seen the normalized cooling capacity increased as the condensing temperature decreased. This is due to the increase in refrigeration effect and compressor volumetric efficiency.

The cooling capacity was normalized based on the baseline cooling capacity at temperature of 35°C. The normalized cooling capacity of ECAC was found over by 5% than that of baseline at 25°C and lower by 7% than that of baseline at 52°C. And the normalized cooling capacity of ACAC was found over by 7% than that of baseline at 25°C and lower by 9% than that of base line at 52°C.

Fig. 6 shows the variation in consumption power of air conditioner with varying condenser inlet air temperature. As can be seen the normalized consumption power decreased as the condensing temperature decreased. This is due to the decrease in condensing pressure and compression ratio.

The consumption power was normalized based on the baseline consumption power at temperature of 35°C. The normalized consumption power of ECAC was found over by 18% than that of baseline at 52°C and lower by 6% than that of baseline at 25°C. And the normalized consumption power of ACAC was found over by 24% than that of baseline at 52°C and lower by 7% than that of baseline at 25°C.

Fig. 7 shows the influence of condenser inlet air temperature on the energy efficiency ratio, EER. When the condensing temperature decreases the refrigeration effect would be increased, which overcomes the increase in consumption power, so the EER would be improved.

The EER was normalized based on the baseline EER at temperature of 35°C. The normalized EER of ECAC was found over by 7% than that of baseline at 52°C and lower by 3% than that of baseline at 25°C. And normalized EER of ACAC was found over by 14% than that of baseline at 25°C and lower by 24%than that of baseline at 52°C.

Fig. 8 shows a comparison between ACAC and ECAC regarding the EER of the refrigeration cycle. The EER of ECAC was found higher by about 21.7% and 49.9% than that of ACAC at 25°C and 52°C respectively.

Figs. 9 to 11 illustrate the ACAC and ECAC unit's variation in performance (cooling capacity, power consumption and EER) across a range of climate conditions in terms of dry bulb and wet bulb temperatures that are mentioned in column charts and represented by the following ambient condition index:
1: 25,18; **2:**30,20; **3:** 35,21.5; **4:** 40,23; **5:** 46, 24; **6:** 52, 25 ^{o}C dry bulb and wet bulb temperatures respectively.
Cooling capacity was as low as 1.04 and 1.205 kW at 52^{o}C respectively, and as high as 1.35 and 1.5 kW at 25^{o}C respectively.
Total power consumption was as high as 0.65 and 0.535 kW at 52^{o}C and as low as 0.44 and 0.4 kW at 25^{o}C respectively.
EER were as low as 5.13 and 7.69 at 52^{o}C respectively, and as high as 10.25 and 12.47 at 25^{o}C respectively.
Fig. 12 illustrates the variation of water consumption by evaporation in ECAC unit with increasing condenser inlet air temperature. Water consumption was as high as 0.05 kg/s at 52^{o}C, and as low as 0.0225 kg/s at 25^{o}C.

Fig. 13 shows a comparison between the present work and results of **Faramarzi, 2010.** It is clear that the EER of air cooled air conditioner coupled with water mist pr-cooling is higher than that of conventional air cooled air conditioner. This is due to the adiabatic cooling of ambient air before entering the condenser, which is taken in water mist system. The average deviation between the present work and results of **Faramarzi, 2010** regarding the EER of ECAC is 23.2% due to tests done under different conditions.

5. CONCLUSIONS

In this study the application of water mist system pre-cooling have been investigated for air cooled split air conditioner under hot and dry climate condition. The applying of adiabatic cooling with air cooled condenser would be more cooling effect and thermal performance enhancement would be more significant if the air condition operates in hot and dry ambient conditions. From the above findings, it can be concluded that:

- The performance enhancement of ECAC compared to conventional air-cooled units is significant in hot and dry conditions.
- The normalized consumption power of ECAC was saved by 13.7 %, while the normalized cooling capacity was enhanced by 15.9% compared with ACAC under the hot and dry climate condition of 52^{o}C.

- The EER of ECAC was improved by an average of 49.9 % compared with ACAC under the same hot and dry climate condition of 52^{o}C.

- ECAC consumes 0.0335 liter/s/kW of cooling capacity by evaporation in adiabatic cooling process at 35^{o}C and 25^{o}C dry and wet bulb temperatures.

- Overall, the test results indicate that the ECAC provides more efficient compared to conventional air-cooled units in all climate conditions.

NOMENCLATURE

h	enthalpy, kJ/kg
m	mass flow rate, kg/s
P	pressure, N/m^2
Q_L	cooling capacity, kW
Q_H	heat rejection, kW
T	temperature, °C
V	volume rate of air, m^3/s
W	moisture content, kg_v/kg_a
W_C	compressor work, kW

Greek symbol

ρ	density, kg/m^3

Subscripts

a	air
cd	condenser
c,e	entering air to condenser
c,l	leaving air from condenser
ev	evaporator
e,r	return air to evaporator
e,s	supply air from evaporator
db	dry bulb
mist	water mist

Abbreviations

ACAC	air cooled air conditioner
COP	coefficient of performance
DB	dry bulb
DX	direct expansion
ECAC	evaporative cooled air conditioner
EER	energy efficiency ratio
WB	wet bulb
RH	relative humidity
VCR	vapor compression refrigeration

REFRERNCES

- ASHRAE, 2009, ASHRAE Fundamentals, *American Society of Heating, Refrigerating and Air-conditioning Engineers, Inc*., Atlanta, GA.
- Birangane V.V., Patil A.M.,2014, *Comparison of air cooled and evaporatively cooled refrigeration systems, Int. Journal of Engineering Research and Applications*, Vol. 4,No. 6, pp. 208–211.
- Faramarzi R., Lutton J., and Gouw S., 2010, *Performance comparison of evaporatively-cooled condenser versus air-cooled condenser air conditioner, Summer Study on Energy Efficiency in Buildings*, ACEEE, pp. 117–127.
- Hajidavalloo E., 2007, *Application of evaporative cooling on the condenser of window-air-conditioner, Applied Thermal Engineering*, Vol .27, pp.1937–1943
- Hajidavalloo E. and Eghtedari H., 2010, *Performance improvement of air-cooled refrigeration system by using evaporative cooled air condenser*, Int. Journal of Refrigeration Vol.33, pp.982–988.
- Hosoz M. and Kilicarslan A., 2004, *Performance evaluations of refrigeration system with air-cooled, water cooled and evaporative condensers*, Int. Journal of Energy Research, Vol. 28, No. 4, pp. 683–696.
- Hwang Y., Radermacher R. and Kopko W., 2001, *Experimental evaluation of a residential-sized evaporatively cooled condenser, Int. Journal of Refrigeration*, Vol. 24, No. 3, pp. 238–249.
- Nasr M.M. and Hassan M.S., 2009, *Experimental and theoretical investigation of an innovative evaporative condenser for residential refrigerator*, Renewable Energy Vol. 34, pp. 2447–2454.
- Radermacher R. and Kopko W., 2001, *An experimental evaluation of residential sized evaporatively cooled condenser, Int. Journal of Refrigeration*, Vol. 24, pp.238–249.
- Singh M., Rai B. and Vasudev V., 2016, *A study on performance comparison of air cooled and water cooled condenser in vapour absorption and compression refrigeration systems,* Int. *Journal of Innovative Science, Engineering & Technology*, Vol. 3, No. 4, pp. 462-468.
- Torgal S., Pawar K. and Puranik S., 2016, Performance enhancement of an air conditioner with condensate mist cooled condenser, Int. Journal of MTST4, pp. 462–468.
- Yang J., Chan K.T., and Wu X., 2009, *Application of water pre-cooling on the air cooled chiller, Eleventh International IBPSA Conference*, Glasgow, Scotland, July 27-30, pp. 2204-2211. .
- Yu F.W. and Chan K. T., 2009, *Modeling of improved energy performance of air-cooled chillers with mist pre-cooling*, Int. Journal of Thermal Sciences Vol. 48, No. 4, pp. 825–836.

Table 1. Split air conditioner specifications**.**

Split air conditioner model DAC-12000 HC2			
Cooling capacity	3510 watt	Refrigerant	R22
Condenser flow rate	900 m^3/h	Input power	1250 watt
Evaporator flow rate	450 m^3/h	Electric supply	1pH-50Hz-220V

Table 2. High pressure pump specifications.

High pressure pump model M51012			
Pump pressure	70 - 100 bar	Input power	0.55 kw, 1450 rpm
Pump flow rate	0.25-1 L/min	Electric supply	1pH-50Hz-220V

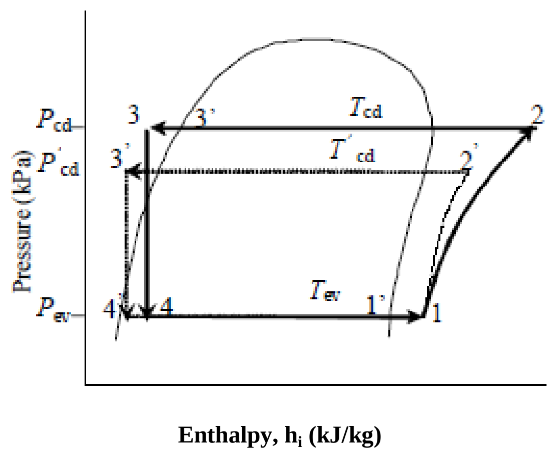

Figure 1. Effect of condensing temperature on VCR cycle.

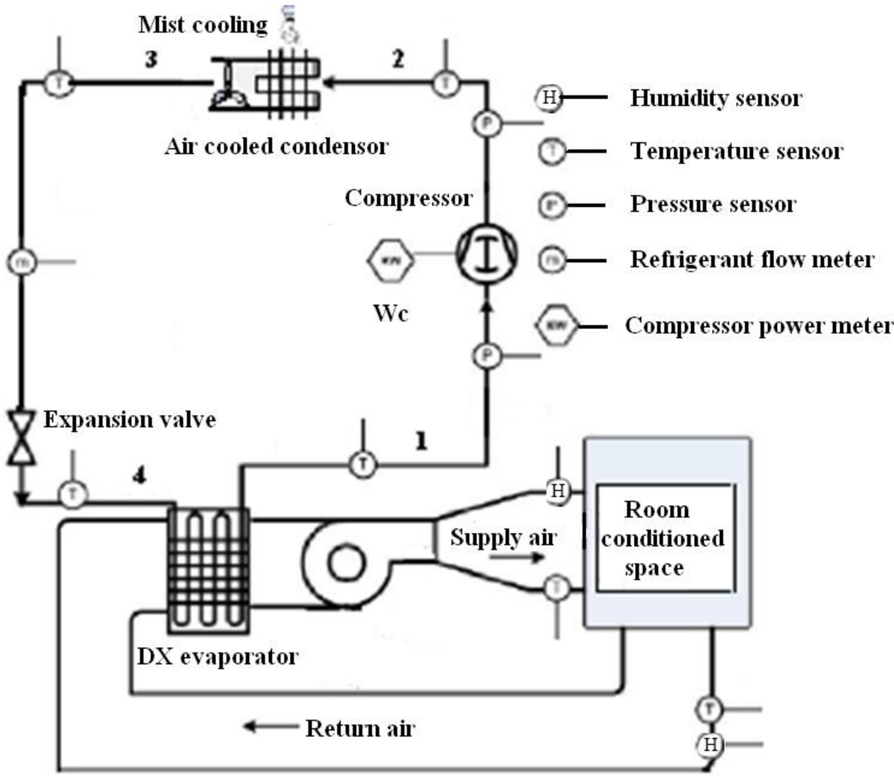

Figure 2. Schematic diagram of VCR with instrumentations.

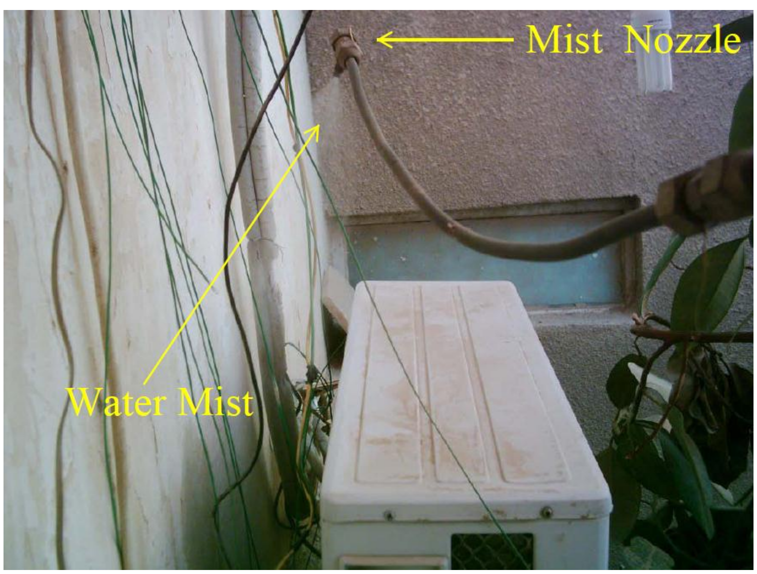

Figure 3. Air conditioner with water mist, ECAC.

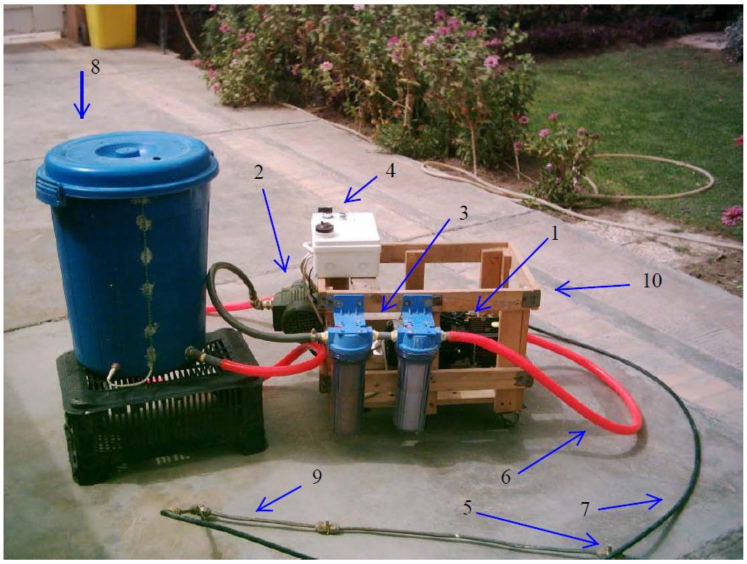

1	High pressure pump	6	Low pressure elastic pipe
2	Low pressure pump	7	High pressure hose
3	5 microns water filter	8	Water tank
4	Operating electrical board	9	Copper Mist network
5	Mist nozzle	10	Wood frame

Figure 4. Water mist system.

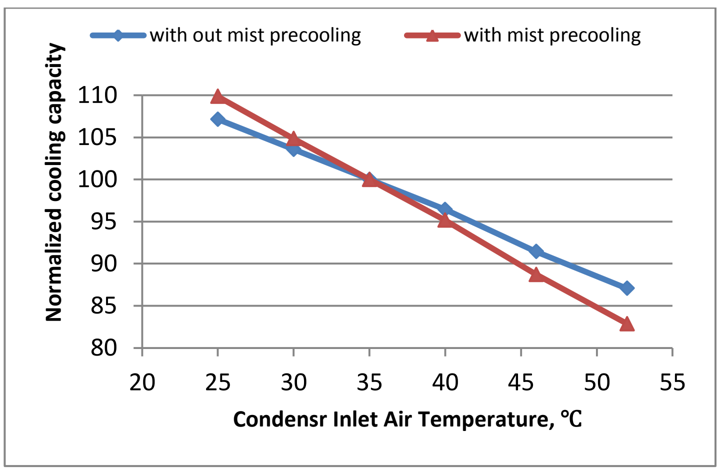

Figure 5. Normalized comparison of cooling capacity between ACAC & ECAC**.**

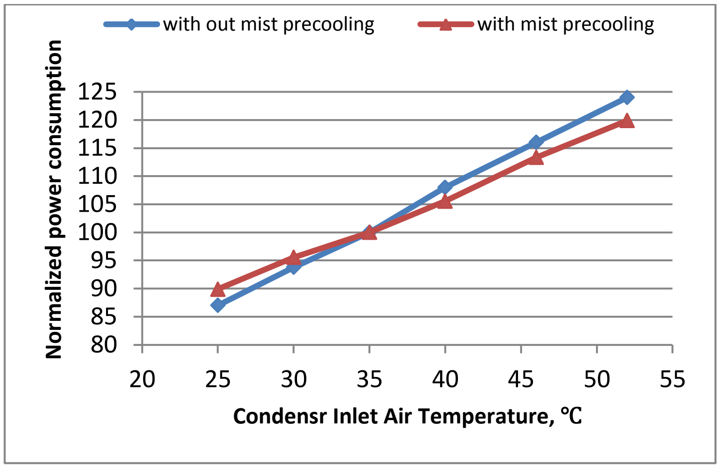

Figure 6. Normalized comparison of power consumption between ACAC & ECAC.

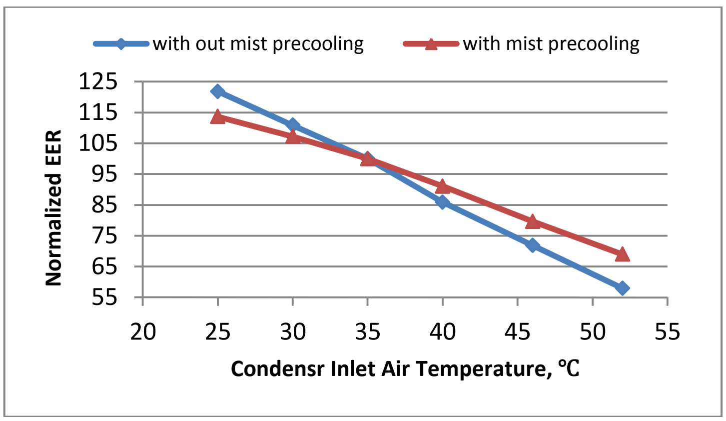

Figure 7. Normalized comparison of EER between ACAC & ECAC**.**

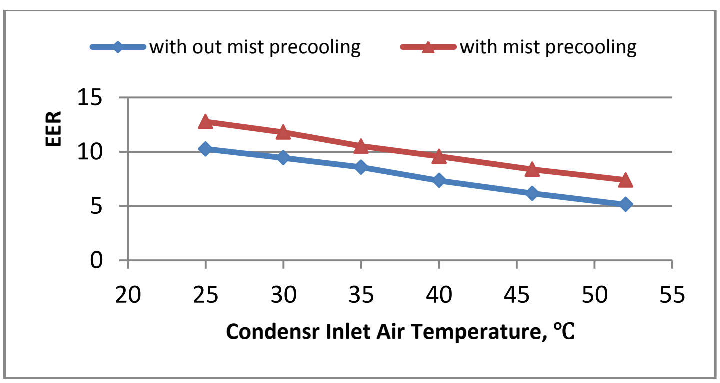

Figure 8. Comparison of EER between ACAC & ECAC**.**

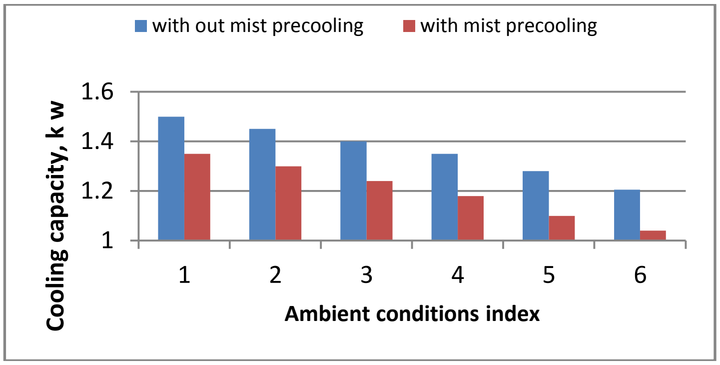

Figure 9. Comparison of cooling capacity between ACAC & ECAC.

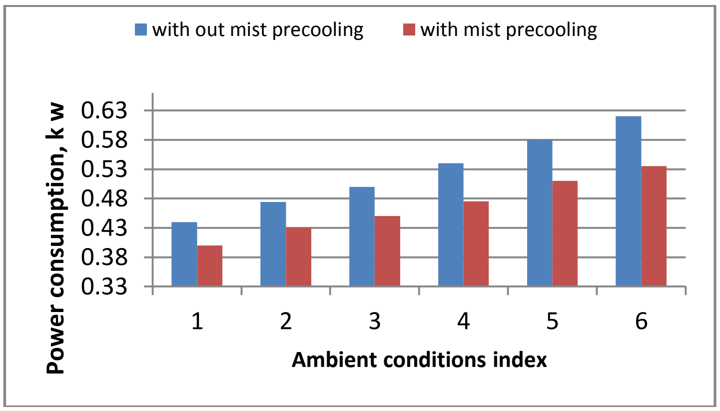

Figure 10. Comparison of power consumption between ACAC & ECAC.

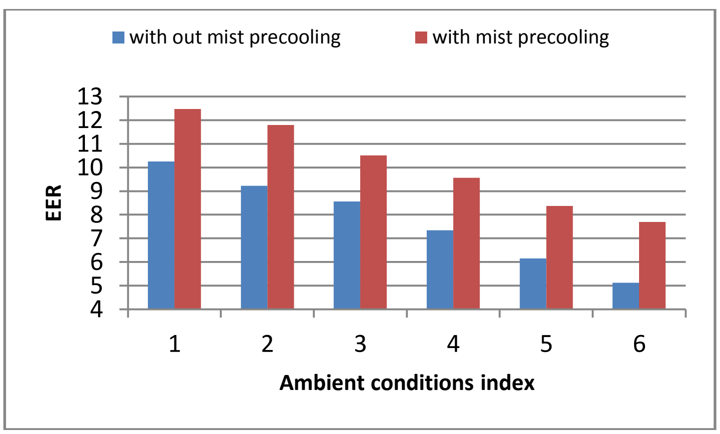

Figure 11. Comparison of EER between ACAC & ECAC.

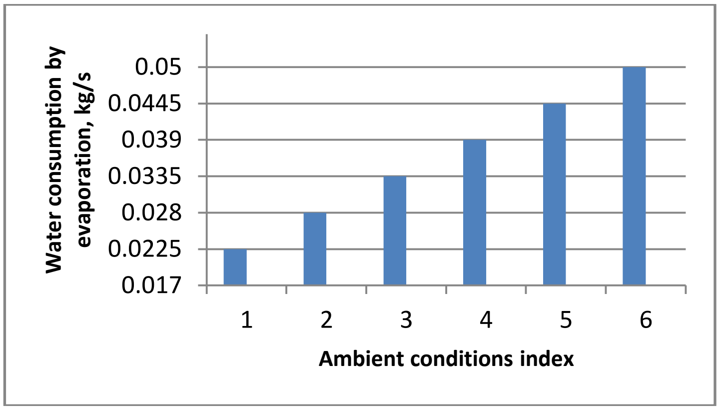

Figure 12. Water consumption by evaporation by ECAC**.**

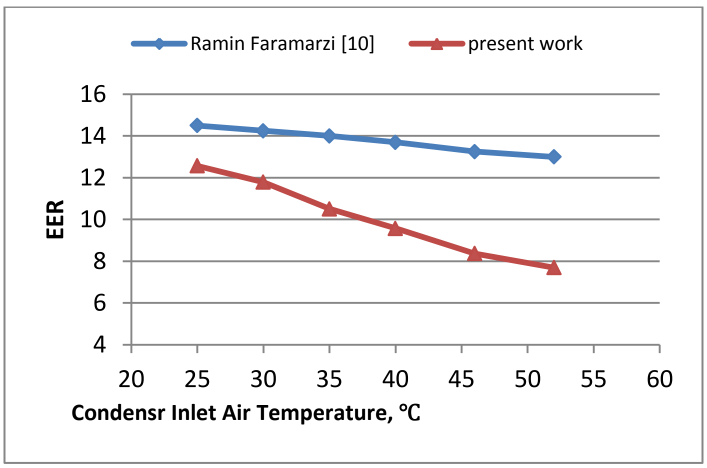

Figure 13. Comparison between present work & Faramarzi, 2010 for the EER of ECAC.

EFFECT OF PVD AND VACUUM PRESSURE ON SATURATED-UNSATURATED SOFT SOILS

Dr. Ala Nasir Aljorany
Professor
Engineering College-Baghdad University
E-mail:alaAljorany@gmail.com

Fatema Safaa Noori
Graduated student
Engineering College-Baghdad University
E-mail:fatemasafaa@yahoo.com

ABSTRACT

Soft clays are generally sediments deposited by rivers, seas, or lakes. These soils are fine-grained plastic soils with appreciable clay content and are characterized by high compressibility and low shear strength. To deal with soft soil problems there is more than one method that can be used such as soil replacement, preloading, stone column, sand drains, lime stabilization and Prefabricated Vertical Drains, PVDs. A numerical modeling of PVD with vacuum pressure was analyzed to investigate the effect of this technique on the consolidation behavior of fully and different depths of partially saturated soft soils. Laboratory experiments were also conducted by using a specially-designed large consolidmeter cell. Five tests were conducted with a vacuum pressure of about 40 kPa applied for a period of 30 days where the degree of consolidation reached 75% based on pore-water pressure distribution. The results showed that using vacuum pressure with vertical drains reduces the consolidation time by about 68%. Existence of an unsaturated soil layer decreases settlement of soil by about 22%, 32%, 425, 54% as the unsaturated depth increases by 1/8, 1/4, 3/8, and 1/2L respectively and causes a rapid increase in soil pore-water pressure.

KEY WORDS: soft soils, PVD, vacuum pressure, unsaturated soil, and degree of consolidation.

تأثير أعمدة التصريف الطولية وضغط التفريغ على الترب الرخوة المشبعة وغير المشبعة

د. علاء ناصر حريب
أستاذ
كلية الهندسه-جامعة بغداد

فاطمة صفاء نوري
طالبة دكتوراه
كلية الهندسه-جامعة بغداد

الخلاصة

تتكون الترب الرخوة في مناطق ترسيب الأنهار، أو البحار، أو البحيرات. و تكون هذه الترب على شكل طبقات تتداخل مع طبقات الرمل والغرين التي تعرضت الى حالات الجفاف والترطيب بصورة دورية قرب السطح. و لغرض دراسة سلوك التربة الرخوة بأستخدام أعمدة التصريف الطولية والمفرغ تم تصميم وإنشاء خلية إنضمام خصيصا لهذه الدراسة. حيث تم إجراء خمسة فحوص بتسليط ضغط سالب (‎-40 kPa‎) لمده لاتقل عن ثلاثين يوما حيث تصل درجة أنضمام التربة الى 75% بالأعتماد على توزيع ضغط الماء. بألأضافه الى الدراسة العملية أجريت دراسة نظرية بالإعتماد على طريقة العناصر المحددة بإستخدام برنامج ABAQUS بإصداره ال 6.13. حيث أظهرت النتائج كفاءة هذه الطريقة في تحسين التربة وتقليل الزمن اللازم للوصول الى إنضمام عالي داخل التربة. إن وجود الطبقة غير المشبعة يعمل على تقليل هطول التربة بنسبه 22%و 32%و 42و 54% عندما تزداد عمق التربة بنسبة 1/8و 1/4و 3/8و 1/2 ولا تؤثر على توزيع ضغط الماء على طول عمود التصريف.

الكلمات الرئيسية: الترب الرخوة، أعمدة التفرغ الطولية ،ضغط التفريغ، الترب غير المشبعة، و درجة الأنضمام.

1. INTRODUCTION

Large areas covered with thick soft clay layers deposits are not suitable for construction of many infra structures. The growth of infrastructures in urban and the lack of sites suitable for development increased land prices dramatically. Accordingly, lands having poor geotechnical properties (low shear strength and high compressibility) were used for construction. Prefabricated Vertical drains (PVDs) together with vacuum preloading have been widely used to accelerate the consolidation of soft soils (**Indraratna and Rujikiatkamjorn 2004, and AL-Shammarie 2013)**. This technique shortened the horizontal drainage path to half of the drain spacing. Moreover, propagation of vacuum pressure along the PVDs increases the hydraulic gradient and creates as an additional surcharge load.

2. THEORETICAL BACKGROUND

Loading of unsaturated soils generates excess pore-water and pore-air pressures; dissipation of pressure with time reduces the volume of soil, i.e., soil consolidation. There are many differential equations to describe the consolidation of unsaturated soils. **Terzaghi, in 1943**, presented a linear differential equation to express the consolidation of saturated soils and **Fredlund and Hasan, in 1979**, derived a non-linear differential equation to describe the consolidation of unsaturated soils. In their derivation they adopted the assumption of Terzaghi together with the following assumptions: air phase is continuous, coefficient of permeability with respect to water and air and moduli of volume change remain constant during the consolidation process, and the diffusion of air and water through the consolidation process is ignored **Fredlund, and Hasan, 1979, Fredlund and Rahardjo 1986, and Shan et al., 2013**. They proposed differential equations to express the variation of air and water with time and degree of consolidation of air and water in addition to time factors as follows:

$$U_w = 1 - \frac{\int_0^{2H} u_w dy}{\int_0^{2H} u_{wi} dy} \quad (1)$$

$$U_a = 1 - \frac{\int_0^{2H} u_a \, dy}{\int_0^{2H} u_{ai} \, dy} \qquad (2)$$

$$U_r = 1 - e^{-\frac{8}{fn}T_r} \qquad (3)$$

$$T_w = \frac{c_v^w t}{H^2} \qquad (4)$$

and

$$T_a = \frac{c_v^a t}{H^2} \qquad (5)$$

where U_w *and* U_a are degrees of consolidation for water and air, respectively; U_r radial consolidation, H thickness of drainage path; u_{wi} *and* u_w initial pore-water and water pressures at any time, respectively; u_{ai} *and* u_a initial pore-air and air pressures at any time, respectively; fn coefficient, T_w *and* T_a time factors for water and air, respectively; T_r time factor for radial consolidation, *t* time; and c_v^w *and* c_v^a coefficients of consolidation with respect to water and air, respectively.

They expressed the variation of pore-pressure as follows:

$$\frac{\partial u_w}{\partial t} = -C_w \frac{\partial u_a}{\partial t} + c_{v1}^w \left[k_w \frac{\partial^2 u_w}{\partial y^2} + \frac{\partial u_w}{\partial y} \frac{\partial k_w}{\partial y} \right] \qquad (6)$$

and

$$\frac{\partial u_a}{\partial t} = -C_a \frac{\partial u_w}{\partial t} + c_{v1}^a \left[(u_a + u_{atm}) \{ k_a \frac{\partial^2 u_a}{\partial y^2} + \frac{\partial u_a}{\partial y} \frac{\partial k_a}{\partial y} \} + k_a \frac{\partial^2 u_a}{\partial y^2} \right] \qquad (7)$$

where k_w *and* k_a coefficients of permeability with respect to water and air, respectively; C_w *and* C_a interactive constants with respect to water and air, respectively; c_{v1}^w and c_{v1}^a coefficients; and u_{atm} atmospheric pressure. Equations 6 and 7 should be solved simultaneously to get the pore pressure.

The average excess pore water pressure under vacuum pressure can be found from equation 8 and 9 based on the drainage condition:

For two-way drainage:

$$u = -pvac\ [\left(1 - \frac{z}{H}\right) - 2/\pi \sum_{n=1}^{\infty} \frac{1}{n} \sin(\lambda_n z) e^{\lambda_n{}^2 .cv.t}] \tag{8}$$

While for one-way drainage:

$$u = -pvac\ [1 - 4/\pi \sum_{n=1}^{\infty} \frac{1}{2n-1} \sin(a_n z) e^{a_n{}^2 .cv.t}] \tag{9}$$

where n is ratio of radius of the axisymmetric influence zone around a single drain to radius of equivalent drain λ_n coefficient equal to $2n/\pi$, and $a_n$coefficient equals to $(2n-1)\pi/2H$ **Chai, and Carter, 2011.** In the nineties of the last century an emphasis was started to be imposed on the implementation of unsaturated soil mechanics into routine geotechnical engineering practices **Fredlund, 2000**. Thereafter the effect of using PVD and vacuum pressure on the consolidation of saturated-unsaturated soils has been investigated by using ABAQUS software.

3. EXPERIMENTAL WORK APPARATUS

In this research a cylindrical steel container (consolidometer cell) was specially designed and manufactured to be used for the investigation of the improvement of the behavior of soft soils by using PVD. The cell was designed to be air and water tight with removable top and bottom flanges. The cell contained seven openings to insert the wires of the piezometers. **Fig. 1** is a schematic representation of the consolidometer used in this research and shows the distribution of the openings along the wall of the cell. The cap of the model contained an opening to connect the vacuum pump; an opening to insert a point gage; and a circular glass window for inspection as shown **in fig 2**. The base of the model contained a drainage hole of 5 mm in diameter and was provided with a valve. Linear differential variable transducer, *LVDT*, was used to measure the settlement of soil surface. However, since the space above the soil in the consolidometer is very humid the performance of the *LVDT* was highly affected. Accordingly, it was found that a point gauge can successfully be used to measure the settlement of the soil surface since the measurement is done through a mechanical vernear placed on the top flange of the consolidometer as shown in **fig. 3**.

4. TEST PROCEDURE

Five separate series of tests were conducted, the first series involved applying a vacuum pressure of 40 kPa at the top of a fully saturated soft-soil while the other four series involved applying a vacuum pressure of 40 kPa at the top of an unsaturated soil layer, 1/8 L, 1/4L , 3/8L, 1/2L, 50% degree of saturation, laid on the top of a fully saturated soft-soil layer, where L is the total depth of the soil placed in the cell. The testing procedure involved three main steps namely preparation of reconstituted clay, installation of the drain, and collection of oedometer samples.

The preparation of reconstituted clay was done according to the procedure suggested by **Burland, 1990**, where the clay specimen was mixed thoroughly with distilled water at water content slightly greater than the liquid limit. The clay was placed and tamped in layers in the apparatus; the unsaturated layer was then placed on the top of the saturated soft soil with a thickness equal to 1/8, 1/4, 3/8, 1/2 from the total depth of the soil sample. Then a 25 mm × 3 mm band drain with discharge capacity equal to 100 m^3/ year was inserted through the total depth of the soil by using a steel mandrel. During the placement of the soil in the cell four piezometers were placed at 19, 35, 50 and 80 cm from the top of the soil. For both tests a vacuum pressure of 40 kPa was applied 720 hours and the corresponding settlement and pore-water pressure were measured. Table 1 shows the physical and chemical properties of the natural soft-soils brought from AL-Basrah city south of Iraq.

5. THEORETICAL ANALYSIS

Numerical modeling by using the software ABAQUS 6.13 was done to investigate the effect of PVD and vacuum pressure on the behavior of saturated-unsaturated soft soils where it was assumed that both layers exhibit an elasto-plastic behavior according to modified cam-clay model. In the analysis it was assumed that the soil element is eight nodded and axi-symmetric, quadrilateral, biquadratic displacement, bilinear pore-water pressure, and reduced integration were adopted, abbreviated as CAE8RP. **Fig. 4** shows the mesh used in the numerical model and nodes where data were extracted. The soft soil was analyzed as elasto-plastic material obeying

Modified Cam-Clay Model, *MCC*. The input data to the *MCC* were: slope of normal consolidation line, λ, 0.18; slope of the critical-state line, *M*, 1.2; initial yield surface, wet surface size, ξ, and flow stress ratio, *k*, both assumed to be 1. The input data to the porous elastic model included: slope of over consolidationed line, κ, 0.08 and passions ratio, υ, 0.3. The unit weight and permeability of the soil were 18 kN/m^3 and $2.11*10^{-8}$ m/sec, respectively. The *PVD* was assumed to behave as an elastic material with young modulus, *E*, equal to 1800 kPa and Poisson's ratio equal to 0.4. A note should be taken that the smear effect has been neglected through the numerical analysis, since the soil is remolded the horizontal and the vertical coefficient of permeability and coefficient of vertical consolidation assumed to be the same. Application of a vacuum pressure on the top of a saturated soft soil results in a suction pressure on the water existing between soil particles and the surface will be under a negative pore pressure. In this research vacuum pressure was modeled as a boundary condition on the soil surface and/or on the top of the *PVD* only.

6. RESULTS AND DISCUSSION

A comparison between the settlement of a fully saturated soft soil with and without PVD under -40 kPa is shown in **fig. 5.** The results show that PVD presentation increases soil settlement 200% for the same time period.

A comparison between the settlement of a fully saturated soft soil and that of a saturated soil overlaid by a layer of unsaturated soil whose thickness is 1/8 of the total soil depth is shown in **fig. 6a** Settlement of soil was measured by using a point gauge and also was theoretically predicted by using the software ABAQUS and a comparison between the two results is shown in **fig. 6b** It can be noticed that a good agreement was obtained between measured and predicted values of soil settlement which indicates that the software can be used with an accepted accuracy to predict settlement of soil with the presence of a vertical drain. It is obvious that the presence of an unsaturated layer decreases soil settlement. The variation of pore-water pressure with time and depth for saturated-unsaturated soil profile is presented in **Fig. 7.** It can be seen that as the thickness of the unsaturated soil layer increases pore-water pressure developed and reaching the final value of applied vacuum gets faster. **Fig. 8a through c** shows the variation of pore-water pressure with time for 24 hours of application of vacuum pressure from which it is clear that rapid variation pore-water pressure occurs through the unsaturated layer but a less appreciable variation is depicted through the fully saturated soil. Based upon the distribution of pore-water pressure, the average degree of consolidation after 30 days was found to be 75% based on the method of **Chu, and Yan, 2005**. Loading soils of stable structures increases pore-water pressure and volume of soil and vice versa; since soft soils possess structures where the volume decreases when applying vacuum loads. This reduction in the volume of soil continues until equilibrium is achieved **Chai, and Carter, 2011, and Huang F., and Wang G., 2012**. Since the degree of saturation through the unsaturated layer was 50 %, the air phase would be continuous and allows the vacuum pressure to propagate faster causing a rapid increase in pore-water pressure through unsaturated soil, **Fredlund and Rahardjo, 1993**.

Fig. 9 shows the numerical analysis results of fully saturated soils for radial variation of pore-water pressure with time from which it is obvious that the variation of pore-water pressure near the drain occurs in a very short time but it takes a longer time near the outer boundary of the model due to soil resistance.

7. CONCLUSIONS

The results of this research showed that a system of prefabricated vertical drains accompanied by the application of vacuum pressure is an effective method to accelerate the consolidation of soft soils. The pore-water pressure decreases significantly when a vacuum pressure is applied. Soil settlement was observed to decreases when an unsaturated soil layer is presence. It can be noticed that the time settlement of half depth of unsaturated soil is about 35% of that of fully saturated full depth soil profile. Pore-water pressure propagated faster in the unsaturated soil layer than in a fully saturated soil. A good agreement was found between the experimental results and the numerical analysis.

REFERENCES

- AL-Shammarie H., 2013, *An Experimental and Theoretical Study on Ordinary and Encased Stone Column Underneath Embankment*, Ph D Thesis, University of Baghdad.
- Chai J., and Carter J. P., 2011, *Deformation Analysis in Soft Ground Improvement*, Springer, London, New York.

- Fredlund D. G., and Hasan U. H., 1979, *One-Dimensional Consolidation Theory: Unsaturated soils*, Canadian Geotechnical Journal, vol. 16, pp 521-531.
- Fredlund D. G., and Rahargjo H., 1986, *Unsaturated Soil Consolidation Theory and Laboratory Experimental Data*, Reproduced with permission from the American Society for Testing and Materials, Philadelphia, ASTM STP 892, pp 154-169.
- Fredlund D. G., and Rahardjo H., 1993, *Soil Mechanics for Unsaturated Soils*, John Wily and Sons.
- Fredlund, D. G., 2000, *The 1999 R. M. Hardy Lecture: The Implementation of Unsaturated Soil Mechanics Into Geotechnical Engineering, R. M. Hardy Address*, Canadian Geotechnical Journal, vol. 37, No. 5, pp. 963– 986.
- Huang F., and Wang G., 2012, *One-Dimensional Experimental Research on Vacuum Degree Transmission Law in Unsaturated Soil*, EJGE, vol. 17, bund W, pp 3313-3322.
- Indraratna, B., and Rujikiatkamjorn, C., 2004, *Laboratory Determination of Efficiency of Prefabricated Vertical Drains*, 15th Southeast Asian Geotechnical Conference, Pathumthani, Thailand, SEAGS, pp 453-456.
- Shan Z, Ling D., and Ding H., 2013, *Analytical Solution for 1D Consolidation of Unsaturated Soil with Mixed Boundary Condition*, Journal of Zhejiang University-SCIENCE, vol. 14, No 1, pp 61-70.
- Chai J., and Carter J. P., (2011): "Deformation Analysis in Soft Ground Improvement," Springer, London, New York.

LIST OF SYMBOLS

a_n	coefficient, 1/m
c_v^a	coefficient of consolidation with air, dimensionless
c_v^w	coefficient of consolidation with respect to water, dimensionless
c_{v1}^a	coefficient, dimensionless
c_{v1}^w	coefficient, dimensionless
C_a	interactive constants with respect air, dimensionless
C_w	interactive constants with respect to water, dimensionless
fn	coefficient, dimensionless
H	thickness of drainage path, m

k_a	coefficients of permeability with respect to air, m/sec
k_w	coefficients of permeability with respect to water, m/sec
n	ratio of radius of the axisymmetric influence zone around a single drain to radius of equivalent drain, dimensionless
u_a	pore-air pressures at any time, kPa
u_{ai}	initial pore-air, kPa
u_{atm}	atmospheric pressure, kPa
u_w	pore-water pressures at any time, kPa
u_{wi}	initial pore-water, kPa
U_a	degrees of consolidation for air, %
U_r	degree of radial consolidation, %
U_w	degrees of consolidation for water, dimensionless%
t	time, sec
T_a	time factors for air, dimensionless
T_r	time factor for radial consolidation
T_w	time factors for water, dimensionless
z	Depth below surface, m and
λ_n	Coefficient, 1/m

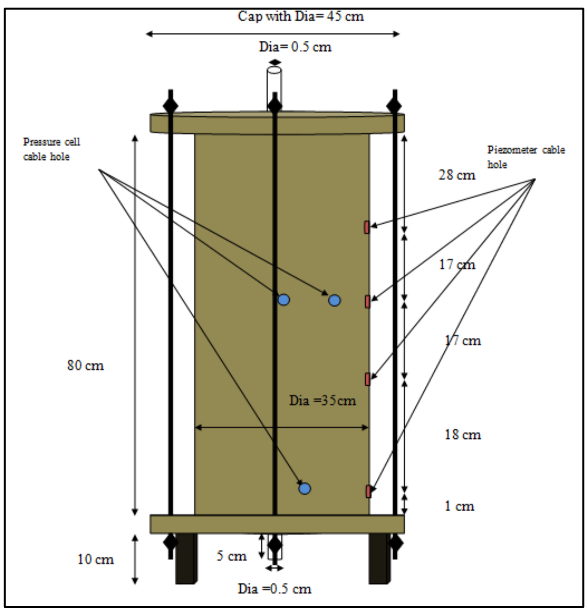

Figure 1. Schematic diagram of the designed consolidmeter cell.

Figure 2. Cap detalies of the consolidometer

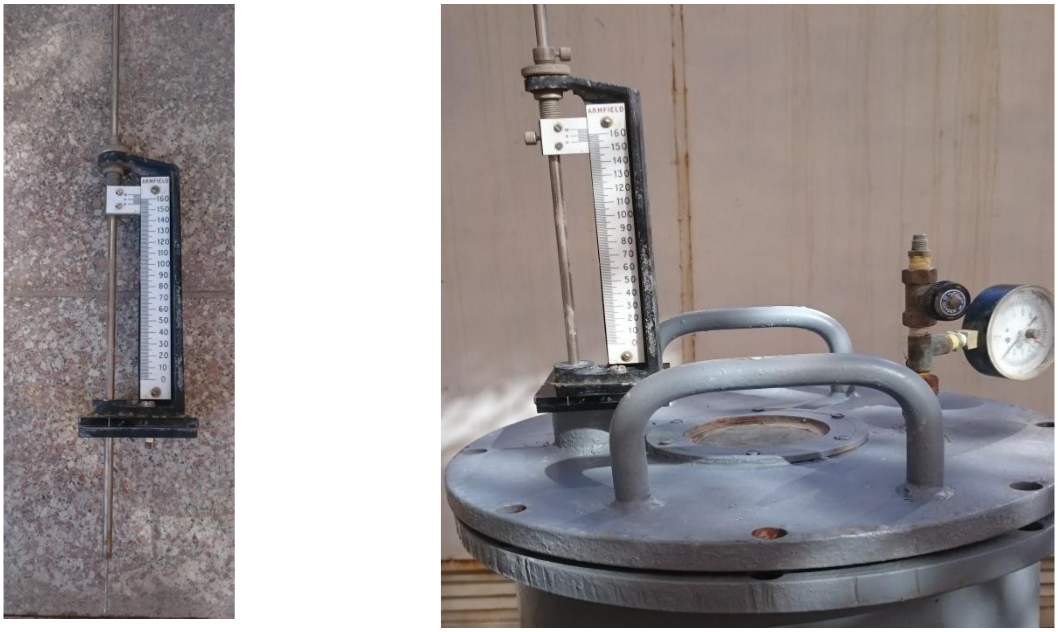

(a) The vernear of the point gage (b) The point gauge placed on the top flange

Figure 3. The point gauge used in this research to measure the settlement of the soil surface.

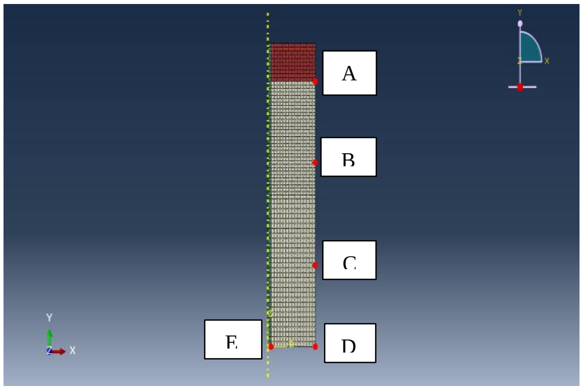

Figure 4. Saturated and unsaturated layers of soil, the mesh, and numbers of nodes used in the numerical modeling.

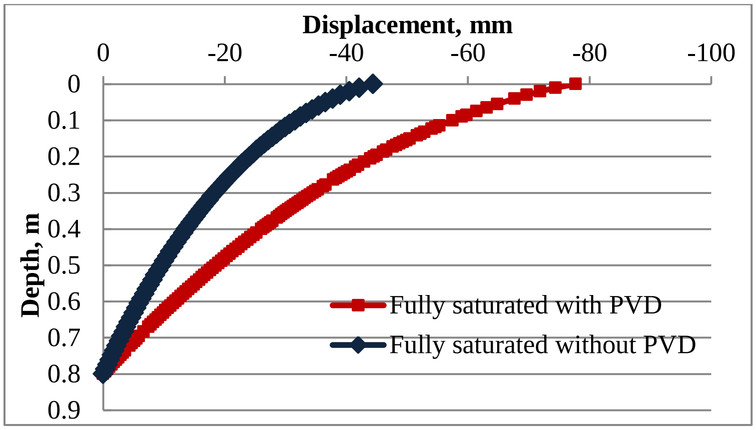

Figure 5. Comparison of soil settlement for fully saturated soils with and without PVD under -40 kPa.

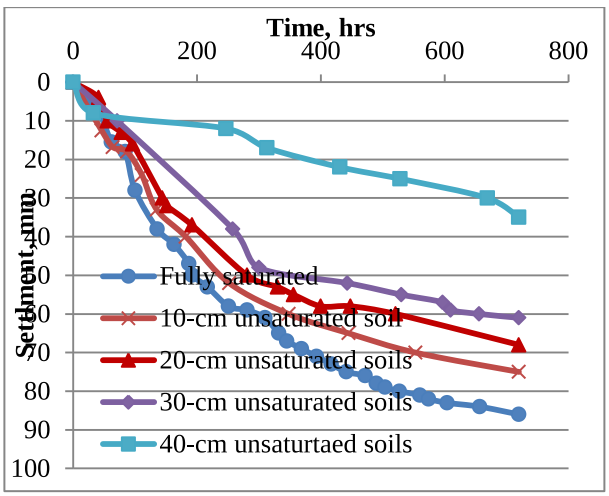

(a) Settlement of soil surface after 30 days.

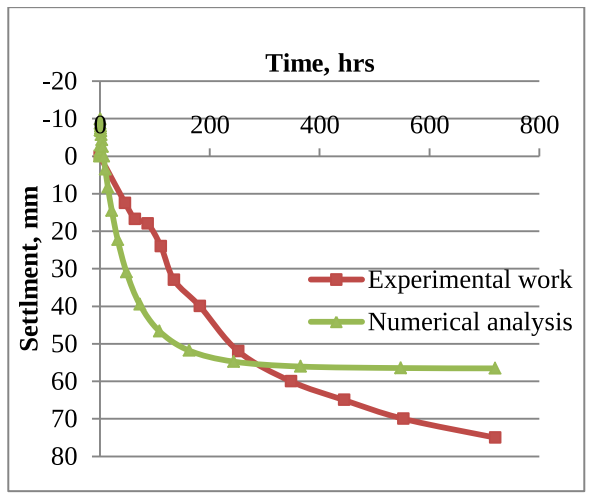

(b) Experimental results and numerical analysis results for 1/8 L unsaturated soil layer.

Figure 6. Comparison of settlement of soil for fully saturated soil with different depth of unsaturated layer.

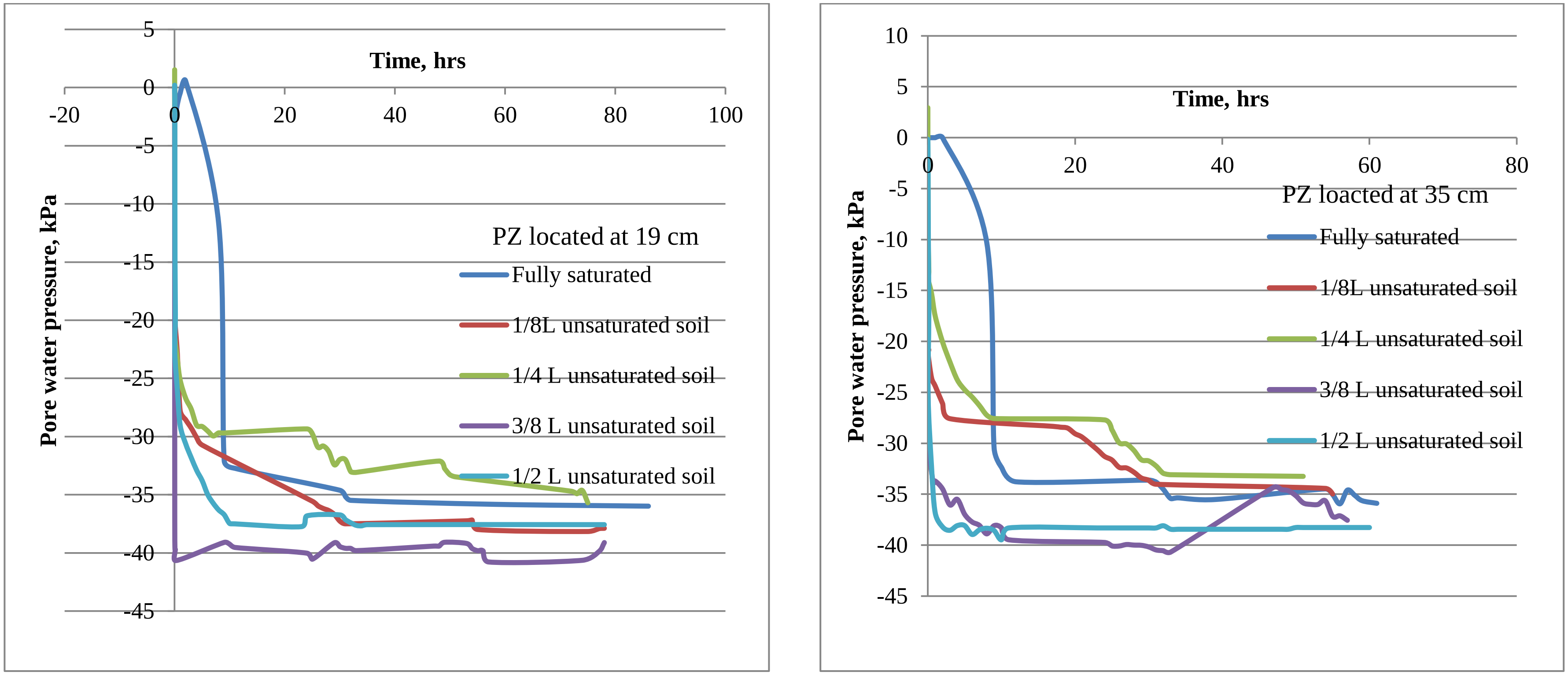

Figure 7. Variation of pore-water pressure with time for 30 hours.

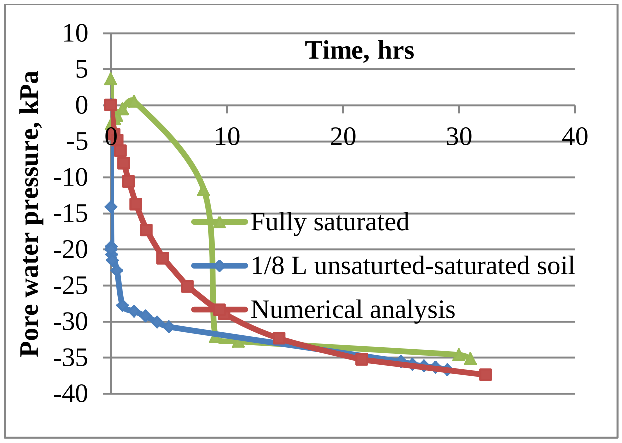

(a) At point A

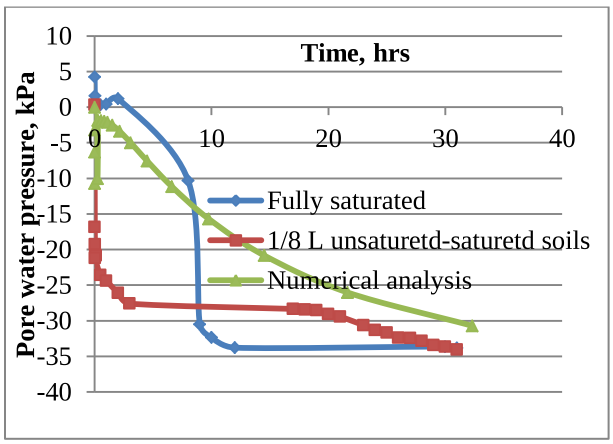

(b) At point B

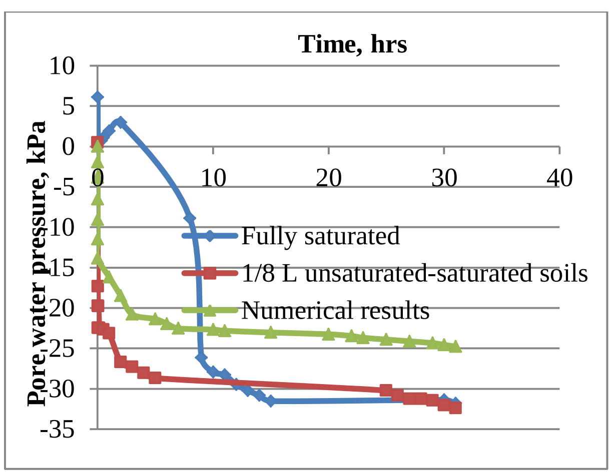

(c) At point C

Figure 8. Comparison of variation of pore-water pressure with time for 1/8 L unsaturated soil.

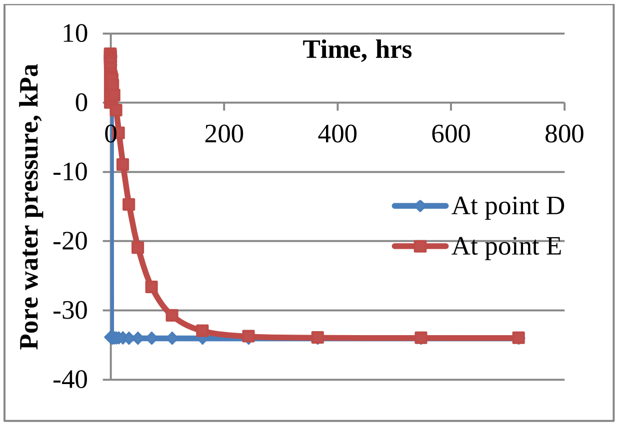

Figure 9. Numerical analysis of radial variation of pore-water pressure with time.

Table 1. Physical and chemical properties of the natural soil used in the tests.

Property	Value
Liquid limit, LL	36 %
Plastic limit, PL	18%
Liquidity index, LI	0.61
Specific gravity, Gs	2.73
Clay content < 0.005 mm	45.3 %
Silt content 0.005 to 0.074 mm	49.21 %
Sand content > 0.074 mm	5.49 %
Maximum dry unit weight, kN/m^3	17.06
Optimum moisture content,	19%
Soil symbol according to USCS	CL
Organic material	2.1 %
SO_3	3.20 %
Total soluble salts	10 %
pH	8.1
Gypsum content	7.224 %
Radiation	Negative
Initial void ratio, e_o	1.092
Compression index, c_c	0.4
Coefficient of vertical consolidation, $c_{v,}$ m^2/day	$1.46*10^{-3}$
Swelling index, c_r	0.03

Adaptive Sliding Mode Controller for Servo Actuator System with Friction

Shibly Ahmed Al-Samarraie
Assistant Professor
Control & Systems Eng. Dept.
University of Technology
E-mail: 60132@uotechnology.edu.iq

Muntadher Mohammed Salih
MSc. Student
Control & Systems Eng. Dept.
University of Technology
E-mail: muntadher_salih@yahoo.com

ABSTRACT

This paper addresses the use of adaptive sliding mode control for the servo actuator system with friction. The adaptive sliding mode control has several advantages over traditional sliding mode control method. Firstly, the magnitude of control effort is reduced to the minimal admissible level defined by the conditions for the sliding mode to exist. Secondly, the upper bounds of uncertainties are not required to be known in advance. Therefore, adaptive sliding mode control method can be effectively implemented. The numerical simulation via MATLAB 2014a for servo actuator system with friction is investigated to confirm the effectiveness of the proposed robust adaptive sliding mode control scheme. The results clarify, after comparing it with the results obtained by using classical sliding mode control, that the control efforts are reduced and the chattering amplitude is attenuated with preserving main features of the classical sliding mode control.

Key words: sliding mode control, adaptive sliding mode control, low pass filter, servo actuator system.

تصميم مسيطر منزلق متكيف لمنظومة المحرك المؤازر بوجود الاحتكاك

الاستاذ المساعد الدكتور شبلي احمد السامرائي
قسم هندسة السيطرة والنظم
الجامعة التكنولوجية

منتظر محمد صالح
طالب ماجستير
قسم هندسة السيطرة والنظم
الجامعة التكنولوجية

الخلاصة

يتناول هذا البحث استخدام مسيطر منزلق متكيف للسيطرة الرصينة على منظومة المحرك المؤازر بوجود الاحتكاك . المسيطر المنزلق المتكيف لديه العديد من المزايا بالاضافة الى مزايا المسيطر المنزلق التقليدي. اولاً، يتم تقليل جهد التحكم الى اقل حد ممكن والتي تحدد بتحقق ظروف الانزلاق. ثانياً، ليس مطلوباً ان تكون الحدود العليا للشكوك معروفة سلفاً. لذلك ، يمكن تطبيق الطريقه المقترحة بفعالية. بعد مقارنة المحاكات العددية بإستخدام برنامج ال MATLAB 2014a لمنظومة المحرك المؤازر بوجود الاحتكاك مع نتائج المسيطر المنزلق النمطي تأكد كفاءة الخطة المعروضة للمسيطر المنزلق المتكيف الرصين. وتوضح النتائج تخفيض جهد التحكم وتقليل الارتجاج مع الاحتفاظ بالملامح الرئيسية للمسيطر الانزلاقي التقليدي.

الكلمات الرئيسية : المسيطر المنزلق، المسيطر المنزلق المتكيف، مرشح المرور الضئيل، منظومة المحرك المؤازر.

1. INTRODUCTION

Sliding mode control (SMC) is an effective nonlinear robust control approach that can deal with system uncertainties. When the perturbations satisfy the matching condition the robustness of control system is very important because various uncertainties exist in practical applications. It has been widely studied and successfully used in practical applications such as pendulum systems, robot manipulators, power converters and motors**, Utkin, et al., 2009**. Therefore, developing simple and robust controllers for uncertain system is of much importance.

Adaptive controller is thus a controller that can adjust its behavior in response to make changes in the dynamics of the process and character of the disturbances**, Astrom,** and **Wittenmark, 2008.** The adaptive sliding mode control (ASMC) is the combination of adaptive control method and SMC approach. It is more flexible and convenient in controller design than SMC and also the control method system stability can be achieved with a smaller control effort than that in SMC.

The conventional SMC uses a control law with high control gains yielding the undesired chattering. While the control system is in the sliding mode the chattering phenomenon is the main drawback of the SMC which can damage actuators and systems. The boundary layer method is the first approach to reduce the chattering where many ways have proposed adequate controller gains tuning**, Slotine,** and **Sastry, 1983.** In the second approach a higher order sliding mode control is used to attenuate the chattering phenomenon**, Bartolini, et al., 2000** and**, Laghrouche, et al., 2007**. However, in these both control approaches; knowledge of parameters uncertainty bounds are required. In**, Chang, et al., 2002** the system performance is satisfactory when more than one parameter adaptation is used in the control law. In**, Yoon,** and **Trumper, 2014** a frequency domain measurement technique was suggested to identify the friction model, and the model is used to compensate the nonlinear friction in the systems. Many controllers based on fuzzy tools**, Munoz,** and **Sbarbaro, 2000** and**, Jiang, et al., 2015** have been published; but, these papers do not ensure the tracking performances. **Hall,** and **Shtessel, 2006** used sliding mode disturbance observer when they proposed a gain-adaptation algorithm. The required knowledge of parameters uncertainty bounds to design observer-based controller is the main obstacle in implementing the proposed adaptive controller.

The purpose of this paper is to design a SMC with parameter uncertainties and external disturbances without requiring knowing the bound of uncertainties. This can be done based on a gain adaptation law derived in reference**, Plestan, et al., 2010.**

The organization of the present paper is as follows. In section 2, the servo actuator system is described including the friction model. In section 3, the SMC is explained briefly while the ASMC algorithm is given in Sec. 4. The simulation of a servo actuator system with friction is illustrated in Sec. 5 and the conclusions are given in Sec. 6.

2. DC SERVO ACTUATOR SYSTEM WITH FRICTION: MATHEMATICAL MODEL DESCRIPTION

The mathematical model of the servo actuator system is represented by a second order dynamic system with friction present between two contacting surfaces **AlSamarraie, 2013**, i.e.,

$$J\ddot{x} = u - F - T_L \tag{1}$$

where J is the moment of inertia; $x, \dot{x}, \ddot{x}$ are the actuator position, velocity and acceleration, respectively; u is the control input torque; F is the friction torque; and T_L is the load torque.

The friction torque is represented by static friction a phenomenon which includes: Coulomb friction, Stiction friction, and the viscous friction, i.e., **Hélouvry, et al., 1994.**

$$F = \left\{F_s \exp\left(-\left(\frac{\dot{x}}{\dot{x_s}}\right)^2\right) + F_c\left(1 - \exp\left(-\left(\frac{\dot{x}}{\dot{x_s}}\right)^2\right)\right) + \sigma|\dot{x}|\right\} * sgn(\dot{x}) \tag{2}$$

where F_c is the Coulomb friction, F_s is the Stiction friction, $\dot{x_s}$ is the Stribeck velocity, and σ is the viscous friction coefficient.

By defining, $e_1 = x - x_d$ and $e_2 = \dot{x} - \dot{x}_d$, the system model in Eq. (1) can be written in a state space structure as:

$$\left.\begin{aligned} \dot{e}_1 &= e_1 \\ \dot{e}_2 &= \left(\frac{1}{J}\right)(u - F - T_l) - \ddot{x}_d \end{aligned}\right\} \tag{3}$$

While the schematic diagram for the closed loop position servo actuator model is shown in Fig. 1.

Now Eq. (3) may also be written in terms of nominal and perturbation terms as;

$$\left.\begin{aligned} \dot{e}_1 &= e_1 \\ \dot{e}_2 &= f_{2o}(e) + g_{2o}u + \delta(e, u) \end{aligned}\right\} \tag{4}$$

where

$$f_{2o}(e) = -\ddot{x}_d,\ \ g_{20} = \left(\frac{1}{J_o}\right),\ \delta(e, u) = \Delta\left(\frac{1}{J}\right)u - \left(\frac{1}{J}\right)(F + T_l) \text{ and } \Delta\left(\frac{1}{J}\right) = \frac{1}{J} - \frac{1}{J_o}$$

The reference signal is chosen to be differentiable function. The position, velocity and acceleration references are chosen as**, Xie, 2007.**

$$\left.\begin{aligned} x_d &= \frac{1}{16\pi}\sin(8\pi t) - \frac{1}{24\pi}\sin(12\pi t) \\ \dot{x}_d &= \sin(10\pi t) * \sin(2\pi t) \\ \ddot{x}_d &= 10\pi * \cos(10\pi t)\sin(2\pi t) - 2\pi * \sin(10\pi t)\cos(2\pi t) \end{aligned}\right\} \tag{5}$$

One of the uses of the following signal would be in the antenna and array positioning system**, Xie, 2007.**

3. SLIDING MODE CONTROL

The SMC includes a discontinuous control which is used to enforce the state trajectories of the system to some manifold. Sliding mode belongs to the motion in the manifold, limited by desired properties of reduced-order differential equations**, Utkin, 2013**. SMC is an extremely fashionable strategy for management of nonlinear uncertain systems, with a really giant frame of applications fields**, Slotine,** and **Sastry, 1983**. Attributable to the utilization of the discontinuous function, its key features are the robustness of closed loop system and the finite time affluence. The main obstacles of pure SMC in practical applications are firstly, the signum function which usually reason to the problem of chattering and sensitivity to the noise of sensors. Secondly, the SMC may has unnecessarily great control signals to overcome all the parametric variations and disturbance input. To avoid these difficulties, for instance, one can use an approximate signum function, equivalent control (Low pass filter) and adaptation method with classic SMC**, Kaynak, et al., 2001**. The adaptation technique for finding the control gain $K(t)$ gives a minimum amount value of discontinuity gain causing in minimization of the chattering effect and control effort as clarified in the following section.

4. ADAPTIVE SLIDING MODE CONTROL

Consider the sliding mode controller with time varying gain $K(t)$ given by;

$$u(s,t) = -K(t)sign\big(s(x(t),t)\big) \tag{6}$$

Where u is the control input to be designed, K is the adaptation gain of control, x is the state vector, s is the sliding variable, and $sign(s)$ is the signum function modeled by

$$sign(s) \coloneqq \begin{cases} 1 & if\ s > 0 \\ -1 & if\ s < 0 \\ \in [-1;1] & if\ s = 0 \end{cases} \tag{7}$$

The adaptation law for the switching gain $K(t)$ is presented as follows**, Utkin,** and **Poznyak, 2013**; let ϵ being a positive parameter, then;

If $|s(x(t),t| > \epsilon > 0$, then $K(t)$ is the solution of the following differential equation

$$\dot{K}(t) = \alpha * |s(x(t), t)| \tag{8}$$

with > 0 , $K(0) > 0$, and ϵ is selected as a small positive constant.
If $|s(x(t), t| \leq \epsilon$, then $K(t)$ becomes

$$\begin{aligned} K(t) &= \beta|\eta(t)| + \gamma \\ \tau\dot{\eta}(t) + \eta(t) &= sign\big(s(x(t), t)\big) \end{aligned} \tag{9}$$

with

$$\beta = K(t^*) \tag{10}$$

where $\gamma > 0$, $\tau > 0$, and t^* is the largest value of t such that

$$|s\ (x(t^* - 0), t^* - 0)| > \epsilon\ , |s(t^*, t^*)| \leq \epsilon$$

Obviously, this controller is based on the real sliding mode concept**, Utkin,** and **Poznyak, 2013.**
By supposing that

$$|s\ (x(0)\ ,0)|\ > \epsilon$$

the ASMC law (Eqs. (8) & (9)) works as follows**, Utkin,** and **Poznyak, 2013**:

The adaptation law uses expanding the gain $K(t)$ to avoid limited uncertainty with unknown bounds in the system if the gain reaches to a value sufficiently huge after that the real sliding mode begins at $t = t_1$. In this time when the absolute of switching control is less than or equal, then $K(t)$ converts to another adaptation law (9) in this equation modify the gain with respect to the present uncertainties and perturbations. If the absolute of switching control is greater than ϵ because of the varying uncertainties and perturbations surpasses $\beta = K(t_1)$, then the real sliding mode will be pulverized and $K(t)$ returns to the first adaptation law (8) with the same steps. For more details about this control you can refer to**, Utkin,** and **Poznyak, 2013.**

5. SIMULATIONS RESULT AND DISCUSSIONS

A servo actuator system model with friction mechanism, which described in Eq. (1), is utilized here as an application to verify the effectiveness and robustness of the ASMC. The simulations are performed using MATLAB simulink fixed step solver OD4 (runge-kutta) with initial condition $e(0) = (\frac{\pi}{3600}\ ,0)$, as in **AlSamarraie, 2013.**

Two sets of simulation results are presented below. In the first set, the nominal system parameters were used while in the second set the parameter values are taken equal to 1.15 of nominal values i.e., each parameter value increased by 15% of its nominal value. In addition, the presence of external disturbance load is considered in the simulation process. For both simulation sets, the results of the present work are compared with the results obtained by using a conventional sliding mode controller. The conventional SMC design details for the servo actuator are found in Appendix A where the control input, u is as given by Eq. (A.10). Also, if $\lambda = 10$, and the reference angle and reference velocity as described in Eq. (5) and the adaptive SMC control input u read as in Eqs. (6), (7), (8), (9) and (10) for $\epsilon = 0.03$, $k(0) = 16$, $\alpha = 9300$, $\gamma = 5$ and $\tau = 10^{-3}$. Finally the system parameters and the external load used in the simulations are given in Table 1 and Table 2.

5.1 Simulation Results with Nominal System Parameters

In **Fig. 2** and **4** the time required to reach the desired angle and velocity respectively is less than 0.5 sec for both controllers (adaptive SMC and conventional SMC). This outcome is checked while plotting the error and maximum error of angle in **Fig. 3**, where it does not exceed 2.5×10^{-4} radian in position. The sliding variable s as shown in **Fig. 5** does not exceed ϵ after $7 * 10^{-3}$ sec for both controllers. The control efforts u for both controllers are clarified in **Fig. 7** while the adaptive gain $K(t)$ is plotted in **Fig. 6**.

As can be easily checked from **Fig. 5** and **7**, the ASMC forces the state to stay at the sliding manifold with 35 present less than control effort of conventional SMC. This is because the control gain $K(t)$ is smaller than that in the classical SMC where its value is decreased in the region $|s| < \epsilon$ according to the adaptation law in Eq. (9). In this region the control action is the equivalent one and sliding manifold is still attractive. As a result the performance of the ASMC resembles that of the classical SMC, as can be deduced from **Fig. 2, 3, 4, 5** and **8**. Moreover the chattering is attenuated since near the sliding manifold the ASMC is the equivalent control (**Fig. 7**). Attenuating system response chatter is clearly seen in **Fig. 5** and **8** when compared with classical SMC design. It must also be noted here that the ASMC designed without the need to know system parameters values and the bound on their values. The only information required to be known is that the variation on the system model uncertainty is bounded. The next simulation test examines the ASMC ability in the presence of system parameters uncertainty and unknown external disturbances.

5.2 Simulation Results with System Parameters which Increased by 15% of their Nominal Values and with the Presence of Disturbance Load $T_L = 2.5$.

In order to test the ability and performance of the ASMC the simulation is repeated here for the servo actuator system but with parameter values increased by 15% of their Nominal Values (for example $F_s = F_{s0} + 0.15 * F_{s0}$) and also with the presence of disturbance load $T_L = 2.5$. Table (2) presents the system parameters used in this set of simulation.

As in the first set of simulation the performance of the ASMC is similar to that for the classical SMC. This can be shown in **Fig 9, 10, 11** and **15**. Again **Fig. 13** and **14** prove that the control effort is decreased by 32 present by using ASMC when compared to the classical SMC as a direct result to the adaptation of $K(t)$ near the sliding manifold (**Fig. 13**). Finally **Fig. 12** and **15** shows that the chattering is attenuated as in the case of the nominal system model parameters.

6. CONCLUSIONS

The theory of adaptive sliding mode control is utilized here to design a robust sliding mode controller to the servo actuator system in the presence of model uncertainty and friction. The existence of a bound on the uncertainty of the system model is the only information required to be known when designing the proposed ASMC. The major feature of classical SMC, which is the insensitivity to model uncertainty and external disturbances during sliding motion, are preserved as can be deduced from the results obtained from the numerical simulations. The obtained results showed also that the ability and performance of the proposed control are similar to the case of using classical SMC. Additionally, the control efforts are smaller and the chattering amplitude is, consequently, attenuated as can be seen when comparing the simulation results with the results obtained using classical SMC.

REFERENCES

- Al-Samarraie S. A.,2013, *Invariant Sets in Sliding Mode Control Theory with Application to Servo Actuator System with Friction*, WSEAS Transactions on systems and control, Vol. 8, No.2, pp. 33-45.
- Astrom, K. J., Wittenmark, B., 2008, *Adaptive Control*, New York: Dover Publications, 2nd ed.
- Bartolini, G., Ferrara, A., Usai E., and Utkin V. I., 2000, *On Multi-Input Chattering free Second Order Sliding Mode Control*, IEEE Transactions on Automatic Control Vol.45, No.9, pp.1711-1717.
- Chang, W. D., Hwang, R. C., and Hsieh, J. G., 2002, *Application of an Autotuning Neuron to Sliding Mode Control*, IEEE Transactions on Systems, Man, and Cybernetics, Part C (Applications and Reviews), Vol. 32, No. 4, pp. 517–522.
- Hall, C. E., and Shtessel, Y. B., 2006, *Sliding Mode Disturbance Observer-Based Control for a Reusable Launch Vehicle*, Journal of Guidance, Control, and Dynamics, Vol.29, No.6, pp.1315-1328.
- Hélouvry, B. A., Dupont, P., and Wit C. C., 1994, *A Survey of Models, Analysis Tools and Compensation Methods for the Control of Machines with Friction*, Automatica, Vol. 30, No. 7, pp. 1083–1138.
- Jiang, Y., Liu, Z., Chen, C., and Zhang, Y., 2015, *Adaptive Robust Fuzzy Control for Dual Arm Robot with Unknown Input Deadzone Nonlinearity,* Springer Nonlinear Dynamics, Vol. 81, No. 3, pp. 1301-1314.
- Kaynak, O., Erbatur, K., and Ertugnrl M., 2001, *The Fusion of Computationally Intelligent Methodologies and Sliding-Mode Control -a Survey*, IEEE Transaction on Industrial Electronics, Vol. 48, No. 1, .pp. 4-17.
- Laghrouche, S., Plestan, F., and Glumineau, A., 2007, *Higher Order Sliding Mode Control Based on Optimal LQ Control and Integral Sliding Surface*, Automatica, Vol.43, No.3, pp.531-537.
- Munoz, D., and Sbarbaro, D., 2000, *An Adaptive Sliding Mode Controller for Discrete Nonlinear Systems,* IEEE Transactions on Industrial Electronics, Vol.47, No.3, pp.574-581.

- Plestan, F., Shtessel, Y., Brégeault, V., and Poznyak, A., 2010, *New Methodologies for Adaptive Sliding Mode Control*, International Journal of Control, Taylor & Francis, Vol.83, No.9, pp. 1907-1919.
- Slotine, J. J., and Sastry, S. S., 1983, *Tracking Control of Nonlinear System using Sliding Surfaces with Application to Robot Manipulators*, American Control Conference, San Francisco, CA, USA, 22-24 June, Vol.38, No.2, pp. 132-135.
- Utkin, V. I., Guldncr, J., and Shi, J., 2009, *Sliding Modes in Electromechanical Systems*, Taylor & Francis, 2nd ed.
- Utkin, V. I., and Poznyak, A. S., 2013, Adaptive Sliding Mode Control, in Bandyopadhyay, B., Janardhanan. S., and Spurgeon, S. K. (Eds.), *Advances in sliding mode control: concept*, *theory and implementation*, Springer, New York, pp.22-53.
- Utkin, V. I., 2013, *On Convergence Time and Disturbance Rejection of Super-Twisting Control*, IEEE Transaction on Automatic Control, Vol.58, No.8, pp. 2013-2017.
- Yoon, J. Y., and Trumper, D. L., 2014, Friction Modeling, Identification, and Compensation Based on Friction Hysteresis and Dahl Resonance, Mechatronics, Vol. 24, No. 6, .pp. 734–741.
- Xie, W. F., 2007, *Sliding Mode Observer Based Adaptive Control for Servo Actuator With Friction*, IEEE Transaction on Industrial Electronics, Vol. 54, No. 3, pp. 1517-1527.

APPENDIX (A)

Consider the nonlinear uncertain system**, (**see for example **Utkin, et al., 2009)**

$$\left.\begin{aligned} e_1 &= e_2 \\ e_2 &= f_2(e) + g_2 u + d(t) \end{aligned}\right\} \qquad (\mathrm{A.1})$$

where $e = [e_1\ e_2]^T$ is the state vector, u the control input to be designed and $d(t)$ is the disturbance term which includes the external load and friction. In terms of nominal and perturbation term Eq. $(\mathrm{A.1})$ can be rewritten by

$$\left.\begin{aligned} e_1 &= e_2 \\ e_2 &= f_{20}(e) + g_{20} u + \delta(e,u) \end{aligned}\right\} \qquad (\mathrm{A.2})$$

Where $f_{20}(e)$ and $g_{20}(e)$ are the nominal functions of $f_2(e)$ and $g_2(e)$ respectively, while $\delta(e,u)$ is the uncertainty term results from the uncertainty in system dynamics and external load. The perturbation term $\delta(e,u)$ is given by

$$\delta(e,u) = \Delta g_2(e)u + \Delta f_2(e) + d(t) = \Delta\left(\frac{1}{J}\right)u - \left(\frac{1}{J}\right)(F + T_l) \qquad (\mathrm{A.3})$$

Let the sliding variable selected as;

$$s = e_2 + \lambda e_1 \qquad (\mathrm{A.4})$$

Then the sliding variable time derivative is

$$\dot{s} = \dot{e}_2 + \lambda \dot{e}_1 \qquad (A.5)$$

From Eq. (A.2) $\dot{s}$ is

$$\dot{s} = f_{20}(e) + g_{20}u + \delta(e,u) + \lambda e_2 \qquad (A.6)$$

To design a sliding mode controller, the elected Lyapunov function is

$$V = |s| \qquad (A.7)$$

And its time derivative $\dot{V}$ is

$$\dot{V} = sgn(s) * \dot{s} \qquad (A.8)$$

Or

$$\dot{V} = sgn(s) * (f_{20}(e) + g_{20}u + \delta(e,u) + \lambda e_2) \qquad (A.9)$$

The request is the selection of u such that $\dot{V}$ is negative definite. In this work u is chosen as in the traditional sliding mode by

$$u = \frac{1}{g_{20}(e)}\left(-f_{20}(e) - \lambda e_2 - K(e) * sign(s)\right) \qquad (A.10)$$

then $\dot{V}$ becomes;

$$\begin{aligned}\dot{V} &= sign(s) * \left(-K(e) * sign(s) + \delta(e,u)\right)\\ &= -K(e) + sign(s) * \delta(e,u)\\ &\leq -K(e) + |\delta(e,u)| \qquad (A.11)\end{aligned}$$

The gain $K(e)$ that will make the inequality (A.11) less than zero (attractiveness of the sliding manifold and sliding motion) is selected as follows;

$$K(e) > |\delta(e,u)| \qquad (A.12)$$

Where

$$\begin{aligned}|\delta(e,u)| &= |\Delta f_2(e) + d(t)| + |\Delta g_2(e)u|\\ &= |\Delta f_2(e) + d(t)| + \left|\Delta g_2 * \{\frac{1}{g_{20}(x)}(-f_{20}(e) - \lambda e_2 - K(e) * sign(s))\}\right|\end{aligned}$$

$$= |\Delta f_2(e) + d(t)| + \left|\frac{\Delta g_2(e)}{g_{20}(e)}\right| * |f_{20}(e) + \lambda e_2| + \left|\frac{\Delta g_2(e)}{g_{20}(e)}\right| * K(e) \qquad (A.13)$$

When substituting Eq. (A.13) in the inequality (A.12) and resolve for the gain $K(e)$ to obtain the following inequality:

$$K(e) > \frac{\max\{|\Delta f_2(e) + d(t)| + \left|\frac{\Delta g_2(e)}{g_{20}(e)}\right| * (|f_{20}(e) + \lambda e_2|)\}}{1 - \max\left(\left|\frac{\Delta g_2(e)}{g_{20}(e)}\right|\right)}$$

Now let $K(e)$ equal to:

$$K(e) = k_0 + \frac{\max\{|\Delta f_2(e)| + \left|\frac{\Delta g_2(e)}{g_{20}(e)}\right| * (|f_{20}(e) + \lambda e_2|)\}}{1 - \max\left(\left|\frac{\Delta g_2(e)}{g_{20}(e)}\right|\right)} \qquad (A.16)$$

where

$k_0 > 0$

$$|\Delta f_2(e) + d(t)| = \left|\frac{1}{J}(F + T_L)\right|$$
$$\leq \left|\frac{1}{J}(F))\right| + \left|\frac{1}{J}(T_L)\right| = \left|\frac{1}{J}(F_c + F_s + \sigma|\dot{x}|)\right| + \left|\frac{1}{J}(T_L)\right|$$
$$\leq \left|\frac{1}{J_{min}}(F_{cmax} + F_{smax} + \sigma_{max}|\dot{x}|)\right| + \left|\frac{1}{J_{min}}(T_{Lmax})\right|$$
$$|\Delta g_2(e)| = \left|\frac{1}{\Delta J_{min}}\right|.$$

The value of $k_0 = 0.25$ and the classical SMC parameters with maximum uncertainty (25%) are presented in the following Table A.1.

Table 1. DC servo actuator and friction model nominal parameters**, Xie, 2007.**

Nominal Parameters	Definition	Value	Unit
J_o	inertia of moment	0.2	Kgm^2
F_{so}	Stiction friction	2.19	Nm
F_{co}	Coulomb friction	16.69	Nm
$\dot{x}_{so}$	Stribeck velocity	0.01	rad/sec
σ_o	viscous friction coefficient	0.65	Nm.sec/rad
T_{Lo}	the load torque	2	Nm

Table 2. DC servo actuator and friction model parameters used in the simulations.

Parameters	Definition	Value	Unit
J	inertia of moment	0.23	Kgm^2
F_s	Stiction friction	2.5185	Nm
F_c	Coulomb friction	19.1935	Nm
$\dot{x}_s$	Stribeck velocity	0.0115	rad/sec
σ	viscous friction coefficient	0.7475	Nm.sec/rad
T_L	the load torque	2.5	Nm

Table A.1. System parameter with 25% uncertainty used for Classical SMC.

Parameters	Definition	Value	Unit
J_{min}	Minimum value of inertia of moment	0.15	Kgm^2
$F_{s\,max}$	maximum value of Stiction friction	2.7375	Nm
$F_{c\,max}$	maximum value of Coulomb friction	20.8625	Nm
σ_{max}	maximum value of viscous friction coefficient	0.8125	Nm.sec/rad
$T_{L\,max}$	maximum value of the load torque	2.5	Nm

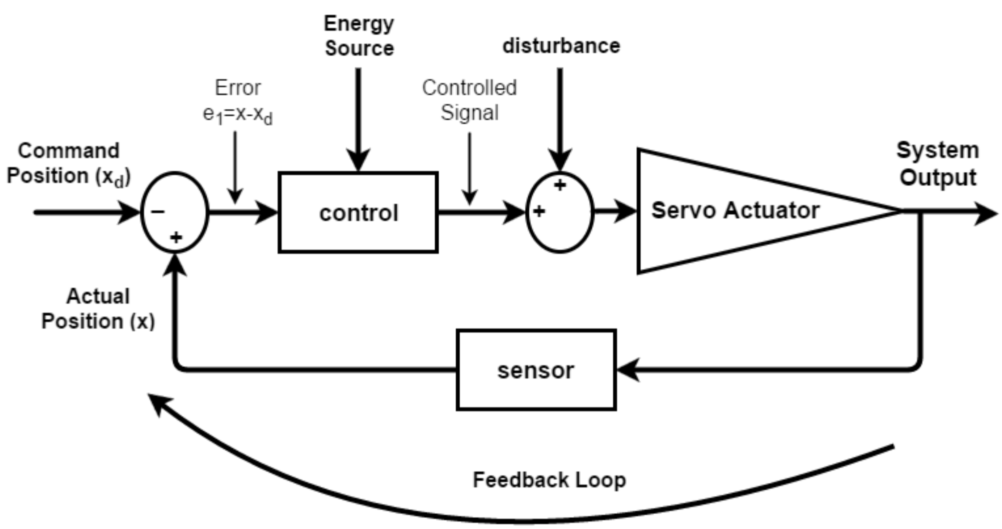

Figure 1. Closed loop position servo actuator model.

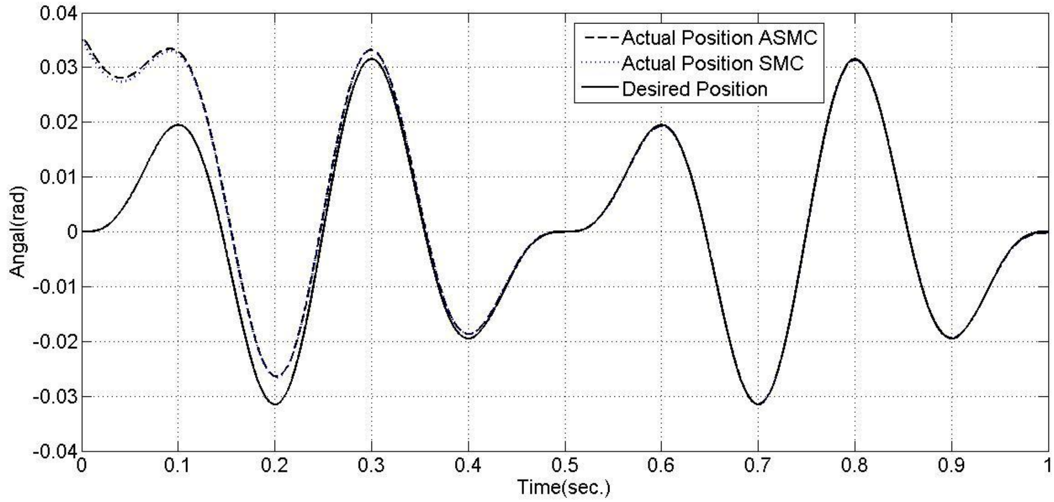

Figure 2. Angle vs. time for the servo actuator.

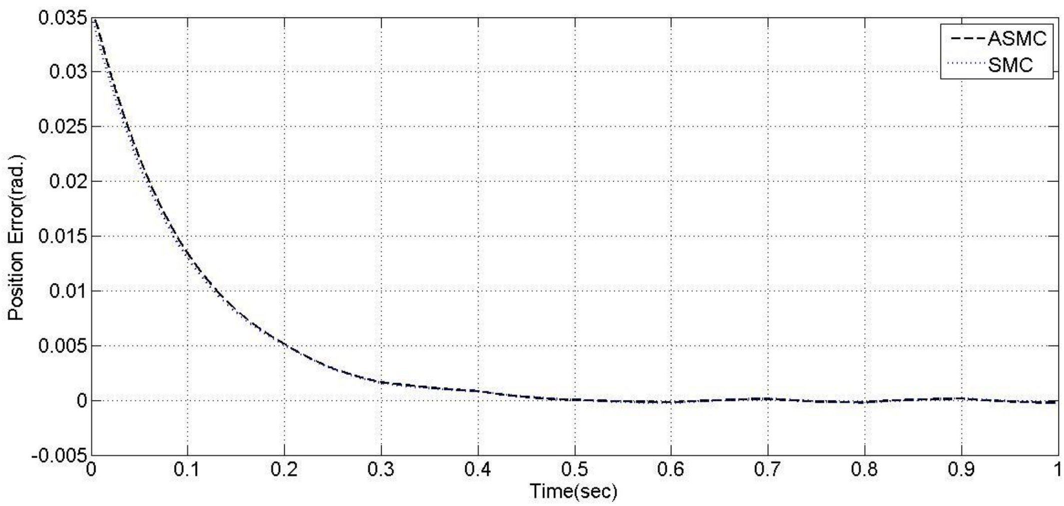

Figure 3. The position error vs. time for the servo actuator.

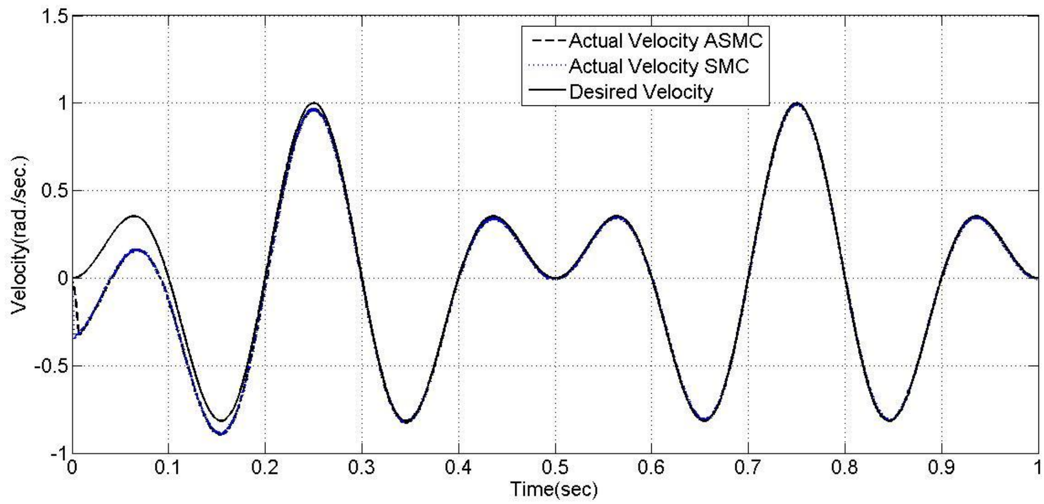

Figure 4. Velocity vs. time for the servo actuator.

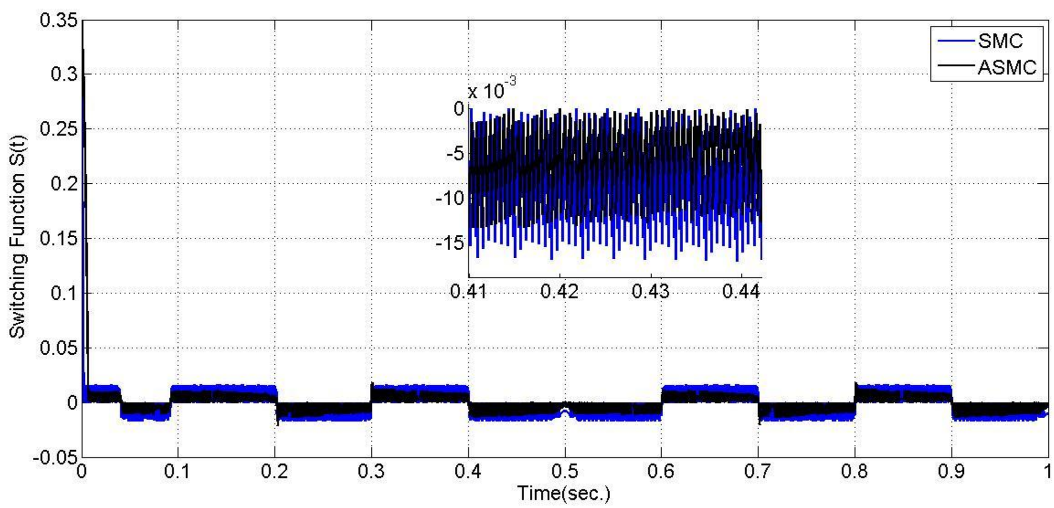

Figure 5. Sliding variable $s(x)$ vs. time for the servo actuator.

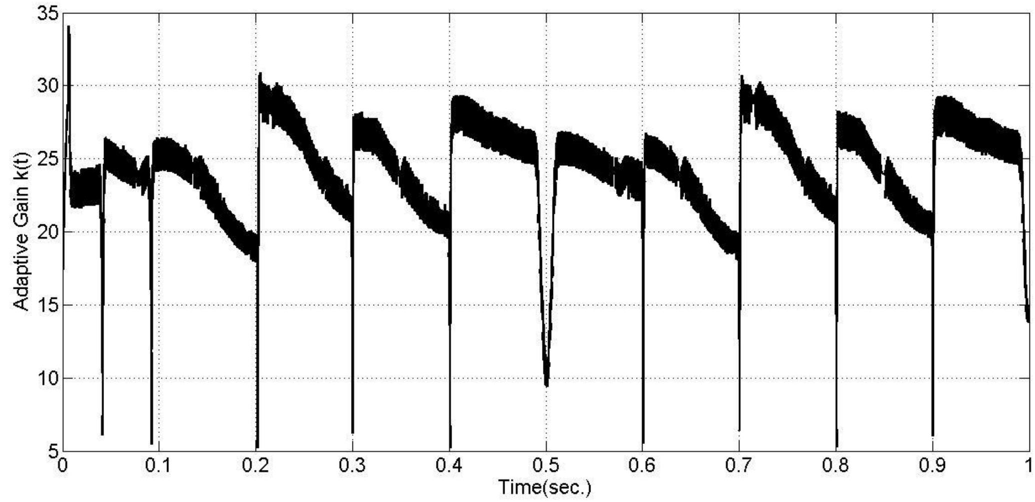

Figure 6. Adaptive gain $K(t)$ vs. time for the servo actuator.

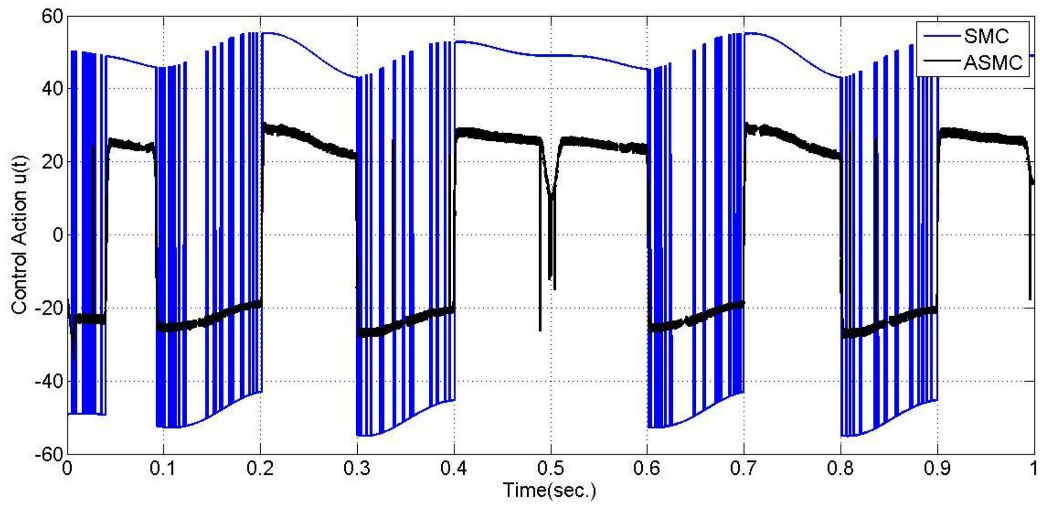

Figure 7. Control input u vs. time for the servo actuator.

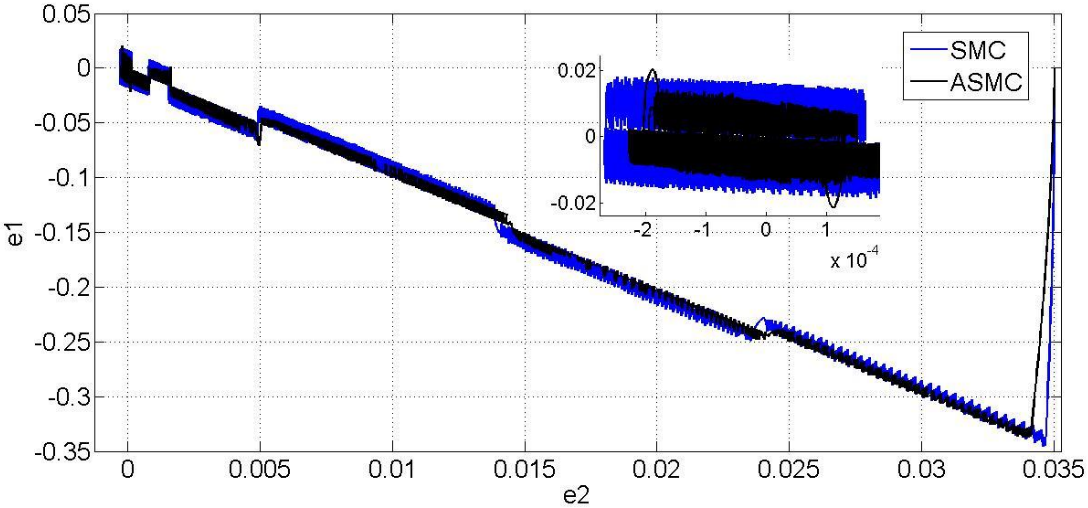

Figure 8. Phase plot of e2 vs. e1 for the servo actuator.

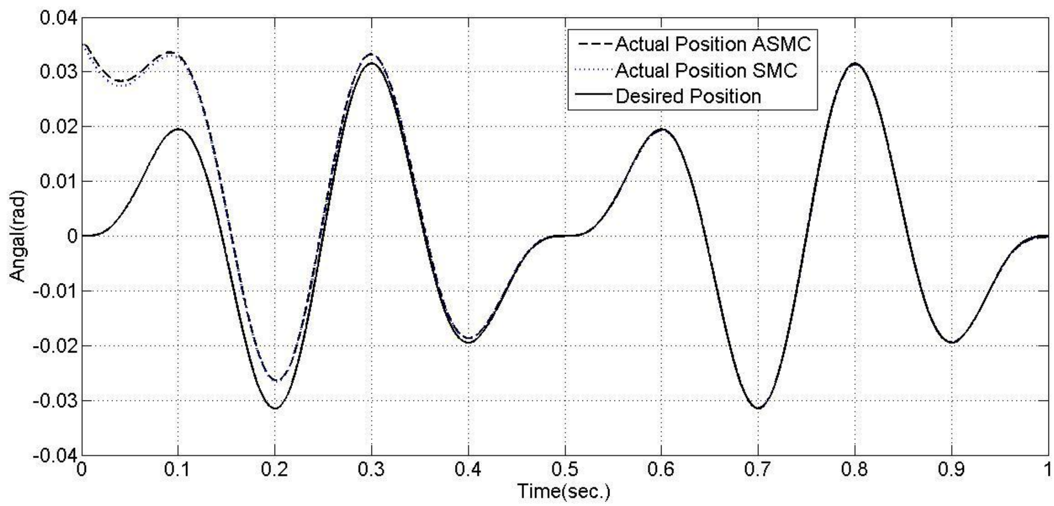

Figure 9. Angle vs. time for the servo actuator with parameter uncertainty and disturbance load.

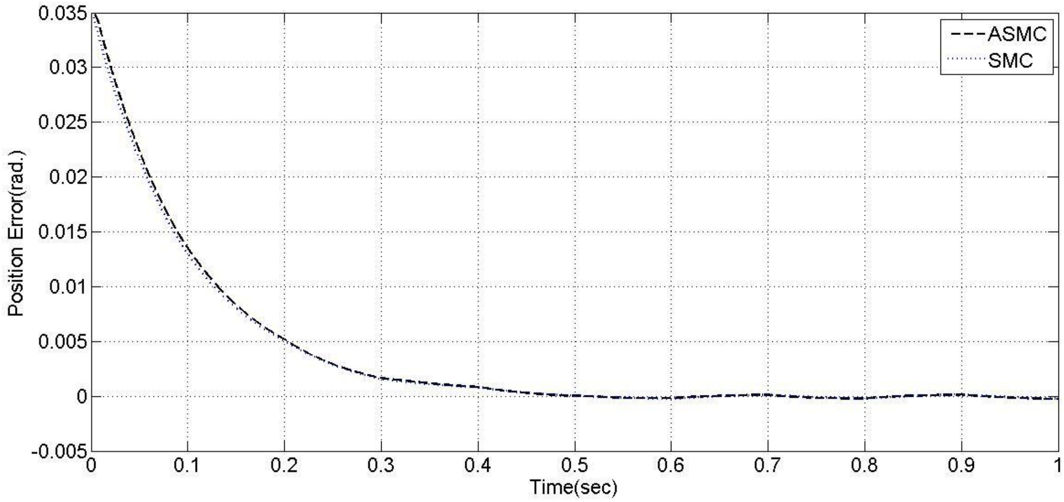

Figure 10. The position error vs. time for the servo actuator with parameter uncertainty and disturbance load.

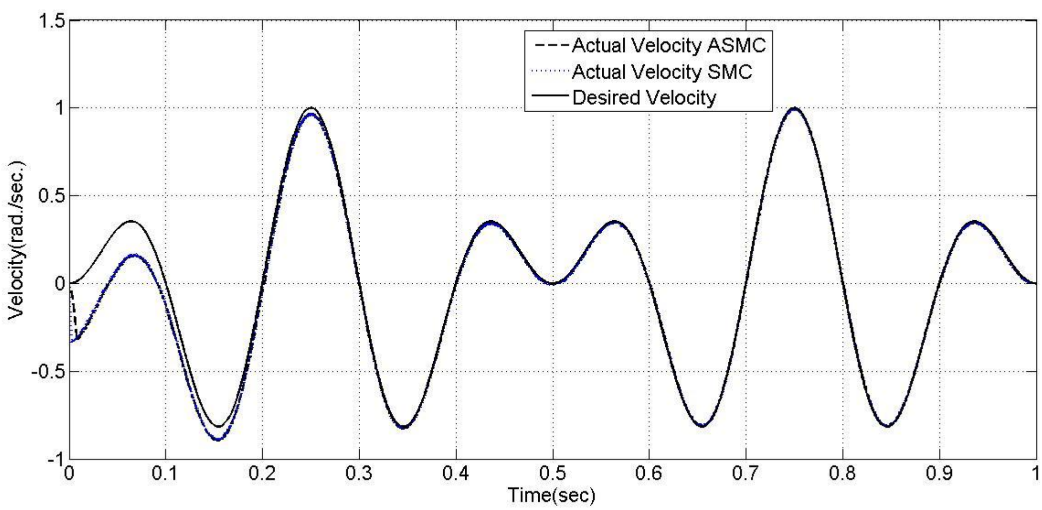

Figure 11. Velocity vs. time for the servo actuator with parameter uncertainty and disturbance load.

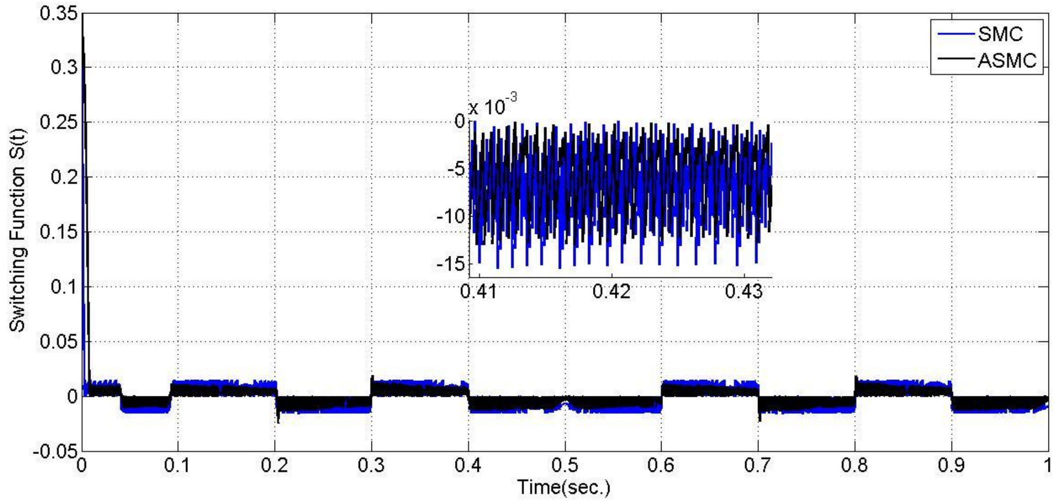

Figure 12. Sliding variable $s(x)$ vs. time for the servo actuator with parameter uncertainty and disturbance load.

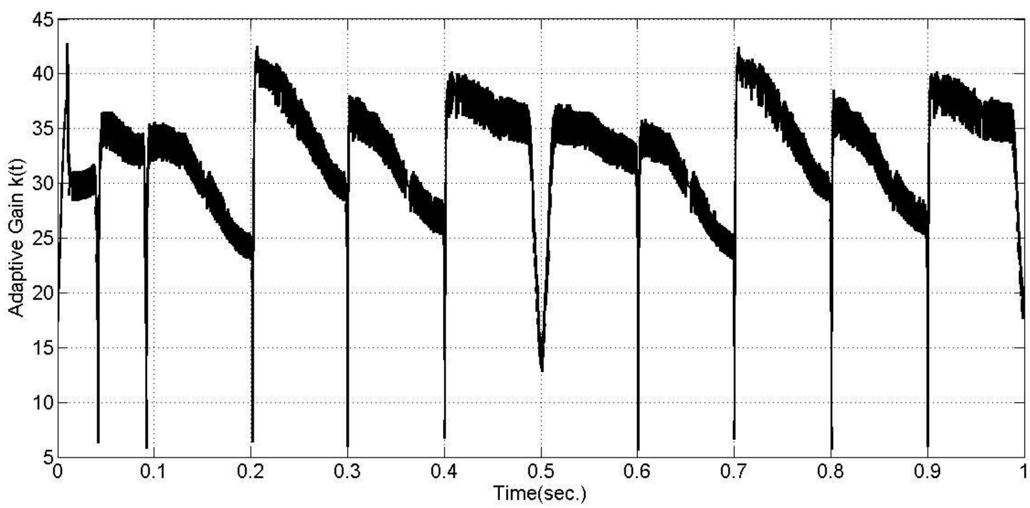

Figure 13. Adaptive gain $K(t)$ vs. time for the servo actuator with parameter uncertainty and disturbance load.

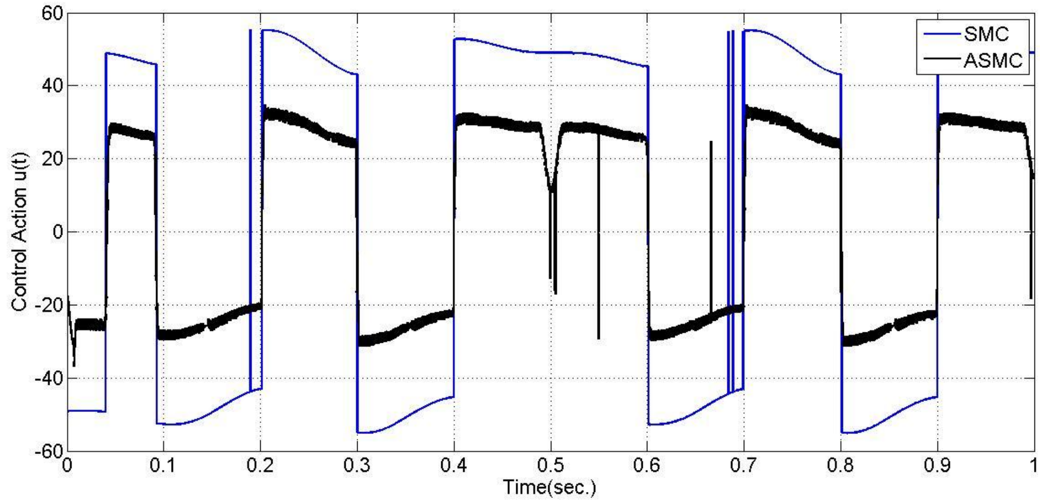

Figure 14. Control input u vs. time for the servo actuator with parameter uncertainty and disturbance load.

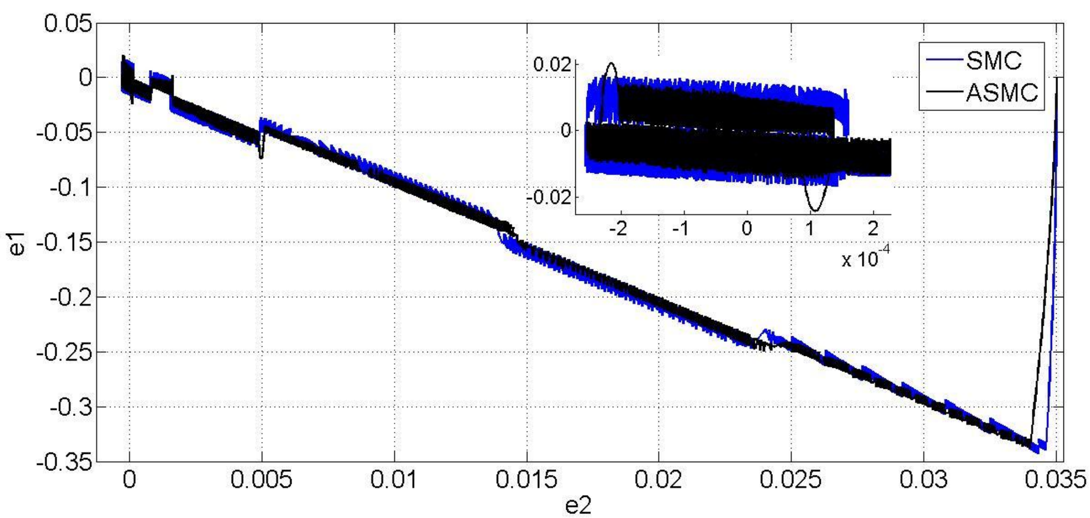

Figure 15. Phase plot of e2 vs. e1 for the servo actuator with parameter uncertainty and disturbance load.

Evaluation of Textile Filter in Field Drains

Amer Hassan Alhaddad
Assistant Professor
Water Resources Eng. Dept.
Ameralhaddad1950@ yahoo.com

Rusul Latteef Naji
MSc. Water Resources Eng. Dept.
alilateef29.al @ Gmail. com

ABSTRACT

The role of drain in agricultural lands is to remove excess surface and subsurface water to create a good environment for root growth and to increase crops yield. The main objective of this research was to evaluate the performance of closed drains when using textile filter instead of crushed gravel filter. The research has been executed in the laboratory using a sand tank model and by using two types of the soil. One of soils was light soil (sandy soil) and the other heavy soil (loamy soil). The tests were classified into four cases; each case was supplied discharge during 10 days. The results showed that the amount of out flow when using graded crushed gravel filter is greater than the amount of out flow in case of using textile filter for the same soil; and the amount of sediment in applying graded crushed gravel filter for the two types of soils was greater than using textile filter. The entrance resistance for textile filter was greater than graded crushed gravel filter and the entrance resistance increase for the two types of filters with time. From the results it can be concluded that the graded crushed gravel is more efficient than the textile filter in sandy soil, while when using the two types of filters with loamy soil the results showed that the two types of filter exhibited low work efficiency.

Keywords: graded crushed gravel filter; textile filter; sand tank; sediment; entrance resistance**.**

تقييم اداء الفلتر النسيجي في المبازل الحقلية

الاستاذ المساعد الدكتور عامر حسن الحداد
قسم هندسة الموارد المائية
جامعة بغداد

رسل لطيف ناجي
قسم هندسة الموارد المائية
جامعة بغداد

الخلاصة

تلعب شبكات البزل انتاج دورا مهما في افراغ الماء السطحي وتحت السطحي الزائد عن حاجة النباتات لتهيئة بيئة ملائمة لنمو الجذوروبالتالي زيادة المحاصيل الزراعية. أن الهدف الرئيسي من الدراسة هو تقييم استعمال الفلتر النسيجي بدلا من فلتر الحصى المدرج المكسر للمبازل المغلقة بأستخدام نوعين من الترببة احداهما تربة خفيفة (رملية) واخرى ثقيلة (مزيجية). تم تقسيم التجربة الى اربعة حالات ولكل حالة يتم اطلاق تصريف لمدة10 ايام. اوضحت النتائج ان كمية التصريف الخارج للفلتر الحصى المكسر اعلى من التصريف الخارج للفلتر النسيجي ولكلا النوعين من الترب, وكمية الرسوبيات للفلتر الحصى المكسر اكثر من الفلتر النسيجي لكلا النوعين من التربة ايضا. واما مقاومة الدخول للفلتر النسيجي فكانت اعلى من فلتر الحصى وتزداد هذه المقاومة مع الزمن, لكلاالنوعين من الفلتر. من النتائج نستطيع ان نستنتج ان الفلتر الحصوي المكسر مرغوب اكثر في التربة الرملية اما في التربة المزيجية فكان كلا الفلترين كفاءة العمل واطئة.

الكلمات الرئيسية: فلتر الحصى المدرج المكسر، الفلتر النسيجي،خزان رمل، رواسب، مقاومة الدخول.

1. INTRODUCTION

Subsurface drainage can be executed by installing an artificial conduit to create a flow path under the water table which means the hydraulic head of the soil to be drained is higher than the head through conduit. The purpose of sub surface drainage is to serve one or more of the following purposes:

- Improving the environment of root zone for vegetative growth by controlling the level of water table and ground water flow by creating a hydraulic gradient towards the drain due to the hydraulic head differential. This phenomenon is to create phreatic line (free water surface) in the vicinity of the conduit.

- Preventing and intercepting water movement into moist areas in order to remove it at the downstream end of the conduit, consequently preserving a flow system.

- Removing runoff water and sewage surface water in order to improve the stability of the appropriate internal slope and to reduce soil erosion.

Many researchers have applied several experiments and research studies by developing drainage criteria to improve the drainage process, and to show that the filters are important to improve and maintain drainage system. Improving the permeability around drain and increasing soil stabilization as the main objective of drain filter. The other playing role of porous material placed around a subsurface drain is to protect the drains from sedimentation of fine soil particles in the drains and to improve hydraulic performance to control the water table. There are several types of filters, including granular mineral materials that consist primarily of coarse sand, gravel and fine crushed stone, located beneath and around the drain pipe. There were many types of organic materials that were used as drain filters including straw envelope, flax straw, rice straw, cereal straw, bamboo, heather bushes, cedar leaf, wood chips, corncobs reeds, flax stems, linen, and sod grass. The other filters used are made from special fabric material such as paper, burlap, or fabric textile material that can be produced from polyamide (PA) and polypropylene (PP) or polyester (PETP) and polyethylene (PE).

1.1Specifications for Gravel Envelopes

United States Army Corps of Engineers **USACE, 1941** used the first criteria that was proposed by Terzaghi for drain envelope which were:

$$D_{15\,filter} \geq 4D_{15\,soil} \tag{1}$$
$$D_{15\,filter} \leq 4D_{85\,soil} \tag{2}$$

where:

$D_{15\,filter}$ = size of particle in filter material, 15% passing sieve.
D_{15soil} = size of particle in soil, 15% passing sieve.
D_{85soil} = size of particle in soil, 85% passing sieve.

SCS, 1971 combined results of envelopes research with specifications to evaluate drainage and granular materials artificially classified for use as drain envelopes. **SCS, 1988** replaced these specifications to distinguish between envelope and filter. Recommendation for using the natural materials or about the mixing these materials that can be used as envelope are:

$D_{100\ filter} \leq 38\ mm$ (3)
$D_{30\ filter} \geq 250\ \mu m$ (4)
$D_{5\ filter} \geq 75\ \mu m$ (5)

where:

D_x = is size of particle in filter material, x is percent % passing sieve.

1.2 Specifications for Prewrapped Loose Material (PLM) Envelopes

In 1994, many scientists and engineers in Europe developed a classification system for the prewrapped loose material **(**PLM). **FAO, 2005** presented three categories of envelopes, depending on the opening size of pores and effectiveness (O_{90}) as follows:

PLM- extra fine $100\ \mu m \leq O_{90} \leq 300 \mu m$ (6)

PLM- fine $300\ \mu m \leq O_{90} \leq 600 \mu m$ (7)

PLM- standard $600\ \mu m \leq O_{90} \leq 1100 \mu m$ (8)

The following minimum thicknesses are required:

- Minimum thicknesses for Synthetic fibrous PLMs are equal to 3 mm as PP fibers.
- Minimum thicknesses for Synthetic granular PLMs are equal to 8 mm as polystyrene beads.
- Minimum thicknesses for Organic fibrous PLMs are equal to 4 mm as coconut fibers.
- Minimum thicknesses for Organic, granular PLMs are equal to 8 mm as wood chips and sawdust.

The following retention criteria for both geo-textiles and PLMs can be accepted:

$1 \leq O_{90}/D_{90\ soil} \leq 2.5$ for envelope thickness ≤1 mm (9)

$1 \leq O_{90}/D_{90\ soil} \leq 3.0$ when envelope thickness (1 to 3) mm. (10)

$1 \leq O_{90}/D_{90\ soil} \leq 4.0$ when envelope thickness (3 to5) mm. (11)

$1 \leq O_{90}/D_{90\ soil} \leq 5.0$ when envelope thickness ≥ 5 mm. (12)

$O_{90} \geq 200\ \mu m.$ (13)

In order to reduce the risk of mineral clogging, it is advisable that the ratio of $O_{90}/D_{90soil} \geq 1$; moreover, envelopes containing O_{90}/D_{90soil} ratios near the maximum limit of the proposed range of values are mostly preferred **FAO, 2005**.

1.3 Review of Literatures

Many researchers studied the effect of filter type on the behavior of flow pattern and on flow through drains. **Lennoz, 1989** studied the influence of envelopes on flow patterns close to a drain pipe and he designed a rectangular sand tank and installed a drain in the central. The aim of the study was to diagnosis the clogging hazard for different soil types, and to choose the most effectives envelope material. He found that all kinds of geo-textile tested were good for sandy soils, but in the case of using fine textured soil (silts and clay), the envelope material needs to have effective properties. He found that, for a sandy soil all envelope materials commercially available were suitable.

Sheard, et al., 1999 used geotextile materials as drain envelopes with three types of soil. The results showed that the clay soil formed a film over geotextile material and clogged the porous of envelope and reduced drainage efficiency. He found that a drain without an envelope, the clay particles were not trapped and needed to be flushed out during the next full flow period.

Agar, 2011 conducted a laboratory research using tub permeameter to compare three types of geotextile filters (woven and non-woven) with gravel and sand filter under the extraordinary hydraulic gradient regarding clogging and preventing siltation in laboratory condition. He used two types of soils (clay, silt loam). All geotextiles functioned better than sand-gravel envelopes in preventing the siltation and their clogging level, and did not affect hydraulic conductivity.

Lal, et al., **2012** studied the performance of geo-synthetic filter materials as a drain envelope in land reclamation in Haryana, north India. The study showed that geo-synthetic envelope materials with O90values >300 μm and woven filters with 60 mesh size could safely be used on lateral and collector drains, respectively, and for medium textured soils.

Nooreldeen, 2013 evaluated the efficiency of crushed gravel and graded gravel filter around field drain, by using sand tank model 70 cm wide, 50cm long and 80 cm deep. She used a pipe drain 5 cm diameter and two types of soils, loam, and sandy loam. The results of the study showed that the crushed gravel filter can work similar to a graded gravel filter after a certain time from the beginning of experiment. It was also found that the discharge and sediment for the case of graded gravel filter were very close to crushed gravel filter and sometimes gave the same results.

2. ENTRANCE RESISTANCE

Total resistance of seepage to subsurface drains consists of four components: horizontal, vertical, radial, and resistance to entry. The first two depend on the porous medium, while the last two depend on both soil and types of drain and envelope. Using the envelope around drainage pipe is to reduce the hydraulic gradient, and reduce the entrance resistance. Equipotential lines become circular and concentric to the drain pipe, which means that full flow through the drain is attained. So, the total head losses due to different resistances can be expressed by:

$$h_T = h_v + h_h + h_r + h_e \tag{14}$$

where:

h_v = head loss due to vertical flow (L),

h_h = head losses due to horizontal flow (L),

h_r = head loss due to radial flow (L), and

h_e = head loss due to resistance of entry (L).

The movement of water from the soil into drain passing through the filter around the pipe contributes to loss apart of the flow effort. These head losses can be measured by knowing the difference in the head of two piezometers, one inside pipe drain and the other in the soil at the edge of trench in which the pipe drain is placed. Several researches evaluated the performance of subsurface drainage materials depending on studying the entrance resistance. The total head losses were always preferred to be a value close to zero in order to facilitate the movement of water from the soil into the drain, and can be calculated as follows **ILRI, 1979**.

$$h_e = \alpha \frac{q}{K_F} \tag{15}$$

where:

α = Resistance coefficient (dimensionless),

[(0.4-0.6) for smooth pipe],[(0.5-1)for corrugated pipe],

q = drain discharge per unit length (L^3/L.T), and

K_F = hydraulic conductivity for envelope drain (L/T).

3. The LABORATORY WORK

A sand tank was manufactured by using acrylic material, with 60 cm wide, 50cm long and 80 cm deep according to advices of **Luithen, 1965**, **Luthin and Haig, 1971** and **Lennoz, 1989**. The experiments of our research were run included testing two types of filters, graded crushed gravel filter, and textile filter type (pp400) and using two types of soil. The numbers of executed tests were four and these are:

1. Graded crushed gravel with soil No.1 (sandy soil).
2. Textile filter with soil No.1 (sandy soil).
3. Graded crushed gravel with soil No.2 (loamy soil).

4. Textile filter with soil No.2 (loamy soil).

Three piezometers were installed around the outlet of drain, one of them (A) was inside the drain, and (B) was adjacent to the drain, and (C) was away in about 15cm from (B) as shown in **Figs. (1-5)**. In order to test working efficiency of the two types of filter and for a long time water was supplied during 10 days for 24 hours. During the continuous time of supplying water, the variation of piezometer for the piezometers A, B and C, were recorded and the discharge of drain was measured. The readings of piezometers A,B, and C were used to observe the variation of entrance resistance for the filter during time of test **Vlotman, 2000**. This work was repeated for the two filters using two types of soil. For all runs some sediment appeared at the beginning of test and disappeared at the end.

3. 1 Textile Filter

To evaluate the performance of a textile filter used in the laboratory, textile filter with the characteristics (ASTM D5261) shown in **Table 4** was used.

Note: since the drain is 5 cm diameter and textile filter of this size is not available, the textile material was weaved around pipe to surround the pipe drain and this was done, by taking textile material from the weaved pipe with 10 cm diameter as shown in **Fig. 12** and **Fig. 13**. The filter was checked by office of engineering constructions/ University of Technology. The date of test was 11-9- 2014.

4. RESULT AND DISCUSSION

4.1 Drain Discharge

The discharge of drain pipe is an important component of any design procedure for a drainage system. This parameter was used to compare between graded crushed gravel filter and textile filter by using two types of soil. The duration of the discharge measurement was 10 days and for both filters and for two types of soil. The results showed that in case. No.1 for sandy soil, the rate of discharge when using crushed gravel filter was approximately constant 3.5 l/min during four days and then decreased to 3.2 l/min and continued to decrease until becoming 2.8 l/min. In case No.2, the value of discharges when using textile filter and after two days of measurements, the discharge decreased from 3.5 l/min to 3.15 l/min and then fell to 2.4 l/min and settled on 2.4 l/min until the end of test. The results are for the two types of filter obtained using sandy soil. **Fig. 6** shows the trend of discharge variation for the two filters and it can be noticed, that the performance of the two filters decreased after four days and this was due to the filling of soil particle the void between crushed gravel particles. Also appeared in textile filter more affected compared with graded crushed gravel in sandy soil.

The other step of laboratory work was to use loamy soil with graded crushed gravel filter (case No.3). The results showed that the amount of out flow when using the graded crushed gravel filter was approximately constant for the first two days and then decreased from 1.2 l/min to 0.85 l/min and continued to decrease to 0.68 l/min and settled at this value. The amount of discharge for textile filter in case No.4 was less than the graded crushed gravel filter in case No.3, and the value of flow rate for textile filter was approximately constant for three days and decreased from 0.85 l/min to 0.4 l/min after some time, and almost settled on this value as shown in **Fig.7** and **Table.1.** But when comparing the performance of filters in the same soil indicates that the graded crushed gravel filter gave an amount of outflow more than when using textile filter and for two types of soil.

4.2Entrance Resistance

The results showed that this value of entrance resistance increases with time for the two types of filter. When comparing the results of entrance resistance for the two types of filter and during the same period of time 10 days, for the same type of soil, it can be found that the entrance resistance of textile filter is higher than that of the graded crushed gravel filters **Fig. 8**.

The entrance resistant in loamy soil, using the two types of filters was high, but the difference between them was small. The results showed that this type of soil had a major impact on the performance due to soil particles size which were small and which may move and settle between the voids of filters and decrease the permeability which means an increasing in the entrance resistance as shown in **Fig. 9** and **Table. 2**.

4.3 Sediment

The sediment is another parameter that can be used to evaluate the performance of a drain filter, because it affects the performance efficiency of drain due to the sedimentation of soil particles in the pipe. The amount of sediments in flow through graded crushed gravel was greater than with textile filter. In the case of using textile filter, the appearance of sediment decreased very strongly and disappeared after 6 hours from.

This appearance of sediment indicates that the two filters follow the same behavior about the carrying of sediments during the first five hours but after six hours, the sediment disappeared in the case of using textile filter (case No.2), but in the case of using graded crushed gravel filter (case No.1), the sediment continues to appear eleven hours as shown **Fig.10**

When using loamy soil, the amount of sediment for graded crushed gravel (case No.3) was higher than when using textile filter (case No.4) as shown in **Fig. 11**. While the amount of sediment when using textile filter was small and decreased with time and disappeared after 7 hours.

This means that the textile filter retained soil particles more than the crushed gravel filter because of the different size of pores for the filters. A high velocity and large discharge in the graded crushed gravel lead to the accumulation of a large amount of sediment which affects soil stability and increases soil erosion. **Table. 3** shows the measured values of sediments for each case.

5. CONCLUSIONS

1. The amount of drain discharge when using graded crushed gravel was greater than the amount of discharge when using textile filter for the same soil. But for the case of using sandy soil, the performance of the two filters gives approximately the same especially at the end of the run.

2. The entrance resistance for textile filter is greater than that of graded crushed gravel filter for all stages. And the entrance resistance for the two types of filters increased with time when using sandy soil would be less, so it is concluded that the emigration of fine particles into filter clogged the filter therefore the head loss of entry increased which increased entrance resistance.

3. The amount of sediment for graded crushed gravel when using the two types of soil was greater than that when using textile due to the characteristics of the opening size of textile filter which is equal to 400 (μm) which is very small as compared with crushed gravel filter.

REFERENCES

- Agar, A.I. ,2011, *Selection of Geo-synthetic Filter Materials as Drain envelopes in Clay and Silty loam soil to Prevent Entry of soil particle into Drain*, African Journal of Agricultural research., 6 (16):3930-3935.
- FAO ., 2005, *Material for Subsurface Land Drainage Systems,* Irrigation and Drainage paper No.60. perv .1. Food and Agriculture Organization of united Nation. Rome.
- ILRI., 1979, *Proceeding of The International Drainage Workshep*, International in situate for Land Reclamation and Improve, Wagening. No 25.
- Lennoz, C.H. ,1989, *Effected of Envelopes on Flow Pattern Near Drain Pipe*, Journal of Irrigation Drainage Engineering 115(4): 626-641.
- Lal, M., Arora[2],V.K and Gupt, S.K., 2012, *Preformance of Geo-synthetic Filter Material as Drain envelope in Land Reclamation in Havyana*, Journal of Agricultural Engineering 49(4).
- Luthin , N.J. ,1965, *Drainage Engineering*, Anand R. Kundaji for Willy Eastern Private Limited. New Delhi.
- Luthin , N.J. and Haig A. ,1972, *Some Factors Effecting Flow into Drain Pipes*, Hilgrodia, 41(10). Nooreldeen, D.M., 2013, *Evaluating The Efficiency of Crushed gravel filters around Field drain*, Department of Water Resource Engineering, Baghdad University, Iraq.
- SCS, 1971, *Drainage of Agricultural Land*, USDA National Engineering Hand book, Section16. USDA soil Conservation Service, Washington, Dc.
- Sherad,.R.W. , Agronomist, P.AG., Turfgrass, G.I.,1999, *Drain envelope to use or no use,*
- U.S. Army Crops of Engineers. ,1941, *Investigation of Filter Requirement for Under drain*, Manual EM1110-2-1901, seepage Control, Appendix D, U.S Army Crops of Engineers.
- Vlotman, W.F, Willardson, L.S and Dierick s, W, 2000, *Envelope Design for Subsurface Drains*, Puble.57. ILRI, Wageningen the Netherlands.

NOMENCLATURE

$D_{15Filter}$	= size of particle in filter material ,15 % passing sieve, L,
$D_{5Filter}$	= size of particle in filter material , 5 % passing sieve, L,
$D_{30Filter}$	= size of particle in filter material , 30% passing sieve, L,
$D_{100Filter}$	= size of particle in filter material , 100% passing sieve, L,
D_{15soil}	= size of particle in soil material ,15 % passing sieve, L,
D_{90soil}	= size of particle in soil material ,90 % passing sieve, L,
h_T	= total head losses due to different resistances, L,
h_v	= the head losses due to vertical flow, L,
h_h	= the head losses due to horizontal flow, L,
h_e	= entrance resistance, L,
K_F	= hydraulic conductivity of the envelope drain, L/T,
PLM	= prewrapped Loose Material,
O_{90}	= opening size pores for envelope, L,
Q	= discharge, L^3/T,
q	= drain discharge into unit length of drain per unit time, $L^3/L.\ T$, and,
α	= resistance coefficient.

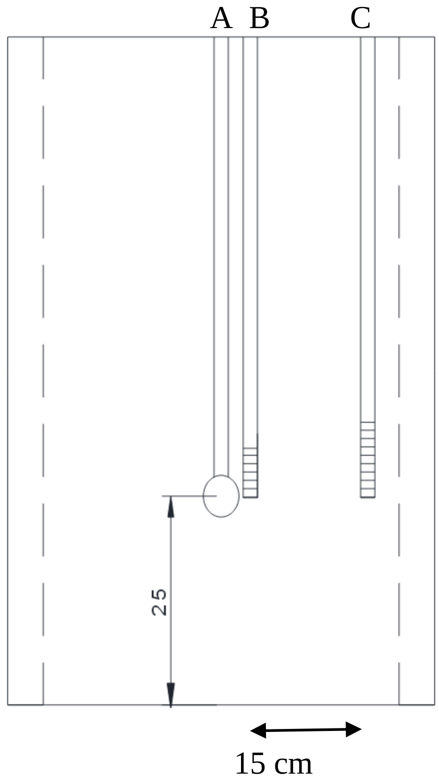

Figure. 1. The location of the piezometers to measure the entrance resistance.

Figure.2. Graded crushed gravel filter with sandy soil, case No.1.

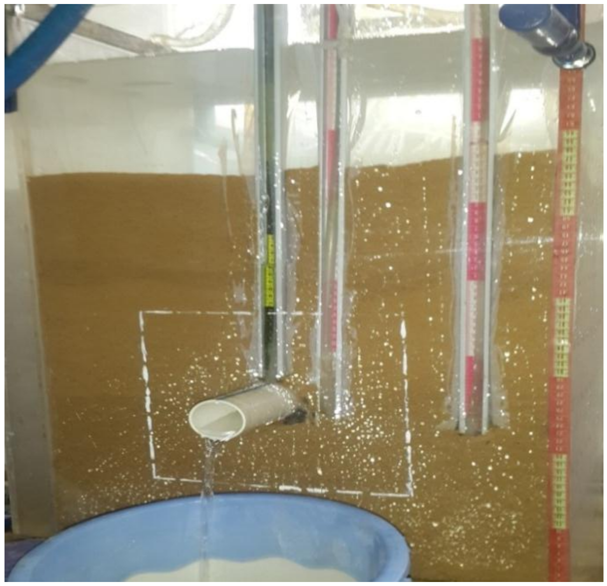

Figure. 3. Textile filter with sandy soil, caseNo.2.

Figure.4. Graded crushed gravel with loamy soil, caseNo.3.

Figure.5. Textile filter with loamy soil, caseNo.4.

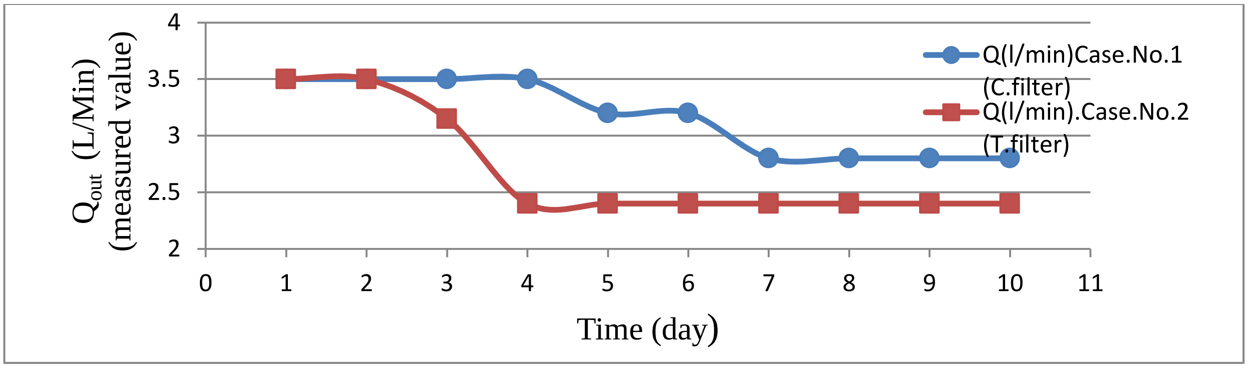

Figure.6. The variation of discharge flow during test time for the two filter using sandy soil

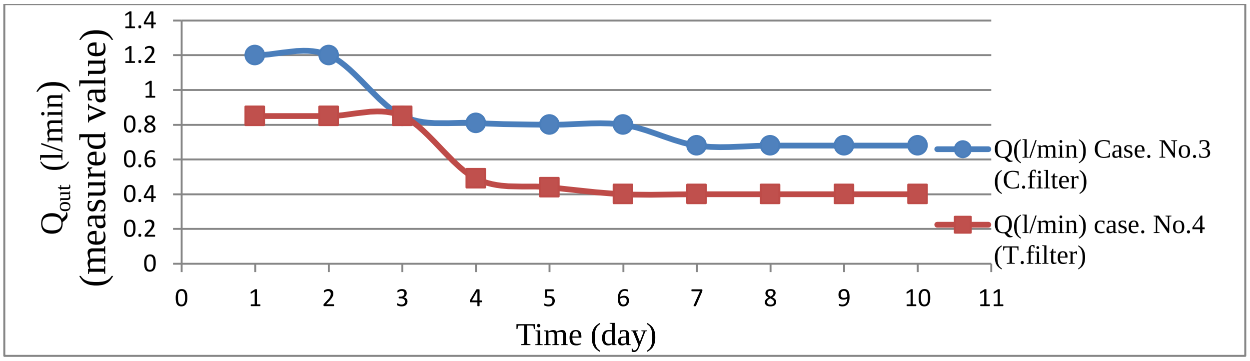

Figure. 7. The variation of discharge flow during test time for the two filters using loamy soil.

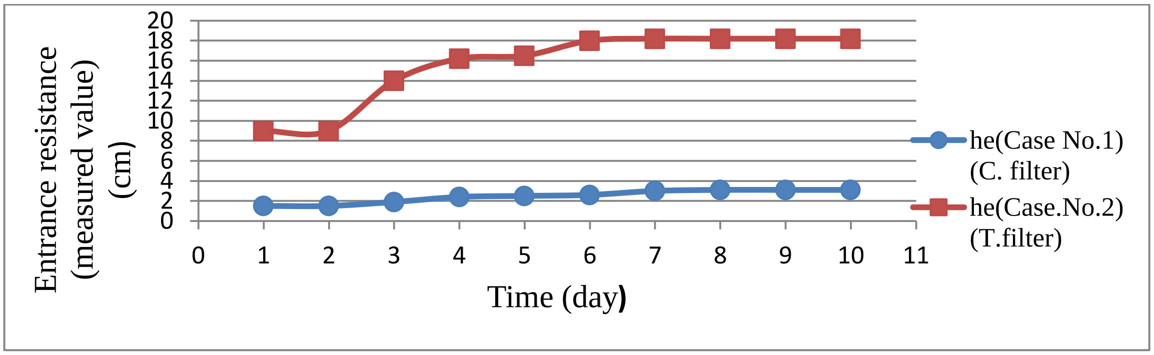

Figure. 8. The variation of entrance resistance with time for two filters, using a sandy soil.

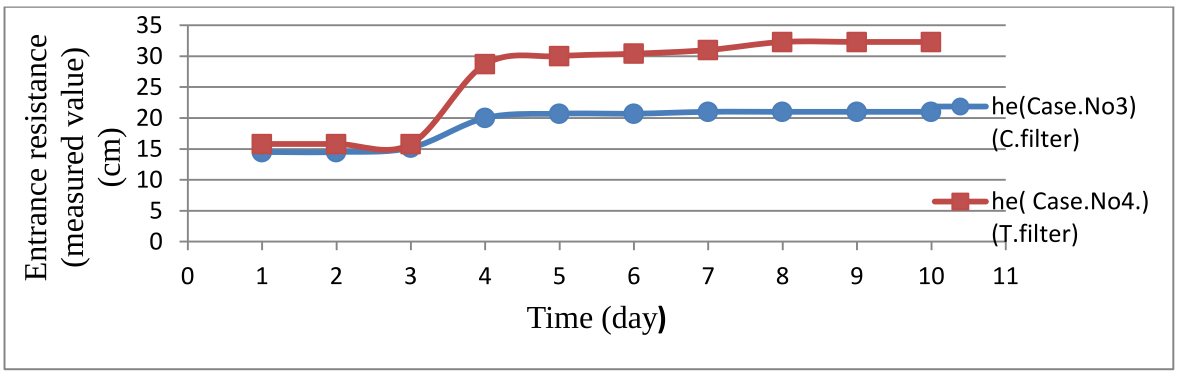

Figure. 9. The variation of entrance of resistance with time for the two filters type when using a loamy soil.

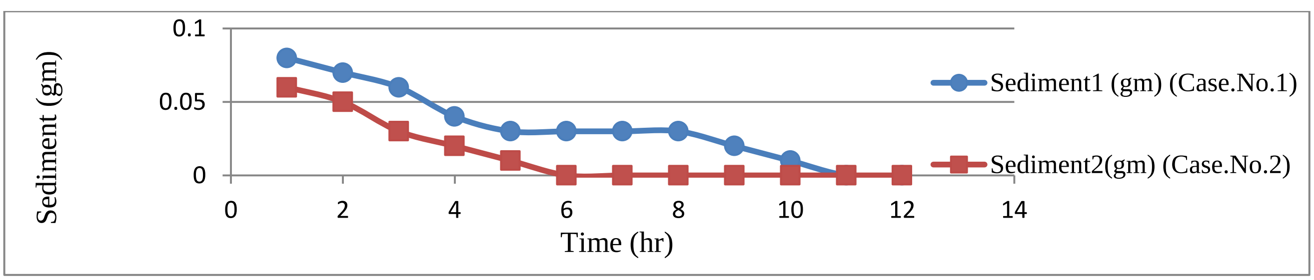

Figure.10. Comparison between the amounts of sediment when using graded crashed gravel, (Case No.1) and textile filter with a sandy soil (Case No.2).

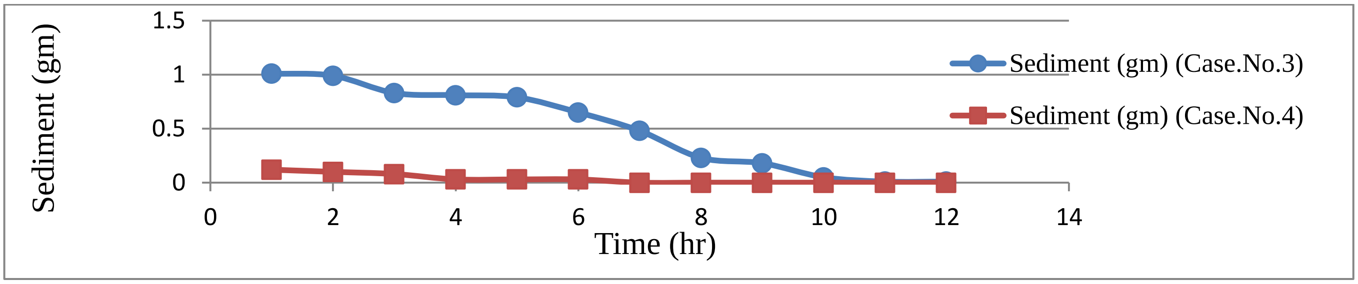

Figure. 11. Comparison between the amounts of sediment when using graded crashed gravel, (Case No.3) and textile filter with a loamy soil (Case No.4).

Figure 12. Pipe drain (5cm) with weaved textile

Figure 13. Laying the drain pipe in the sand tank

.

Table. 1. Measured of values of outflow discharge for each case.

Time (day)	Case.No.1 (C. filter) Q(l/min)	Case.No.2 (T. filter) Q(l/min).	Case. No.3 (C. filter) Q(l/min)	Case. No.4 (T. filter) Q(l/min)
1	3.5	3.5	1.2	0.85
2	3.5	3.5	1.2	0.85
3	3.5	3.15	0.85	0.85
4	3.5	2.4	0.81	0.49
5	3.2	2.4	0.8	0.44
6	3.2	2.4	0.8	0.4
7	2.8	2.4	0.68	0.4
8	2.8	2.4	0.68	0.4
9	2.8	2.4	0.68	0.4
10	2.8	2.4	0.68	0.4

Table. 2. Measured values of entrance resistance for each case.

Time (day)	he (cm) (Case No.1)	he (cm) (Case.No.2))	he (cm) (Case.No.3)	he (cm) (Case.No4)
1	1.5	9	14.5	15.8
2	1.5	9	14.5	15.8
3	1.9	14	15.2	15.8
4	2.4	16.2	20	28.7
5	2.5	16.5	20.7	30
6	2.6	18	20.7	30.4
7	3	18.2	21	31
8	3.1	18.2	21	32.3
9	3.1	18.2	21	32.3
10	3.1	18.2	21	32.3

Table. 3. Measured values of sediment for all cases.

Time (hr)	Sediment (gm) (case.No.1)	Sediment (gm) (Case.No.2)	sediment (gm) (case.No.3)	sediment (gm) (case.No.4)
1	0.08	0.06	1.01	0.12
2	0.07	0.05	0.99	0.1
3	0.06	0.03	0.83	0.08
4	0.04	0.02	0.81	0.03
5	0.03	0.01	0.79	0.03
6	0.03	0	0.65	0.03
7	0.03	0	0.48	0
8	0.03	0	0.23	0
9	0.02	0	0.18	0
10	0.01	0	0.05	0
11	0	0	0.01	0
12	0	0	0.01	0

Table.4. Textile filter characteristics

Filter material	It consist polypropylene fibers pp400
O_{90} - range	400 µu
Filter transmittance	The filter curb 90% of the particles that bigger than 400µu.
Description	The drain pipe was wrapped 5.8 mm thickness of polypropylene fiber.
Specific weight	425 g/m^2
The histological examination filter to meet international standards ASTMF800 and specification results ASTM D 5261	

Two – Dimensional Mathematical Model to Study Erosion Problem of Tigris River Banks at Nu'maniyah

Dr. Hayder AbdulAmeer. K. AL-Thamiry
Assistant Profess
College of Engineering – University of Baghdad
email:dr_hydr@yahoo.com

Taymaa Maziad AbdulAzeez
Instructor
College of Engineering –
email:t_maziad@yahoo.com

ABSTRACT

The high and low water levels in Tigris River threaten the banks of the river. The study area is located on the main stream of Tigris River at Nu'maniyah City and the length of the considered reach is 5.4 *km*, especially the region from 400 *m* upstream Nu'maniyah Bridge and downstream of the bridge up to 1250 *m* which increased the risk of the problem that it heading towards the street and causing danger to nearby areas.

The aim of this research is to identify the reason of slope collapse and find proper treatments for erosion problem in the river banks with the least cost. The modeling approach consisted of several steps, the first of which is by using "mini" JET (Jet Erosion Test) device provides a simple method of measuring scour depth with the time for the riverbank and finding values of critical shear stress and erodibility factor for ten soil samples taken from right bank and bottom of Tigris River; the second of which involved setting up a static BSTEM software for two models (with and without treatment), then calculating the erosion amounts and factor of safety for the ten soil samples; the third approach involved implementing a two dimensional RMA2 to simulate four scenarios to find the velocity, water depth, and water surface elevation distributions for two models (with and without treatment). Therefore, observed erosion in other discharges in natural case near the right bank [especially at cross section that are located in Tigris River at Nu'maniyah City from 500 *m* upstream Nu'maniyah Bridge and cross section that are located from 1800 *m* downstream Nu'maniyah Bridge] is high because of high erodibility coefficient in those cross sections that causes high erosion. Also, failure occurs in natural case of Tigris River at Nu'maniyah City because of erosion near the right bank and does not occur because of slope stability failure for right bank where the range of the velocities near the right bank for the study area for most discharges is between 0.67 and 0.91 *m/s*. In addition to experimental work using "mini" JET device shows high erodibility coefficient in those cross sections and (2+900) which confirms that this device is very good indicator for the possibility of bank scour. The velocities upstream of the island and near the right bank in the study area are between 0.64 and 1.47 *m/s*, while downstream of the island is between 0.64 and 1.04 *m/s.* In addition to soil of Tigris River right bank at Nu'maniyah is silty soil, the scour velocity is higher than 0.5 *m/s*, therefore the right bank is safe against scour only when the discharges of Tigris River are less than 500 m^3/s. Thus, vegetation is unsafe treatment on right bank of Tigris River at Nu'maniyah City. The velocity causes removal of plants since treatment for river bank is 0.61 *m/s* where velocities near bank at most discharges are higher than this limit. Thus, treatment by riprap is the proper choice on the right bank of Tigris River at Nu'maniyah City because its cost with maintenance is 2 billion IQD less than gabion treatment in addition to velocity reduction

ratio along the right bank by riprap ranges from 15% to 85%, while velocity reduction ratio along the right bank by gabion ranges from 8% to 25%, respectively.
Key words: erosion, cost, SMS, riprap, gabion, vegetation.

النموذج الهيدروليكي لدراسة مشكلة النحر والمعالجات اللازمة في ضفاف نهر دجلة عند النعمانية

الخلاصة

ان مستويات المياه العالية والمنخفضة في نهر دجلة تهدد ضفاف النهر من خلال ظهور تشققات كبيرة وانهيارات في ضفاف النهر الناجمة عن تدفقات المياه المضطربة.

تقع منطقة الدراسة على نهر دجلة في مدينة النعمانية بطول 5.4 كم، خصوصا في المنطقة الممتدة من 400 متر مقدم جسر النعمانية وحتى مؤخره لمسافة تصل الى 1250 متر، ومما يزيد من خطر المشكلة أن التآكل يتجه نحو الشارع ويسبب خطرا على المناطق القريبة منها بالإضافة إلى تراكم الترسبات في النهر و على الضفة اليسرى منه وزيادة السرع في الجانب الآخر.

ان الهدف من هذا البحث هو لتحديد سبب انهيار الجوانب، والتوصل الى أفضل السبل لمعالجة مشكلة تآكل ضفة النهر بأقل كلفة . ممكنة. تم استخدام نموذج رياضي هيدروليكي لدراسة تآكل الضفاف ومقارنة سبل المعالجة المتاحة التي تلبي المتطلبات الهيدروليكية وبأقل كلفة ممكنة.

يتضمن البحث عدة خطوات، أولها استخدام جهاز الميني جت الذي يوفر طريقة بسيطة لقياس عمق التآكل مع الزمن لضفة النهر وايجاد قيمة اجهاد القص الحرج ومعامل التعرية لعشر عينات من التربة، والثانية اعداد نموذجين (احدهما بدون استخدام معالجة والآخر باستخدام نوعين من المعالجة وهما تكسية حجرية وغطاء نباتي) باستخدام برنامج استقرارية الضفة وتآكل بداية النهر وحساب كميات التآكل ومعامل الامان للعينات العشرة، والثالثة اعداد نموذجين (احدهما بدون استخدام معالجة والآخر باستخدام ثلاثة أنواع من المعالجة وهي تكسية حجرية وقفة صخرية وغطاء نباتي) باستخدام برنامج نمذجة المياه السطحية الثنائي البعد وحساب سرعة وعمق ومنسوب الماء متمثلة بأربعة سيناريوهات، ولهذا لوحظ حدوث تآكل في تصريفات اخرى في الحالة الطبيعية بالقرب من الضفة اليمنى وخصوصا في المقطعين العرضيين (2 + 600) و (4 + 000) بنسبة عالية بسبب معامل التعرية العالي في هذين المقطعين. كما يحدث الفشل في الحالة الطبيعية لنهر دجلة في مدينة النعمانية وخصوصا في المقاطع العرضية (2 + 600) و (4 + 000) بسبب تآكل بالقرب من الضفة اليمنى ولا تحدث بسبب فشل ثبات الميول للضفة اليمنى حيث أن قيم السرع بالقرب من الضفة اليمنى لمنطقة الدراسة بالنسبة لمعظم التصاريف ما بين0.67 و0.91 م / ثا.

اضافة الى أن العمل المختبري باستخدام جهاز الميني جت أظهر ارتفاع معامل التعرية للمقاطع العرضية (2+600)، (2+900) و(4+000) مما يؤكد احتمالية تآكل ضفة النهر حيث أن السرعة في مقدم الجزرة وبالقرب من الضفة اليمنى لمنطقة الدراسة تتراوح ما بين 0,64 و1,47 م / ثا، في حين تتراوح السرعة في مؤخر الجزرة ما بين 0,64 و1,04 م / ثا، بالاضافة الى أن التربة للضفة اليمنى لنهر دجلة في النعمانية هي تربة غرينية، وسرعة التآكل فيها أعلى من 0.5 م / ثا، وبالتالي فإن الضفة اليمنى سوف تكون آمنة ضد التآكلات فقط عندما يكون تصريف نهر دجلة أقل من 500 م^3 / ثا.

ان الغطاء النباتي هو من سبل المعالجة غير الآمنة على الضفة اليمنى من نهر دجلة في مدينة النعمانية حيث ان سرعة إزالة النباتات تبلغ 0.61 م / ثا بينما كانت نتائج السرع بالقرب من ضفة النهر اليمنى في معظم التصاريف هي أعلى من هذا الحد. ان علاج ضفة النهر اليمنى باستخدام التكسية الحجرية هو الخيار الافضل في مدينة النعمانية لأنه أقل كلفة بحوالي 2 مليار دينار من العلاج بواسطة القفة الصخرية بالإضافة إلى أن معدل نسبة تخفيض السرع على طول الضفة اليمنى باستخدام التكسية الحجرية يتراوح بين 15٪ الى 85 ٪، في حين أن معدل نسبة تخفيض السرع على طول الضفة اليمنى باستخدام الكابيون يتراوح بين 8 ٪ الى 25 ٪ على التوالي.

الكلمات الرئيسية: التآكل، الكلفة، نظام نمذجة المياه السطحية، التكسية الحجرية، القفة الصخرية، الغطاء النباتي.

1. INTRODUCTION

1.1 General

Erosion threatens riverbank, particularly those located in cities such as roads, residential buildings, and other facilities. During the last twenty years growing islands have become noticeable features in Tigris River within Iraq, the number of islands is increasing with time. In addition to the impact of human activities in dam building, bank lining, and dumping of debris within the channel has led to change in the geometry of the river and its ability to carry flood waters.

The stability of a bank primarily depends on channel and flow characteristics, and the strength of the bank materials and instability can be inherent in some channel systems as a result of the nature of the river system such as high energy braided rivers and historic or geomorphic factors such as tectonic uplift. Patterns of erosion and deposition are influenced by many factors, including: storm frequency, flow properties, bank material composition, bank geometry, bank moisture conditions, channel geometry, the local topography, vegetation and man-induced factors.

The study area is located on the main stream of Tigris River at Nu'maniyah City and the length of the considered reach is 5.4 *km*, see **Fig. 1**.

2. OBJECTIVES

The main objective of the present study is to investigate the flow process that causes scour in the river bank and the recent treatments that can be used in Iraqi rivers.

Tigris River was considered as a case study with the use of the adopted suitable bank treatments of least cost.

3. LITERATURE REVIEW

Khalaf ,1999. presented numerical models, (hydrodynamic and morphological) to predict Tigris river behavior under certain conditions. The first model was a two dimensional depth-averaged hydrodynamic model. Based on the conservation of mass and momentum equations to compute the velocity field and water depths. This model was verified by applying it to an idealized channel, a channel 10 *m* long, and a channel with 180◦ bend. The application gave good agreement between computed and analytical or published data.

Ibraheem ,2011. analyzed four cases of flow conditions for the circumferential open canal in the University of Baghdad Campus in Al-Jaderiya by using RMA2 model. The first case represented the current flow conditions; other cases represented modification of the flow within the canal. The researcher found that under the initial flow conditions, the velocities were very low along the canal. By increasing the supplied discharge the flow conditions within the canal were enchased. In the case of increasing the supplied discharge to the maximum capacity of the supply pipe, the flow along the canal was the best compared with other smaller discharges.

Holttschlag and **Koschik ,2002.** developed a two-dimensional hydrodynamic model of St. Clair–Detroit River Waterway in the Great Lakes Basin by using the generalized finite-element code RMA2 to compute flow velocities and water levels as part of a source-water assessment of public water intakes. Seven steady-state scenarios were used to calibrate the model. The researchers found an agreement between simulated and expected flows in major channels and water levels at gaging stations.

Mclean, et al, 2003. used a two – dimensional numerical model to study clear-water scour at a bridge contraction with a cohesive bed. They used flow data, variable or constant, to calculate scour and update the bed of the model. The model output (velocity, depth, and water surface), and SMS data calculator were used to calculate time –dependent scour based on the erosion function at each coordinate in the model. An ultimate scour depth, the unit flow rate, and other model parameters at a particular time step can also be calculated. Finally, their study covered the methodology and results for calculating time – dependent as well as ultimate scour using a two – dimensional finite element computer model.

Hanson and **Hunt ,2007.** used two types of soil (silty sand and lean clay) in laboratory experiments laboratory JET. The soils were air dried, sieved by using sieve #4, and then thoroughly mixed with water to achieve the desired water content. The soils were stored for a minimum of 48 hours to allow time for the soil particles to hydrate.

The soil was compacted in the standard mold with a manual rammer, then placed and compacted in the mold in three layers.

Once a test is started, scour readings were taken with a point gage. The point gage is aligned with the jet nozzle so that the point gage can pass through the nozzle to the bed to read the depth of scour. The point gage diameter is nominally equivalent to the nozzle diameter so that when the point gage rod passes through the nozzle opening, flow is effectively shut off. A deflection plate is attached to the jet tube and was used to deflect the jet, protecting the soil surface, during initial filling of the submergence tank.

They observed from the above plots of scour depth versus time that the water content had a significant effect from the driest sample to middle range water content, but it showed less effect from the middle range water content to the wettest sample for each soil and erodibility factor varies over several orders of magnitude depending on soil texture and plasticity, compaction effort, and water content.

4. CAUSES OF BANK FAILURE

Garanaik and Sholtes, 2013 stated that bank erosion is a natural process in stable rivers; however, it can become accelerated and exacerbated by direct and indirect human impacts.

Also erosion leads to failure of riverbanks by factors such as, **Talukdar, 2012**:

1. Rapid drops in water after flood.
2. Banks saturation.
3. Deflection and accelerated flow around infrastructure, barriers, and plants in the river.
4. Removal or disturbance of vegetation from riverbank because of trees that fall from bank.
5. Rainfall interval.
6. Direct erosion of the riverbank such as Livestock trampling and removal of riparian vegetation.
7. Indirect erosion of the riverbank such as channel incision, thus widening from hydrologic alteration in watershed.
8. Sloughing of saturated bank caused by rapid drawdown.
9. Liquefaction of saturated silty and sandy bank material.
10. Erosion due to seepage from banks at low river discharge.
11. Scour along waterline due to wind or wave wash of passing vessels.

5. PROCESSES OF RIVERBANK EROSION

Bank Erosion includes three main groups of processes:

1. Hydraulic instability caused by scour at the toe of a marginally stable bank, debris and vegetation, removal of bank vegetation, secondary current etc., **Islam, 2008**.

2. Gravitational mass failure processes detach sediment primarily from cohesive banks and make it available for fluvial transport, **Talukdar, 2012**.
3. Geo-technical instability caused by detachment of more coarse-grained layers in any given alluvial bank, by water flowing out of the bank face, termed as "piping" or "sapping",**Hagerty and Hamel, 1989**.

6. TIGRIS RIVER CHARACTERISTICS AT NU'MANIYAH CITY

The topographic survey department at the Center of Studies and Engineering Designs in Ministry of Water Resources (MoWR) during November 2013 snapped levels of Tigris River in Nu'maniyah Region for 5.4 *km* according to the needs of the mathematical models, including fifty-four cross-sections were measured along Nu'maniyah Reach.

The hydrological data of Tigris River during flood of 1988 in the study area were supplied by the National Center of Water Resources, MoWR, as listed in **Table. 1**.

The value of river roughness coefficients is 0.03, **Abdul-Sahib, 2014**, and bank protection such as (gabion, riprap, and vegetation) are listed in **Table. 2**.

The adopted hydraulic data include a gradient value of 7 *cm/km* for high discharges and 5 *cm/km* for low discharges, **Geohydraulique, 1977**.

Abdul-Sahib, 2014 computed the rating curve for 900 *m* upstream of Nu'maniyah gaging station where the river cross section is more suitable as a gaging station, see **Fig. 2**.

7. FIELD WORK

In order to measure the erosion rate at the river bank, ten soil samples were taken from right bank and toe of Tigris River during the period from 27 to 30 April 2015. Locations of the soil samples are listed in **Table 3**.

7.1 Laboratory Work and Equipment

Al-Madhhachi, 2013 manufactured "mini" JET device to measure scour depths with time for the riverbank. This device was used to find the values of critical shear stress (τ_c, Pa) and erodibility factor ($k_d, cm^3/Ns$) for ten samples, **Table 4**.

8. STATIC BSTEM SOFTWARE

BSTEM is one of the models used for bank stability that was developed by the National Sedimentation Laboratory in Oxford, Mississippi. BSTEM is used to design river channels and exists as a simple spreadsheet tool in Microsoft Excel software.

The main objective of the BSTEM software is to compute erosion rate, factor of safety, and slope stability of the bank, **Fig.3**.

The necessary data of these mathematical calculations were divided into the following groups: Bank Geometry, Flow Conditions, Bank Material, Toe Model Output, Bank Model Output, and Bank Vegetation and Protection.

9. APPLICATION OF RMA2 MODEL

RMA2 has a wide range of applications in many types of engineering problems that need to simulate it with numerical modeling and from these applications, **Militello,** and **Zundal, 1999**:

1. Calculation of the water levels and flow patterns in rivers.
2. Calculation of water levels and flow distribution around islands.
3. Investigation of the circulation and transport in water bodies with wetlands.

4. Calculation of the flow at bridges having one or more relief openings and in contracting and expanding reaches.
5. Calculation of the flow inside and outside canal hydropower plants, at rive junctions.

9.1 Governing Equations

The program computes flow depth and velocity in two dimensions by solving the depth-averaged Reynolds equations. These equations are derived from Navier-Stokes equations (1) and (2) by integrating them over depth and including a number of modifications to account for turbulent flow, external tractive forces of Coriolis effects, boundary friction, and wind stress at the free surface. The received second order partial differential equations are described in the two horizontal directions x and y by **King, 2005**. Force momentum Eq. (1) and Eq. (2).

In this project, the Coriolis effects and wind stress at the free surfaces are neglected. Equations (1) to (3) are solved for each element in the mesh by using the Galerkin finite element method of weighted residuals. The local equations are then collected in a global matrix which is solved by using Gaussian integration. Derivates in time are substituted by a nonlinear finite differentiation approximation and variables are assumed to vary over each time step as Eq. (4) below, **King, 2005**:

$$h\frac{\partial u}{\partial t}+hu\frac{\partial u}{\partial x}+hv\frac{\partial u}{\partial y}-\frac{h}{\rho}\left[E_{xx}\frac{\partial^2 u}{\partial x^2}+E_{xy}\frac{\partial^2 u}{\partial y^2}\right]+gh\left[\frac{\partial \alpha}{\partial x}+\frac{\partial h}{\partial x}\right]+\frac{gun^2}{\left(1.486h^{\frac{1}{6}}\right)^2}(u^2+v^2)^{\frac{1}{2}}=0 \quad (1)$$

$$h\frac{\partial v}{\partial t}+hu\frac{\partial v}{\partial x}+hv\frac{\partial v}{\partial y}-\frac{h}{\rho}\left[E_{yx}\frac{\partial^2 v}{\partial x^2}+E_{yy}\frac{\partial^2 v}{\partial y^2}\right]+gh\left[\frac{\partial \alpha}{\partial y}+\frac{\partial h}{\partial y}\right]+\frac{gvn^2}{\left(1.486h^{\frac{1}{6}}\right)^2}(u^2+v^2)^{\frac{1}{2}}=0 \quad (2)$$

Continuity Eq. (3)

$$\frac{\partial h}{\partial t}+h\left(\frac{\partial u}{\partial x}+\frac{\partial v}{\partial y}\right)+u\frac{\partial h}{\partial x}+v\frac{\partial h}{\partial y}=0 \quad (3)$$

$$f(t)=f(t)_0+at+bt^c \qquad t_o\le t<t_o+\Delta t \quad (4)$$

The solution received is implicit and the set of equations are solved by the Newton-Raphson nonlinear iteration scheme, **King, 2005**.

9.2 Boundary Conditions

There are conditions that apply along the flow boundaries and are required to find the constants of integration that arise when the governing equations are integrated numerically to solve for u, v, and h in the interior of the solution domain.

The input parameters in this model include the upstream boundary conditions (discharge (Q) = 500, 1000, 1500, 2000, 3000 m^3/s) and the downstream boundary condition (water surface elevation at Nu'maniyah Region (W.L.) =17, 18.5, 20, 21.34, and 22.43 *m a.m.s.l.*,).

9.3 Friction Coefficient and Eddy Viscosity

The model allows assigning roughness by two methods as follows, **Abdul-Ridha, 2015**:

1. Global assignment: assignment can be made by element level or by material type.
2. Roughness by depth: The method accounts for the vegetation structural properties and flow depth.

Eddy viscosity parameters are used to control the numerical stabilization and describe energy losses related to viscosity and turbulence. A value for eddy viscosity must be assigned as well to allow the model to solve the equations. As a guideline for selecting reasonable values for the turbulent exchange coefficients for a given material is listed in **Table 5** which includes some representative ranges of eddy viscosity.

9.4 Mesh Generations

The finite element mesh was generated by using the SMS software package for the case study of AL- Nu'maniyah region. All regions in the domain were represented by two-dimensional, depth-averaged elements. The mesh was built by using an adaptive tessellation technique for triangular elements and a patch technique for rectangular ones. The finite element mesh was generated to represent the natural case as shown in **Fig. 4**, the bank protection case as shown in **Fig. 5**. **Table 6** represents the number of nodes and elements in each implemented case.

9.5 Topography

Bathymetry data for the study site was collected in the form of x, y, and z coordinates, **Center of Studies and Engineering Designs/ Ministry of Water Resources, 2013**. In order to create a numerical model, information about the topography in the study area is needed. From this survey, around 1855 scattered points were received with x-, y- and z-coordinates. For the pre-construction situation, these points were simply converted into contour lines by using the scatter module within SMS as shown in **Fig. 6**.

9.6 Input Parameters and Boundary Conditions

In order to receive reliable results from the RMA2 computations, input parameter values have to be properly assigned. The input parameters in this model include the upstream boundary conditions (discharge (Q) = 500, 1000, 1500, 2000, and 3000 m^3/s) and the downstream boundary condition (water surface elevation at Nu'maniyah Region (W.L.) =17, 18.5, 20, 21.34, and 22.43 *m.a.m.s.l.,*), the Manning's roughness coefficient (n), and the eddy viscosity (E).

These parameters and the assigned values for the simulations are listed in **Table 2**. The roughness coefficient values were chosen to be (0.03) for channel in the areas free of reeds, (0.04) for riprap, (0.027) for gabion, and (0.02) for vegetation while it was taken (0.1) in the dense reeds areas and partitioned area, **Drainage Design Manual for Maricopa County, 2013,** and **Chow, 1959**. Distribution of n in several regions according to their properties is shown in **Figs. 7** to **10**.

10. SMS MODELING

10.1 First Scenario: natural case, see Table 7.

In Scenario (1-A), the results of the velocity distribution using RMA-2 software at discharge of 500 m^3/s are presented in **Fig.11**. The range of the velocities upstream of the island in the study area is between 0.64 and 1.47 *m/s*, the velocity in the island is zero, and the range of the velocities downstream of the island is between 0.64 and 1.04 *m/s*. The maximum velocity is about 0.64 *m/s* at cross section (3+300).

In Scenario (1-B), the results of the velocity distribution at discharge of 1000 m^3/s are presented in **Fig. 11**. The range of the velocities near the right bank in the study area is between 0.60 and 0.88 *m/s*. The maximum velocity of 0.98 *m/s* occurs near cross section (3+200), and the range of the velocities at the island is between 0.77 and 0.97 *m/s*.

For Scenario (1-C), the results of the velocity distribution at discharge of 1500 m^3/s are presented in **Fig. 11**. The range of the velocities near the right bank in the study area is between 0.55 and 0.98 *m/s* and the range of the velocities in the island is between 0.92 and 1.03 *m/s*.

Fig.11 shows the velocity distribution results for a discharge of 2000 m^3/s for Scenario (1-D). It is obvious that the water depth near the right bank is between 3.25 and 4.68 *m*. The maximum velocity of 0.78 *m/s* occurs near cross section (4+000). Also the velocities ranged between 0.67 and 0.91 *m/s* near the right bank and they are between 0.82 and 0.94 *m/s* in the island.

The velocity distribution results at discharge of 3000 m^3/s for Scenario (1-E) varied between 1.13 and 1.20 *m/s* upstream the islands; the velocity in the downstream in the same section varied between 0.96 and 1.04 *m/s*; velocity near the right bank ranged between 0.96 and 1.20 *m/s*. The maximum velocity of 1.22 *m/s* occurred near cross section (4+000). The variation of velocity throughout the whole reach is shown in **Fig. 11**.

Accordingly, since the soil of the right bank is silty soil, the scour velocity is higher than 0.5 *m/s*, **Bundaberg Regional Council, 2013**; therefore when the discharge is not greater than 500 m^3/s the right bank is safe against scour. In other words, all cross sections need treatment except that previously treated by the Client.

10.2 Second Scenario: Treated right bank of Tigris River at Nu'maniyah City by riprap, see **table 7**.

Fig. 12 presents least velocity near the right bank over the area at a discharge of 500 m^3/s in Scenario (2-A). The velocity at island upstream the study area varied between 0.20 and 0.28 *m/s*, the velocity is zero in the island, the velocity downstream the island is between 0.01 and 0.1 *m/s*, and the velocity near the right bank is between 0.1 and 0.2 *m/s*. **Fig. 12** presents the velocity distribution over the area at a discharge of 1000 m^3/s in Scenario (2-B). The velocity at island upstream the study area varied between 0.98 and 1.31 *m/s*, the range of the velocities in the island is between 0.66 and 1.31 *m/s*, velocity downstream island is between 0.23 and 0.86 *m/s*, and the velocity near the right bank is in the range of 0.23 to 0.98 *m/s*. Also **Fig. 12** shows the velocity distribution over the area at a discharge of 1500 m^3/s in Scenario (2-C). The velocity at island upstream the study area varied between 0.75 and 0.93 *m/s*, the range of the velocities in the island is between 0.85 and 0.92 *m/s*, velocity downstream island is between 0.55 and 0.74 *m/s*, and the velocity near the right bank is between 0.55 and 0.93 *m/s*. Scenario (2-D) is almost like the results at a discharge of 2000 m^3/s in Scenario (2-C).

The velocity distribution results at a discharge of 3000 m^3/s for scenario (2-E) varied between (0.93-1.11) *m/s* upstream of the island; the velocity downstream in the same section varied between (0.58-0.86) *m/s*; velocity near the right bank ranged from

0.58 to 1.11 *m/s*. The maximum velocity is about 1.21 *m/s* occurs near cross section (4+000). The variation of velocity throughout the whole reach is shown in **Fig. 12**.

10.3 Third Scenario: Treated right bank of Tigris River at Nu'maniyah City by gabion, see **Table 7**.

Fig. 13 shows the velocity distribution over the area at a discharge of 500 m^3/s in Scenario (3-A). The velocity at the island upstream the study area varied between (0.66-0.98) *m/s*, the velocity is zero in the island, the velocity downstream the island is between (0.43-0.52) *m/s*, and the velocity near the right bank is between 0.43 to 0.98 *m/s*.

For Scenario (3-B), the velocity distribution at a discharge of 1000 m^3/s is shown in **Fig. 13**, the velocities ranged between 0.63 to 0.98 *m/s* at island's upstream, velocity downstream the island is between 0.22 to 0.78 *m/s* and the velocity near the right bank is between 0.22 to 0.63 *m/s* were a velocity of 0.60 occurs near cross section (4+000) and a velocity of 1.04 occurs near cross section (2+600).

Fig. 13 shows the velocity distribution over the area at a discharge of 1500 m^3/s in scenario (3-C). The velocity at island upstream the study area varied between 0.64 to 0.93 *m/s*, the range of the velocities in the island is between 0.64 to 0.80 *m/s*, the velocity downstream the island is between 0.54 to 0.80 *m/s*, and the velocity near the right bank is between 0.54 to 0.93 *m/s*. A discharge of 2000 m^3/s in Scenario (3-D) gives the same results as above.

The velocity distribution at a discharge of 3000 m^3/s for Scenario (3-E) varied between 0.91 to 1.11 *m/s* upstream of the island; the velocity downstream in the same section is varied between 0.58 to 0.92 *m/s*; velocity near the right bank ranges from 0.58 to 1.11 *m/s*. The maximum velocity is about 1.10 *m/s* occurs near cross section (4+000). The variation of velocity throughout the whole reach is shown in **Fig. 13**.

10.4 Fourth Scenario: Treated right bank of Tigris River at Nu'maniyah City by vegetation, see **table 7**.

Fig. 14 shows the velocity distribution over the area at discharge of 500 m^3/s in Scenario (4-A). Velocity upstream the island varied between 0.75 to 0.96 *m/s*, velocity is zero in the island, velocity downstream the island is between 0.43 to 0.47 *m/s*, and velocity near the right bank is between 0.43 to 0.96 *m/s*.

Fig. 14 shows the velocity distribution over the area at discharge of 1000 m^3/s in Scenario (4-B). Velocity upstream the island varied between 0.92 to 1.05 *m/s*, velocity downstream the island is between 0.22 to 0.92 *m/s*, and velocity near the right bank is between 0.22 to 1.05 *m/s*.

Fig. 14 shows the velocity distribution over the area at a discharge of 1500 m^3/s in Scenario (4-C). Velocity upstream the island varied between 0.89 to 0.92 *m/s*, velocity in the island is about 0.87 *m/s*. velocity downstream the island is between 0.54 to 1.1 *m/s*, and velocity near the right bank is between 0.54 to 0.92 *m/s*.

Scenario (4-D) at a discharge of 2000 m^3/s gives the same results.

The velocity distribution at a discharge of 3000 m^3/s for Scenario (4-E) varied between 0.91 to 1.12 *m/s* upstream the island; the velocity downstream in the same section varied between 0.58 to 0.89 *m/s*; velocity near the right bank ranged from 0.58 to 1.12 *m/s*. The maximum velocity is about 1.22 *m/s* occurs near cross section (4+000). The variation of velocity throughout the whole reach is shown in **Fig. 14**.

From Scenario 4, it is clear that the range of velocities is high, more than 0.7 *m/s*, in most regions for all discharges with vegetation treatment on the right bank of Tigris River at Nu'maniyah City.

Accordingly, since the maximum limit of velocities to remove plants is 0.61 *m/s*, **Varyu,** and **Fotherby, 2012**, vegetation on the right bank at all discharges in Scenario 4 will be damaged and destroyed before the occurrence of flood in the region.

Finally, vegetation is an unsafe treatment on the right bank of Tigris River at Nu’maniyah City and will be the excluded from treatment methods.

From the above Scenarios of bank protection on the riverbank by gabion treatment, the presence of a high speed at the right bank was noticed but does not mean erosion of riverbank.

Velocity reduction ratio for each type of treatments of Tigris River at Nu’maniyah City is shown in **Table 8**.

To choose the applicable type of treatment, cost of the treated reach of Tigris River at Nu’maniyah City by riprap and gabion, except cross sections (3+400) and (3+800) were calculated with an assumed maintenance cost of 10% of the total cost as shown in **Table. 9**.

Finally, riprap gives the best treatment to reduce erosion on right bank of Tigris River at Nu’maniyah City because its total cost is 2 billion IQD which is less than of the gabion treatment and riprap is the long term success in bank protection. Also riprap is required less maintenance and stayed for several decades compared with the gabion.

11. CONCLUSIONS

According to results of the present study, the following conclusions can be withdrawn:

1. Experimental work using "mini" Jet device shows high erosion coefficient of cross sections (2+600), (2+900) and (4+000) which confirms that this device is a very good indicator for the possibility of bank scour. The velocities upstream of the island and near the right bank in the study area are between 0.64 and 1.47 *m/s,* while downstream of the island is between 0.64 and 1.04 *m/s.*
2. Failure occurs in natural case of Tigris River at Nu’maniyah City especially at cross sections (2+600) and (4+000) because of erosion near the right bank and does not occur because of slope stability failure for right bank where the range of the velocities near the right bank for the study area for most discharges is between 0.67 and 0.91 *m/s.*
3. Soil of Tigris River right bank at Nu’maniyah is silty soil, the scour velocity is higher than 0.5 *m/s,* therefore the right bank is safe against scour only when the discharge of Tigris River is not greater than 500 m^3/s.
4. Vegetation is an unsafe treatment on right bank of Tigris River at Nu’maniyah City. The velocity that removes plants when used as a treatment for river bank is 0.61 *m/s* and velocities near bank at most discharges are higher than this limit.
5. Treatment by riprap is the best choice on the right bank of Tigris River at Nu’maniyah City because its cost with maintenance is 2 billion IQD which is less than that of gabion treatment; moreover, velocity reduction ratio along the right bank by riprap ranges from 15 to 85 %, while velocity reduction ratio along the right bank by gabion ranges from 8 to 25 %.

REFERENCES

- Abdul-Ridha, M. S., Hydraulic analysis of the Samarra AL-Tharthar system, M. Sc., 2015. Department of Water Resources, University of Baghdad, Chapter 3.

- Abdul-Sahib, A. A., 2014, *Roughness Characteristics of the Kut-Nu'maniyah Rearch of the Tigris River and its Effect on Nu'maniyah Gaging Station,* Thesis, University of Baghdad-Department of Water Resources, chapter 4, pp. 59.
- Al-Madhhachi, A. T., Hanson, G. J., Fox, G. A., Tyagi, A. K., and Bulut, R., 2013, *Measuring Soil Erodibility Using a Laboratory "Mini" Jet*, Transactions of the ASABE Vol. 56(3), American Society of Agricultural and Biological Engineers ISSN.
- Annandale, G. W., Melville, B., and Chiew, Y. M., 2002, *Scour Case Studies,* PP. 43.
- Breusers, H. N., Nicollet, G., and Shen, H. W., 1977, *local Scour around Cylindrical Piers,* Journal of Hydraulic Research, Vol. 15, No. 3, PP. 211-252.
- Bundaberg Regional Council, 2013, *Improving Dwelling Resilience to Flood Induced Scour*, Guide Lines for Dwellings Constructed within a Flood Hazard Area.
- Charles, R. Neill, 1973, Discussion of *Erosion of Sand Beds around Spur-Dikes,* by Gill M. A., Journal of Hydraulic Division, ASCE, HY5, May, PP. 860-862.
- Chow, V.E., 1959, *Open-Channel Hydraulic,* Mc Graw-Hill Book Company Inc., University of Illinois, Tokyo.
- Donnell, B. P. and King, I., 2003, *User Guide to WES-RMA2,* Version 4.5, U. S. Army, Engineer Research and Development Center, Water Ways Experiment Station, Coastal and Hydraulic Laboratory, by Wex Tech System. Inc.
- Fischenich, J. C., 1989, *Channel Erosion Analysis and Control*, in Woessmer, W. and D. F. Potts, eds. Proceedings Headwaters Hydrology. American Water Resources Association Bethesda, Md.
- Flood Control District of Maricopa County, Arizona, *Drainage Design Manual*, Hydraulics, 2013.
- Garanaik, A. and Sholtes, J., 2013, *River Bank Protection,* CIVE 717.
- Geohydraulique, 1977, *Tigris River Training Project within Baghdad City*, report submitted to the Ministry of Irrigation-Iraq., Paris.
- Hagerty, D. J. and Hamel, J. V., 1989, *Geo-Technical Aspects of River Bank Erosion*, In Proceedings of the 1989.
- Islam, Sh., 2008, *River Bank Erosion and Sustainable Protection Strategies.*
- King, I., 2005, *Users Guide to RMA2 WES*-Version 4.5, New York: Wex Tech Systems. Inc.
- Millitello, A., and Zundel, A.K., 1999, *Surface-Water Modeling System Tidal Constituents Toolbox for ADCIRC,* US Army Corps of Engineers.
- Ministry of Water Resources, Center of Studies and Engineering Designs, 2013, *Scatter Data (XYZ) Coordinates of the Tigris River for the Study Area*, unpublished data.
- Ministry of Water Resources, *Center of Studies and Engineering Designs Report*, 2015

- Ministry of Water Resources, National Center for Management Water Resources, 1988, *Discharge and Water Level During Flood for the Study Area*, unpublished data.
- Talukdar, B., 2012, *River Bank Erosion-A Perspective,* Assam Engineering College.
- Varyu, D., and Fotherby, L., 2012, *Vegetation Calibration in a Sediment Transport Model of the Middle Rio Grande, New Mexico*, PP. 7.

NOMENCLATURE

a= constant, dimensionless.
b= constant, dimensionless.
BSTEM= bank stability and toe erosion model
c= constant, dimensionless.
DEM= digital elevation model
E_{xx}= eddy viscosity coefficient on x-axis, pascal.sec.
E_{yy}= eddy viscosity coefficient on y-axis, pascal.sec.
E_{xy}, E_{yx}= shear direction on each surface, pascal.sec.
F= a set of terms, dimensionless
g= acceleration due to gravity, m/sec^2
h= water depth, m.
k_d= erodibility factor, cm^3/Ns
n= manning's roughness coefficient, dimensionless.
p= pressure, pascal.
Q= discharge, m^3/sec.
SMS= surface modeling system.
t= time, sec.
u= velocity in the x direction, m/sec.
v= velocity in the y direction, m/sec.
W.L.= water level, m.
X= cartesian coordinate in x-direction.
Y= cartesian coordinate in y-direction.
Z= cartesian coordinate in z-direction.
α= bottom elevation, m
μ= viscosity, pa*s.
ρ_d= dry density, gm/cm^3.
τ_c= critical shear stress, pascal.
τ = boundary shear stress, pascal.

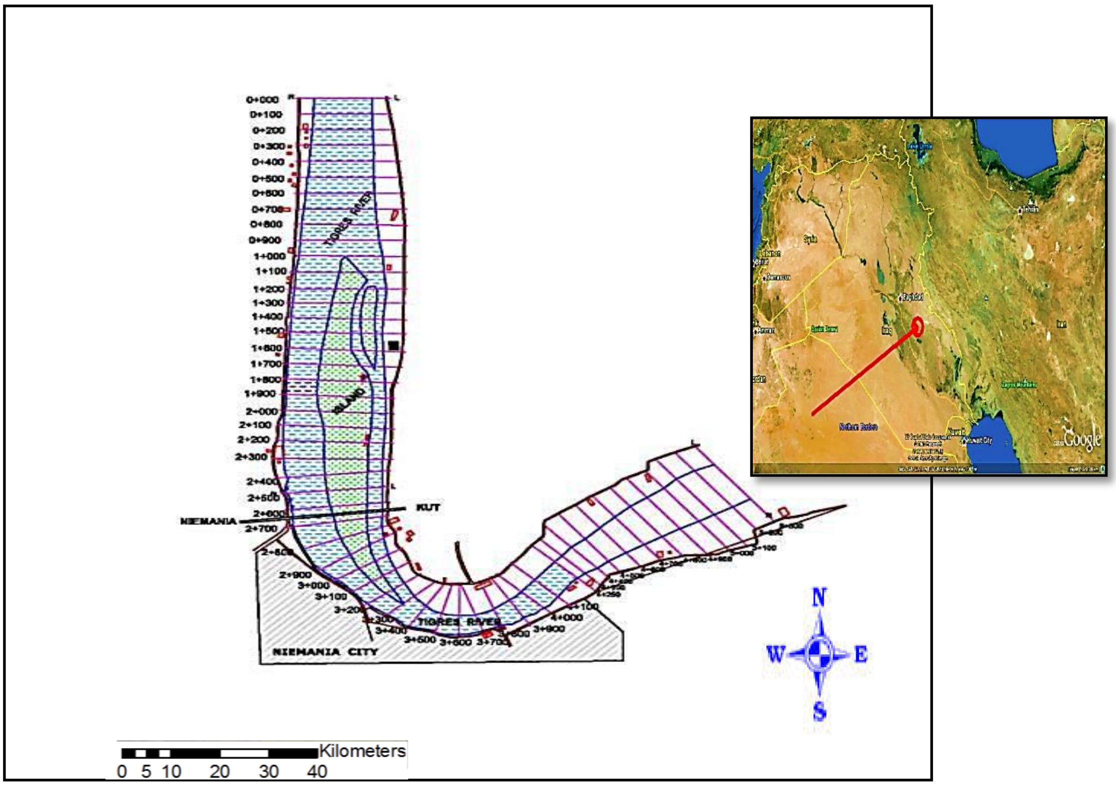

Figure. 1. Location of the study area, **Center of Studies and Engineering Designs Report, 2015**.

Table 1. Hydrological data during flood of 1988 in Nu'maniyah City, **[Abdul-Sahib, 2014]**

Discharge (Q) ***(m^3/s)***	**Water Level (W.L)** ***(m)***
500	17
1000	18.5
1500	20
2000	21.34
3400*	22.43*

*Flood, **National Center for Management Water Resources, 1988.**

Table 2. Manning's n for bank protection such as gabion, riprap, and vegetation, [**Drainage Design Manual for Maricopa County, 2013, Chow, 1959**].

Type of Bank Protection	Hydraulic Roughness (Manning's n)		
	Minimum	**Normal**	**Maximum**
Gabion		0.027	
Grouted Riprap	0.028	0.030	0.040
Vegetation	0.005-0.010	0.010-0.025	0.025-0.050

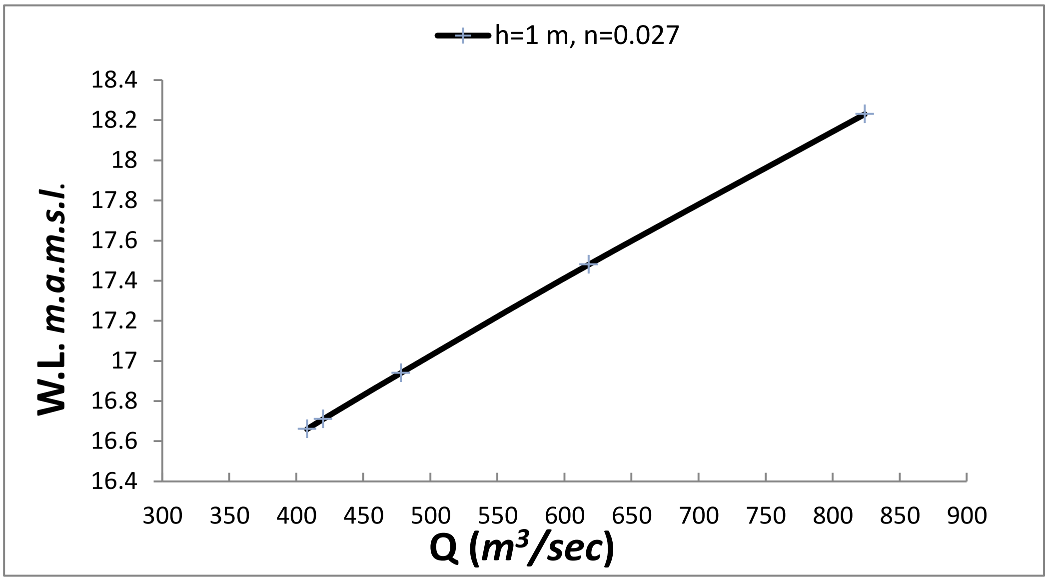

Figure. 2. Rating curve of upstream reach (C.S.22) for multigate openings for Tigris River, **Abdul-Sahib, 2014**.

.

Table 3. The location of soil samples as numbered cross section on map.

Cross Section Number at Map	Riverbank	River Toe
C.S (2+600)	01B	01R
C.S (2+900)	02B	02R
C.S (3+400)	03B	03R
C.S (3+800)	04B	04R
C.S (4+000)	05B	05R

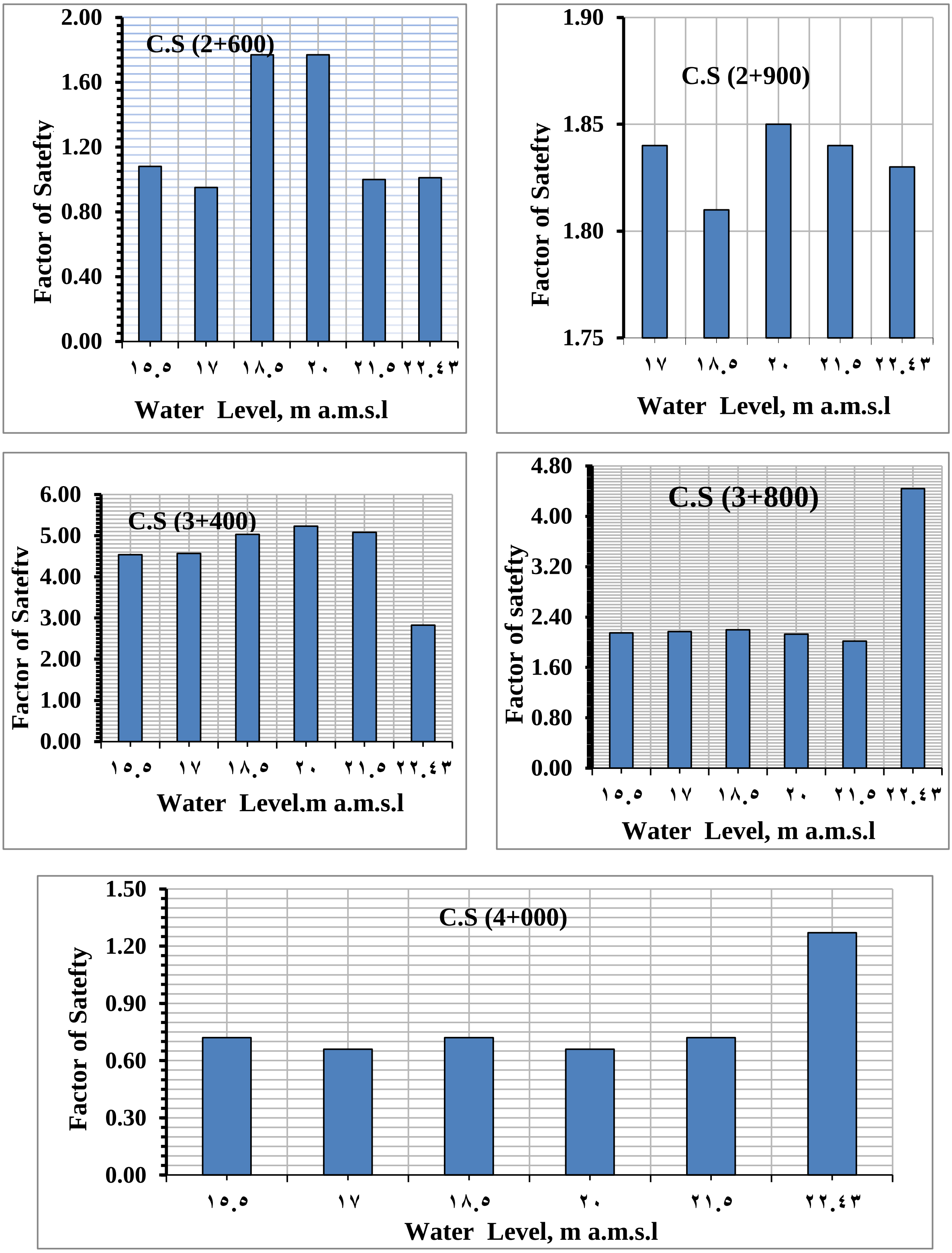

Figure. 3. Factor of safety with water level charts by using BSTEM software.

Table 4. Results from special equation when using mini Jet device.

Sample Location	Sample Number	Dry Density (ρ_d) *gm/cm³*	Erodibility Factor (k_d) *cm³/Ns*	Critical Shear Stress (τ_c) *Pa*	Boundary Shear Stress (τ) *Pa*
C.S (2+600)	01B	2.03	2.16	0.08	21.52
	01R	2.05	1.11	0.38	21.52
C.S (2+900)	02B	1.88	1.19	0.18	21.52
	02R	2.04	1.13	0.33	21.52
C.S (3+400)	03B	1.89	1.72	0.13	21.52
	03R	1.78	2.41	0.06	21.52
C.S (3+800)	04B	1.93	2.56	0.04	21.52
	04R	1.73	2.09	0.07	21.52
C.S (4+000)	05B	2.01	2.20	0.09	21.52
	05R	2.00	1.20	0.40	21.52

Table 5. Model control parameters.

Description	Value
Iterations	4
Depth convergence	0.05 meters
Dry depth	0.05meters
Wet depth	0.09 meters
Latitude	Neglected
Wind speed	Neglected
Rainfall/Evaporation	Neglected

Table 6. Number of nodes and elements in the mathematical model of the study area.

Details	Number of Nodes	Number of Elements
Natural case	6023	2874
Bank protection case	5628	2697

Table 7. Some representative ranges of eddy viscosity, [**Donnell,** and **King, 2003]**.

Type of Problem	E , Pa. s
Homogenous horizontal flow around an island	500-5000
Homogenous horizontal flow at a confluence	1100 -5000
Steady-State flow for thermal discharge to a slow moving river	1000-50000
Tidal flow in a marshy estuary	2500-10000
Slow flow through shallow pond	10-50

Table 8. Description of the adopted Scenarios for the study area.

<table>
<tr><th>S</th><th>Description</th><th>A</th><th>B</th><th>C</th><th>D</th><th>E</th></tr>
<tr><td>First (1)</td><td>Natural case</td><td rowspan="4">Q=500 m³/s at U/S and W.L.=17m at D/S</td><td rowspan="4">Q=1000 m³/s at U/S and W.L.=18.5 m at D/S</td><td rowspan="4">Q=1500 m³/s at U/S and W.L.=20 m at D/S</td><td rowspan="4">Q=2000 m³/s at U/S and W.L.=21.34 m at D/S</td><td rowspan="4">Q=3000 m³/s at U/S and W.L.=22.43 m at D/S</td></tr>
<tr><td>Second (2)</td><td>Riprap case</td></tr>
<tr><td>Third (3)</td><td>Gabion case</td></tr>
<tr><td>Forth (4)</td><td>Vegetation case</td></tr>
</table>

Figure. 4. The finite element mesh with bank protection case.

Figure. 5. The finite element mesh in the natural case.

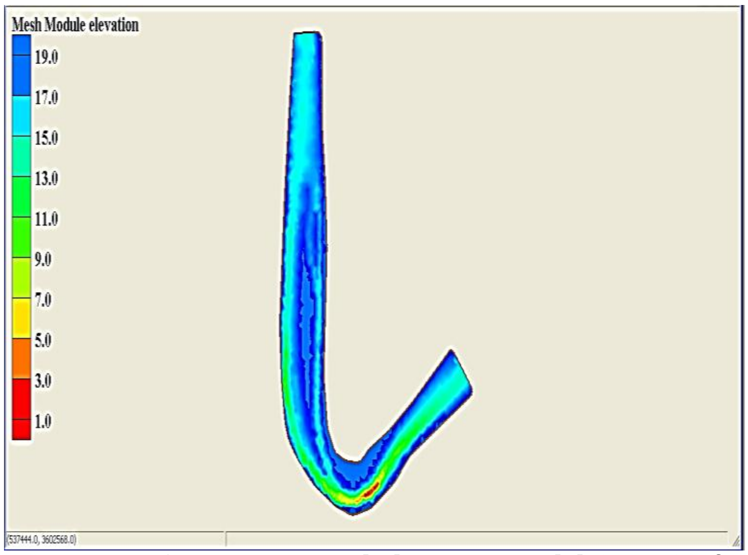

Figure. 6. Digital elevation model (DEM) of Tigris River at Nu’maniyah City.

Figure.7. Manning's n in natural case at Q=500 m^3/s.

Figure. 8. Manning's n in natural case at Q= (1000, 1500 and 2000) m^3/s.

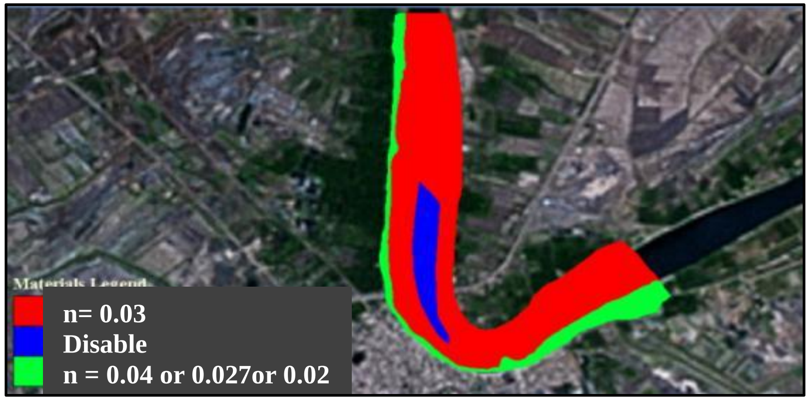

Figure. 9. Manning's n with bank protection by (riprap, gabion, and vegetation) at Q=500 m^3/s.

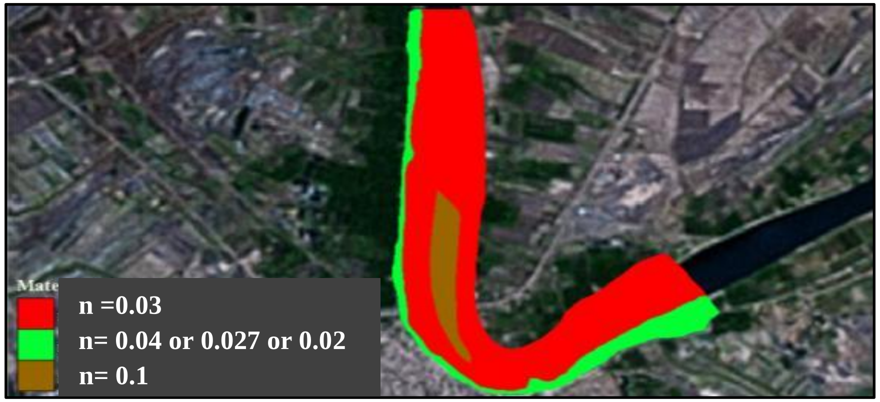

Figure. 10. Manning's n with Bank Protection (riprap, gabion, and vegetation) at Q= (1000, 1500 and 2000) m^3/s.

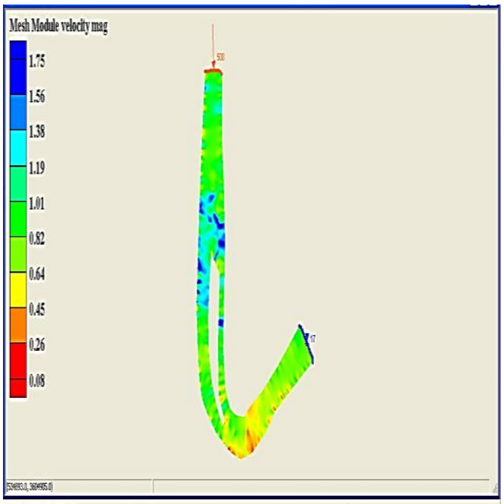

a. Q=500 m^3/s.

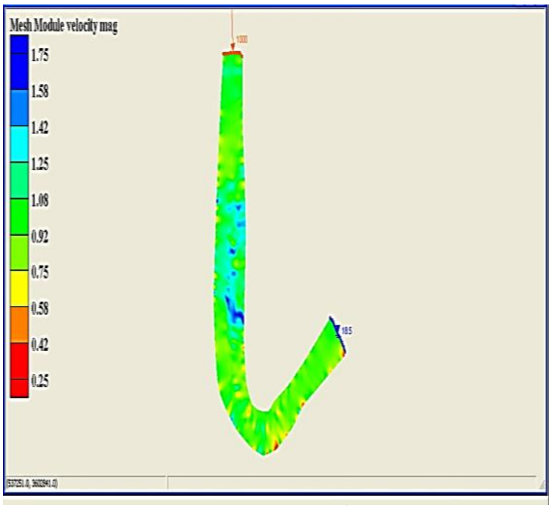

b. Q=1000 m^3/s.

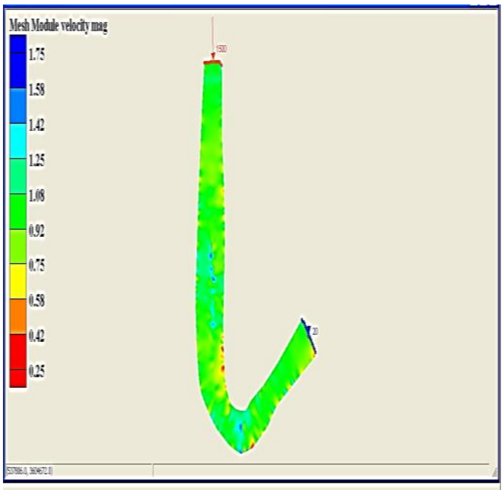

c. Q = 1500 m^3/s.

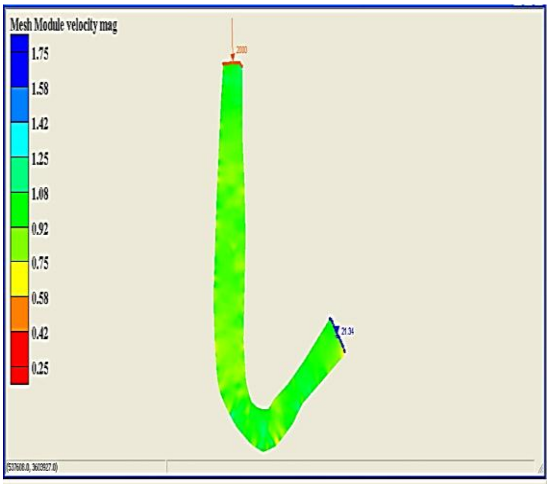

d. Q = 2000

m^3/s.

e. Q = 3000 m^3/s.

Figure. 11. Velocity distribution for Scenario 1 of Tigris River at Nu'maniyah City for natural case with discharges of (500, 1000, 1500, 2000 and 3000) m^3/s and D/S water levels of (17, 18.5, 20, 21.5 and 22.43) *m a.m.s.l.* ,respectively.

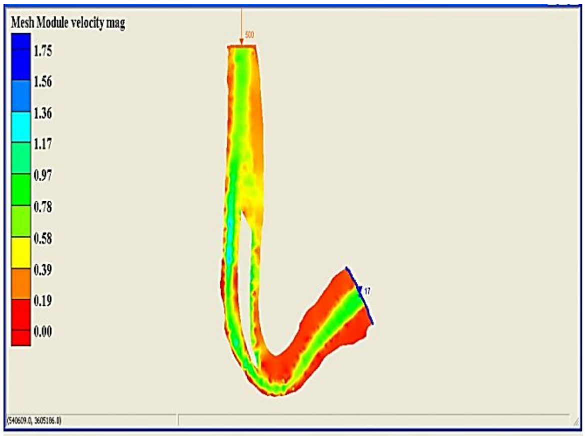

a. Q=500 m^3/s.

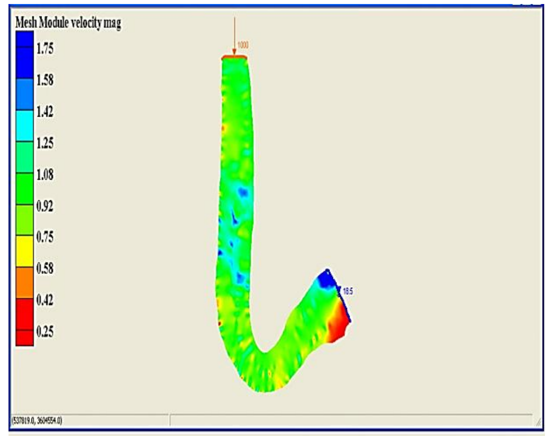

b. Q=1000 m^3/s.

c.Q=1500 m^3/s.

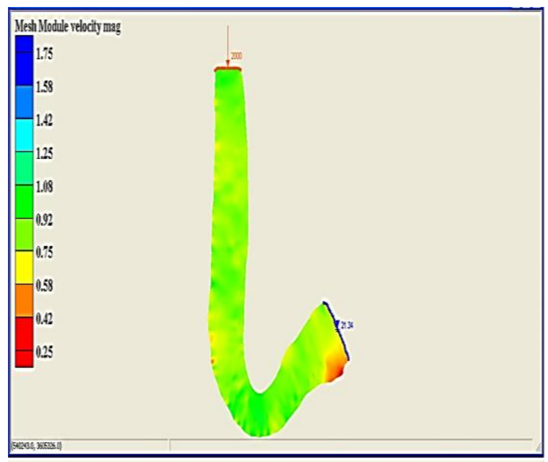

d. Q=2000 m^3/s.

e. Q=3000 m^3/s.

Figure. 12. Velocity distribution for Scenario 2 of Tigris River at Nu'maniyah City for treated banks by riprap with discharges of (500, 1000, 1500, 2000 and 3000) m^3/s and D/S water level of (17, 18.5, 20, 21.34 and 22.43) *m a.m.s.l.*, respectively.

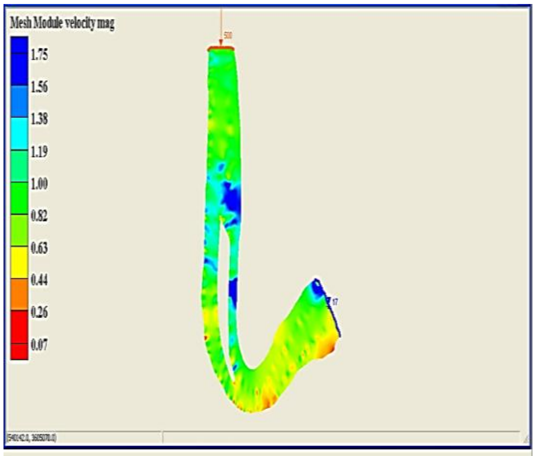

a. Q=500 m³/s.

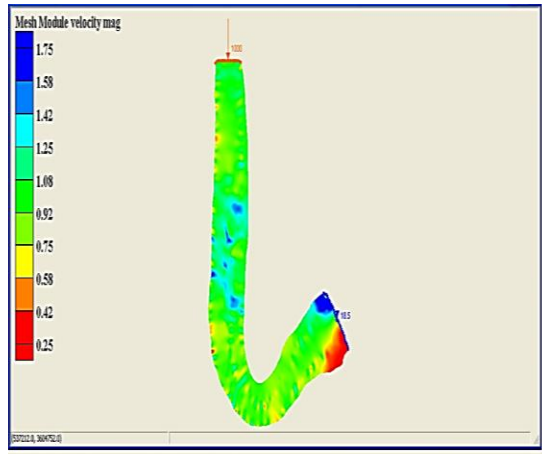

b. Q=1000 m³/s.

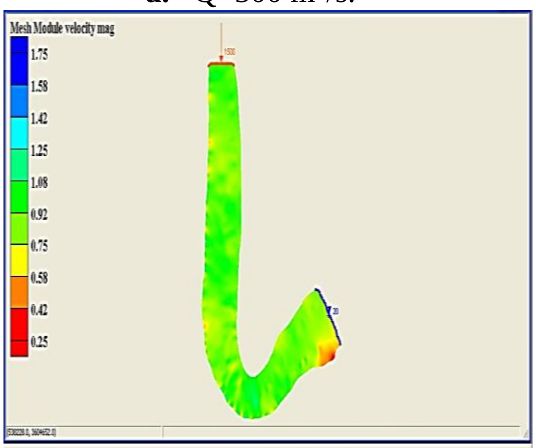

c.Q=1500 m³/s.

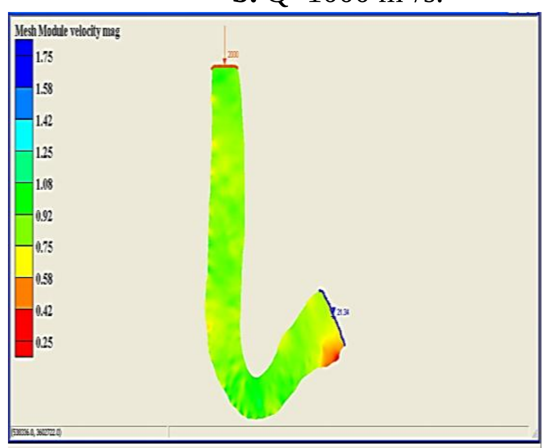

d. Q=2000 m³/s.

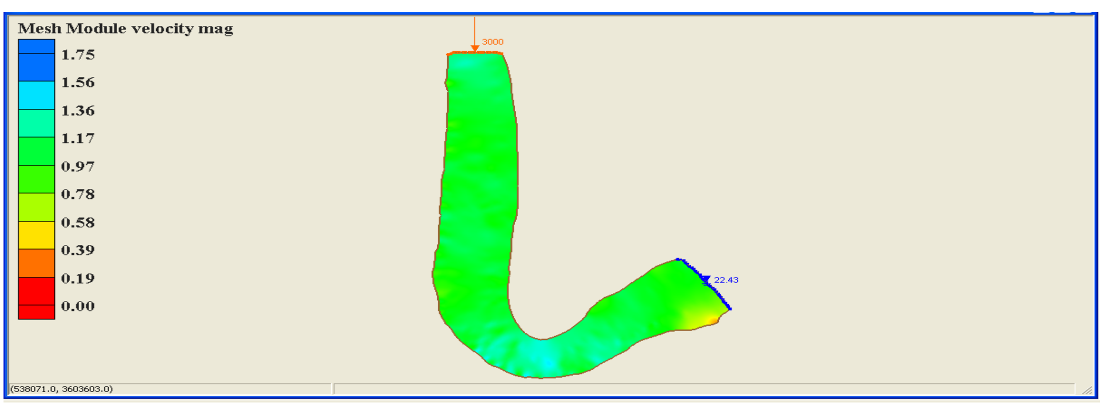

e. Q=3000 m³/s.

Figure. 13. Velocity distribution for Scenario 3 of Tigris River at Nu’maniyah city for treated banks by gabion with discharges of (500, 1000, 1500, 2000 and 3000) m^3/s and D/S water level of (17, 18.5, 20, 21.34 and 22.43) *m a.m.s.l.*, respectively.

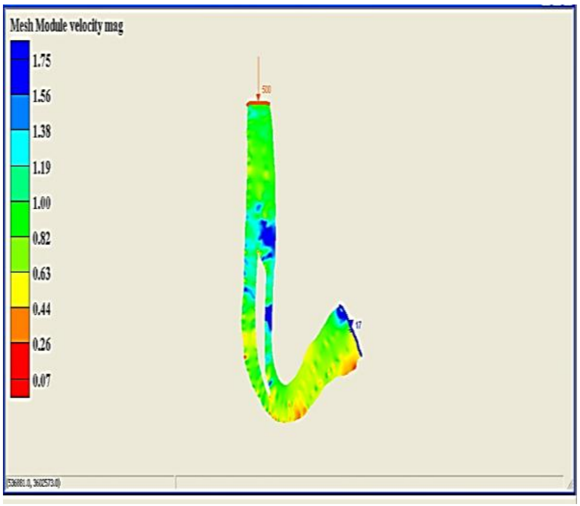

a. Q=500 m^3/s.

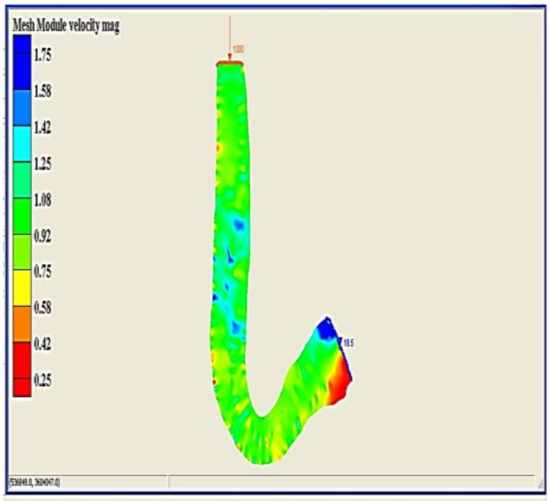

b. Q=1000

c. Q=1500 m^3/s.

d. Q=2000 m^3/s

d. Q=3000 m^3/s.

Figure. 14. Velocity distribution for Scenario 4 of Tigris River at Nu'maniyah City for treated banks by vegetation with discharges of (500, 1000, 1500, 2000 and 3000) m^3/s and D/S water level of (17, 18.5, 20, 21.34 and 22.43) *m a.m.s.l.*, respectively.

Table 8. Average velocity reduction ratio along the right bank of Tigris River at Nu'maniyah City for each good treatment.

Treatment Type	Discharge *(m^3/s)*	Average Velocity Reduction Ratio %
Riprap	500	85
	1000	35
	1500	15
	2000	15
	3000	8
Gabion	500	25
	1000	35
	1500	10
	2000	10
	3000	8

Table 9. Cost of the treated reach of right bank of Tigris River at Nu'maniyah City with riprap and gabion bank protections for 30 years each with maintenance as 10% from the total cost.

Treatment Type	Implementation Cost (ID)	Maintenance of Construction (Year)	Design Life (Year)	Maintenance Cost (IQD)	Total (IQD) in 30 years
Riprap	7,464,666,300	15	30	1492933260	8,957,599,560
Gabion	4,222,865,338	5	15	1266859601	10,979,449,879

Effects of Bedding Types on the Behavior of Large Diameter GRP Flexible Sewer Pipes

Dr. Adnan Falih Ali
Professor
College of Engineering, University of Baghdad
Email: af_bas1@yahoo.com

Raad Abdulkhudhur Sehaib
Assistant Lecturer
Engineering of Building and Construction,
University of Technology
Email: raad_1972_sehaib@yahoo.com

ABSTRACT

Flexible pipes, such as GRP pipes, serve as effective underground infrastructure especially as sewer pipeline. This study is an attempt for understanding the effects of bedding types on the behavior of large diameter GRP flexible sewer pipes using three dimensional finite element approaches. Theoretical and numerical analyses were performed using both BS EN 1295-1 approach and finite element method (ABAQUS software). The effects of different parameters are studied such as, depth of backfill, bedding compaction, and backfill compaction. Due to compaction, an increase in the bedding compaction modulus (E'_1) results in a reduction of both stresses and displacements of the pipe, especially, for well compacted backfill. An increase of (E'_1) from 14MPa to 30MPa results in a reduction in stresses 40% and about 25% in displacements. Maximum reductions in stresses were found to be about 25% only while the reduction in displacement was found to be less than 10%. As backfill material compaction modulus (E'_2) is increased from 14MPa to 40MPa, a maximum reduction in stresses within the pipe was found to be not less than 60% while the displacement reduces up to 65%.

Key words: Flexible Pipes; GRP Pipes, Bedding Compaction, Backfill Compaction, ABAQUS

تاثيرات أنواع طبقة الفرش على تصرف أنابيب المجاري المرنـة ذات الأقطار الكبيرة من نوعGRP

د. عدنان فالح علي
استاذ
قسم الهندسة المدنية*كلية الهندسة*/جامعة بغداد

رعد عبدالخضر سحيب
مدرس مساعد
قسم هندسة البناء والانشاءات-الجامعة التكنولوجية

الخلاصة

تعتبرالأنابيب المرنة كأنابيب GRP المطمورة من خطوط انابيب البنى التحتية الفعالة وخصوصا" في خطوط أنابيب المجاري.هذه الدراسة محاولة لفهم تأثيرات أنواع الفرش على سلوك أنابيب المجاري المرنة ذات الأقطار الكبيرة من نوع GRP باستخدام نظرية العناصر المحددة ثلاثية الأبعاد. حيث أجريت التحليلات النظرية والعددية باستخدام كل من (BS EN 1295-1) وطريقةالعناصرالمحدودة ثلاثيةالأبعاد بأستخدام (برنامجABAQUS). تم دراسة تأثيرعدة متغيرات مثلا":عمق مادة الدفن ، رص مادة الفرش تحت الأنبوب ورص مادة الدفن. بسبب الزيادة في حدل مادة الفرش (E'_1) فانه ينتج انخفاض في كل من الأجهادات والتشوهات في الانبوب، وخصوصا" عندما تكون تربة الدفن محدولة جيدا". زيادة (E'_1) من14MPa الى 30MPa ينتج اكبر انخفاض في الاجهادات ب40% وحوالي 25% في التشوهات. اكبر انخفاض في الاجهادات حوالي 25% فقط بينما الانخفاض في التشوهات اقل من 10%. عندما رص مادة الدفن(E'_2) يزداد من 14MPa الى 40MPa فان اكبر انخفاض في الاجهادات خلال الانبوب يكون اكبر من 60% بينما التشوهات تقل باكبر من 65%.

الكلمات الرئيسية: الانابيب المرنة،انابيب GRP، رص مادة الفرش، رص مادة الدفن ، برنامج ABAQUS

1. INTRODUCTION

Buried pipes for sewer systems are usually subjected to external forces caused by backfill and additional surcharge due to traffic loading. Accordingly, stresses within the pipe walls will be developed, those stresses are assumed to be depending on the type of backfill, depth of backfill and the bedding type in additional to pipe diameter. The present paper presents a theoretical investigation of the behavior of large diameter sewer pipes made of (GRP) when buried at different depths, moreover, the study presents the effect of bedding type on the developed stresses, strains and displacements of the pipe walls using finite elements analysis implemented in the ready software ABAQUS.

2. OBJECTIVES

The main objectives of the current work are:

(a) To provide a comparative analysis of flexible sewer pipes taking into account variation of the following factors,

- Depths of the pipes variation relative to the pipe diameter.
- Properties of the soil used to backfill above the pipe.

(b) To study the effect of bedding type on the behavior of flexible sewer pipes

(c) To present numerical case studies by implementing the finite element procedure so as to provide a more accurate behavior of the flexible pipe and to compare the results with the available procedure currently in use to assess the pipe behavior.

3. ANALYTICAL APPROACH of (BS EN 1295-1)

An analytical method is recommended in UK by **[BS EN 1295-1**], and is summarized in the following steps:

3.1 Soil Modulus

Soil modulus is the parameter of the most influence on the structural calculation, as soil stiffness will generally be significantly greater than the pipe stiffness. Spangler modulus values have been determined from empirical measurements and are indicated in **Tables 1** for the native soil**.** The soil modulus adjustment factor (C_L), is used to take into account the influence of native soil properties on the overall soil modulus (E'), and can be calculated by using Eq.(1) as shown below: **["Design and Installation Manual of Ridgidrain, Ridgisewer and Polysewer"].**

$$\boldsymbol{C_L} = \frac{\mathbf{0.985}+(\mathbf{0.544}\boldsymbol{B_d}/\boldsymbol{B_c})}{[\mathbf{1.985}-\mathbf{0.456}(\boldsymbol{B_d}/\boldsymbol{B_c})](\boldsymbol{E'_2}/\boldsymbol{E'_3})-[\mathbf{1}-(\boldsymbol{B_d}/\boldsymbol{B_c})]} \quad (1)$$

$$E' = E'_2 \times C_L \quad (2)$$

3.2 Vertical Soil Pressure (P_e)

The vertical dead load applied to the pipe system is typically restricted to the soil pressure generated by the pipe backfill material. The load is taken as the pressure imposed by the prism of soil directly overlying the pipe. No allowance is made within the available standards for the effect of shear between the backfill material and the trench walls. Where the density of the backfill material is not available, (value of 19.6kN/m^3) may be assumed for design purposes.

$$P_e = \boldsymbol{\gamma} \times H \quad (3)$$

3.3 Surcharge Pressure (P_s)

The imposed pressure from vehicle traffic is largely dependent on the depth of cover above the pipe. Surcharge loads are calculated using Boussinesq's theory which is plotted in **Fig.1**

3.4 Deflection Lag Factor (D_L)

An empirical factor is used to account for relaxation, or creep, of the pipe/soil system and other general long-term settlement effects. A conservative design approach is taken by assuming no beneficial effect is derived from frictional forces between the trench walls and backfill material, in addition to the use of a long-term pipe stiffness parameter. Values generally range from **1.0** to **1.5**, dependant on the type of pipe surround used and its level of compaction. A well installed gravity flow pipe, utilising a single sized granular bed and surround, a value of **1.0** is typically taken for the deflection lag factor.

3.5 Deflection Coefficient (K_X)

A bedding factor is used to represent the extent of lateral support provided by the pipe bedding. For pipes receiving support over the full **180°** lower half of the pipe a value of **0.083** should be used, whereas bedding providing only a line load support, a value of **0.100** would be more appropriate.

3.6 Pipe Deformation

The deformation of flexible pipes under load results in the ovalization of the pipe (a reduction in the vertical diameter and an increase in the horizontal diameter). As the horizontal diameter of the pipe increases, it derives support from the sidefill and trench wall. This passive earth pressure increases as the pipe deforms further until the pipe-soil system comes into equilibrium.

Ovalization can be calculated using Eq. (4) as shown below:

$$\frac{\Delta}{D} = \frac{K_x[(D_L P_e)+P_s]}{(8EI/D^3)+(0.061E')} \quad (4)$$

3.7 Buckling Resistance of Buried Pipeline

The buckling resistance of buried, flexible non-pressurized pipelines is a combination of the pipes inherent buckling resistance and support afforded by the pipe surround. The critical buckling pressure of a buried pipe is substantially greater than that for unrestrained pipes subject to external loading. Bending stress can be calculated by using Eq. (5) as shown below:

$$\sigma_{bs} = E\, D_f\left(\frac{\Delta}{D}\right)\left(\frac{t}{D}\right) \quad (5)$$

4. FINITE ELEMENT MODEL

Numerical applications using Finite Element Analyses are carried out to assess the behavior of buried pipes in trench installations. In the numerical analyses, effects of pipe material, height of fill above the pipe, soil properties are investigated. In the current study, effects of bedding types on the behavior of large diameter GRP flexible sewer pipes are studied by using FE. The FE analyses were carried out using ABAQUS**, [Hibbitt, Abaqus Manual,(2009)],** program in addition to the analysis based on the traditional procedure used for structural design of buried pipelines which is used under various conditions of loading **[BSI. 1295-1] ,British Standard,1998.**

Each of the above mentioned parameters was varied within an acceptable practical range and the corresponding results of stresses and deformations have been calculated numerically to explain the global response, as follows:

- Pipe diameter is equal to (3 m).
- Trench width is equal to (4 m).
- Depths of the pipes are varied such that the soil depth above the pipe equals to:
  - Pipe outside diameter (m).
  - Pipe outside diameter +1.5 m.
  - Pipe outside diameter +3 m.
- Properties of the soil surrounding the pipe and the bedding material were varied such that:
  - Bedding Soil Modulus, **E'$_1$**, of bedding material to have values of 14, 20 and 30MN/m^2.
  - Embedment Soil Modulus, **E'$_2$**, of backfill material to have values of 14, 30 and 40 MN/m^2.
  - Native Soil Modulus, **E'$_3$**, to have values of 14, 20 and 30MN/m^2.

The three-dimensional finite element models of pipe-soil interaction were performed by using, ABAQUS, version 6.10-1, computer program. The finite element method is one of the most popular numerical methods used for obtaining an approximate solution for complex problems in various fields of engineering.
The flexible sewer pipeline model including five steps following:

4.1 Types of Loads on a Pipeline

The design and analysis of buried flexible pipelines are carried out for the total loads, comprising the effects of the dead load exerted by soil and the live load caused by traffic.
Both, dead and live loads acting directly on the pipeline are assumed vertical and of static nature acting on the pipeline.

4.1.1 Dead Load

The weight of soil, which is generally called dead load, is calculated using ABAQUS program.
ABAQUS calculates the loading using the acceleration magnitude that one may enter in the gravity load definition and the density is specified in the material definition.

$$\textit{Unit weight } (kN/m^3) = \textit{Mass density } (kg/m^3) \times \textit{Gravity load } (9.81 m/sec^2) \qquad (6)$$

The dead load on the buried pipeline is normally substantially greater than the live load because the effects of live load, usually due to traffic, diminish rapidly with depth of soil above the pipe.

4.1.2 Live Load

The pressure exerted on pipelines by concentrated surface surcharges, such as vehicle wheels, construction vehicles, or track railway, are generally called live load.

HS Loadings

The HS loadings are illustrated in **Fig.2**. They consist of a tractor truck with semi-trailer or of the corresponding lane loading. The HS loadings are designated by the letters HS followed by a number indicating the gross weight in tons of the tractor truck. The variable axle spacing has been introduced in order that the spacing of axles may approximate more closely the tractor trailers now in use. The variable spacing also provides a more satisfactory loading for continuous

spans, in that heavy axle loads may be so placed on adjoining spans as to produce maximum negative moment, **[The American Association of State Highway and Transportation Officials, (2002)].**
Traffic load is represented as a rectangle area over the surface backfill as shown in **Fig.3** in ABAQUS program.

4.2 Material Properties

4.2.1 Soil Properties
There exist several types of soils: clay, sand, rock, undistributed granular soils, placed granular soils and compacted backfill ground around buried pipelines placed in an excavated trench.
In this study, the soil is divided into two types: bedding and backfill soils. The types of soil and their mechanical properties are shown in **Table 2**

4.2.2 Pipeline Properties
Large diameter fiberglass reinforced plastic (GRP) pipelines which are used for trunk sewer construction or sewer networks are assumed to possess the properties shown in **Table 3**.

4.3 Models of the Soil and the Pipeline
In this study, the finite element models of the pipeline and the soils are established using the package ABAQUS to carry out the analysis of flexible buried pipelines. In the ABAQUS program, the soil model is defined as a three-dimensional (3D) deformable solid body and elastic characterised, which is divided into two types: bedding and backfill soils as shown in **Fig.4**.
On the other hand the pipeline is simulated as a three-dimensional (3D) deformable shell model as shown in **Fig.5**.

4.4 Surfaces of the Soil and the Pipeline
Definition surfaces of the soil and pipeline to generate contact interaction between the parts of the model. The limits of each type are shown in **Fig.6** and **Fig.7**.

4.5 Assembly of Pipeline and Soil
A physical model is typically created by assembling various components. The assembly interface in ABAQUS allows analysts to create a finite element mesh using an organizational scheme that parallels the physical assembly. In ABAQUS, the components that are assembled together are called part instances. An assembly is a collection of positioned part instances of soil and pipeline as shown in **Fig.8**. An analysis is conducted by defining boundary conditions, constraints, interactions, and a loading history for the assembly.

4.6 Interaction between the Soil and a Pipeline
In ABAQUS, the types of constraints include tie, rigid body, display body, coupling, MPC (Multi- Point Constraint), shell-to-solid coupling, embedded region and equation. A tie constraint ties two separate surfaces together so that there is no relative motion between them.
One constraint (called tie) is adopted for simplicity to connect bedding top surface and backfill bottom surface, backfill surface and pipeline top surface as well as bedding surface and pipeline bottom surface, which are fully bonded to each other as shown **Fig.9**.

4.7 Boundary Conditions
In a 3D-finite element model related to soil and pipeline, two boundary conditions of 3D- finite element soil model need to be considered; bottom surface and four side surfaces of 3D-finite

element soil model whereas 3D-finite element pipeline model, boundary conditions need to be considered at two end surfaces of a pipeline and circumferential pipeline surface which comes into contact with soil.

4.7.1 Boundary Condition of Soil's 3D-Finite Element Model

First, the four side surfaces (left, right, front, and back) of the 3D-finite element soil model are supposed to be on rollers as shown in **Fig.10** since these surfaces for left, right, front, and back restrain only the horizontal movement (i.e. u = w = 0).. Additionally, the bottom surface of the 3D-FE soil model is proposed to be completely fixed (i.e. u = v = w = 0) in order to restrain horizontal (i.e. u = w = 0) and vertical movement (i.e. v= 0). This is because the bottom boundary is selected at the known location of a bedrock surface, **Rao, (1999)**.

4.7.2 Boundary Condition of Pipeline's 3D-Finite Element Model

Boundary condition of proposed of 3D-finite element pipeline model is shown in **Fig.11**; Two end surfaces of the pipeline and surrounding the pipeline surface come into contact with soil.

4.8 Element Types

Under the comprehensive consideration of buried pipelines, the 3D reduced integration continuum brick element with twenty nodes with a second-order (or quadratic) interpolation, C3D20R was selected for the (bedding and backfill) soils as shown in **Fig.12**.

The (3D) reduced shell continuum element with eight nodes with a second-order (or quadratic) interpolation, S8R was selected for the pipeline as shown in **Fig.13**.

The second-order elements are more effective than the first-order elements because the second-order elements can deal with bending dominant problems which cannot be solved by the first-order elements, **Lee, (2010)**.

4.9 Defining Loads

In ABAQUS, self-weights of both soil and pipelines are represented as gravity loads, while the traffic load is represented as a pressure load over the surface backfill as shown in **Fig.14**.

4.10 Meshing both Soil and Pipeline Model

The mesh module contains tools that allow ABAQUS/CAE to generate a finite element mesh on created models. Various levels of automation and control are available so that a mesh is produced. The mesh is the step related to dividing the models into lots of small parts. These divided 3D small meshed elements in models play an important role to offer suitable results in accordance with the chosen number of elements and the type of element as shown in **Fig.15**.

4.11 Creating an Analysis Job

Once all of the tasks involved in defining the model are finished, it is necessary to use job module for analysing the created model. The job module allows ABAQUS/CAE to interactively submit a job for analysis and monitor its progress.

4.12 Displacement of a Buried Pipeline

The pipeline can deform like an oval shape along the whole length under the subsiding soil involved in short-term serviceability issue. A typical deformation of a pipeline under static loads is shown in **Fig.16**.

4.13 Stresses in GRP Pipelines

The maximum longitudinal stress has been computed from the general elastic static analysis. The static loads, which are simulated vertically, caused the pipeline to be deformed into an oval shape and allowed the maximum longitudinal stress of a buried pipeline to occur at both the crest and the invert of a pipeline as shown in **Fig.17**.

It is possible to conclude that the generated maximum stress of a pipeline at both crest and invert of the pipeline makes the flexible pipeline to buckle at these positions of the pipeline. This means that if there is not enough strength of a pipeline for resisting static loads, the buckling will be generated at both the crest and the invert of a pipeline and the flexible pipeline will totally collapse when stresses reaches a critical buckling level.

5. NUMERICAL RESULTS AND DISCUSSIONS OF CASE STUDIES

Using the procedure adopted in the previous section, parametric studies are carried out and presented in the current section, and these parametric studies take into consideration variation of several parameters as follows:

5.1 Effect of Bedding and Backfill

Under various bedding and backfill conditions, when examining the analysis results given in **Fig. 18** to **19** it can be noted that:

1. Bedding compaction was found to be of important influence on both stresses and displacements of the pipe irrespective of pipe diameter as predicted by the (FE) approach. It was also found that increasing bedding compaction (E'_1) results in a reduction of both stresses and displacements of the pipe, especially, for well compacted backfill. This behavior is attributed to the tendency of rigid behavior of the pipe, the underneath, and surrounding materials. An increase of (E'_1) from 14MPa to 30MPa results in a maximum reduction in stresses by 40% and to about 25% in displacements.
2. If the backfill material (E'_2) is loose, bedding compaction was found to be effective mainly in cases of shallow pipes where the stresses still reduce with compaction but the displacements were found to be less affected. Maximum reductions in stresses were found to be about 25% only while the reduction in displacement was found to be less than 10%.

3. The procedure suggested by the (BSI) were found to lead to results which are close to those predicted by the (FE) in the following cases
   - Well and very well compacted bedding ($E'_1 \geq 20$ MPa)
   - Relatively narrow trenches as compared to the pipe diameters
   - Well compacted backfill surrounding pipes of relatively small diameters
   - However, displacements of the pipes as predicted by the FE approach were found to be close to those predicted by the BSI approach in cases of well compacted bedding and backfill for pipes of medium and small diameters.

This behavior is related to the increase in angle of repose of the backfill materials which results almost in a solid medium behavior which is assumed by both the FE and the BSI procedure.

5.2 Effect of Depth of Backfill

From **Fig.20** and **Fig.21**,the maximum longitudinal stress of GRP pipe increases with depth increasing for bedding soil modulus (E'_1) 14, 20 and 30MPa and for backfill soil modulus (E'_2) 14, 30 and 40MPa. Also The maximum vertical displacement of GRP pipe increases with depth increasing for bedding soil modulus (E'_1) 14, 20 and 30MPa and for backfill soil modulus (E'_2) 14, 30 and 40MPa.

6. CONCLUSIONS AND RECOMMENDATIONS

6.1 Conclusions

1. The stresses and deformations within the pipe walls increase with pipe depth below the ground surface, however, the rate of increase in stresses and deformations becomes less as the depth exceeds 2 times the diameter due to the increase in the arch action.
2. The stresses within the pipe were found to maintain constant values or slightly decrease with the increase of trench width.

3. In cases of loose bedding materials, displacements within the pipe were found to reduce with the increase of trench width, especially in cases of deep pipes.

6.2 Recommendations

1. A study on the flexible sewer pipes in underground water should be made.
2. Effects of seismic load on buried pipeline are another topic for future study.

REFERENCES

- Hibbitt, Karlsson and Sorenson, 2009, *Abaqus Theory Manual*, Version, Inc., INC
- Design and Installation Manual of Ridgidrain, Ridgisewer and Polysewer. Available at,(www. Polypipe Civils.co.uk.).
- The American Association of State Highway and Transportation Officials, (2002).
- AWWA (American Water Works Association), 2005,*"Fiberglass Pipe Design",* M45, Second Edition
- British Standard, 1998," *Structural design of buried pipelines under various conditions of loading*", BS EN 1295-1
- Lee, H., 2010," *Finite element analysis of a buried pipeline*", M.Sc. Thesis, University of Manchester, School of Mechanical, Aerospace, and Civil Engineering
- RAO, S. S., 1999, "*The Finite Element Method in Engineering*", Boston, Butterworth-Heinemann.

NOMENCLATURE

C_L: Soil Modulus Adjustment Factor
D: Mean Diameter of Pipe
D_f : Strain Factor
D_L: Deflection Lag Factor
E': Average Values of Modulus of Soil Reaction
E'_1: Bedding Soil Modulus
E'_2: Embedment Soil Modulus (Backfill)
E'_3: Native Soil Modulus
K_X: Deflection Coefficient (Bedding Constant)
P_e: Vertical Soil Pressure, kN/m^2
P_S: Surcharge Pressure, kN/m^2
S22**:** Maximum Longitudinal Stress, N/m^2
t: Thickness of the Pipe Wall, mm
U: Vertical Displacement

Δ: Pipe Deflection
γ: Unit Weight of Soil, kN/m^3.
σ_{bs} : Bending Stress in Pipe Wall
AB**AQUS/CAE:** Complete Abaqus Environment
AWWA: American Water Works Association

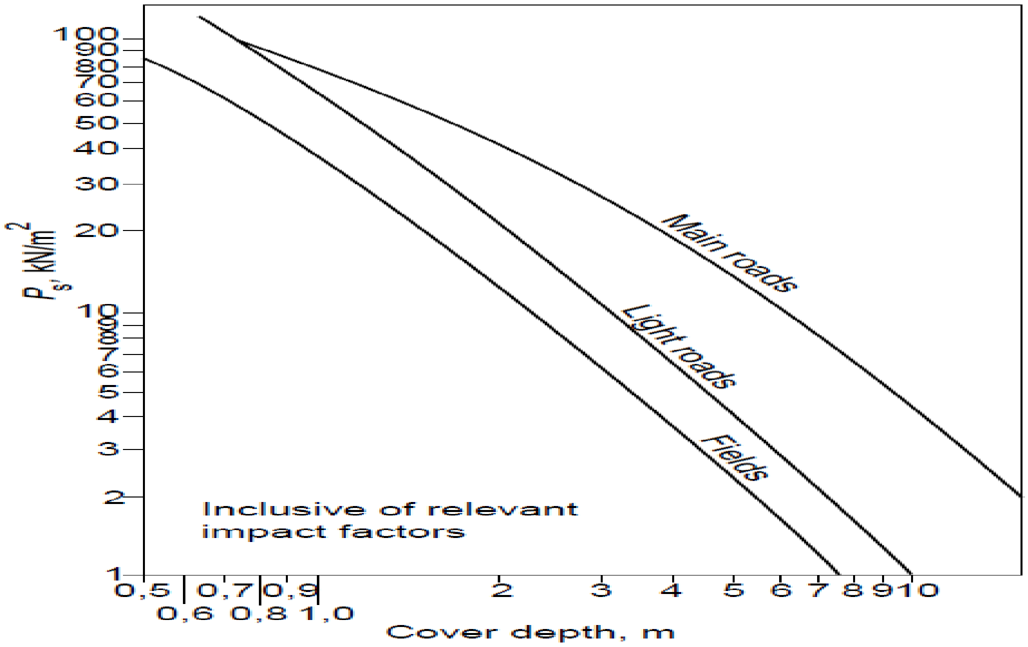

Figure1. Surcharge pressure P_s due to vehicle wheels, British standard, (1998).

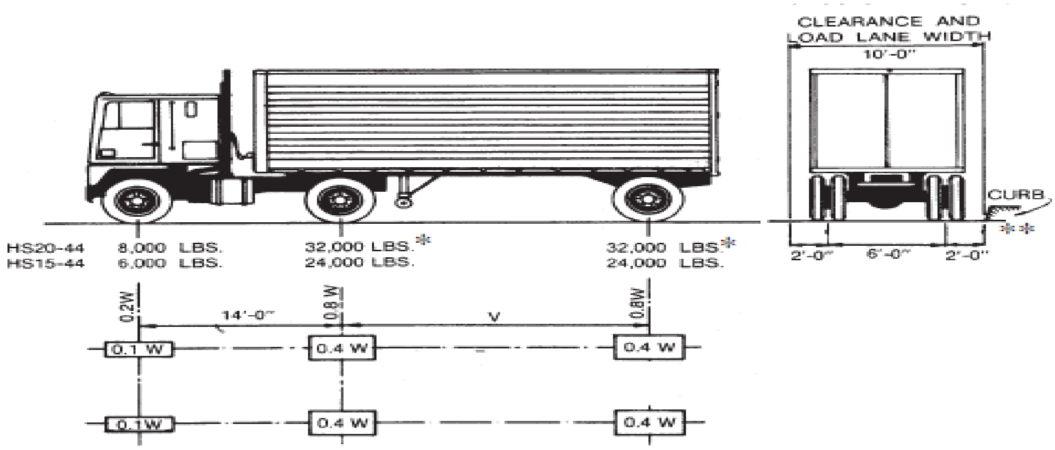

Figure2. Standard HS trucks, the American Association of State Highway and Transportation Officials, (2002).

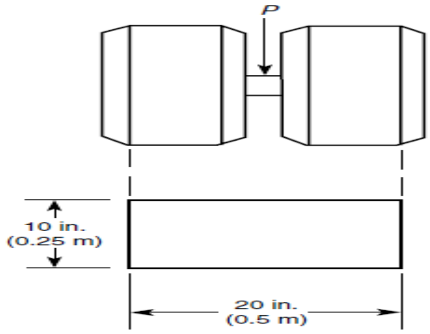

Where:

P: wheel load magnitude

P= 72k N for AASHTO HS-20

Pressure load$= \frac{Traffic\ load}{Area\ of\ tire\ imprint} = \frac{72\ \text{kN}}{(0.5\times0.25)m^2} = 576\,\frac{\text{kN}}{m^2}$

Figure3. Representation of tire imprint of HS-20 live load over the surface backfill, AWWA-M45, (2005)

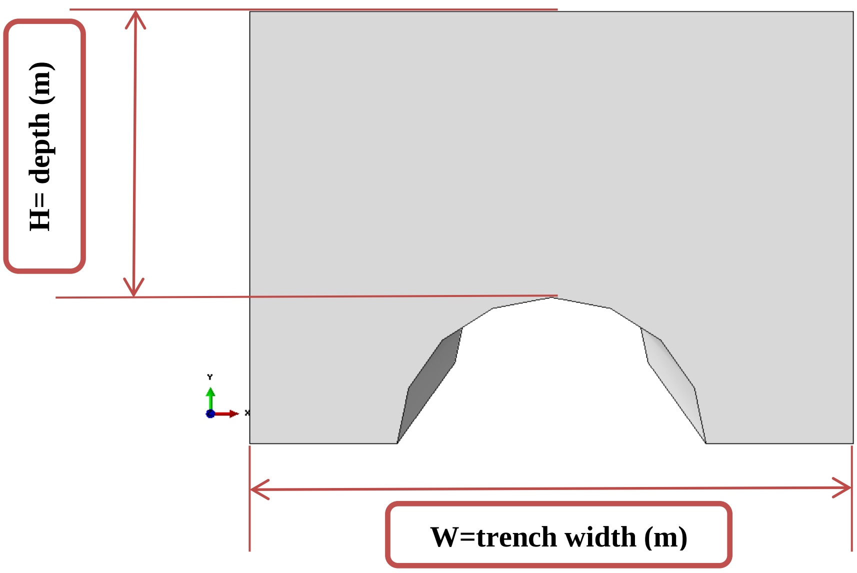

(a) Backfill soil

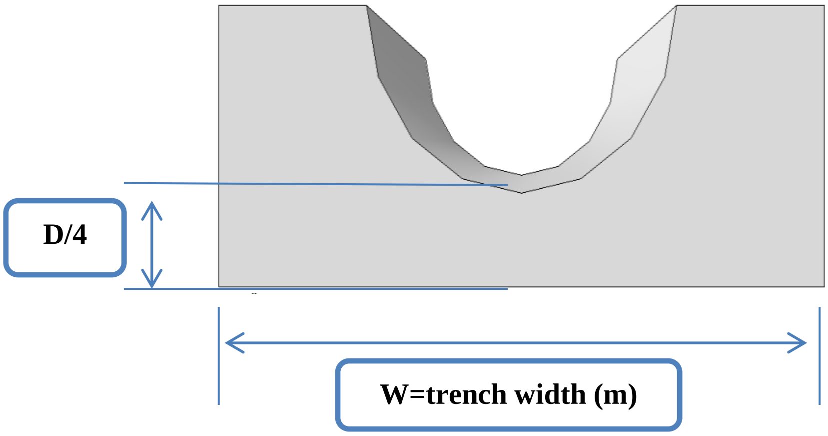

(b)Bedding soil

Figure4. Soil model in ABAQUS program

Figure5. Pipeline model in ABAQUS program

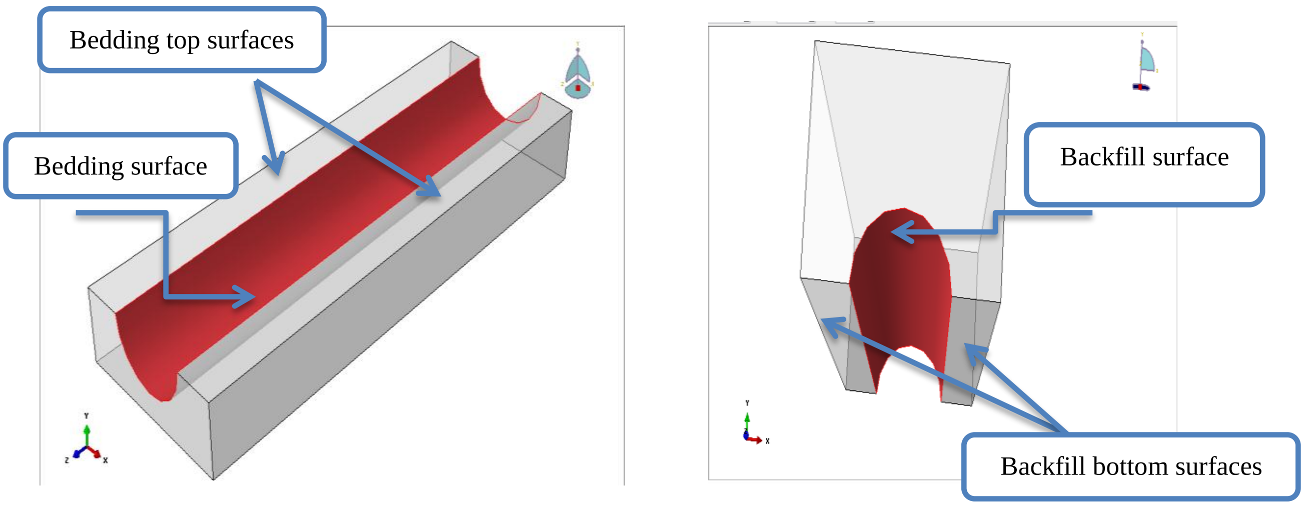

Figure6. Limits of bedding and backfill soils

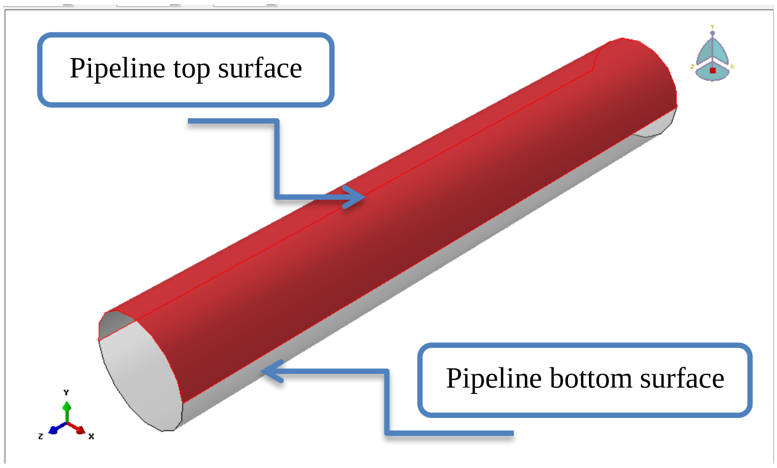

Figure7. Surfaces of a pipeline

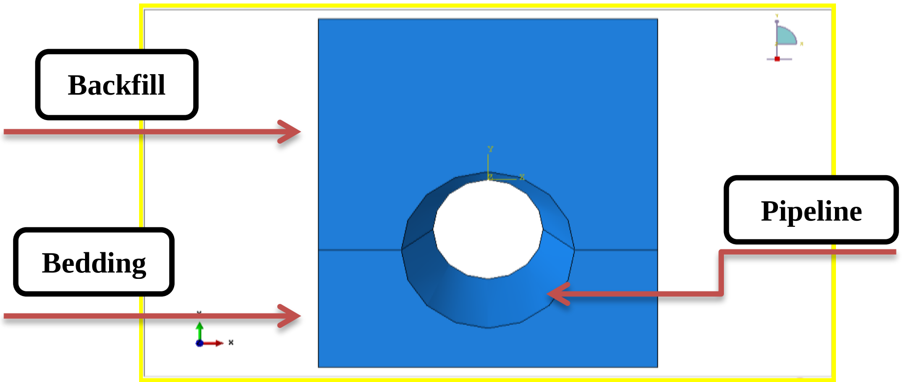

Figure8. Assembly of pipeline and soil

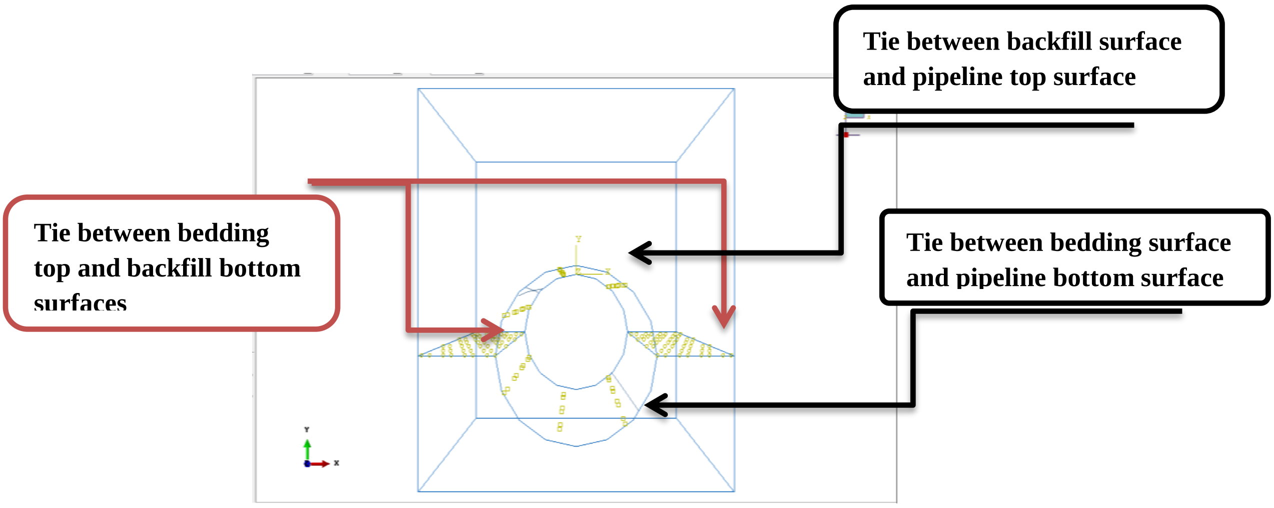

Figure9. Interaction between the soil and a pipeline

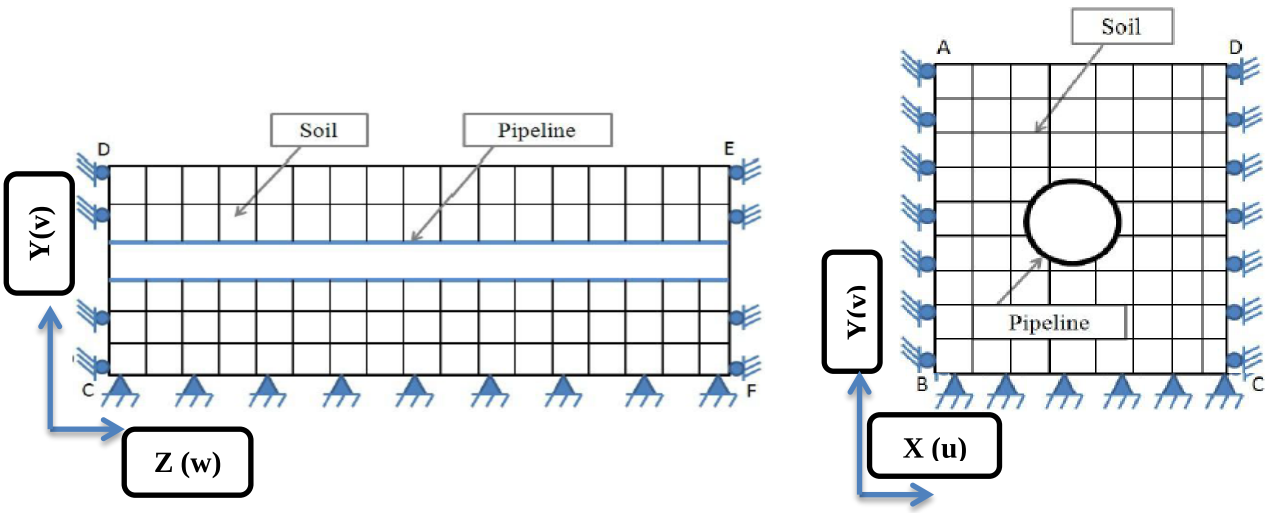

Figure10. Boundary conditions of the 3D-finite element of soil model, **Lee, 2010.**

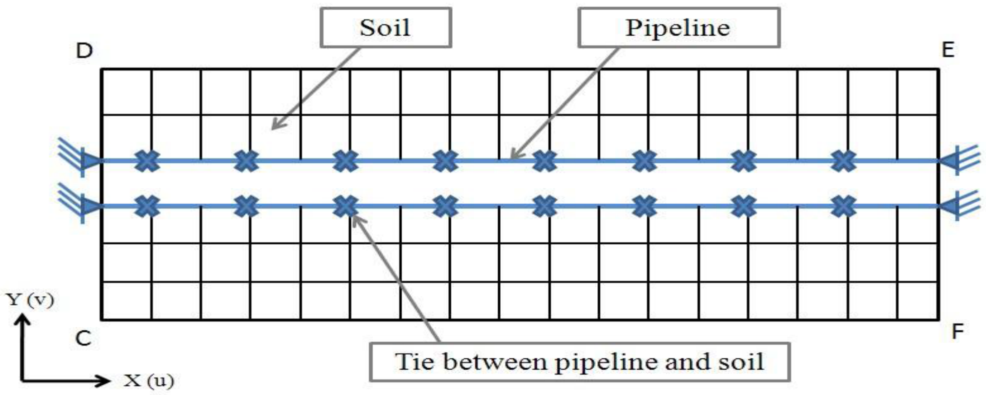

Figure11. Roller boundaries for two end surfaces of pipeline**, Lee, 2010**

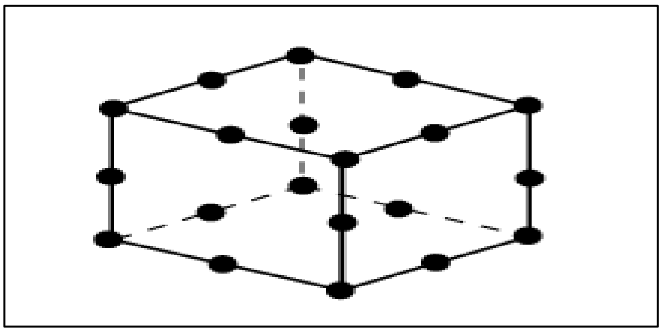

Figure12. Quadratic element (20-node brick, C3D20R), **Abaqus Theory Manual, 2009**

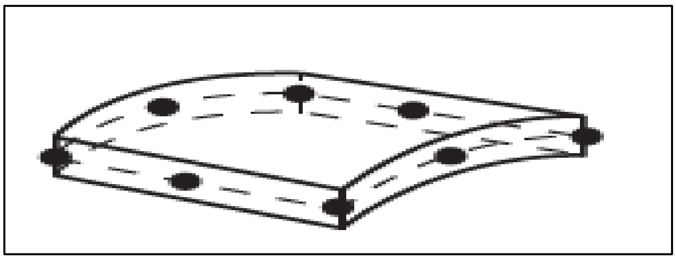

Figure13. Shell element (8-node shell, S8R)**, Abaqus Theory Manual, 2009**

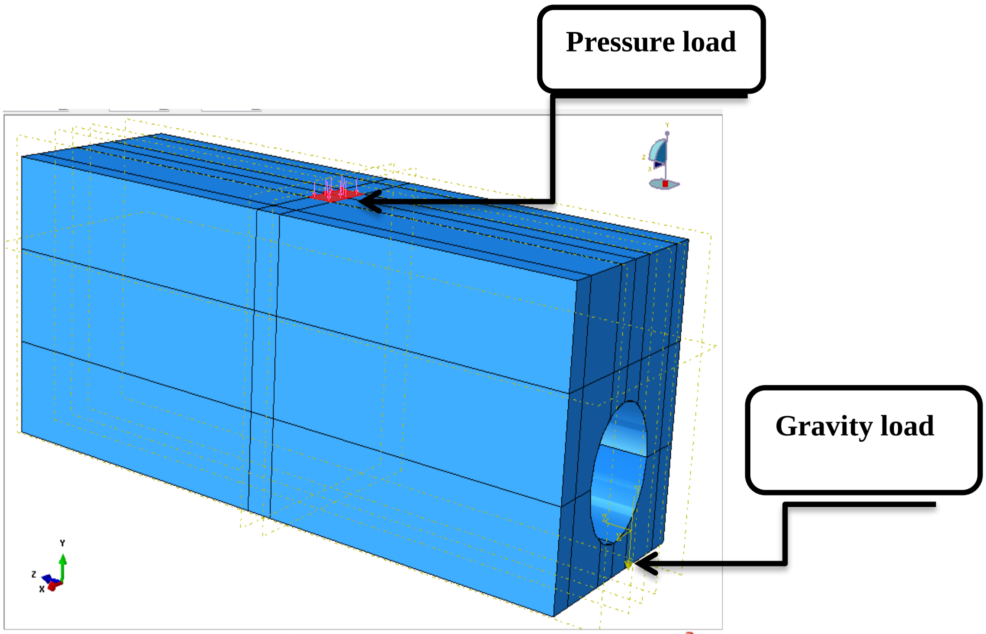

Figure14. Representation of loads on assembly of soil and pipeline models

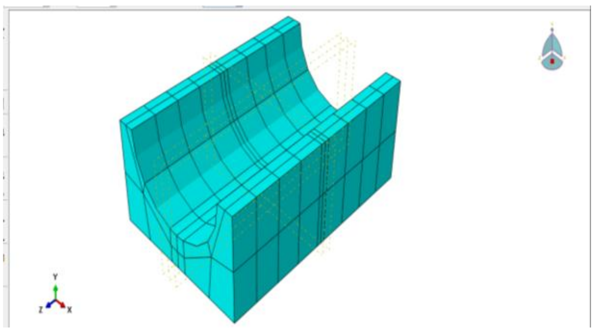

(a) Bedding Model

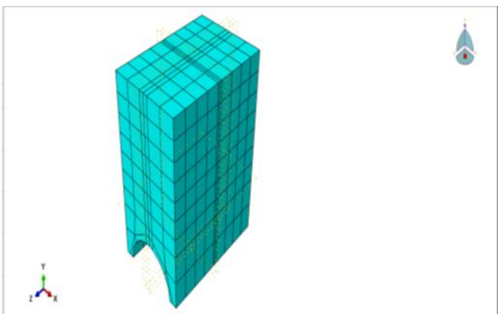

(b) Backfill Model

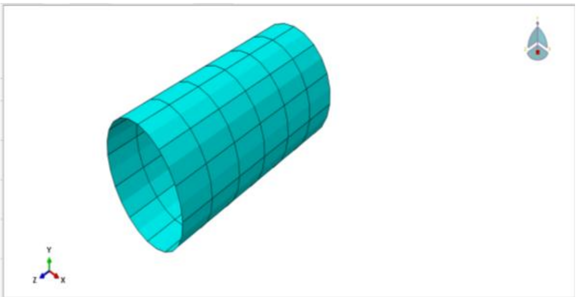

(c) Pipeline Model

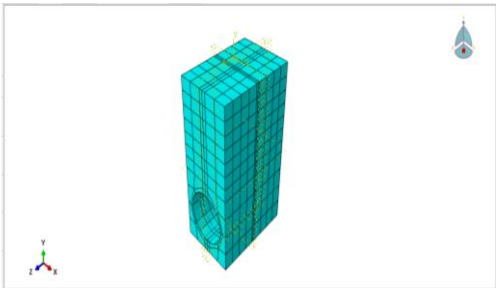

(d) Assembly Model

Figure15. Meshing of soil and pipeline

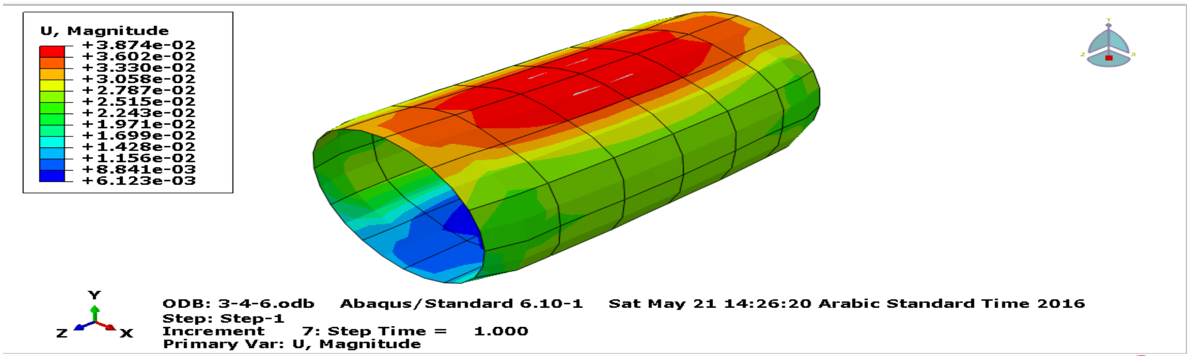

Figure16. Deformations of GRP pipelines

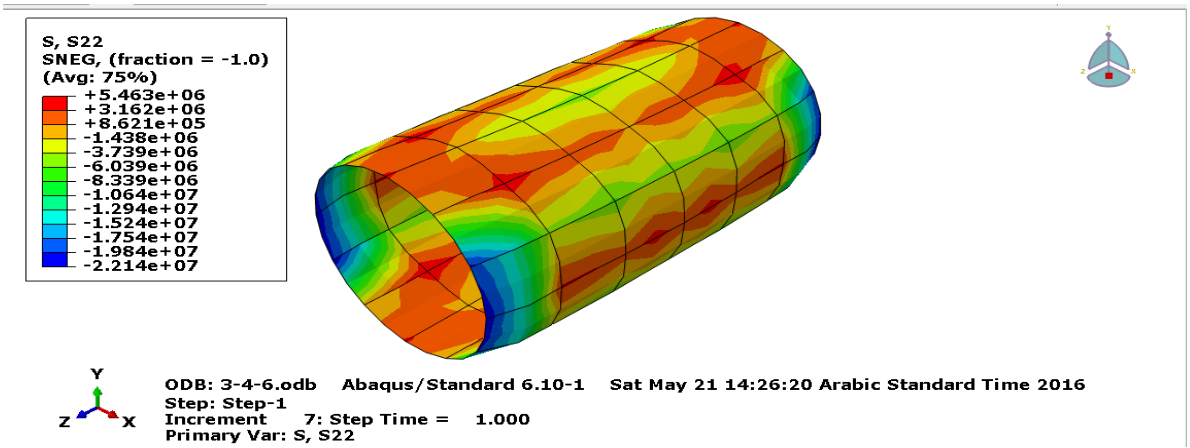

Figure17. Stresses in GRP pipelines

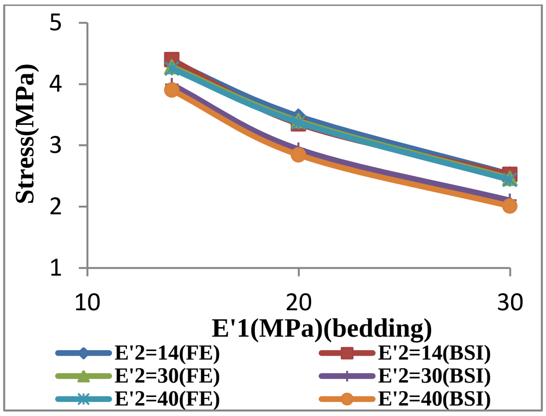

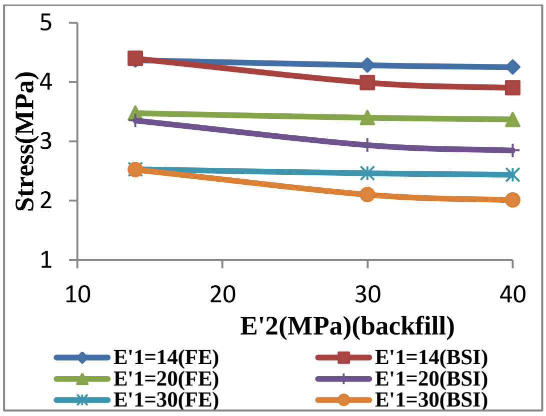

Diameter=3m, trench width=4m, depth=3m

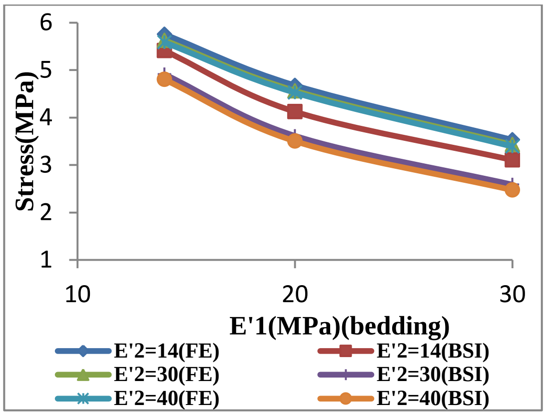

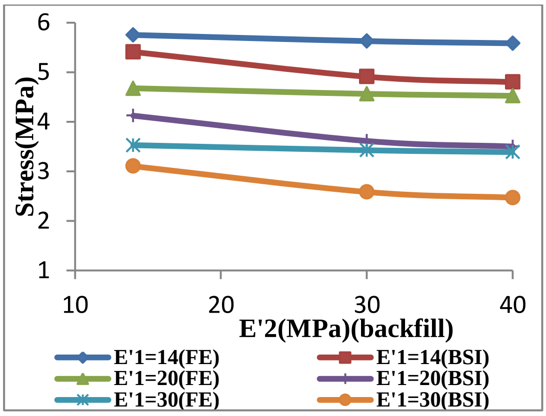

Diameter=3m, trench width=4m, depth=4.5m

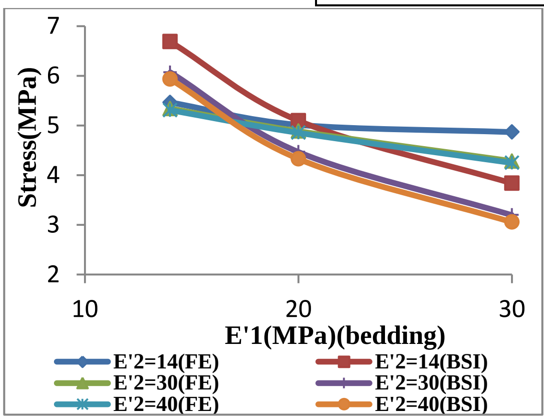

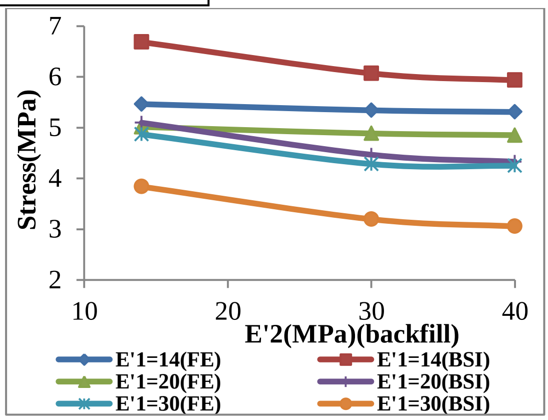

Diameter=3m, trench width=4m, depth=6m

Figure18. Maximum longitudinal stress in GRP pipe of (3.0m) diameter placed in different types of soil (Bedding and Backfill).

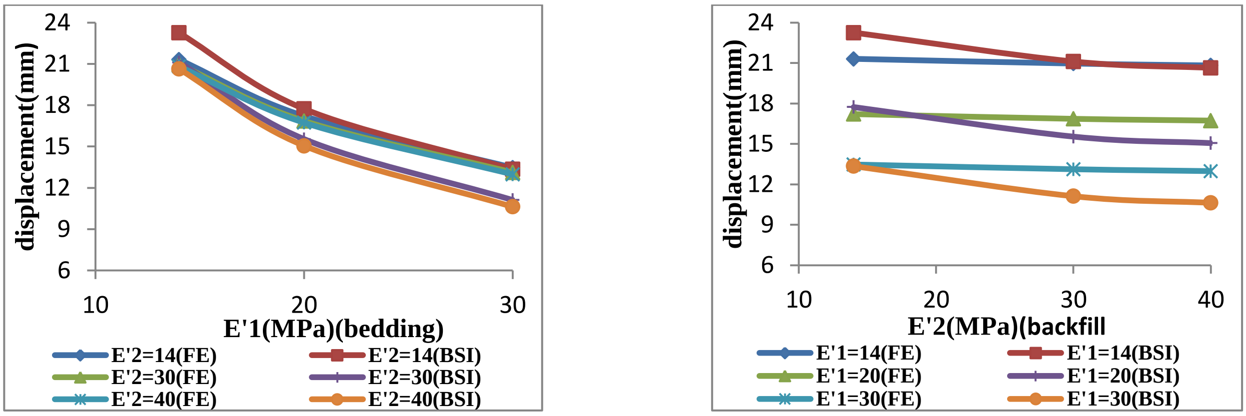

Diameter=3m, trench width=4m, depth=3m

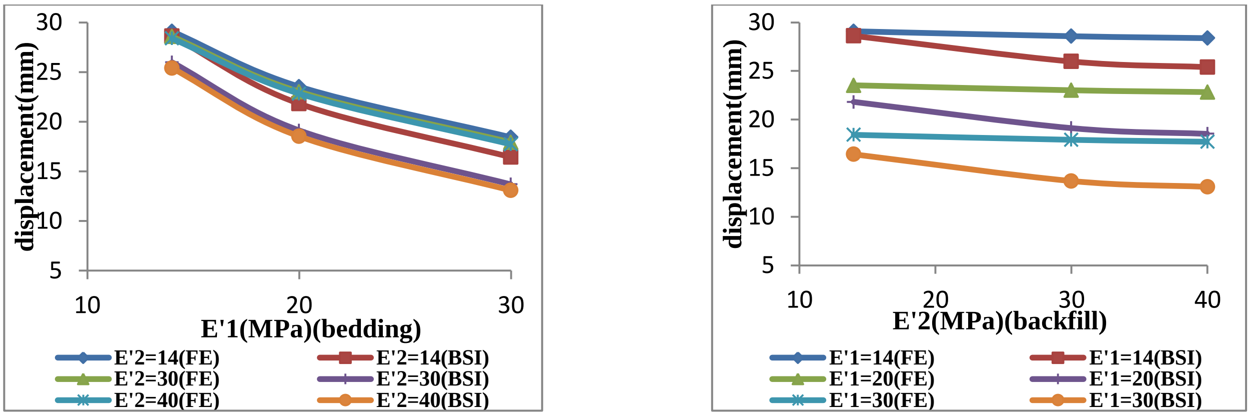

Diameter=3m, trench width=4m, depth=4.5m

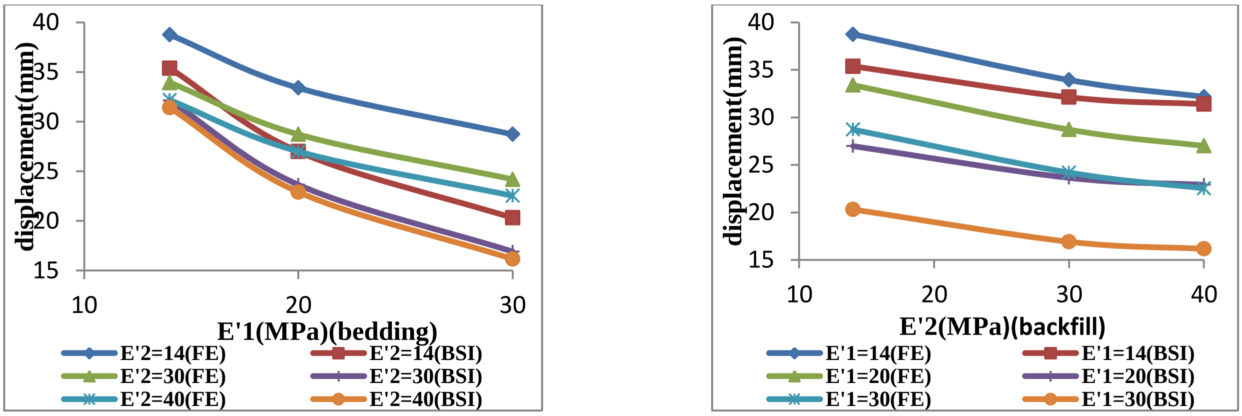

Diameter=3m, trench width=4m, depth=6m

Figure19. Maximum vertical displacement in GRP pipe of (3.0m) diameter placed in different types of soil (Bedding and Backfill).

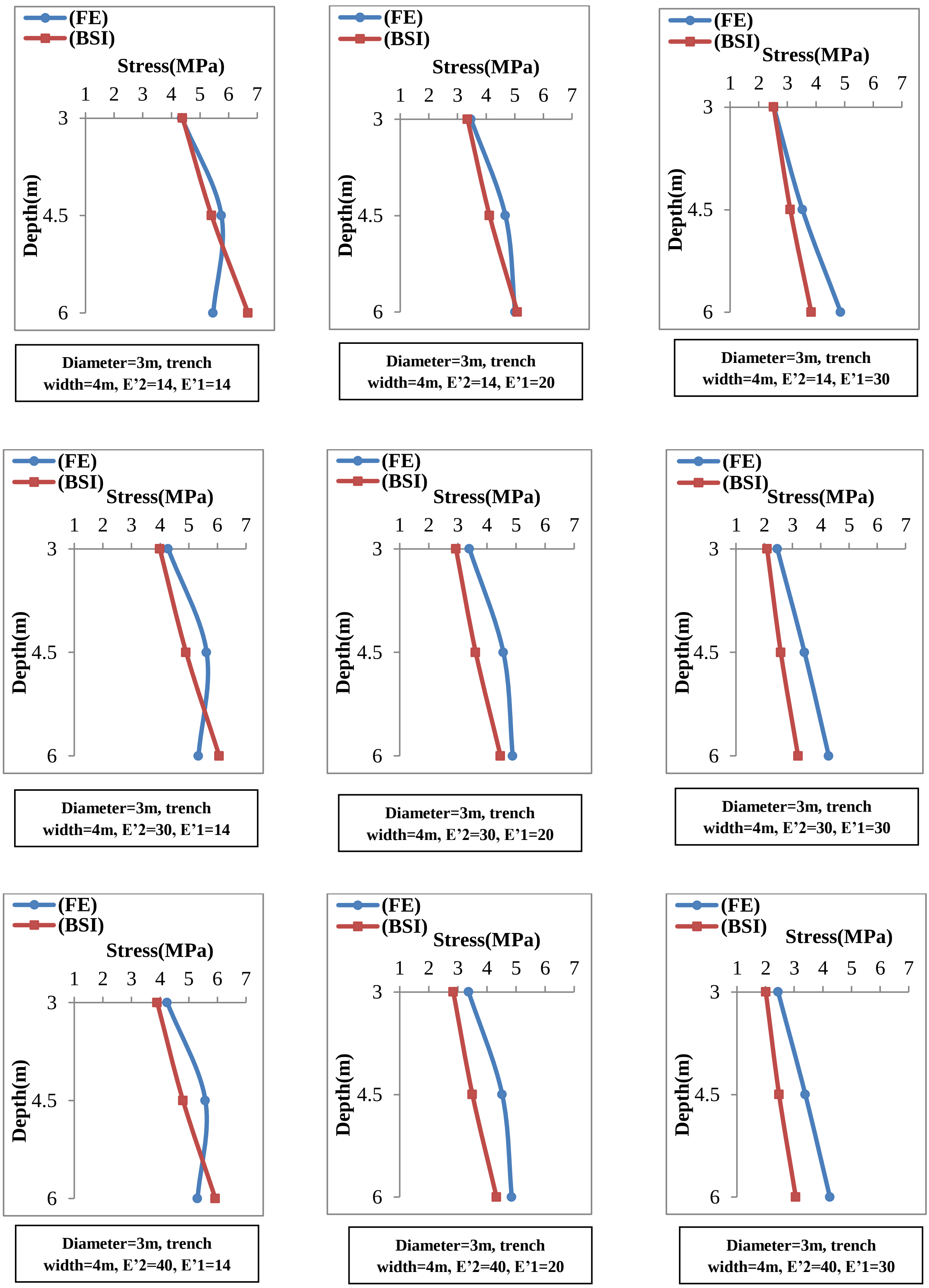

Figure20. The variation of maximum longitudinal stress within the GRP pipe wall versus depth of backfilling above pipe

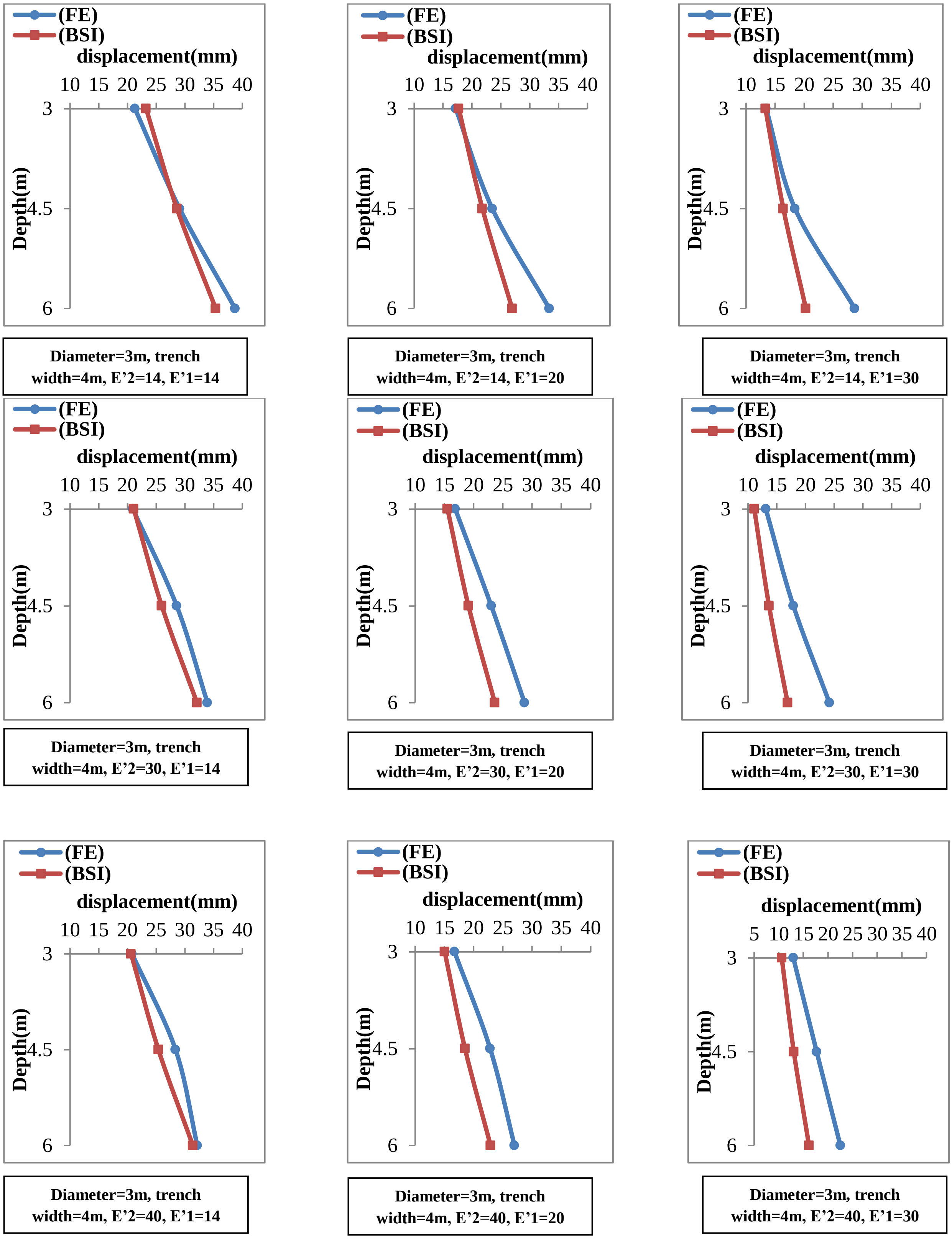

Figure21. The variation of maximum vertical displacement (deformation) within the GRP pipe wall versus depth of backfilling above pipe

Table1. Guide values of Spangler modulus for native soils (E'_3)**, (BS EN 1295-1), 1998**

Soil type	**Spangler modulus for soils in various conditions (MN/m^2)**				
	Very dense	**Dense**	**medium dense**	**Loose**	**Very loose**
Gravel	Over 40	15to 40	9 to 15	5 to 9	3 to 5
Sand	15 to 20	9 to 15	4 to 9	2 to 4	1 to 2
Clayey, silty sand	10 to15	6 to 10	2.5 to 6	1.5 to 2.5	0.5 to 1.5
Clay	Very hard	11 to 14			
	Hard	10 to 11			
	Very stiff	6 to 10			
	Stiff	4 to 6			
	Firm	3 to 4			
	Soft	1.5 to 3			
	Very soft	0 to 1.5			

Table2. Properties of bedding and backfill soils used in the study

Term	**Bedding**	**Backfill**
Density (kg/m^3)	1950	1950
Young's modulus (MPa)	14	14
	14	30
	14	40
	20	14
	20	30
	20	40
	30	14
	30	30
	30	40
Poisson's ratio	0.3	0.3

Table3. Material properties of GRP pipeline**, BS 5480, (1977)**

Term	**value**
Mass density (kg/m^3)	1850
Stiffness (N/m^2)	5000
Young's modulus (MPa)	(stiffness*D^3)/I
Poisson's ratio	0.3

Evaluating Water Damage Resistance of Recycled Asphalt Concrete Mixtures

Prof. Saad I. Sarsam
Professor, Civil Eng. Department
College of engineering-University of Baghdad
E-mail: saadisasarsam3@yahoo.com

Ehsan A. Hasan
B.Sc. Civil Eng. Department
College of engineering-University of Baghdad
E-mail: ehsanali1987@yahoo.com

ABSTRACT

Recycling process presents a sustainable pavement by using the old materials that could be milled, mixed with virgin materials and recycling agents to produce recycled mixtures. The objective of this study is to evaluate the impact of water on recycled asphalt concrete mixtures, and the effect of the inclusion of old materials into recycled mixtures on the resistance of water damage. A total of 54 Marshall Specimens and 54 compressive strength specimens of (virgin, recycled, and aged asphalt concrete mixtures) had been prepared, and subjected to Tensile Strength Ratio test, and Index of Retained Strength test. Four types of recycling agents (used oil, oil + crumb rubber, soft grade asphalt cement, and asphalt cement + Sulphur powder), were adopted to prepare recycled mixtures, and the recycling agent of (soft grade asphalt) was used to prepare mixtures with further old materials contents. It was found that the Tensile Strength Ratio exceeds 75% for all recycled mixtures, and the recycled mixture with (oil + rubber) and 50% old materials content, had the highest Tensile Strength Ratio value comparing to other recycled mixtures. Results of Index of Retained Strength showed that mixtures with (Soft Ac) and (Ac + Sulphur) and 50% old materials, exceeded the Index of Retained Strength value for virgin mixture. Index of Retained Strength values decreased as the old materials content increased, Index of Retained Strength was (80.5%, 74.5%, 71.6%, and 67.62%) for recycled mixtures with (50%, 60%, 70%, and 80%) old materials content respectively.

Key words: recycled asphalt concrete, water damage, tensile strength ratio, index of retained strength, recycling agent.

تقييم مقاومة التأثير الضار للماء لخلطات الخرسانة الاسفلتية المعاد تدويرها

سعد عيسى سرسم
استاذ- كلية الهندسة
قسم الهندسة المدنية - كلية الهندسة – جامعة بغداد

احسان علي حسن
طالب دراسات عليا
قسم الهندسة المدنية – كلية الهندسة – جامعة بغداد

الخلاصة

ان عملية اعادة التدوير تقدم طبقة تبليط مستدامة عن طريق استخدام المواد القديمة التي يتم قشطها من هذه الطبقة، هذه المواد من الممكن مزجها مع المواد الجديدة ومعاملات اعادة التدوير لانتاج خلطات الخرسانة الاسفلتية المعاد تدويرها، ان الاهداف الرئيسية من هذه الدراسه هي تقييم التأثير الضار للماء على خلطات الخرسانه الاسفلتية المعاد تدويرها، وتاثير احتواء الخلطات المعاد تدويرها على كميات اكبر من المواد القديمه على مقاومة تاثير الماء. ٥٤ نموذج مارشال و ٥٤ نموذج مقاومة الانضغاط لكل من (الخلطات الجديدة، الخلطات المعاد تدويرها، والخلطات المتقادمه) تم تحضيرها، وتم تعريض هذه النماذج لفحص نسبة الشد غير المباشر، ولفحص مؤشر القوة المتبقية، لتقييم مقاومة هذه النماذج لتاثير الماء. اربع انواع من معاملات اعادة التدوير (الزيت المستعمل، الزيت+فتات المطاط، الاسفلت

السمنتي ذو تدرج الاختراق العالي، و الاسفلت السمنتي + مسحوق الكبريت)، تم استخدامها لتحضير الخلطات المعاد تدويرها، ومعامل اعادة التدوير (الاسفلت السمنتي ذو تدرج الاختراق العالي) تم استخدامه لتحضير خلطات بكميات اكبر من المواد القديمة. لقد تم ايجاد ان قيم نسبة الشد غير المباشر كانت اكبر من ٧٥% لكل الخلطات المعاد تدويرها، وان الخلطات المعاد تدويرها التي تحتوي على (الزيت+فتات المطاط) ومواد قديمة بنسبة ٥٠%، اظهرت قيمة اعلى لنسبة الشد غير المباشر مقارنة بانوع الخلطات المعاد تدويرها الاخرى. فحص مؤشر القوة المتبقية اظهر اداء جيد للخلطات المعاد تدويرها، حيث ان الخلطات التي تحتوي على (الاسفلت السمنتي ذو تدرج الاختراق العالي) و (الاسفلت السمنتي + مسحوق الكبريت) ومواد قديمة بنسبة ٥٠%، تجاوزت مؤشر القوة المتبقية للخلطة الجديدة. ان مؤشر القوة المتبقية تناقص مع ازدياد محتوى المواد القديمة في الخلطات المعاد تدويرها، قيم مؤشر القوة المحتجزة كانت (٨٠،٥ %، ٧٤،٥ %، ٧١،٦ %، و ٦٧،٦٢%) للخلطات المعاد تدويرها التي تحتوي (٥٠%، ٦٠ %، ٧٠ %، و٨٠ %) مواد قديمة بالتتالي.

الكلمات الرئيسية: خرسانة اسفلتية معادة ،الضرر بالرطوبة، معامل قوة الشد، معامل القوة المتبقية، معيد التاهيل

1. INTRODUCTION

The continuous process of construction and maintenance of pavement structures and the increasing costs of pavement materials had put the light on the recycling approach as a worthwhile technique to be considered, **Ramanujam, 2000**. Recycling is the process of reuse the existing pavement materials that are no longer serve the traffic effectively. Recycling could be considered as a step toward sustainable roadway construction, **Sarsam, 2011.** When the pavement mixture reaches its service life, milled materials still maintain considerable value. The milled materials, reclaimed asphalt pavement (RAP), can be reused in virgin hot asphalt mixture to reduce the amount of new material that needs to be used, **Al-Qadi et al., 2007**. The reclaimed asphalt pavement (RAP) is a removed and processed pavement material containing old aggregate and asphalt binder which is oxidized (aged) during service in the field. In a hot-mix recycling process, the RAP is combined with virgin (new) asphalt, virgin aggregate and, in some cases, recycling agent to produce a recycled asphalt mixture, **Doh et al., 2008**. **Colbert and You, 2012** investigated the influence of fractionated reclaimed asphalt pavement (RAP) materials on asphalt mixture performance. The RAP mixture percentages used were 15%, 35%, and 50% in the study**.** The asphalt mixture moisture susceptibility results for the TSR tes**t** showed that RAP mixtures of 35% RAP and 50% RAP have a TSR value greater than 0.80. The control mixture has a TSR value of 0.72. **Miro et al., 2011** studied the behavior of high modulus bituminous mixes with low penetration grade bitumen and high reclaimed asphalt pavement (RAP) percentages. Four mixtures with RAP percentages of 0%, 15%, 30% and 50%, respectively, were analyzed. In order to evaluate moisture sensitivity, specimens were conditioned by immersion in water for 72 hour at 40ºC. The Indirect Tensile Strength Ratio (ITSR) was determined for conditioned and non-conditioned cylindrical specimens at 15ºC. Values were higher than 80%, suggesting that mixtures had good resistance to the action of water. However, these values dropped with increasing RAP content. **Sarsam and Shujairy, 2015** Assessed the fatigue life of reclaimed asphalt concrete after it was recycled with Nanomaterial additives using roller compacted asphalt concrete specimens. **Sarsam and Al-Zubaidi, 2015** studied the resistance to moisture damage of recycled asphalt concrete pavement using indirect tensile strength test. **Sarsam and AL-Shujairy, 2016** investigated the influence of recycling agent type on resilient modules and rutting resistance of asphalt concrete pavement using wheel tracking test on slab specimens.

2. MATERIALS PROPERTIES

2.1 Virgin Materials

2.1.1 Asphalt Cement

Asphalt cement of penetration grade (40-50) was used as a virgin binder and introduced into mixtures, it was brought from Al-Duarah refinery**.** Tests conducted on asphalt cement confirmed that its properties complied with the specifications of State Commission of Roads and Bridges, **SCRB, 2003**. **Table 1** presents the physical properties of asphalt cement.

2.2 Coarse and Fine Aggregate

Crushed coarse aggregate (retained on sieve No.4) was obtained from AL-Nibaee quarry. Crushed sand was used as Fine aggregate (particle size distribution between sieve No.4 and sieve No.200), it was brought from the same source. It consists of hard, tough grains, free from loam and other deleterious substances. Coarse and fine aggregate were tested and the physical properties are listed in **Table 2**.

2.3 Mineral Filler

Mineral filler used in this study is limestone dust obtained from Erbil, the physical properties of the filler are listed in **Table 3**.

2.4 Selection of Aggregate Gradation

The selected gradation in this study followed the **SCRB, 2003** specification, with 12.5 (mm) nominal maximum size. **Table 4** and **Fig.1** show selected aggregate gradation.

2.5 Aged Materials

The Reclaimed asphalt mixture was obtained from milled highway in specific project in Al-Aadhamiya at Baghdad. This highway was constructed in 1988 by French company, before milling, the highway was heavily deteriorated with various cracks and ruts existing on the surface, the milling depth of the project was 5 cm. Reclaimed asphalt mixture obtained was assured to be free from deleterious substances and loam that gathered on the top surface. The reclaimed mixture was subjected to extraction test according to **ASTM D1856, 2009** procedure to obtain binder and filler content, gradation and properties of aggregate, **Table 5** presents the properties of aged materials after extraction test. Gradation for the old aggregate obtained from aged mixture was determined, ten samples has been selected randomly from the milled material stack, these samples were subjected to extraction test to isolate binder from aggregate, then aggregate was sieved and separated to various sizes to calculate gradation for each sample, the differences between samples were in a minor extent, and the average gradation of the ten samples obtained to be the old aggregate gradation as shown in **Table 6**.

2.6 Recycling Agents

2.6.1 Used Oil

Used oil obtained from gasoline motor vehicle with a run period of 3200 (km) have been used in this study as a recycling agent.

2.6.2 Used Oil Blended with Crumb Rubber

Crumb rubber was obtained from local market as a disposal of tires that grinded. It was blended with used oil and chlorine in the following components percentages: (77% used oil + 22% crumb rubber + 1 % chlorine) as addressed by **Sarsam, 2007**. The used oil was heated to nearly 100ºc and crumb rubber was added to it with stirring, then chlorine was added as a solvent to increase the homogeneity of blend. Particle size distribution of crumb rubber is presented in **Table 7**.

2.6.3 Soft Grade Asphalt Cement

Asphalt cement of penetration grade (100-110) from Al-Dora refinery was adopted in this study. Its physical properties are listed in **Table 8**.

2.6.4 Asphalt Cement Blended with Sulphur Powder

It was addressed by **Elian, 1989** that recycled mixes with Sulphur exhibit significantly better engineering properties than conventional mixtures. Iraq produce Sulphur, consequently it could be economically possible to use Sulphur in recycling process. Same type of AC (40-50) that was used as a virgin binder, was heated to nearly 110ºc, and the Sulphur powder was added to the AC with stirring until homogenous blend was achieved. It should be aware that this process conducted in good ventilated room. The component percentage of the blend was 20/80 Sulphur/asphalt. Its physical properties are listed in **Table 9.**

3. PREPARATION OF SPECIMENS

3.1 Preparation of Virgin Mixture

The combined aggregate was heated to a temperature of (160ºC) before mixing with asphalt cement. The virgin asphalt cement was heated to a temperature of (135ºC) to produce a kinematic viscosity of (170±20) centistokes. Then, asphalt cement was added to the heated aggregate to achieve the desired amount, and mixed thoroughly until all aggregate particles are coated with asphalt cement.

3.2 Preparation of Recycled Mixture

First, the mixing ratio of virgin/old material should be determined, to specify the amount of RAP, amount and gradation of virgin aggregate, amount of virgin binder and recycling agent that should be added. RAP was heated to approximately 140ºC. Coarse and fine aggregate was combined with mineral filler to meet the specified gradation, and then aggregate was heated to 160ºC. Virgin binder and recycling agent were heated to 130ºC separately before they were added to the heated RAP and aggregate at the desired amount, and mixed thoroughly until all aggregate particles were coated with asphalt cement and recycling agent. The recycled mixture was prepared with using Four mixing ratios of (50/50, 40/60, 30/70, and 20/80) virgin/old material were prepared, and Four types of recycling agents have been used in recycled mixture (used oil, used oil with crumb rubber, soft asphalt cement, asphalt cement with Sulphur).

3.3 Preparation of Aged Mixture

Aged mixture was prepared from the aged material obtained from field. It was heated to 145ºC. Aged mixtures were tested to investigate the improvement in performance after recycling of mixtures.

3.4 Compaction of Asphalt Concrete Specimens

3.4.1 Marshall Specimen

It is a cylindrical specimen of 4 inches (102 mm) in diameter and 2.5 ±0.05 inches (63.5 mm) in height. Marshall Mold, spatula, and compaction hammer were heated on a hot plate to a temperature between (120-150ºC). The temperature of mixture immediately prior to compaction temperature was (145-150ºC). The mold assembly was placed on the compaction pedestal and 75 blows on the top and the bottom of specimen were applied with specified compaction hammer.

3.4.2 Compressive Strength Specimen

It is a cylindrical specimen of 4 inches (101.6 mm) in diameter and 4 inches in height. It was compacted using gyratory compactor, because this method of compaction simulates field compaction in a progressive way. The mold of gyratory compactor was heated to 140ºC. The asphalt mixture was placed in the preheated mold at temperature of (140-150ºC). By introducing the necessary information about specimen height, mass, and theoretical density for the device software, the compaction process started. When specimen reaches the specified height, compaction process will stop automatically and the mold will be discharged from the device.

4. TESTING PROGRAM

The testing program include subjecting virgin specimens, recycled specimens of the four types of recycling agents and old materials content of 50%, recycled specimens with (soft grade AC) and different old materials contents (60%, 70%, 80%) , and aged specimens to tensile strength ratio test, and index of retained strength test.

4.1 Tensile Strength Ratio Test

The procedure followed **ASTM D-4867, 2009**. A set of six specimens were prepared, three specimens were tested for indirect tensile strength by storing in a water bath at 25ºC for 30 minutes, and an average value of ITS for these specimens was computed as S_I (ITS for unconditioned specimens). The other three specimens were conditioned by placing in a water bath for 24 hours at 60ºC, then they were placed in a water bath at 25ºC for 1 hour, and they were tested for indirect tensile strength, the average value was computed as S_{II} (ITS for moisture-conditioned specimens). The indirect tensile strength ratio could be calculated from the following equation:

$$\boldsymbol{TSR = \frac{S_{II}}{S_I} \times 100} \quad \ldots\ldots\ldots\ldots\ldots\ldots\ldots (1)$$

TSR = indirect tensile strength ratio, %

S_I= average ITS for unconditioned specimens, kPa

S_{II} = average ITS for moisture-conditioned specimens, kPa

4.2 Index of Retained Strength Test

The test followed the procedure of **ASTM D1075-2009**. A set of six specimens were prepared for this purpose. Three specimens were stored at air bath for 4 hours at 25ºC, and then tested for compressive strength and the average value was recorded (S_I). The other three specimens were stored in a water bath at 60ºC for 24 hours, then they were stored in another water bath at 25ºC for 2 hours, and the compressive strength test was performed on these specimens, and also the average value was recorded (S_{II}). The index of retained strength could be calculated by the following equation:

$$\boldsymbol{IRS = \frac{S_{II}}{S_I} \times 100} \quad \ldots\ldots\ldots\ldots\ldots\ldots\ldots\ldots \text{(2)}$$

IRS = Index of Retained Strength, %
S_{II} = average compressive strength of moisture-conditioned specimens, kPa
S_I = average compressive strength of dry specimens, kPa

5. RESULTS AND DISCUSSION

5.1 Tensile Strength Ratio Test

The results of tensile strength ratio showed that recycled mixtures had good resistance to the action of water. The tensile strength ratio was higher than 75% for all recycled mixtures with mixing ratio of 50/50 old/virgin materials, **Fig.2**., and the recycled mixture with (Oil + Rubber) had the highest T.S.R value comparing to other recycled mixtures, although T.S.R values for all recycled mixtures were lower than virgin mix, but the results revealed high improvement in tensile strength for these mixtures comparing to aged mixture. Results were close for mixtures with (Oil, and Ac + Sulphur) recycling agents, which were lower than mixture with (Soft Ac). Results revealed that tensile strength ratio values decreased when the old materials content increased into recycled mixtures, which means that recycled mixtures with higher old materials content might become more affected by water damage, and this result meets with the findings of **Miro et al., 2011**. **Fig.3** illustrates tensile strength ratio results for recycled mixtures with different mixing ratios.

5.2 Index of Retained Strength Test

Results of I.R.S showed a good performance for recycled mixtures, as mixtures with (Soft asphalt cement) and (asphalt cement + Sulphur) and old materials content of 50% exceeded the I.R.S value for virgin mixture, which indicates that these mixtures were less susceptible to moisture damage as compared with virgin mix. This behavior may be explained by the hardened binder contained in recycled mixtures and the role of recycling agents which lead to more water resistance mixture. All (I.R.S) values for recycled mixtures with mixing ratio (50/50) old/virgin materials, exceeded 70 %, and achieved the criteria of **SCRB, 2003** for index of retained strength. **Fig.4** presented the results for I.R.S. Index of retained strength values decreased as the content of old materials into recycled mixtures increased, that confirms the reduction in water resistance of mixtures with higher old materials content, however all recycled mixtures except mixture with 80%

old materials achieved the criteria of **SCRB, 2003** for I.R.S (> 0.7). **Fig.5** illustrates the result values of index of retained strength.

6. CONCLUSIONS

1- The recycled mixture with (Oil + Rubber) had the highest T.S.R value (79.72%) comparing to other recycled mixtures with mixing ratio of (50/50) old/virgin materials.
2- Tensile Strength Ratio results revealed high improvement for recycled mixtures with mixing ratio (50/50) old/virgin materials, comparing to aged mixture. The percentages of improvement for these mixtures were (60%, 57%, 56%, and 65%) for mixtures with (soft AC, AC + Sulphur, oil, and oil + rubber) respectively.
3- All (I.R.S) values for recycled mixtures with mixing ratio (50/50) old/virgin materials, exceeded 70 %, and achieved the criteria of (SCRB 2004) for index of retained strength.
4- Index of Retained Strength values decreased as the content of old materials into recycled mixtures increased, the values of Index of Retained Strength were (80.5%, 74.5%, 71.6%, and 67.62%) for recycled mixtures with (50%, 60%, 70%, and 80%) old materials content respectively.
5- Recycled mixture with (soft AC) and old materials content of 80% had I.R.S value of 67.62% and did not achieve the criteria of (SCRB 2003) for index of retained strength.

REFERENCES

- ASTM, 2009, *Road and Paving Materials*, Annual Book of ASTM Standards, Volume 04.03, American Society for Testing and Materials, USA.

- Al-Qadi, I., Elseifi, M., and Carpenter, S., 2007, *Reclaimed Asphalt Pavement—A Literature Review*, Report No. FHWA-ICT-07-001, Illinois Centre for Transportation, Rantoul, IL.

- Colbert, B., and You, Z., 2012, *The Determination of Mechanical Performance of Laboratory Produced Hot Mix Asphalt Mixtures Using Controlled RAP and Virgin Aggregate Size Fractions,* Construction and Building Materials, Vol. 26, pp. 655-662.

- Doh Y.S., Amirkhanian S.N., and Kim K.W., 2008, *Analysis of Unbalanced Binder Oxidation Level in Recycled Asphalt Mixture Using GPC,* Construction and Building Materials, Vol. 22, pp. 1253–1260.

- Elian, A.A., 1989, *Recycling of Old Asphalt Pavement and the Use of Sulphur in Asphalt Mixes in Jordan*, IRF 11th World Meeting, Proceeding Vol. 3, Korea, PP. 103-109.

- Miro, R., Valdés, G., Martinez, A., Segura, P., Rodriguez, C., 2011, *Evaluation of High Modulus Mixture Behavior With High Reclaimed Asphalt Pavement (RAP)*

Percentages for Sustainable Road Construction, Construction and Building Materials, Vol. 25, PP. 3854–3862.

- Ramanujam, J.M., 2000. *Recycling of Asphalt Pavements*, Department of Transport and Main Roads, Queensland, Internet link http://www.docstoc.com/docs/42047013/recycling-of-asphalt pavements

- Sarsam S.I., 2007. *A Study on Aging And Recycling of Asphalt Concrete Pavement*, University of Sharjah Journal of Pure & Applied Sciences, Vol. 4, No. 2, pp. 79-96.

- Sarsam S. I. 2011. *Recycling is a step toward sustainable roadway construction*, Proceedings, 1st symposium of sustainable engineering, University of Baghdad, April.

- Sarsam S. and Shujairy A. 2015. *Assessing Fatigue Life of Reclaimed Asphalt Concrete Recycled with Nanomaterial Additives*, International Journal of Advanced Materials Research, Public science framework, American institute of science, Vol. 1, No. 1, pp. 1-7 USA.

- Sarsam S. and Al-Zubaidi I. 2015. *Resistance to moisture damage of recycled asphalt concrete pavement*, Journal of Engineering, Vol.21, No. 5, pp 48-57.

- Sarsam S. I. and AL-Shujairy A. 2016. *Influence of recycling agent type on resilient modules and rutting resistance of asphalt concrete pavement*, Applied Research Journal, ARJ. Vol.2, Issue, 1, pp.10-18, January.

- SCRB, 2003. State Commission of Roads and Bridges, *Standard Specification for Roads & Bridges*, Ministry of Housing & Construction, Iraq.

NOMENCLATURE

Symbol	Definition
AC	Asphalt Cement
ASTM	American Society for Testing and Materials
IRS	Index of Retained Strength
ITSR	Indirect Tensile Strength Ratio
RAP	Reclaimed Asphalt Pavement
SCRB	State Commission of Roads and Bridges
TSR	Tensile Strength Ratio

Table 1 Physical Properties of Asphalt Cement.

Property	Test Conditions	ASTM Designation	Value	SCRB Specification
Penetration	25ºc, 100gm, 5sec	D5-06	42 (1/10mm)	40-50
Softening Point	(ring and ball)	D36-95	53 ºc	-
Ductility	25ºc, 5cm/min	D113-99	125cm	+100
Specific Gravity	25ºc	D70-97	1.04	-
Flash Point	Cleveland open cup	D92-05	280 ºc	>232
After thin film oven test properties D1754-97				
Retained Penetration of Residue	25ºc, 100gm, 5sec	D5-06	73 %	>55
Ductility of Residue	25ºc, 5cm/min	D113-99	67 cm	>25
Loss on Weight	163ºc, 50g,5 hrs		0.2 %	-

Table 2 Physical Properties of Coarse and Fine Aggregate.

Property	value	ASTM Designation No.
Coarse Aggregate		
Bulk specific gravity	2.564	C127-04
Apparent specific gravity	2.597	C127-04
Water absorption %	0.502 %	C127-04
Wear% (Los Angeles abrasion)	18.5%	C131-03
Fine Aggregate		
Bulk specific gravity	2.599	C128-04
Apparent specific gravity	2.826	C128-04
Water absorption %	3.092 %	C128-04

Table 3 Physical Properties of Mineral Filler.

Property	Value
Bulk Specific Gravity	2.87
% Passing Sieve No.200	99

Table 4 Properties of Aged Materials after Extraction Test**.**

Material	**Property**		**Value**
Asphalt binder	Binder content %		2.1%
Coarse aggregate	Bulk specific gravity		2.553
	Apparent specific gravity		2.6
	Water absorption %		1.2%
	Wear% (Los Angeles abrasion)		22%
Fine aggregate	Bulk specific gravity		2.590
	Apparent specific gravity		2.819
	Water absorption %		4.4%
Mineral filler	Percent passing sieve no.200		98%
	Specific gravity		2.82
Aged Mixture	Marshall Properties	Stability	3.6 kN
		flow	1.6 mm
		Air voids	7.4%
		Bulk density	2.192 gm/cm^3

Table 5 Gradation of Old Aggregate Obtained from Aged Mixture

Sieve no.	**Sieve size (mm)**	**% passing by weight**
3/4"	19	100
1/2"	12.5	95
3/8"	9.5	87
No.4	4.75	65
No.8	2.36	51
No.50	0.3	12
No.200	0.075	2

Table 6 Particle Size Distribution of Crumb Rubber

Sieve no.	**Sieve size (mm)**	**% passing by weight**
No.4	4.75	100
No.8	2.36	94
No.50	0.3	22
No.200	0.075	0

Table 7 Physical Properties of Soft Asphalt Cement Recycling Agent

Property	**Test Conditions**	**ASTM Designation No.**	**Value**
Penetration	25ºc, 100gm, 5sec	D5-06	104 (1/10mm)
Softening Point	(ring and ball)	D36-95	25 ºc
Ductility	25ºc, 5cm/min	D113-99	80 cm
Flash Point	Cleveland open cup	D92-05	250 ºc
After thin film oven test properties D1754-97			
Retained Penetration of Residue	25ºc, 100gm, 5sec	D5-06	66 %
Ductility of Residue	25ºc, 5cm/min	D113-99	46 cm
Loss on Weight	163ºc, 50g,5 hours		0.35 %

Table 8 Physical Properties of Asphalt Cement Blended with Sulphur powder

Property	**Test Conditions**	**ASTM Designation No.**	**Value**
Penetration	25ºc, 100gm, 5sec	D5-06	66 (1/10mm)
Softening Point	(ring & ball)	D36-95	42 ºc
Ductility	25ºc, 5cm/min	D113-99	110 cm
Flash Point	Cleveland open cup	D92-05	270 ºc
After thin film oven test properties D1754-97			
Retained Penetration of Residue	25ºc, 100gm, 5sec	D5-06	80 %
Ductility of Residue	25ºc, 5cm/min	D113-99	75 cm
Loss on Weight	163ºc, 50g,5 hours		0.15 %

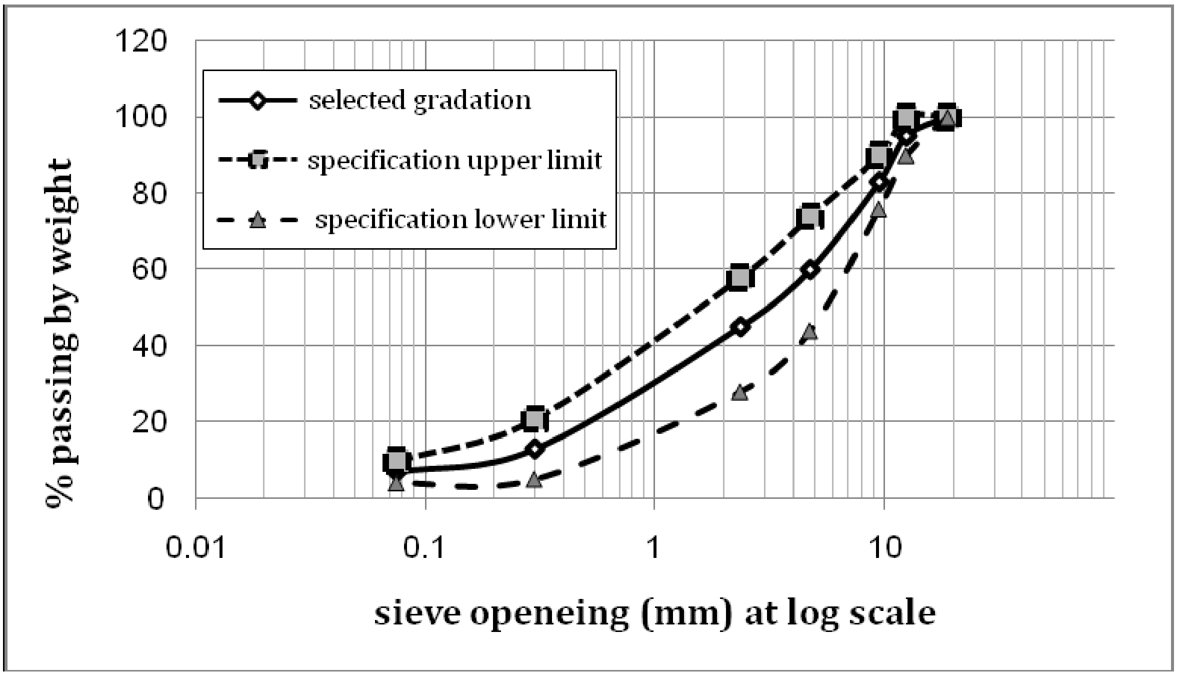

Figure.1 Selected Aggregate Gradation and Specification Limits.

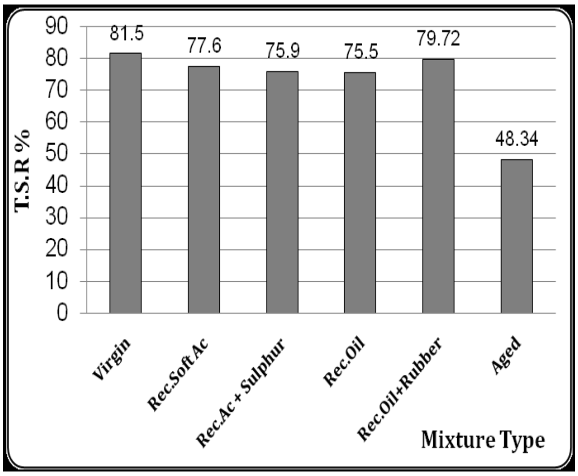

Figure. 2 TSR for various mixtures.

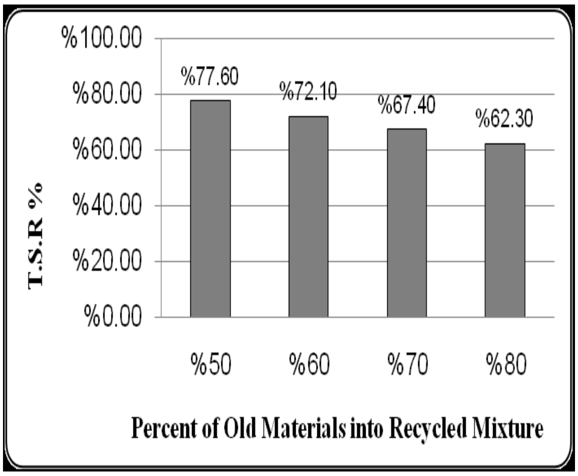

Figure. 3 TSR with Different Mixing Ratio

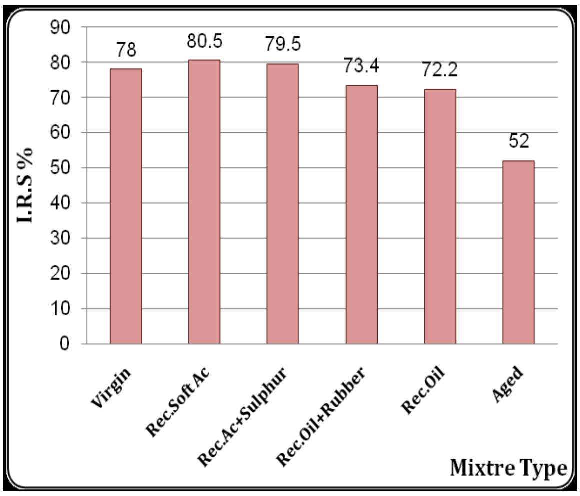

Figure. 4 IRS for various mixtures

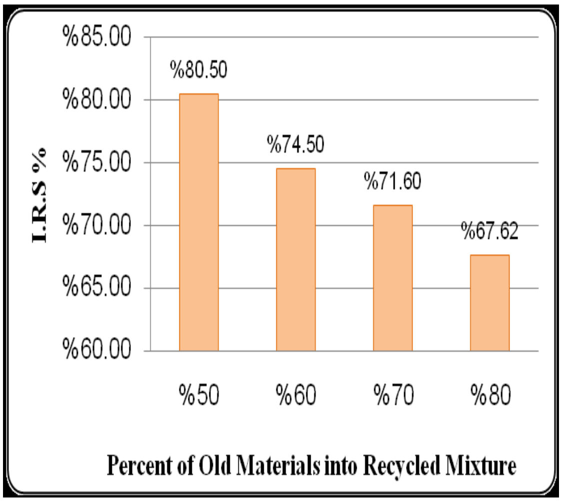

Figure.5 IRS with Different Mixing Ratio

ISSN 1726 - 4073

Journal of Engineering

A Scientific Refereed Journal
Published by
College of Engineering
University of Baghdad

January
2017

Number 1
Volume 23

ISSN 1726 - 4073

مجلة الهندسة

مجلة علمية محكمة تصدرها
كلية الهندسة ـ جامعة بغداد

كانون الثاني
2016

العدد 1
المجلد 23